Ligand Lifecycle

Throughout Inorganic Nanomaterial Processing:

From Synthesis to Sintering

Breena M. Sperry

A dissertation
submitted in partial fulfillment of the
requirements for the degree of

Doctor of Philosophy

University of Washington
2022

Reading Committee:
Christine Luscombe, Chair
Lucien Brush
Eleftheria Roumeli

Program Authorized to Offer Degree:
Materials Science and Engineering

University of Washington

Abstract

Ligand Lifecycle Throughout Inorganic Nanomaterial Processing: From Synthesis to Sintering

Breena M. Sperry

Chair of the Supervisory Committee:
Professor Christine Luscombe
Department of Materials Science and Engineering

Organic ligands serve several critical roles during the solution-processing of nanomaterials (NMs). As a result, much effort has gone into understanding and engineering the ligands' ability to tailor NM synthesis, and later, the suspension of NMs into solution for deposition and post-processing. While the ligand's ability to tailor the final NMs properties has been widely studied, observations of ligand side-reactivity during synthesis and post-processing (*i.e.,* sintering) are emerging. Chapter 1 introduces the known processes of nanomaterials and ligands during synthesis and sintering, and the remaining chapters seek to define the internal and external variables which influence structural changes to the ligand during synthesis (Chapters 2 and 3), and how ligand selection can be leveraged to control the morphology of sintered NM thin films (Chapter 4). As a whole, this work aims investigate the lesser-known roles of the ligand during both nanomaterial synthesis and sintering, and in doing so, provides strategies on how to leverage ligand selection.

Acknowledgements

First and foremost, I graciously thank my husband, the soon-to-be Dr. Julian Freedland. Together we've conquered undergrad, and now, together we will have conquered our PhDs. Over these years, you've endlessly inspired me and have helped me become a both better person and scientist. I couldn't have done this without your support, so thank you for (literally) everything.

To my family. While this apple may have rolled far from its' tree, I thank you for always encouraging me to be me and pursue my dreams.

Thank you to all the mentors and allies who have made a great impact on me over the years. To my high school engineering teacher (Mr. Anthony Cassale) and chemistry teacher (Mr. Adam Labuda), your enthusiasm fueled my love for science and engineering and sparked my interests in clean technologies. To my undergraduate research professor (Prof. Harry Efstathiadis) for the opportunity to engage and lead hands on research when I was just finding my footing. To my industry mentor (Mr. Manikandan Ramani) for being an incredible educator and advocate, your support gave me the motivation and confidence I needed to pursue a PhD. To my teaching mentor (Dr. Luna Huang), by working alongside you I grew so much as both a leader and colleague during my PhD. Above all else, these individuals showed me that there are no limits to the sky, and encouraged me to reach for the stars.

A thank you to the Clean Energy Institute, which has been integral to my graduate experience. When coming to UW, I wanted to not only work on clean energy materials but to also to learn about the deployment and impact of clean technologies. With the support of the Clean Energy Institute (and especially Suzanne Offen) I was able to chase this dream and do so much more. Along a similar vein, I deeply thank GRID, their officers, and the entire Social Impacts

Team. You are all doing incredible and inspiring work, and I know you will achieve great things. Thank you for giving me and others the space to become a better collaborators and leader, and for all of the memories along the way!

Finally, this work would not be possible without the generous opportunity to do research with the Luscombe Group. Along the way, I have been fortunate to cross paths with many kind and brilliant people, and have learned and grown so much. I also thank the members of the MAF, MRSEC, and my committee for all your suggestions and help.

Table of Contents

List of Figures

List of Tables

List of Schemes

Chapter 1: Background and Introduction

1.1. Nanomaterials

In the past several decades, considerable effort and advancements have been made to precisely and consistently manipulate matter on the nanoscale. These advancements have generated a class of materials known as nanomaterials. Appropriately named, nanomaterials are defined by their dimensions: their size spans between 1 to 100 nanometers and they occupy either 0D (0-dimensions; *e.g.,* quantum dots), 1D (*e.g.*, nanowires, nanorods), 2D (*e.g.*, graphene, nanosheets), or 3D (*e.g.,* nanoparticles) space. Nanomaterials are designed to have deliberate physical, chemical, and functional properties by controlling size,[1–5] shape,[2,4,6,7] composition,[2,8–10] defect chemistry,[2,8–10] and surface functionality.[4,11–13] Due to their unique and engineered properties, nanomaterials are used in a wide variety of fields, including electronics, optics, magnetics, nanobiotechnology and pharmacology, catalysis, textiles, and more.[14–22]

1.1.1. A Brief History of Nanomaterials

Despite the field of nanoscience emerging only in the last century, nanomaterials have been used throughout history. Artifacts dating back thousands of years contain nanomaterials: early examples include reinforced cement (nanofibers; 2000 BC), stained and colored glass (which owes

its vibrant colors to metallic nanoparticles; 4th – 18th century), pottery glaze with metallic luster (nanoparticle-glass composites; 9th – 17th century), and reinforced steel blades (carbon nanotubes; 13th – 18th century).[23–27] Nanomaterials can also naturally form in nature: gold nanoparticles (60 – 600 nm) lie within metal ores, calcium nanostructures naturally biomineralize in biological systems, and fullerenes (C_{60}, C_{70}) and polyaromatic hydrocarbons are found in interstellar nanosoot.[28–31]

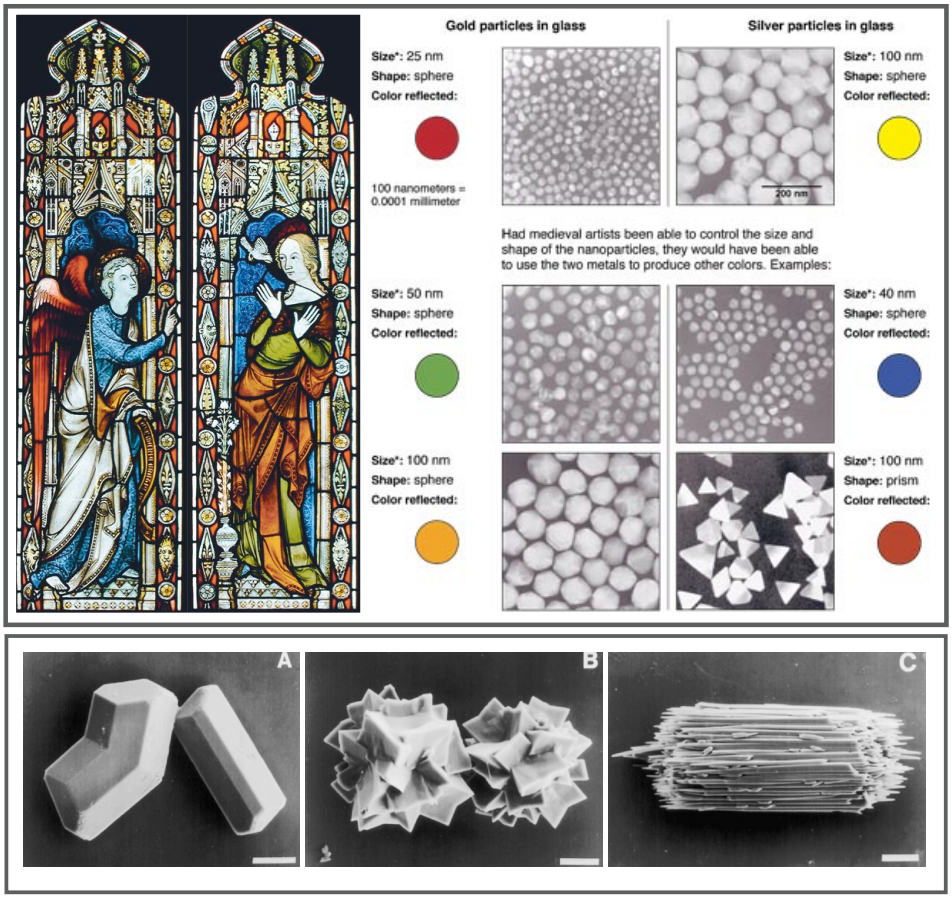

Figure 1.1. (top) Early examples of nanomaterials include stained glass (from the Stained Glass Museum, Britain) are comprised of gold and silver nanoparticles of different sizes, which give unique colors (scanning electron micrograph images from Markin, C. A., Institute of Nanotechnology, Northwestern University).[32] **(bottom)** Example of natural micron-sized particle forming through the biomineralization of calcium oleate extracted from various plants from Ref [30].[30]

Scientists have also synthesized nanomaterials well before the term 'nano' was introduced into the nomenclature. Between the 1850s and 1950s, nanomaterial synthesis was well-theorized and studied within the field of colloidal science, which lies at the intersection between chemistry, physics, and interfacial science.[33] However, early studies were typically more focused on the preparation of particles rather than the careful engineering and control over desirable material properties.

It wasn't until 1960 when physicist Richard Feynman introduced the field of nanotechnology by inviting scientists to look closer at the properties of materials and their applications.[34] As a quantum physicist, Feynman was astute in predicting that quantized materials — or materials with reduced dimension (0D, 1D, 2D) — exhibit unique properties that differ from their bulk counterparts (*i.e,* color being dependent on size). Accurately, he also predicted that the creation of smaller circuitry and semiconductor devices would be necessary for reducing the size of digital electronics and that exerting atomic control could generate novel materials for new applications.

The subsequent influx of interest in the bottom-up synthesis of nano-sized materials have enabled scientists to achieve remarkable control over engineering nanomaterials. As new materials have been discovered (*e.g.* graphene, 2004),[35] considerable effort has also been made to find avenues to synthesize them. Today, there are many thorough review papers that address the processing and applications of a large variety of nanomaterials.[14,15,17–20,22,23,36–39]

1.1.2. The Bottom-Up Synthesis of Inorganic Nanomaterials

Synthesized nanomaterials hold many advantages over traditional materials. For example, the bottom-up production of nanomaterials is less expensive, energy intensive, hazardous, and time

consuming than traditional top-down approaches which utilize bulk (≥ 1000 nm, 3D) materials.[40–47] This is because bottom-up syntheses do not require expensive or energy-intensive processing conditions and equipment. Instead, synthesized nanomaterials benefit from lower thermal budgets, less material waste, and fewer processing steps, which all allow for economically advantageous high throughput production.[40–46] Bottom-up synthesized nanomaterials are also excellent building blocks for producing bulk materials with controlled microstructure and, by extension their electrical, mechanical, magnetic, optical, or thermal properties can be tailored.[42,47–53]

The bottom-up synthesis of nanomaterials is traditionally achieved *via* two processes (nucleation and growth) that require (at minimum) two types of material (solvent and precursor). Today, the theory behind nanomaterial synthesis is well defined[11,14,22,30,54–59] and will be discussed in the following subsections. In this dissertation, we primarily focus on a class of nanomaterials known as crystalline inorganic nanomaterials.

1.1.2.1 Nucleation and growth theory

Nucleation is a process that results in a new stable phase of material (*i.e.*, nuclei) formed from a metastable parent phase. These nuclei represent the smallest stable building blocks that act as templates for further growth. For example, nucleation can describe the initial stages of ice crystal formation, the condensation of water vapor onto dust particles to form droplets, and the formation of rock candy from supersaturated solutions of sugar in water. In these examples, nucleation occurs when a material's temperature falls below the phase transformation point (*e.g.*, ice formation from water) or when the solubility limit of a solute in solution is exceeded (*e.g.* condensation of water vapor, rock candy from sugar water).[57]

In nanomaterial synthesis, nuclei form due to supersaturation of a solute (from precursor materials) in a solvent.[22,42,60–62] Supersaturation is achieved once a solute's concentration surpasses a solution's equilibrium concentration, making the solution metastable. Solutions in a metastable state have an exorbitantly high free energy and will favorably undergo a phase transition into a phase of material with an overall lower free energy. (Free energy is the thermodynamic driving force for chemical reactions or phase transformations). Classical Nucleation Theory has been used to describe the nucleation of particles (lower free energy) in a supersaturated vapor (higher free energy). These equations (**Eqns. 1.1 – 1.2**) are listed in **Table 1.1**.[57,63,64]

The nucleation of a new stable phase of material, or nuclei, from a metastable parent phase originates from the collision, arrangement, and densification of free ions or atoms in solution into clusters. An energy potential must be overcome to form these clusters, which is dependent on the solution concentration, volume, surface area, and surface energy of the nuclei being made (see **Eqn. 1.3**). Certain variables (volume, surface area, and surface energy) are highly influenced by the radii size of a stable nuclei. Clusters with radii above a critical size ($> r_c$) remain stable in solution as nuclei, whereas clusters below a critical size ($< r_c$) readily dissociate back into solution. The critical radius of stable clusters is determined by the solute concentration and the surface energy of the particle, a relationship connected by **Eqn. 1.4.**

The activation energy barrier for nucleation can be modulated depending on whether nucleation is homogenous, heterogenous, or nonclassical. Homogenous nucleation occurs as the direct crystallization of free-standing particles in solution. Heterogenous nucleation occurs on foreign solid surfaces such as the reaction crucible, seed particles, impurities, templates, or substrates. Here the energy barrier for heterogenous nucleation is typically lower than homogenous nucleation because the interfacial energy between ions (in solution) and a solid surface is lower

than the interfacial energy of forming a new surface (*i.e.,* a free-standing particle) in solution. Nonclassical nucleation, on the other hand, has the lowest energy barrier for nuclei formation and commonly occurs during nanomaterial synthesis. Here, amorphous clusters (with radii > r_c) are readily nucleated and then undergo a phase transition into a crystalline material.[62] The resulting two-step process has an overall lower free energy because the phase transformation of amorphous clusters into ordered crystallites requires less energy than direct crystallization.[62]

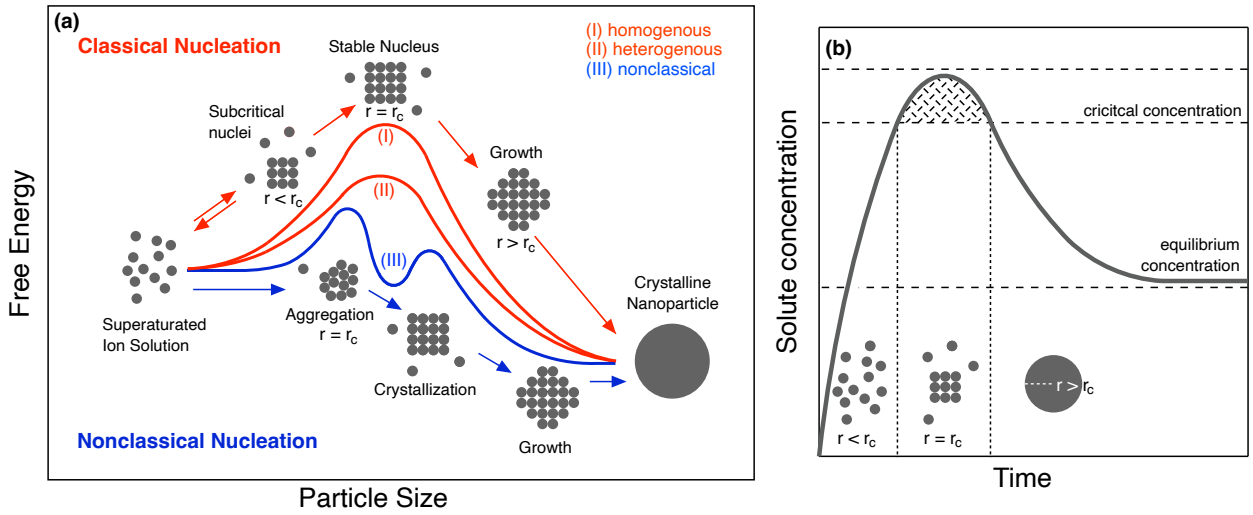

Figure 1.2. (a) The free energy model of classical (red) and nonclassical (blue) nucleation. Under classical nucleation, liberated ions locally arrange to form subcritical nuclei. These small particles readily dissociate back into solution due to high surface energy. As the ion concentration increases, larger particles can form, generating stable nuclei with radius $r > r_c$ (see **Eq. 1.4**). Under nonclassical nucleation, local aggregation into amorphous clusters occurs, requiring less energy to form stable nuclei. This multi-step process includes an additional low energy barrier to crystallize the amorphous clusters. **(b)** Relation between solute concentration and particle size. As solute are liberated by the solvent, solute concentration increases beyond a critical point, where nucleation can easily occur. Solute is consumed *via* the formation and growth of nanomaterials, resulting in the gradual decline of solute concentration until a stable equilibrium is reached. Inspired from Ref [26]. [26]

Table 1.1: Summary of equations relevant to the nucleation of nanomaterials.

	Equation	Description
(**Eqn. 1.1**)	$\Delta G_v = G_{v,new\ phase} - G_{v,parent\ phase}$	When the $\boldsymbol{G_v}$ of the parent phase becomes higher than that of another phase of material, a transformation into this later phase results in a favorable net reduction in free energy.
(**Eqn. 1.2**)	$\Delta G_v = -\frac{k_B T}{\Omega} \ln\left(\frac{C}{C_{eq}}\right)$	$\boldsymbol{\Delta G_v}$ is dependent on the $\boldsymbol{C}$ and the $\boldsymbol{C_{eq}}$. When $\boldsymbol{C} \leq \boldsymbol{C_{eq}}$, the solution is not supersaturated, and the parent phase is more stable ($\boldsymbol{\Delta G_v} \geq 0$) so a transformation will not occur. When $\boldsymbol{C} > \boldsymbol{C_{eq}}$, supersaturation is achieved and the solution and becomes metastable ($\boldsymbol{\Delta G_v} < 0$), making a transformation to a lower energy phase favorable.
(**Eqn. 1.3**)	$\Delta G_{barrier} = -V * \Delta G_v + SA * \gamma$ $V_{sphere} = \frac{4}{3}\pi r_c^3 \ ; \ SA_{sphere} = \frac{4}{3}\pi r_c^3$	The energy barrier to nucleating particles is dependent on the volume, surface area, and surface energy of the material being made. Equations for the $\boldsymbol{V}$ and $\boldsymbol{SA}$, and of a spherical particle are also provided and can be substituted for other geometries (*e.g.*, rods, wires).
(**Eqn. 1.4**)	$r_c = -\frac{2\gamma}{\Delta G_v} \ ; \ r_c \propto \left(\ln\left(\frac{C}{C_{eq}}\right)\right)^{-1}$	The $\boldsymbol{r_c}$ is directly proportional to $\boldsymbol{\gamma}$, however $\boldsymbol{\gamma}$ also has an inverse relation with $\boldsymbol{r_c}$ (see **Eqn. 1.4**). Additionally, $\boldsymbol{r_c}$ is dependent on supersaturation. Thus, $\boldsymbol{r_c}$ is smaller under higher supersaturation levels, and conversely, $\boldsymbol{r_c}$ is larger under lower supersaturation levels.

$\boldsymbol{\Delta G_v}$ = Gibb's free energy per unit volume [J·mol·m^{-3}]; $\boldsymbol{k_B}$ = Boltzmann's constant [J·K^{-1}]; $\boldsymbol{T}$ = temperature [K]; $\boldsymbol{\Omega}$ = unit volume [m^3·mol^{-1}]; $\boldsymbol{C}$ = solute concentration [mol·L^{-1}]; $\boldsymbol{C_{eq}}$ = equilibrium concentration [mol·L^{-1}]; $\boldsymbol{\Delta G_{barrier}}$ = free energy barrier for the formation of the nucleus [J·mol·m^{-3}]; $\boldsymbol{V}$ = volume of nuclei [m^3]; $\boldsymbol{SA}$ = surface area of nuclei [m^2]; $\boldsymbol{r_c}$ = critical nuclei radius [m]; $\boldsymbol{\gamma}$ = surface free energy [J·m^{-2}].

Regardless of the nucleation mechanism, the size- and concentration-dependent growth of large particles is known as 'ripening'.[22,60,61] Similar to Classical Nucleation Theory, ripening occurs in particles of smaller sizes that are relatively less stable due (in part) to their increased surface energy. A concentration gradient between the surface of the particle and the solute operates as a driving force for diffusion. As a result, smaller particles that are more soluble diffuse into solution, while larger particles consume ions in solution and grow into large crystalline nanomaterials.[22,60,61] This process can result in a broader size dispersion as particles shrink and grow in size. This contrasts strongly from particles made though homogenous burst nucleation, in

which supersaturation is rapidly achieved and causes particles to simultaneously nucleate and grow equal in size to form monodisperse nanomaterials.[22,60,61]

Importantly, as solute is increasingly consumed during nucleation and growth, the concentration of solute will eventually decline below supersaturation levels and inhibit further nucleation or growth.[22,61] Thus, the final particle size is contingent on diffusion equilibrium between a nanomaterial's surface and the parent solution, which can be controlled by carefully modulating the reaction concentration, time, and temperature. Once growth is completed, nanomaterials are stabilized (either sterically or electrostatically) to allow these otherwise non-dispersible inorganic materials to be suspended in solvent for later use.[22,56,60]

1.1.2.2 Solutes and solvents

The solute (*i.e.*, precursor materials) and solvent are the minimum required materials for nucleation and growth. Common inorganic nanomaterial precursors include metal salts (*e.g.,* M–Cl, M–Br) and organometallic frameworks (*e.g.,* acetates, acetylacetonates, nitrates, halides, carbonyls, sulfates, alkoxides) that require judicious selection. Precursors that retain strong ionic bonds (*e.g.,* salts) or are highly chelated (*e.g.,* acetylacetonates) often have greater dissociation energies that heavily influence nucleation mechanisms, such as supersaturation levels, induction time for nucleation to occur, and overall reaction kinetics. To assist with the liberation of ions into solution, higher reaction temperatures may be required for the thermal decomposition of precursors, as well as the use of reducing agents to assist in precursor dissolution.[11,22,57,60]

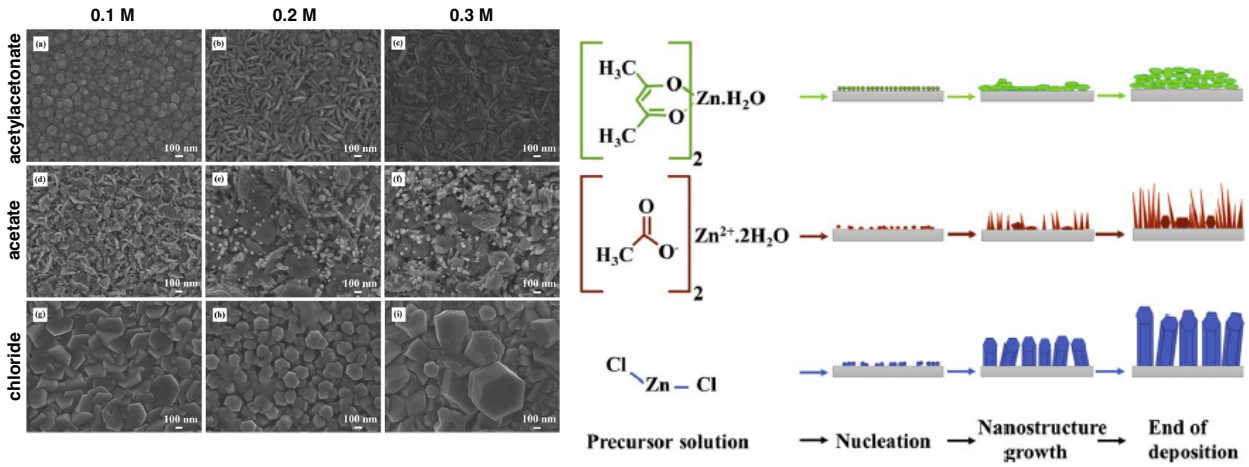

Figure 1.3. ZnO nanomaterials of different shape and properties, synthesized under the same conditions with different precursors and precursor concentrations from Ref [65].[65] **(Left)** Scanning electron microscopy (SEM) images of the nanoparticles, and **(right)** schematic showing the precursors and their growth pattern. Other examples from Refs [66] and [67].[66,67]

The primary function of the solvent is to dissolve precursor materials to form ionic monomers.[22,42,60–62] Solvents include both inorganic (*e.g.,* water) and organic (*e.g.,* organic molecules, proteins) liquids. Some solvents also serve additional purposes by directly reducing or coordinating with precursors, influencing the crystallization or stabilization of nanomaterials, and assisting with dispersion. In cases where thermal decomposition of precursor materials is required (or when the desired phase is stable/favorable at elevated temperatures), high-boiling point solvents may be necessary. In such instances, a class of material called ligands is used as a primary solvent. These ligands and their properties are covered in detail in **Chapter 1.2.**

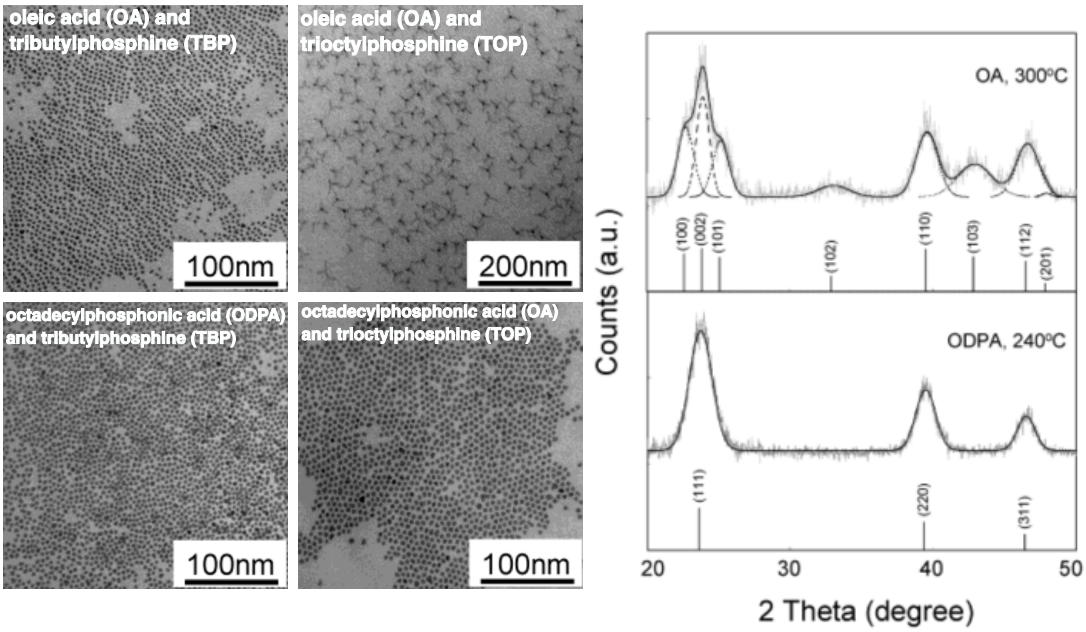

Figure 1.4. CdSe nanomaterials of different shape and structure, synthesized under the same conditions with different solvents (ligands, labeled) from Ref 68.[68] **(Left)** Transmission electron microscopy (TEM) images of the nanoparticles, and **(right)** X-ray diffraction (XRD) diffractograms of the particle's crystal structure. Other examples from Refs [69] and [70].[69,70]

1.1.3. The Post-Processing (Sintering) of Nanomaterials

While it is often desirable to retain the initial size and shape of certain nanomaterials, nanomaterials can alternatively be used as a precursor for creating bulk materials at reduced temperatures. For example, conductive and semiconducting materials utilize thermal treatments (known as sintering) to densify nanomaterial thin films to minimize grain boundaries and interfaces, which operate as premature electron and hole recombination or trap sites.[51,52,71,72] In the following subsections, we will discuss the mechanisms involved with transforming nanomaterials into micron-sized grains.

1.1.3.1 Sintering and grain growth theory

Sintering entails the heating of nanomaterial films to form dense polycrystalline grains ranging from nanometers to microns in size. The generalized process that occurs during sintering includes particle necking, coarsening, densification, and grain growth, as shown in **Figure 1.5**.[60,73–76]

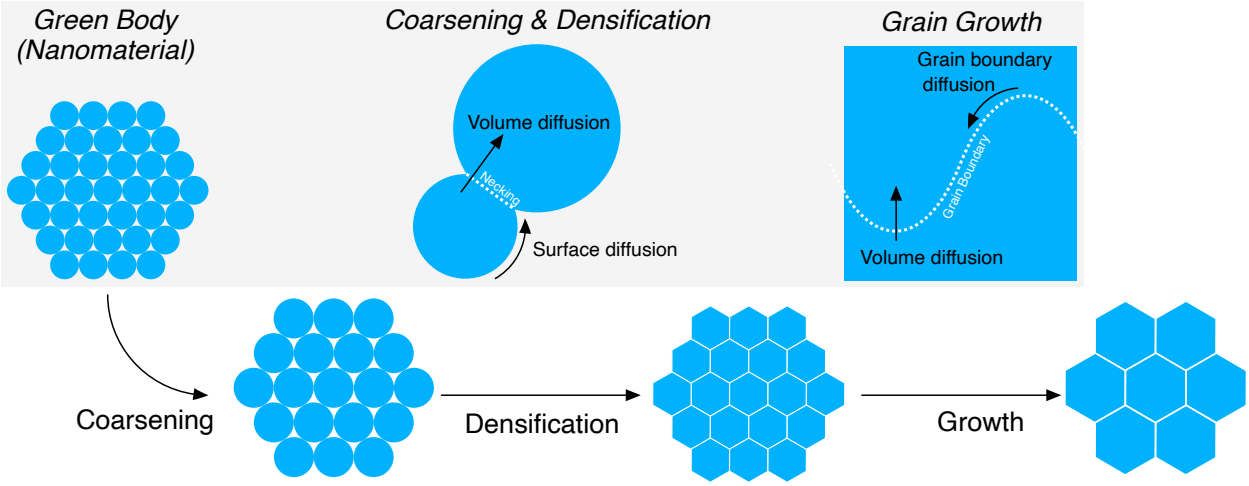

Figure 1.5. The sintering process begins with loose powdered particles (nanomaterials often termed a 'green body') followed by coarsening (necking followed by diffusion of mass from small to large particles) and densification (reduction of pore space). Finally, grain growth occurs (atomic diffusion, forming large grains while reducing grain boundary energy).

The initial stage of sintering begins with necking, or the adjoining of adjacent particles.[60,74,75] For nanomaterials, necking can occur at low temperatures ('cold-sintering') due to the alignment of identical crystalline planes ('facets').[75,77] However, heat is more commonly used to initiate necking across populations of particles. Inter-particle mass transport, or 'coarsening', subsequently increases the size of these particles. Similar to nanomaterial ripening, diffusion is driven by the annihilation of small particles and pores of higher surface energy.[60,78] As particles

shrink, their surface area and internal pressure increases, diffusing atoms into larger, more stable particles.

After densification depletes small particles and pores, further growth occurs *via* atom diffusion at grain boundaries.[60,74,75] This is only possible after densification: small particles and pores create high local pressure that prevent grain boundary motion. As a result, at least 90% densification must occur before growth can begin. Similar to the initial stages of sintering, diffusion through grain boundaries is dependent on interfacial energy as atoms diffuse from convex surfaces to concave surfaces as pictured in **Figure 1.5**.[60] Diffusion will continue until the interface is flat.

Table 1.2: Summary of equations relevant to the sintering of nanomaterials

	Equation	Description
(**Eqn. 1.5**)	$\Delta p = p_i - p_0 = \gamma\left(\frac{1}{r_1}+\frac{1}{r_2}\right)$	The generalized Young-Laplace[60,73] equation. The difference of p_0 and p_i is based on γ and the principal radii of curvature. For spherical particles, $r_1 = r_2$.
(**Eqn. 1.6**)	$\frac{\mathrm{d}\rho}{\mathrm{d}t} = \frac{C\gamma D N_{pore}}{{d_{avg}}^n} = D\exp\left(-\frac{E_a}{RT}\right)$	The rate of densification.
(**Eqn. 1.7**)	${d_{avg}}^n = {d_0}^n + kt\exp\left(-\frac{E_a}{RT}\right)$	The average grain size is a function of initial particle size, sintering duration, and the Arrhenius rate of grain boundary motion.[79–81] The rate is dependent on the activation energy of grain boundary motion, which changes with initial particle size and shape, grain boundary angle, sintering temperature, and diffusivity of atoms cross the grain.

Δp = change is pressure [kg·m^{-1}·s^{-2}]; p_0 = external pressure [kg·m^{-1}·s^{-2}]; p_i = internal pressure [kg·m^{-1}·s^{-2}]; ρ = grain density [grains·μm^{-2}]; t = sintering duration [s]; γ = surface energy [J·m^{-2}]; D = diffusion coefficient [m^2·s^{-1}]; N_{pore} = number of pores per grain; d_{avg} = average final grain size [μm]; d_0 = initial particle size [μm]; n = grain growth exponent (*n = 2 for interface controlled process*); k = rate constant of grain boundary motion [μm·s^{-1}]; t = sintering duration [s]; E_a = activation energy [kJ·mol^{-1}]; **R** = molar gas constant [kJ·K^{-1}·mol^{-1}]; T = temperature [K].

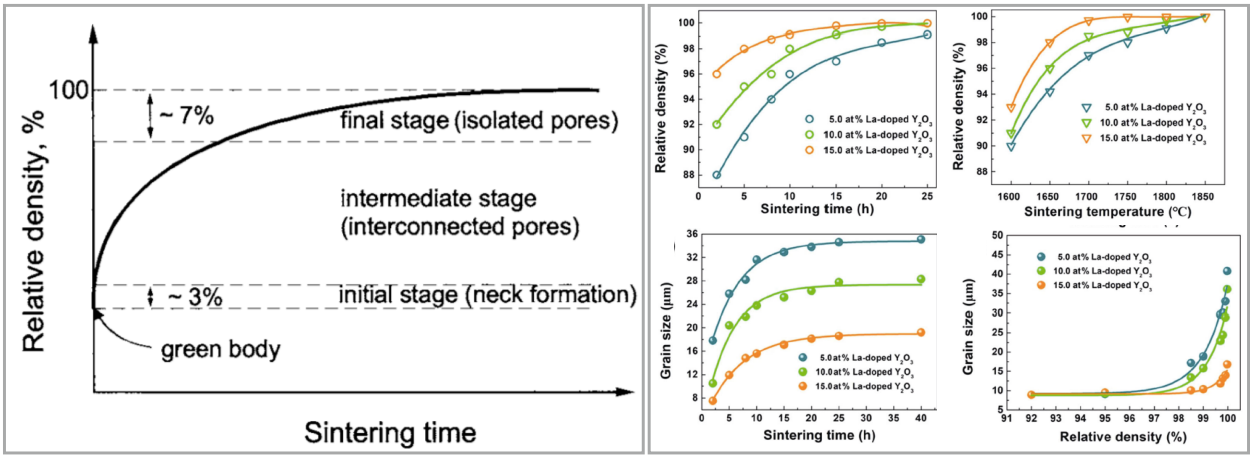

Figure 1.6. (left) Breakdown of the stages of sintering: from beginning with the loose nanomaterial (green body), to initial necking, the coarsening, and densification of grains (intermediate stage). The final stage of eliminating pores (densification) allows for the growth of grains. From Ref [82].[82] **(right)** Results from an empirical study which highlights the real time densification and growth of grains depending on time and temperature, and additional highlights how the final grain size is limited by percentage of densification. From Ref [80].[80]

1.1.3.2 Engineering densification and grain growth

The densification and growth of nanomaterials can be modulated by diffusivity, surface energy, or the activation energy for grain boundary motion by altering factors such as processing conditions, and the inclusion of additives, or the initial nanomaterial size.

Equation 1.7 reveals that longer sintering times result in larger grains and that the rate of particle growth increases at higher temperatures. As a direct result, time and temperature are often used to modulate grain size.[60,73,74,80] However, other approaches for increasing grain size are preferred; for instance, at high temperatures materials can evaporate and films can crack.[83–86] Therefore, adjusting parameters such as activation energy to modulate the rate of grain boundary motion can serve as a better alternative to high temperatures.

One approach for controlling densification and growth is through 'liquid-assisted sintering', which includes a material which melts or vaporizes at sintering temperatures.[87–89] This additional material, called a fluxing agent, wets the particles surface and occupies the pore channels between particles, thereby decreasing the activation energy for diffusion.[88,90,91] The fluxing agent is then incorporated into the final sintered material as an alloy or dopant, residing at the grain boundaries and interfaces as a precipitate, or can volatilize.[88,91] Since fluxing agents are consumed over time, they only assist during early stages of sintering (*i.e.,* necking) unless a constant supply of flux provided.

Alternatively, reducing the melting temperature can also decrease the activation energy of diffusion. Although melting temperature is an intrinsic material property, it can be modulated by including dopants or reducing the nanomaterial size (*e.g.*, T_M = 156 °C for bulk indium, T_M = 120 °C for 4 nm indium particles, T_M = 50 °C for 0.4 nm indium particles).[92] This occurs because smaller nanoparticles have higher surface energy, promoting the out-diffusion of atoms.[73–75,92,93]

Table 1.3: Additional equations related to the sintering of nanomaterials

	Equation	Description
(**Eqn. 1.8**)	$T_M(d) = T_{MB}\left(1 - \left(\frac{4\sigma_{sl}}{H_f \rho_s d}\right)^2\right)$	Melting point derived from the Gibb-Thomson equation, determined by to the bulk materials melting point and intrinsic properties, only being altered by the particle size (***d***). When ***d*** is large, the second term approaches 0 and has negligible effect on the melting temperature.

$\boldsymbol{T_M}$ = size-dependent melting point [K]; $\boldsymbol{T_{MB}}$ = bulk material's melting point [K]; $\boldsymbol{\sigma_{sl}}$ = energy of the solid-liquid interface [kJ·m^{-2}]; $\boldsymbol{H_f}$ = bulk heat of fusion [kJ·kg^{-1}]; $\boldsymbol{\rho_s}$ = density of solid [kg·m^{-3}]; ***d*** = particle diameter [m].

1.1.4. Nanomaterials of Interest

Previously, we introduced synthesis conditions that generally affect the production of nanomaterials. In this work, we turn our focus towards a specific solution-processed nanomaterial: kesterite $Cu_2ZnSn(S_xSe_{1-x})_4$, which is used in photovoltaic applications.

Kesterite $Cu_2ZnSn(S_xSe_{1-x})_4$ (CZTSSe) is a *p*-type (hole-rich) semiconducting material with material properties that can be carefully tuned. CZTSSe's hole concentration can be adjusted by introducing intrinsic defects (*e.g.,* copper vacancies).[44,94] CZTSSe also has a direct bandgap in the visible range and be modulated based on the ratio between sulfur and selenium (1.5 eV for CZTS, and 0.9 eV for CZTSe).[44] The optoelectronic properties of CZTSSe makes for an ideal absorber (active) material for photovoltaic applications. Additionally, CZTSSe has garnered attention as a substitute for other solution-processable active materials (*e.g.*, GaAs, CdTe, PbS, and $Cu(In,Ga)Se_2$) that utilize highly toxic (As, Cd, Pb) and/or rare earth elements (Ga, Cd, In, Te). [43,95–100]

To make CZTSSe photovoltaic devices, hole-rich (copper-poor) CZTS NPs nanoparticles are first produced by simply adjusting the ratio of the precursor materials. These particles are then suspended into a nanoparticle ink and deposited onto a back-contact material (*i.e.,* a Mo substrate). After deposition, the NP thin film (< 1000 μm) is heated to 500 °C in the presence of Se.[44] Se is not only incorporated into the material's lattice (by substituting S atoms), but also expedites grain growth as a fluxing material when constantly supplied.[101] Such grain growth is ideal for photovoltaic devices since grain boundaries and interfaces operate as electron recombination sites for charge transport, thereby hindering device performance.[40–47] Finally, an n-type buffer layer and front contact are deposited, completing the photovoltaic device.

CZTSSe also has a variety of other important applications.[102] A list of applications (including relevant binary chalcogenide derivates of CZTS (CuS, ZnS, and SnS), metal derivatives of CZTS (Cu, Zn, Sn), and the metal oxide derivatives of CZTS (CuO, ZnO, SnO)) are available in **Table 1.4**.

Table 1.4. Materials used in this study

Material	Applications
CZTS	photovoltaics,[103] hole transport layer,[104] photocatalysis [102]
Cu	catalysis,[105] metal electrodes[106]
Cu_xO	photocatalysis,[107] antibacterial surfaces[107]
Cu_xS	catalysis,[108] photocatalysis,[108] p-type semicondutor[44]
Zn	metallics, alloying
ZnO	photocatalysis, transparent electrodes[109]
ZnS	photocatalysis,[110] sensors,[110] photovoltaics,[110] light emitting diodes,[110] insulators[44]
Sn	metallics, alloying
SnO_x	photocatalysis,[111] catalysis[112], antibacterial surface,[111] sensors[111]
SnS_x	n-type semiconductor,[44] photodetector[113]

1.2. Ligands

The synthesis temperature of CZTS (225 °C) requires the use of high-boiling point solvents such as ligands. Ligands are organic or inorganic solvents which, during nanomaterial synthesis, coordinate with metal atoms to control precursor reduction, arrangement, and crystallization.[69,114–117] Thus, ligands have considerable impact on the formation of nanomaterials. The ligand also anchors the surface sites of nanomaterials using electrostatic attraction or covalent bonds to create

a nanomaterial 'ink'.[42,115–118] These versatile inks can be deposited to form nanomaterial assemblies and solution-processable thin films.

The primary objective of the ligand is to form a stable ink when depositing uniform thin layers (10 nm - 1000 nm) of nanomaterial. Beyond this purpose, the ligand is intentionally removed to prevent impurities or defects in the bulk material.[47] Typically, ligands can be removed through ligand exchange or calcination (a heat treatment, *e.g.*, sintering).[47,87,106,118,119]

In this section (**Chapter 1.2**), we introduce the ligand and its known functionalities related to the synthesis and sintering (calcination) of nanomaterials. In the following section (**Chapter 1.3**), we discuss our research motivation in relation to these ligands and processes.

1.2.1. Introduction to Ligands

Ligands are ions or molecules that can form covalent bonds with metal atoms (or ions). There are three different types of ligand classifications: (1) neutral L-ligands, which donate 2 electrons to the metal center (2) X-ligands, which donate and accept 1 electron to and from the metal center, and (3) neutral Z-ligands, which accept 2 electrons from the metal center. **Figure 1.7** visualizes this bonding and **Table 1.5** contains common ligands relevant for nanomaterials and their classifications. Of these three classifications, L-ligands and X-ligands are most relevant to our work with chalcogenide (*i.e.,* sulfides and selenides) and metallic nanomaterials.

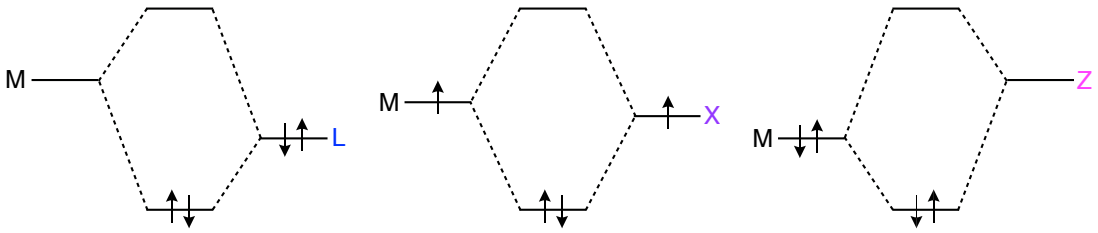

Figure 1.7. Highest occupied and lowest unoccupied molecular orbit levels for bonding between metal centers and the three different types of ligands.

1.2.1.1 L-ligands

L-ligands are electron-rich (nucleophiles) with a lone pair of electrons, classifying L-ligands as a Lewis base. Unlike the mutual donation of electrons found in conventual covalent bonds, L-ligands donate two free electrons (*e.g.*, lone pair electrons) to an electron-deficient (electrophilic) metal center to form a metal-ligand complex. The uneven donation of electrons forms a 'dative' covalent bond. Often, multiple L-ligands can donate electrons to a single metal center to form a coordination complex (see **Figure 1.8**). In nanomaterial synthesis, L-ligands form coordination complexes with cations in solution or cationic sites on the surface of the nanomaterial.[12]

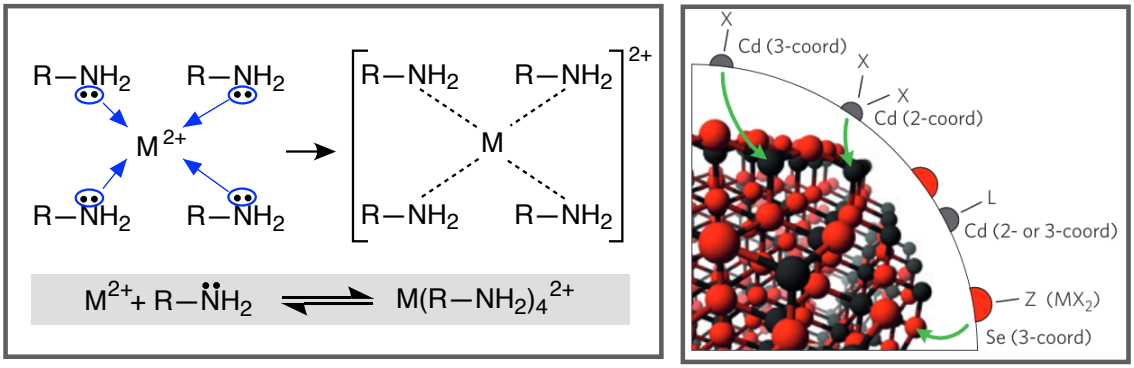

Figure 1.8. Example of how an amine, which has one lone pair of electrons from the from amine's nitrogen atom, forms a coordination complex with an electrophilic metal ion center via dative bonding (dashed lines). Example of X-, L-, and Z-ligand bonding and coordination to the surface of CdSe nanoparticles, from Ref [116].[116]

1.2.1.2 X-ligands

X-ligands interact with a metal center by each donating one electron to form a conventual covalent bond. X-ligands are commonly ionic (either anionic or cationic) and form covalent bonds

with other ions (in solution or on the nanomaterial's surface sites). Often, these X-ligands are the charged analogs (*e.g.*, R-COO^-, R-S^-, Cl^-) of compounds which have been deprotonated or ionized in solution (*e.g.*, R-COOH, R-SH, M-Cl). **Table 1.5** below includes common X-type ligands used in nanomaterial synthesis, along with various L- and Z- type ligands.

Table 1.5. Examples of ligands and their classification from Ref [115][116]

	Ligand Functional Group
L-ligands	Amines (RNH_2) Phosphines (R_3P) Water (H_2O) Carboxylic acids (RCOOH)
X-ligands	Carboxylates ($RCOO^-$) Hydroxyl (HO^-) Thiolates (RS^-) Phosphonates ($RPO(OH)O^-$) Inorganic anions (Cl^-, I^-, S^{n-}, $InCl_4^-$) Protons (H^+)
Z-ligands	$Pb(RCOO)_2$ $CdCl_2$

* Atoms/ions highlighted in red are responsible for the donation/acceptance of electrons.

1.2.2. Ligand's Role During Nanomaterial Synthesis

A large library of materials that classify as ligands have been used in nanomaterial synthesis (*e.g.,* water, organic molecules, polymers, proteins). The wide versatility and diversity of ligands offer the ability to carefully tune several critical functions of nanomaterial synthesis. Ligands, for instance, can also serve as a solvent and reducing agent, a facilitator for the nucleation and growth of particles, a stabilizing agent, and for screening nanomaterials from their environment.[12,13,16,68,120–123]

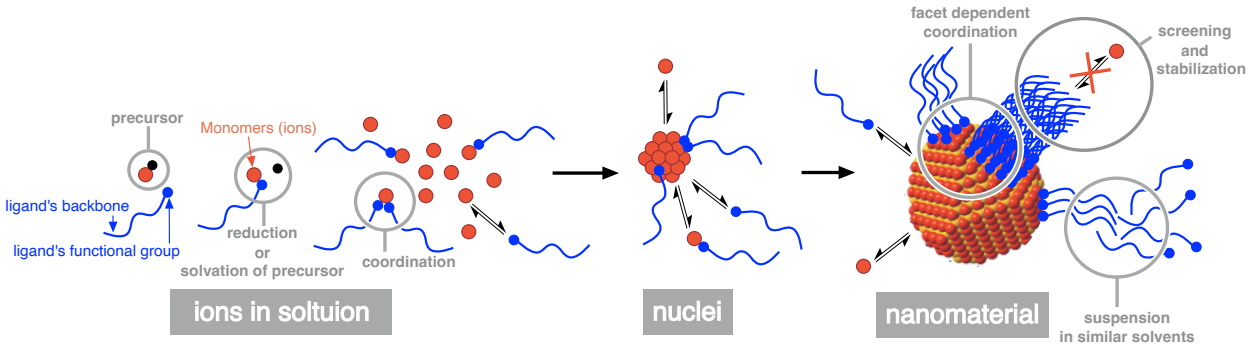

Figure 1.9. Schematic summary of the ligand's role during the synthesis of nanomaterials, inspired from Ref [124].[124]

1.2.2.1 Dissolution and decomposition of precursors: ligand as a solvent and reducing agent

As discussed in **Chapter 1.1.2.2**, solvents are required for the dissolution or decomposition of precursor materials to form homogeneous solutions. During nanomaterial synthesis, ligands are commonly used as the primary solvent and modulate synthesis depending on their polarity, functional group(s), and boiling point.

For example, in the synthesis of metal oxide nanomaterials, polar metal chloride precursors dissolve when using polar water or alcohol as a ligand.[125] Here, water forms a hydration shell similar to a coordination complex, causing solvation. Alternatively, precursor dissolution may occur if the ligand's functional group operates as a reducing agent. Common ligands which operate as reducing agents are Lewis bases (L-type ligands) such as phosphines (*e.g.*, trioctylphosphine oxide, trioctylphosphine) and amines (*e.g.,* hydrazine, hydroxylamine, tributylamine, alkylamines, alkaloids, amino acids, polyvinylpyrrolidone) which donate their lone pair electrons to metal centers.[126–130] Similarly, deprotonated acids (*e.g.,* ascorbic acid, tannic acid, decanoic acid, sodium citrate, carboxylic acids) are X-type ligands that are often used as reducing agents during nanomaterial synthesis.[126–131]

It is often advantageous to synthesize nanomaterials at higher temperatures (100 – 300 °C). During these reactions, thermally-stable organic monomers and polymers (with high boiling points) are used to thermally reduce or decompose metal precursors, to form stable materials at elevated temperatures, and can even be used to control nucleation.[12,13,16,68,120–123]

1.2.2.2 Controlling nucleation and growth: ligand stabilization and screening

The specific bonding properties within the ligand-metal complex (*i.e.*, stability of individual bonds, coordination number, ligand sterics) can impose another impact on the nucleation and growth of nanomaterials.

For example, an unstable (labile) bond results from poor affinities (*i.e.*, mis-matched hard/soft acid-base pairs) and can easily dissociate for a more favorable acid-base match. A particularly stable (non-labile) ligand can dampen growth and stabilize nanomaterials as there is an increased energy required for ligand dissociation.[116,132] The ligand's ability to highly coordinate or chelate (*via* single ligands which form multiple coordination bonds) with metal centers is similarly important: once encapsulated by a ligand shell, the metal center is screened from its environment and inter-diffusion of ions from solution is inhibited.[116–118,133] Additionally, bulkier ligands have a lower diffusivity, lower coordination numbers, and a higher efficacity for screening ions compared to smaller ligands (*e.g.,* short-chained aliphatic).[133] Ligands with low diffusivity cause slow nucleation and growth rates, and their high stearic hindrance prevents the interdiffusion of ions resulting in smaller and more stable particles.[133,134]

Ligand lability and coordination can also influence the shape and structure of the nanomaterial. For example, chelating ligands with multiple anchors can promote unidirectional growth (*e.g.,* nanowires, nanorods), mixtures of different organic ligands can promote the

nucleation and growth of different crystal phases (*e.g.,* wurtzite and stannite), and preferential coordination of the ligand's anchoring (functional) group can result in expression of low-energy atomic planes (*e.g.,* (111), (100)).[42,116,117,132]

1.2.2.3 Forming dispersions: ligand as an encapsulant and surfactant

The formation of ligand-based 'encapsulation' or 'capping' layer, which coats the surface of the nanomaterial, functions as a barrier between the nanomaterial and its surrounding environment. In addition to screening the nanomaterials, the encapsulation layer is critical for dispersing the nanomaterial in different solvents, determined by the structure and polarity of the ligand backbone. For instance, ligands with a long hydrocarbon backbone (non-polar) allows otherwise non-dispersible inorganic nanomaterials to be suspended in other nonpolar solvents. These dispersions (suspensions) are known as nanomaterial 'inks' and can be used in further processing, such as the deposition or printing of inks to form thin films.[42,115–118]

1.2.3. Ligand's Role During Sintering

Beyond its function for nanomaterial dispersion and deposition, the ligand often serves no further purpose. For sintered nanomaterial films, ligands are expected to directly impede the sintering process as they must desorb from the nanomaterial surface for necking to occur.[135,136] The desorption of ligands through thermal heating (calcination) is thought to occur *via* the thermal decomposition, melting, or volatilization of ligands from the surface of the nanomaterial.[136] Alternatively, chemically-induced sintering chemically reduces the encapsulation agent *via* the use of reactive gases.[137]

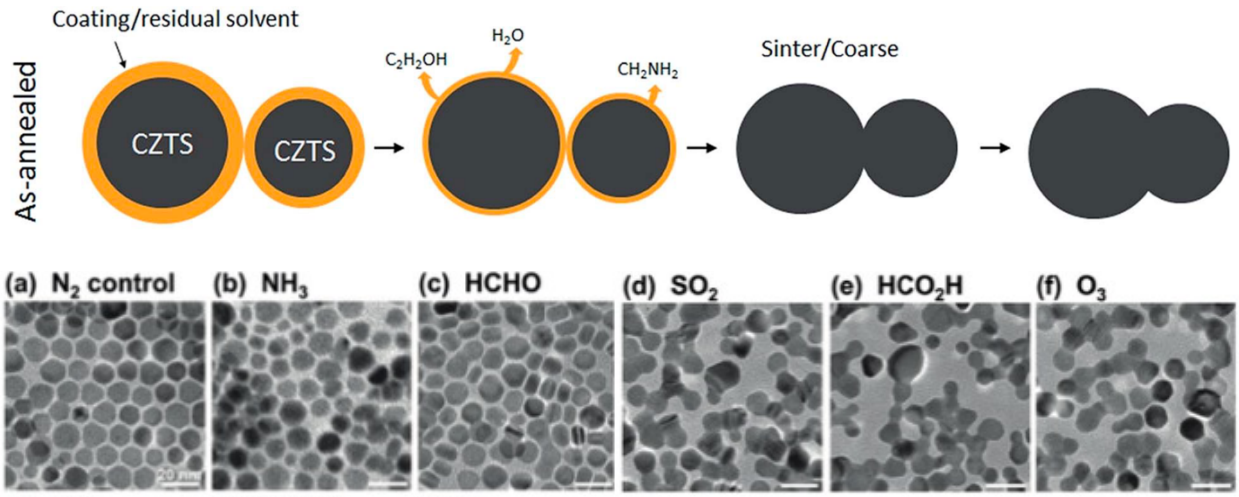

Figure 1.10. (top) Proposed nanoscale formation mechanism for organic ligands during the sintering of CZTS nanoparticles from Ref [87].[87] **(bottom)** The chemical sintering of nanoparticles by reactive gases from Ref [137].[137]

In most instances, the volatilization of the during sintering is ideal, as residual ligands can act as impurities or defects within the final material.[47,135,138] However, there is lack of consensus on how adequate sintering is for total ligand removal.[119] For instance, residual carbon from organic ligands can pyrolyze (thermally decompose) and become trapped within the final film (see **Figure 1.11**).[83–85,87,91,103,119,138–144]

Furthermore, it is possible that the ligand also participates in the densification and coalescence of nanoparticles during sintering. When stripping a nanomaterial or exchanging the ligand with a low-carbon content molecule, for instance, coalescence occurred with poor densification and grain growth.[142,145] A complementary study increased the weight percentage of the ligand that led to the formation of large grains at the expense of more residual carbon remaining within the film.[142] These studies indicate that the ligand encapsulation layer influences the formation of large grains during the sintering process. One proposal suggests that the capping

ligand operates similar to fluxing agents that wets the nanoparticle surface and promotes ion diffusion.[142,145] However, no further investigations have been conducted to identify the underlying role of the ligand in the promotion or hinderance of grain growth.

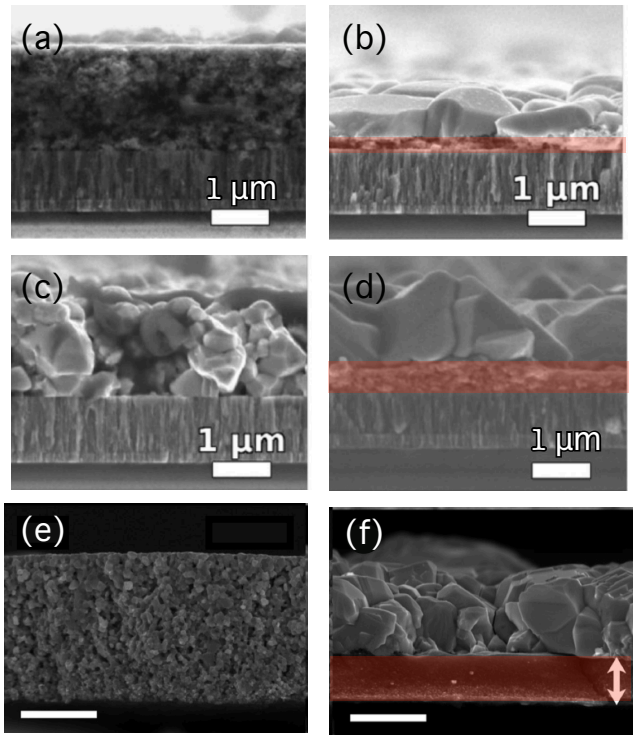

Figure 1.11. With sufficient sintering times and temperatures, organic ligands decompose into a carbon-rich fine-grain-layer (FGL) which forms underneath an inorganic large-grain-layer (LGL). Micrographs highlighting the impact of carbon content on $Cu_2ZnSn(S,Se)_4$ grain growth from two separate studies.[142,145] **(a)** Stripped NPs compared against **(b)** NPs capped with oleylamine ($C_{18}H_{37}N$).[142,145] **(c)** NPs capped with $C_{18}H_{37}N$ compared against **(d)** NPs capped with polystyrene ($(C_8H_8)_n$).[142,145] **(e)** NPs capped with formamide (CH_3NO) compared against **(f)** NPs capped with oleylamine ($C_{18}H_{37}N$).[145] Micrographs to the left (low carbon content) are porous and have comparatively inhibited grain growth. Micrographs to the right experience greater densification and contain an organic FGL (highlighted in red). From Refs [142] and [145].

1.2.4. Ligands of Interest

As listed in **Table 1.5**, a large library of ligands can be used in the synthesis of nanomaterials, which includes amines, phosphines, phosphonates, carboxylic acids, carboxylates, hydroxyls, thiols, thiolates, and aqueous solvents. In this work, we focus primarily on two classes of ligands: organic amines and carboxylic acids. This specifically includes alkylamines (dodecylamine, oleylamine, linoleylamine) and alkyl carboxylic acids (stearic acid, oleic acid, and linoleic acid).

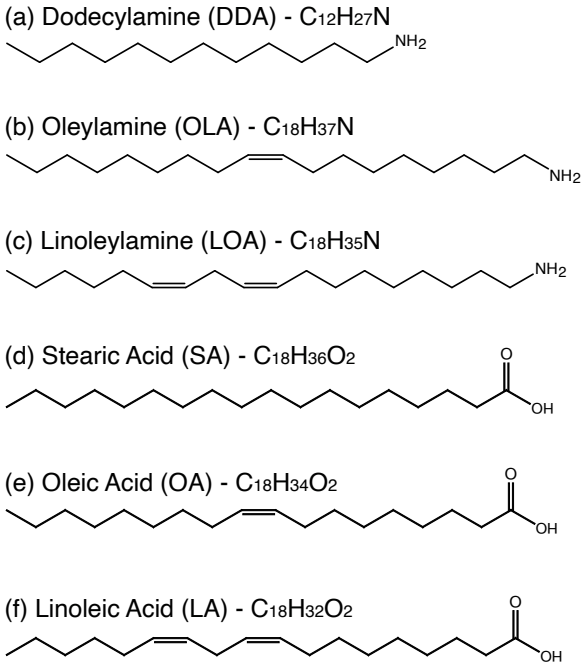

Figure 1.12. Chemical structures of the ligands used in this study. This includes **(a-c)** amine ligands and **(d-e)** carboxylic ligands of varying bond saturation; unsaturated **(a)** DDA and **(d)** SA, monounsaturated **(b)** OLA and **(e)** OA, and polyunsaturated **(c)** LOA and **(f)** LA.

1.2.4.1 Alkylamines

Alkylamines are L-ligands that contain an amine functional group (NH_2) connected to a linear alkyl hydrocarbon backbone. Common examples used in nanomaterial synthesis include

octadecylamine (ODA), hexadecylamine (HDA), dodecylamine (DDA), and oleylamine (OLA), all of which are primary amines with a straight-chain aliphatic hydrocarbon backbone consisting of 12 – 18 carbon atoms.[117] These ligands can operate as the primary solvent during synthesis and are suitable for high reaction temperatures (260 °C < T_{BP} < 350 °C). As an L-type ligand, the amine functional group ($R - \ddot{N}H_2$) can donate both electrons to a metal ion, contributing to the reduction of the metal precursors and forming a metal-ligand coordination complex.[116,117,146] Similarly, the amine can coordinate with electrophilic dangling bonds on the surface of the nanomaterial *via* the formation of dative bonds. As the amine anchors to the surface of the nanomaterial, the nonpolar hydrocarbon backbone suspends the nanomaterial in other nonpolar solvents. Toluene and hexane are common solvents selected for the dispersion of alkylamine nanomaterials because they preserve the dative bond between amine and surface sites and will only interact with the hydrocarbon backbone. These solvents allow for the formation of highly concentrated (200 mg/mL) nanomaterial inks for deposition and solution-processing.

1.2.4.2 Alkyl carboxylic acids

Similar to alkylamines, alkyl carboxylic acids of similar chain length (*e.g.*, stearic acid (SA), oleic acid (OA), linoleic acid (LA)) can function as high boiling point solvents (230 °C < T_{BP} < 360 °C). The primary differences between alkylamines and alkyl carboxylic acids lies with the ligand's functional groups and the ability of carboxylic acid to operate as both L- and X-ligands.[12]

Specifically, oxygen from the carbonyl group (C=O) and the oxygen from the hydroxyl group (OH) both have two sets of lone pair electrons that operate similarly to the amine's lone pair: the unbound electrons can reduce metal precursors, form metal-ligand coordination

complexes, and coordinate to metallic surface sites.[116,117,146–149] Additionally, carboxylic acids can become deprotonated or ionized during synthesis.[149] In this instance, the oleate ions (COO^-) and hydroxide ions (OH^-) operate as X-ligands which donate electrons to metallic surface sites.

1.2.5. Role of the Ligand: From the Synthesis of CZTS to the Sintering of CZTSSe

As established in **Chapter 1.1.4**, CZTSSe is an important material of interest for photovoltaic applications. Additionally, in **Chapter 1.2.4** we introduced various organic ligands: alkylamines (dodecylamine, oleylamine, and linoleylamine) and alkyl carboxylic acids (stearic acid, oleic acid, and linoleic acid). In this section, we unite these materials and their roles both during synthesis and sintering.

During the synthesis of CZTS nanoparticles (NPs), metal precursors are first mixed and heated with an organic ligand (*e.g.*, oleylamine) to form a metal-ligand coordination complex.[116,117,146] A ligand-sulfur solution (polysulfide) is separately prepared *via* inverse vulcanization to be used as the sulfur source (the synthesis of polysulfides is described in further detail in **Chapter 1.2.6.2**).[146,150,151] This polysulfide is then injected into the precursor-ligand solution at elevated temperatures, rapidly producing hydrogen sulfide (H_2S) which instantly reacts with metal precursors to nucleate metal sulfide NPs.[146,150,151] Under controlled reaction times, temperatures, optoelectronic (kesterite) CZTS (Cu_2ZnSnS_4) NPs form. Upon cooling, excess ligands and polysulfides coordinate to the NP surface *via* their functional groups.[116,117] These encapsulation agents stabilize the NPs, preventing aggregation or further growth.[116,117,133] Finally, the ligand's hydrocarbon backbone allows the NPs to be suspended into nonpolar solvents to form a printable NP ink.[116,117,152]

From here, the CZTS NP ink can be deposited onto a Mo substrate/back contact through several methods, including spin coating, spray pyrolysis, or roll-to-roll printing techniques such as knife coating or inkjet printing.[40] As discussed, a sintering process known as selenization is used to promote grain growth and to modify the material's band gap. This process involves heating the printed CZTS NP film in a tube furnace under a flow of selenium vapor to form CZTSSe. Final sintered films consist of micron-sized grains which have comparatively improved optical and electronic properties for photovoltaic devices.

Sintering does not convert the entire layer of CZTS NPs into large grains of CZTSSe. Rather, a distinct bilayer forms as pictured in **Figure 1.11** and **Figure 1.13**. The bilayer is characterized by the presence of a large grains of CZTSSe which forms on top of a fine-grain-layer (FGL) embedded with carbon.[84] Here, the formation of this carbon-rich FGL layer is currently thought to arise from temperature-assisted desorption and pyrolysis of the organic encapsulation layer.

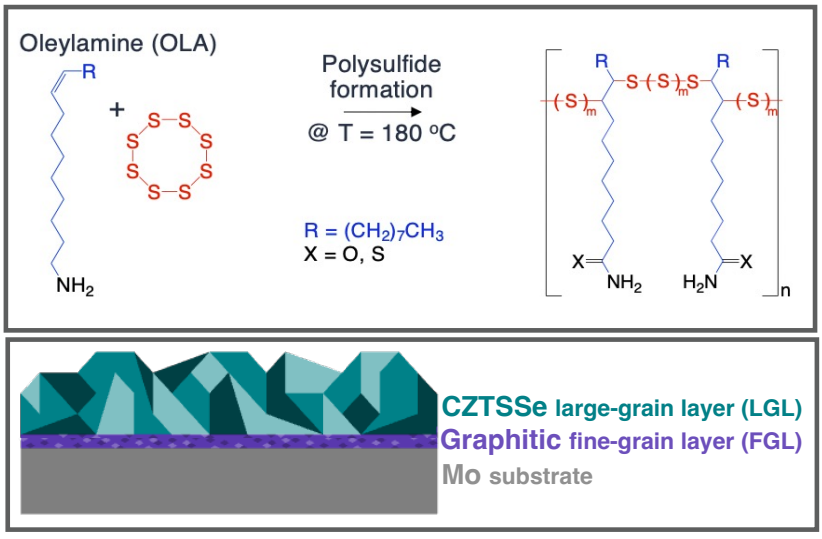

Figure 1.13. (top) inverse vulcanization of oleylamine in the presence of sulfur, forming a polysulfide[153] and **(bottom)** formation of the bilayer during sintering; large grains of active material (CZTSSe) above carbon-rich fine-grain-layer (FGL) inspired by Ref [84].[84]

1.2.6. Ligands in Other Processes

The same ligands used in the production of CZTS nanoparticles have recently been observed to undergo side-reactions during the synthesis of an array of nanomaterials, which can influence the kinetics of nanomaterial synthesis or result in carbon defects or impurities. [154,155] As these ligands are well known to be used in other scientific applications, including in polymerization reactions, the synthesis of rubber, pyrolysis of biofuels, and in carbon dot synthesis, these studied mechanisms may be highly relevant for nanoparticle synthesis.

1.2.6.1 Polymers

The synthesis of many commercially produced polymers such as polyethylene and polypropylene (commodity plastics), polyolefins, and poly(cycloalkenes) are achieved through the polymerization of alkenes.[156] Catalysts are often used to reduce the energy barrier of polymerization, allowing for the creation of polymers under milder reaction conditions (< 200 °C).[156] Ziegler-Natta catalysts are primary used in alkene polymerization, which most commonly include titanium or vanadium chlorides with an organoaluminium co-catalyst, or organometallic metallocene's with a transition metal ion center (usually titanium, zirconium, hafnium).[156,157] Similar to precursors used in nanomaterial synthesis, these catalysts can be metal chlorides (M-Cl) or metal acetylacetonates (M-$(acac)_x$).[156]

In relation to ligands, α-olefins such as 1-octodecene can undergo alkene polymerization in the presence of organometallic catalysts.[156,158–160] Alkene carboxylic acids can also undergo

polymerization in the presence of catalysts.[161] In addition to ligands, organometallic catalysts used in the alkene polymerization have been reported to result in the production of nanomaterial by-products, illustrating that under the right conditions, nanomaterials can be produced in tandem with polymers.[162]

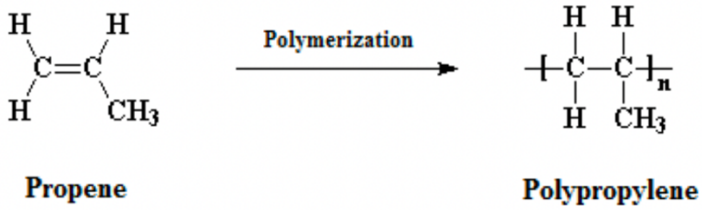

Figure 1.14. A generalized illustration of alkene polymerization from Ref [159].[159]

1.2.6.2 Rubbers and polysulfides

Rubber is comprised of polysulfides and synthesized *via* a process known as inverse vulcanization. This process requires a linear sulfur chain, where both terminal sulfur atoms are either radicalized or ionized. Radical linear sulfur is produced by the homolytic cleavage of cyclic elemental sulfur (S_8), achieved at temperatures ~ 160 °C. Ionic linear sulfur is produced by the reduction of elemental sulfur at lower temperatures (~ 110 °C) through nucleophile reduction by a Lewis base. These radical or ionic sulfur atoms reduce the double bond of organic olefins creating branched structures. Linear sulfur can link multiple organic olefins together to create cross-linked sulfur polymers, or polysulfides.

This inverse vulcanization method has been well studied with a large variety of organic olefins.[163–168] Amongst the monomers, both alkylamines and alkyl carboxylic acids have been used. This includes unsaturated amines (*e.g.,* oleylamine) and carboxylic acids (*e.g.,* oleic acid, linoleic acid).[146,150,167,169–171] Alkylamines are especially ideal, as their amine functional group can reduce the elemental sulfur at low temperatures, whereas additives are typically needed to catalyze

the reaction between alkyl carboxylic acids and elemental sulfur.[1] Catalysts can include metal precursors such as Zn stearate, $ZnCl_2$, $CuCl_2$, as well as metal oxides (*e.g.,* ZnO, CuO).[167,169,172,173]

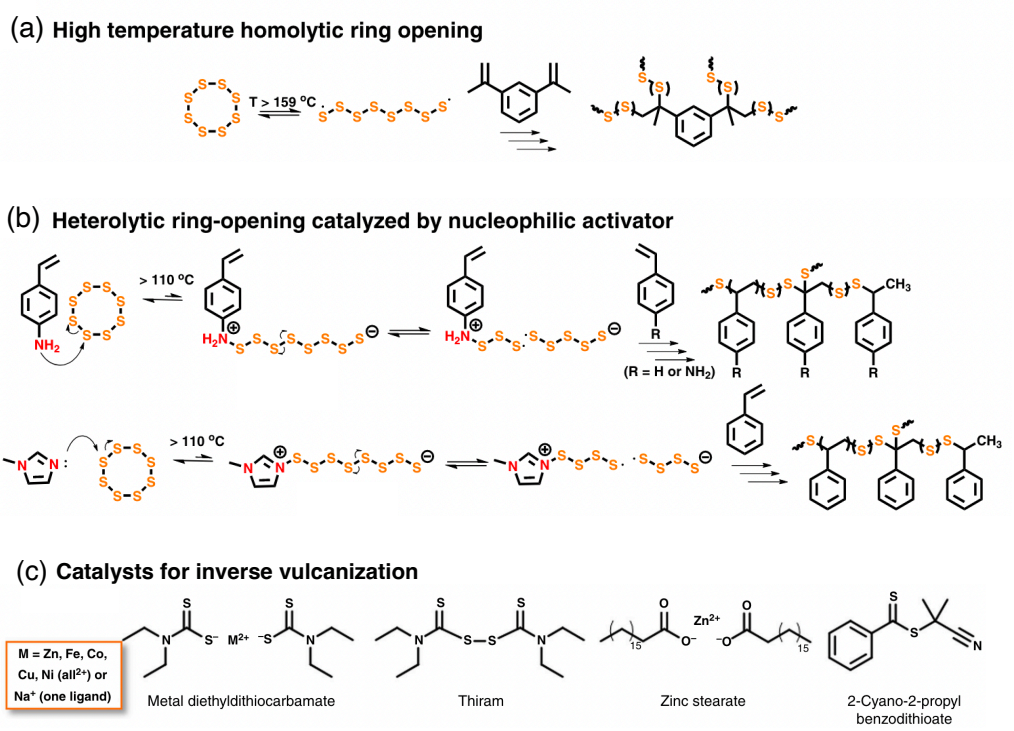

Figure 1.15. The proposed mechanisms for inverse vulcanization between elemental sulfur (cyclic S_8) and an alkene from Ref [164].[164] **(a)** The high temperature homolytic cleavage of sulfur results in a sulfur diradical which will react with an organic comonomer's double bonds to form a polysulfide. **(b)** The ring opening of elemental sulfur by a nucleophile (amines) result in ionic sulfur which will react with an organic comonomer's double bonds to form a sulfur polymer. **(c)** Catalysts trialed for inverse vulcanization from Ref [172].[172]

This inverse vulcanization process for forming rubber has become increasingly relevant to the synthesis of nanomaterials.[146,150,151] Organic alkylamine ligands, namely oleylamine, have been used to form polysulfides with elemental sulfur and operate as the source of sulfur during the synthesis of metal chalcogenide nanomaterials (including CZTS NPs).[146,150,151]

1.2.6.3 Fuel pyrolysis

Pyrolysis is the process in which a material undergoes thermal decomposition without interacting with other materials (*i.e.,* catalysts, oxygen). Specifically, the pyrolysis of hydrocarbons in inert environments has been well studied.[174] This is in part due to hydrocarbons being an affordable and abundant fuel source for combustion. For example, carboxylic acids — including stearic acid, oleic acid, and linoleic acid — can all be derived from natural sources (*e.g.,* palm oil, sunflower oil) and are all researched as biofuel candidates.[175–179]

Under elevated temperatures (350 – 1000 °C), cleavage of C—C bonds results in smaller chained hydrocarbon fragments with radicals. These radicals can further accelerate decomposition; they readily participate in propagation reactions with other molecules which generate additional free radicals. This can result in the material being more susceptible to structural change, such as further bond cleavage, formation of olefins, double bond migration, hydrogenation of double bonds, or branching. The decomposition of hydrocarbons which contain 5 to 20 carbon atoms can result in intermolecular cyclization to form cyclic products such as polyaromatic hydrocarbons (PAHs) or soot.

PAHs and soot can also form from the pyrolysis of olefins through an alternative reaction pathway, a Diels-Alder reaction, under similar conditions. Here, the mechanism is not dependent on the formation of free radicals, rather dienes and dienophiles must both be present during pyrolysis.[178,180]

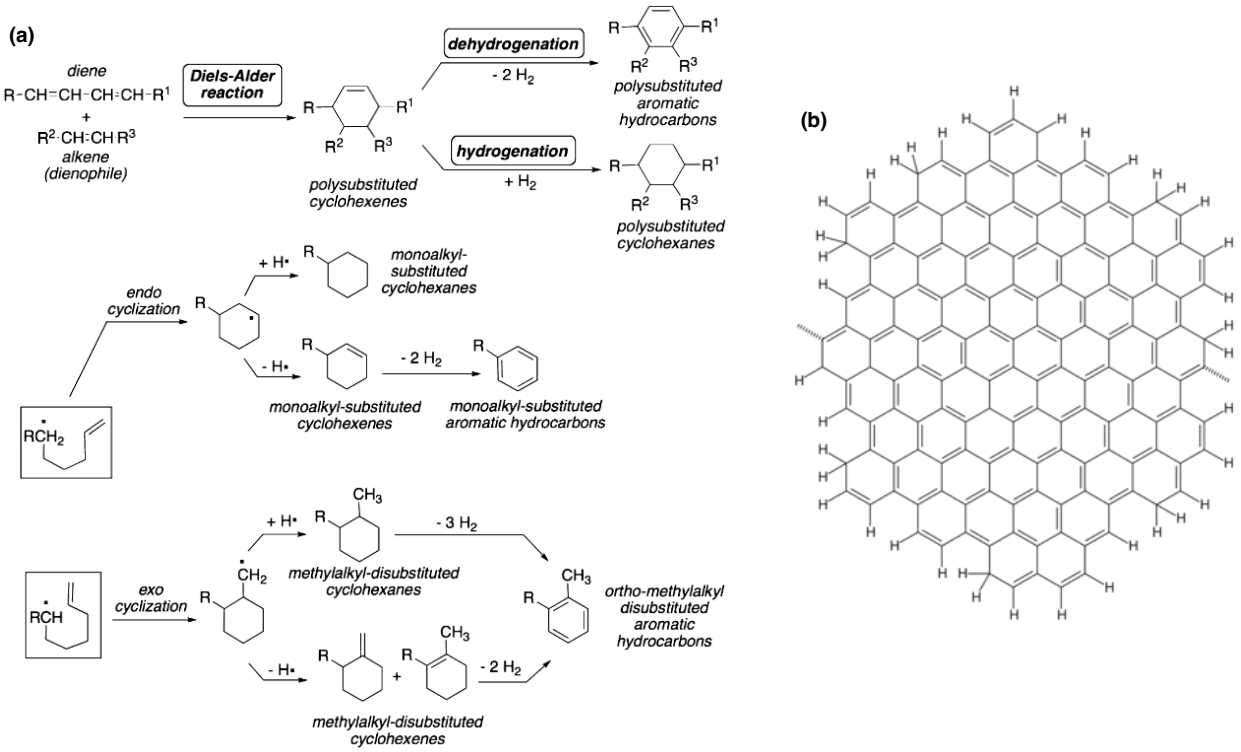

Figure 1.16. (a) Proposed mechanism for Diels-Alder reaction and intermolecular cyclization of dienes and radicals during the pyrolysis of organic monomers, from Ref [178].[178] This reaction can propagate to form polycyclic products, such as soot. **(b)** The idealized structure of soot from Ref [174].[174]

1.2.6.4 Carbon dots

Carbon dots are 0D carbon-based nanomaterials which were accidentally discovered during the washing, or purification, of carbon nanotubes after synthesis.[181] Since then, these carbon dots have been studied for their ideal optical properties, stability, low toxicity, and other novel properties.[58,182–186] Many new synthetic methods for forming carbon dots have been developed (*e.g.*, hydrothermal, solvothermal, micro-wave assisted) and have resulted in the establishment of new subtypes of carbon dots (*e.g.,* graphene quantum dots, carbon quantum dots, carbon nanodots, carbonized polymer dots).[58,185]

Amongst low-temperature (150 – 300 °C) bottom-up methods of producing carbon dots, ligands and reducing agents (*e.g.,* oleic acid, oleylamine, citric acid)[186–188] have been used as a carbon source. The specific synthesis mechanisms of carbon dots are still being understood. One possible mechanism is through the clustering of cross-linked and polymerized organic monomers followed by the carbonization, thermal degradation, or pyrolysis of the cluster.[58] Depending on the method, conditions, and reactants used for the synthesis, the carbon dot's properties can widely vary (*e.g.,* crystalline *v* amorphous). Much work is still underway to better understand the synthetic mechanisms and engineer the desired products.

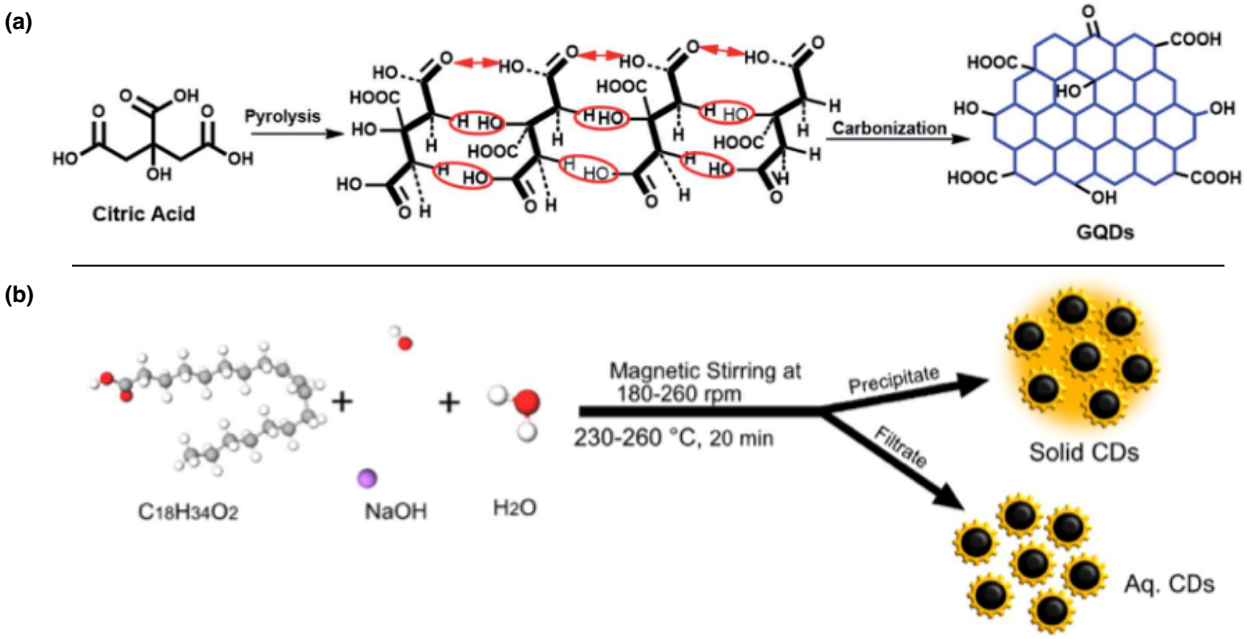

Figure 1.17. (a) Proposed mechanism for the synthesis of nanographite from the direct pyrolysis of citric acid at 200 °C, from Ref [189].[189] This mechanism can be described as the condensation of citric acid, followed by carbonization. **(b)** Synthesis condition for forming carbon nanodots from oleic acid, from Ref [187].[187] This mechanism can be described as the aggregation and pyrolysis/carbonization of oleic acid.

1.3. Scope of Work

Thus far, we have introduced both nanomaterials and ligands and their known processes during both synthesis and sintering. This background not only introduces the reader to the relevant functions of these materials, but also should highlight the robust knowledge established regarding nanomaterial synthesis, sintering, and the ligand. In recent years however, there has been emerging reports that the ligand is not inert during nanomaterial synthesis or sintering, renewing interest in investigating the ligand's role during these processes.[106,119,135,142,145,190]

During the synthesis of nanomaterials, reports have noted that ligands participate in side-reactions that result in reaction impurities.[154] Additionally, while the ligand is widely acknowledged as a critical component to nanomaterial systems, less attention has been given to the role of these ligands during sintering. However, ligand selection has increasingly been shown to influence film morphology and thus, film properties.[135,140,145,191]

In the following chapters, we directly explore the lesser-explored roles of the ligand during synthesis and sintering. First, we study the structural changes (*i.e.,* decomposition) of the oleylamine ligand during the synthesis and sintering of CZTS and CZTSSe (**Chapter 2**). Then, we expand this work to include additional alkylamines and alkyl carboxylic acid ligands, with a focus on understanding how ligand's backbone structure and the precursor selection influence ligand decomposition during nanomaterial synthesis (**Chapter 3**). Finally, we investigate the impact of the ligand backbone structure on the final morphology and properties of sintered CZTSSe films (**Chapter 4**).

This work aims to provide a deep understanding of the lifecycle and role of organic ligands during the synthesis and sintering of nanomaterials.

Chapter 2: Decomposition of the Oleylamine Ligand and the origins of the Organic Fine-Grain-Layer

This chapter is reproduced from published work entitled "Ligand Pyrolysis during Air-Free Inorganic Nanoparticle Synthesis" *Chem. Mater.* 2021, 33, 1, 136–145. doi: 10.1021/acs.chemmater.0c03088).[192]

2.1. Introduction

As discussed in **Chapter 1**, bottom-up syntheses of nanomaterials consist of the dissolution or reduction of precursors by a solvent or reducing agent, often a ligand.[42,46,115,193] In addition to operating as a solvent and reducing agent, the ligand can influence nanoparticle (NP) size and shape, and cap and stabilize the suspension of NPs in compatible organic solvents.[115–117,144,193–196]

While these capping ligands are critical for the synthesis and deposition of NPs through solution-processing, the ligand hinders charge transport between particles, making deposited NP films insufficient for practical devices due to their poor charge mobility.[51,71,115,116,197] Ligand exchange with conductive ligands can be employed,[71,115,116] however exchange methods are laborious and have limited scalability. Alternatively, thermal treatments promote ligand desorption and overall NP densification, universally improving conduction throughout the film.[51,71,83–

[85,87,91,103,116,139–143,197] During heating, the ligand desorbs to free the NP surface for sintering, however, the organic material is not eliminated from the film as expected.[71,119,144,198,199] With sufficient annealing times and temperatures, this process results in a residual pyrolyzed graphitic carbon fine-grain-layer (FGL) underneath a large-grained inorganic layer (LGL).[83–85,87,91,103,119,139–143] The impact of the carbon-rich layer on film conduction has been debated, with claims that it impedes carrier transort[200] or is benign.[201–203] Nonetheless, attempts have been made to reduce the thickness of the carbon-rich layer with limited success.[83,119]

A commonality across these observations is the use of the organic capping ligand oleylamine (OLA) which operates as a high boiling point solvent, a reducing agent, and surfactant that caps and screens NPs from their environment.[117,194,196,204,205] While OLA has been widely utilized and investigated within NP synthesis,[117,145,146,150,153,206] the restructuring of OLA into graphitic carbon, to our knowledge, has received no attention.

In this chapter, we investigate the pyrolysis of OLA and the residual organic constituents within OLA-capped Cu_2ZnSnS_4 (CZTS) NP films and their sintered $Cu_2ZnSn(S_xSe_{1-x})_4$ (CZTSSe) counterparts. Through the usage of Raman spectroscopy and X-ray photoelectron spectroscopy (XPS), the temperature-driven decomposition and restructuring of OLA is assessed. Moreover, XPS and glow discharge optical emission spectroscopy (GDOES) provide insight into a comprehensive model of the ligand's fate during the solution processing of CZTS NPs. By identifying both the decomposition conditions, resulting pyrolyzed structure, and origin of the FGL, a strategy to control the carbon layer in sintered NP films is proposed.

2.2. Methods

2.2.1. Oleylamine Decomposition

Microscope slides (2.5 cm × 2.5 cm) were sequentially sonicated in distilled water, acetone, and isopropyl alcohol (IPA) for 10 min per wash, and then each substrate was air-dried. In air, substrates were heated to their set point temperature, and then 0.2 mL of technical-grade oleylamine (70%, Sigma-Aldrich) was drop-cast onto the substrate. After 20 min, the substrate was removed from the hot plate and allowed to cool.

2.2.2. Nanomaterial Synthesis

Copper(II) acetylacetonate (1.5 mmol, 99.99%, Sigma-Aldrich), zinc acetylacetonate (0.75 mmol, 99.995%, Sigma-Aldrich), tin(IV) bis(acetylacetonate) dibromide (0.75 mmol, 98%, Sigma-Aldrich), elemental sulfur (99.98%, SigmaAldrich), and technical-grade oleylamine (70%, Sigma-Aldrich) were used in the synthesis of Cu_2ZnSnS_4 NPs. For the oxygen-free reaction, anhydrous $CuCl_2$ (1.5 mmol, 99.995%, Sigma-Aldrich), anhydrous $ZnCl_2$ (0.75 mmol, 99.995, Sigma-Aldrich), and anhydrous $SnCl_2$ (1.5 mmol, 99.99%, Sigma-Aldrich) substituted the acetylacetonate precursors. The metal precursors were sealed in a 100 mL three-neck round-bottom flask in an inert (N_2) atmosphere in a glovebox. Upon transfer to a Schlenk line, 10 mL of OLA was injected into the flask and heated at 130 °C by a heating mantle, forming a blue solution. The solution was vigorously mixed and cycled between vacuum and N_2 for 1 h, until there was no bubbling under vacuum. Under N_2, the solution was heated to 225 °C and immediately injected with 3 mL of a separately prepared sulfur−oleylamine solution (1 M sulfur in oleylamine, mixing at 50 °C for 1 h under air). NP nucleation was initiated by the injection of the sulfur−oleylamine solution, as indicated by a rapid change in color from blue to black. After 2 h of mixing at 225 °C,

the flask was raised from the heating mantle and allowed to cool to 80 °C. A mixture of 30 mL of IPA and 5 mL of toluene was poured into the flask. The solution was centrifuged at 13.5k rpm for 15 min. Upon decanting the supernatant, sedimented NPs were dispersed in a 2:1 solution of IPA to toluene, where the centrifuging and decanting process were repeated. The residual solvent was removed with a rotovap, forming a final NP powder, referred to as "powdered" NPs. Samples were further dried for 24 h under vacuum.

2.2.3. Nanoparticle Ink Formation and Thin Film Deposition

CZTS NPs (200 mg) were suspended in 1 mL of toluene and subjected to 1 h of pulsed ultrasonication (10 s ON/5 s OFF) to form an NP ink. Prior to deposition, 2.5 cm × 2.5 cm substrates of molybdenum-coated soda lime glass (Mo/SLG) were sequentially sonicated in distilled water, acetone, and IPA for 10 min per wash. Each substrate was air-dried and then plasma-cleaned for 5 min. 10 μL of ink was pipetted onto the cleaned substrates, followed by immediate doctor blading. For uniform coverage, a doctor blading machine was used with a sweeping rate of 50 mm/s and a spacer height of 25 μm. After 15 min of controlled drying in air, a second layer of ink was deposited (10 μL), with an adjusted spacer height of 50 μm. No heat was applied to dry the films.

2.2.4. Sintering via *Selenization*

Sintered CZTSSe films were achieved by incorporating selenium into the system. Se pellets (400 mg) were evenly distributed around two samples in a graphitic box. These samples were loaded into a tube furnace and purged 3 times, alternating between vacuum and inert Ar (15 min per cycle). Under a constant Ar flow (100 cm^3/min) and atmospheric pressure, the tube was heated to 500 °C. The sample was inserted into the furnace for 20 min followed by rapid cooling.

2.2.5. Graphitic Flake Isolation and Dispersion

CZTS NPs were washed for a third time in IPA and toluene (1:1), and the supernatant was collected. Within 2 weeks, all material had sedimented from the collected supernatant. Photographs of supernatants collected from each subsequent wash are provided in **Figure 2.16**. Without perturbing the sedimented material, the top solvent was pipetted off and the remaining solvent was removed with a rotovap (*i.e.,* decanted), isolating a black powdered material. Isolated material (4 mg) was suspended either in 1 mL of IPA or 1 mL of toluene. To form a dispersion, the material was mixed for 20 min, followed by 20 min of sonication. The dispersions were left to stand for 3 h.

2.2.6. Spatial and Bulk Composition of CZTS and CZTSSe Thin Films

To determine the spatial composition of CZTS and CZTSSe films, Glow Discharge Optical Emission Spectroscopy (GDOES) spectra were acquired with the *Horiba GD-Profiler 2*. A 4 mm diameter anode ablates CZT(S,Se) films with a plasma (conditions and calibrations modeled after Clark et al)[85] to obtain a signal of voltage as a function of time. The sample was fully ablated once the raw voltage for Mo reached 0.2 V, signifying penetration of the substrate material.

To extract compositional data [mols] from the voltage signal, calibration factors and the bulk material's composition were used. The bulk composition was collected though energy dispersive spectroscopy (EDS), using the *FEI Sirion XL30*'s FEI EDS detector. Data acquisition occurred when samples were at a working distance of 5 mm and acceleration energies of 7 and 20 kV were used with respective spot sizes of 5 and 4 (30−50% dead time, total counts of 1 000 000). A total of fifty-four spots across nine substrates were collected.

The relative spatial depth of the sample were extracted from time [s]. For each sample, the first 5 s was excluded due to surface contamination and stabilization. The resulting x-axis is equated to the spatial penetration [%], but measurements with the *Bruker OM-DektakXT Profilometer* allows for equating the spatial penetration [%] to sample depth [nm]. For film thickness measurements of CZTS films, a diamond stylus with a 2 μm radius tip was installed.

2.2.7. Structural Characterizations: Raman Spectroscopy, XRD, and XPS

Structural confirmation of CZTS, the organic ligand, and carbon byproducts was performed with the *Renishaw InVia Raman Confocal Microscope* at an excitation wavelength of 514 nm. Samples were exposed to 5 to 50 % maximum laser intensity for 10 s (P_{max} = 8 mW). No background subtraction was used unless otherwise specified. For background subtraction, either a 4-point linear background subtraction (CZTS) or polynomial spline background subtraction (carbon byproducts) were used. Peak intensities and positions were determined *via* deconvoluted Gaussian fits using MagicPlot Software following the strategies for peak fitting outlined for CZTS (*e.g.*, Fernandes *et al* [207] and Cheng *et al* [208]), for the organic ligand (*e.g.*, Larkin),[209] and for carbon byproducts (Sadezky *et al* [210] and Merlen *et al* [211]).

X-ray diffraction (XRD) was used for further confirmation of the CZTS and CZTSSe structure. The *Bruker D8 Discover Microfocus X-ray Diffractometer* was used, with Cu Kα (λ = 1.54059 Å) radiation was used and step size of 0.02° 2θ. The Mo COD 9008543 (110) peak center at 40.501° 2θ was used to calibrate the spectra, and CZTS COD 2105813 was used for the reference spectra. Lorentzian fits *via* MagicPlot Software were additionally used for crystallite size analysis of the (112), (200), and (312) planes of CZTS. (X-ray diffractograms and analysis are included in **Figure 2.11)**.

To determine the structure of carbon throughout CZTS NP films, XPS was used. The *Surface Science Instruments S-Probe spectrometer* was used with a monochromatized Al X-ray source and a low-energy electron flood gun for charge neutralization, X-ray spot size of 800 × 800 μm^2, analytical chamber pressure below 5 × 10−9 Torr, pass energy for survey spectra (composition) of 150 eV, and sata analysis performed with the Hawk 7 Analysis program (Service Physics, Bend OR). High resolution XPS spectra were calibrated to the hydrocarbon C 1s peak at 285.0 eV.

2.2.8. Imaging of NPs and Thin Films

Transmission Electron Microscopy (TEM) and Scanning Electron Microscopy (SEM) were used to respectively image the CZTS NPs and CZT(S,Se) thin films. The *FEI Technai G2 F20* was used to collect TEM micrographs. A 200 kV accelerating voltage and a spot size of 3 were used. The NP ink was diluted dispersion (10 μL) was suspended on a 300-mesh copper TEM grid and stored under vacuum overnight. Micrographs are included in **Figure 2.11**.

Top down and cross sectional micrographs of CZTS and CZTSSe films were aquired with the *FEI Sirion XL30* Scanning Electron Microscopy (SEM). Micrographs were obtained at an acceleration energy of 5 kV and a spot size of 2. Cross-sectional samples were prepared by diamond scribing on the substrate SLG and fracturing the sample. Carbon tape was used to cover as much of the exposed SLG as possible to reduce sample drift and charging. Micrographs are included in **Figure 2.12**.

2.2.9. Thermal Analysis (TGA)

Dynamic thermal gravitational analysis (TGA) was collected with the *TA Instruments Q20 ThermoGravimetric Analyzer* from room temperature to 500 °C at a heating rate of 10

°C/min. A platinum pan was used for all experiments. Sample gas (either air or N_2) was purged at a continuous flow rate of 40 mL/min.

2.3. Results and Discussion

2.3.1. Thermal Decomposition of Oleylamine

Throughout OLA's lifecycle, the ligand is exposed to several high temperature processes, including NP synthesis (225 °C), annealing (100 °C – 300 °C), and sintering (500 °C). To understand how OLA thermally decomposes, the ligand was incrementally heated from 100 °C to 500 °C in the absence of CZTS NPs (**Figure 2.1**). No change in OLA was observed until 150 °C, when partial evaporation was observed despite the temperature being well below the ligand's boiling point of 348 °C. Volatilization at this temperature is likely due to low-boiling point impurities within technical grade OLA such as short-chain alkylamine moieties and nitroalkanes.[212] OLA cooled from 100 °C and 150 °C formed a waxy white surface film, attributed to saturated hydrocarbon impurities which solidify at room temperature.[212] At 200 °C and 225 °C, the film emitted smoke and transformed into an orange-brown liquid. Increased smoking may have resulted from bond cleavage at OLA's allylic bond, leading to lower molecular weight hydrocarbons that readily evaporate at these temperatures.[213] Furthermore, upon cooling these films no additional colorimetric change transpired, signifying that irreversible structural decomposition had occurred. Above 250 °C, the films formed a glassy-black-brown solid with high opacity. Above the ligand's boiling point (> 400 °C, not pictured), the material rapidly

vaporized and combusted, leaving little residual material in agreement with previous works.[214]

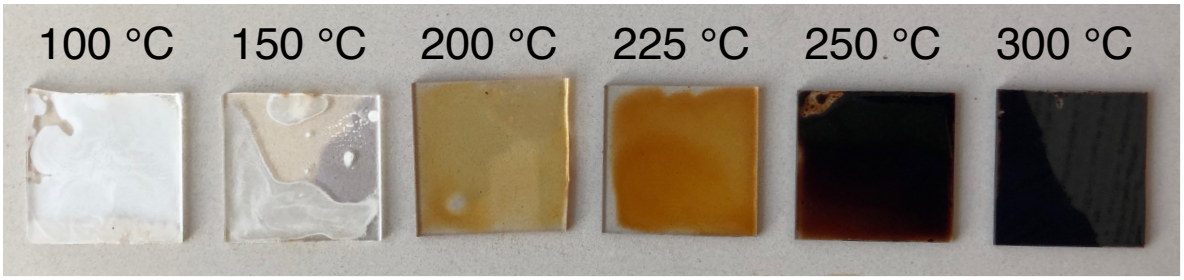

Figure 2.1. From left to right, OLA annealed on microscope slides at 100, 150, 200, 225, 250, and 300 °C. 0.2 mL of OLA per substrate, each heated for 20 min in air.

To investigate the structural transformation of OLA during pyrolysis, Raman spectroscopy was performed (**Figure 2.2**). The resulting room-temperature spectrum is consistent with literature, with marked bands that identify the ligand's terminal group (CH_3 bending vibrations at 1439 cm^{-1}), unsaturated bond (*cis* C=C bending vibrations at 1656 cm^{-1}), and hydrocarbon backbone (C–H stretching vibrations from 2800 cm^{-1} to 3006 cm^{-1}).[117,212,215] When the ligand was heated to 300 °C, corresponding to the fully darkened structure shown in **Figure 2.1**, no residual OLA was detected, rather, graphene's in-plane vibrational mode (G at 1588 cm^{-1}) was observed and accompanied by a disorder (D at 1366 cm^{-1}) and second-order band (D + D' at 2944 cm^{-1}).[216–220] The predominant D band, low D + D' signal, absence of signature second-order bands (2D at 2717 cm^{-1}), overall peak attenuation, and fluorescent background are all indicative of the formation of highly disordered graphene, functionalized graphene, or a graphitic carbon systems with sub-micron order.[216,218–224] The formation of nanoparticle graphitic flakes corresponds well with the calculated crystallite size of 6.44 nm, as determined by the Tuinstra and Koenig relation (**Equation 2.1**).[218,220,225,226]

$$L_a\ (crystallite\ size)\ = C(\lambda)\ *\ \frac{I_G}{I_D} \qquad \textbf{(Eqn. 2.1)}$$

The crystallite size is a function of the relative fit intensities between the G and D peaks (I_G/I_D) and is proportionate to $C(\lambda)$, an empirical constant found to be 4.4 nm for 514 nm excitation wavelengths. This result is in correspondence with the graphitic carbon found within sintered NP films,[145,214] however, the onset of decomposition as observed within **Figure 2.1** is the lowest known reported temperature of OLA ligand pyrolysis.

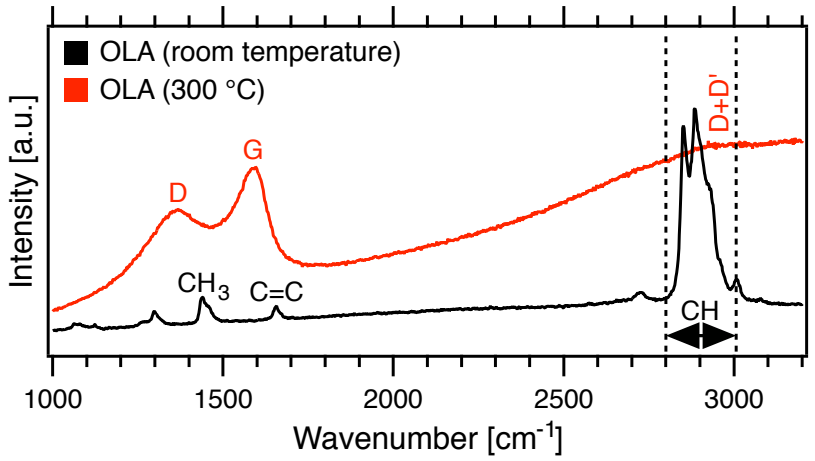

Figure 2.2. Raman spectra of room temperature OLA (black) and OLA annealed at 300 °C (red). Corresponding identifiable peaks are labeled.

While OLA has been used to intercalate for graphitic carbon systems,[202,227] the formation of graphitic carbon from the pyrolyzed OLA has not been previously reported. Graphite, graphene, and graphene oxide have been produced through pyrolysis of short-chain hydrocarbons; however, this is achieved through epitaxial growth on crystalline substrates that requires temperatures exceeding 900 °C.[228–230] More appropriately, low temperature multistep carbonization initiated from pyrolytic condensation of OLA may have occured.[231–234] While this has not been previously been reported for OLA, condensation through the formation of nanostructured (< 2 nm) polycyclic

aromatic hydrocarbons (PAHs) is plausible. PAHs can form from allylic cleavage, yielding an alkyl radical and a terminal double bond which participate in intermolecular cyclization.[178,213] As OLA contains an allylic site due to the ligand's double bond, the ligand likely undergoes similar decomposition, enabling OLA-based carbonization to form the observed ~ 6 nm graphitic carbon flakes.

2.3.2. Graphitic Carbon Formation During CZTS Nanoparticle Synthesis

Graphitic carbon has consistently been first detectable within CZTS NP films sintered at 500 °C,[84,135,142,145,214,235] a significantly higher temperature then what is required to pyrolyze OLA. This alludes to the possibility that graphitic carbon formation begins far below the NP sintering temperatures used in literature; rather, the ligand may restructure as early as the CZTS NP synthesis at 225 °C. As such, a Raman spectrum of post-synthesized powdered CZTS NPs capped with OLA is presented in **Figure 2.3**.

In additional to CZTS signature peak at 338.5 cm^{-1} and second order band at 660 cm^{-1}, both the D and G bands were detected at 1379 cm^{-1} and 1575 cm^{-1}, respectively. The presence of the D and G bands within powdered CZTS NPs is distinct and verifies that the ligand is restructuring to form the graphitic carbon material during NP synthesis. Furthermore, these band were respectively red and blue shifted due to an uptake in structural defects.[144,218,236] Deconvoluted left-edge band tailing associated with disordered graphite (1200 cm^{-1}) and an amorphous carbon network (1400 cm^{-1} to 1500 cm^{-1}) were also more pronounced.[216,237] This rise in defects and amorphous nature can be attributed to metal ions and NPs complicating the formation pathway of graphitic carbon, presumably resulting in an overall less conductive carbon material.[144]

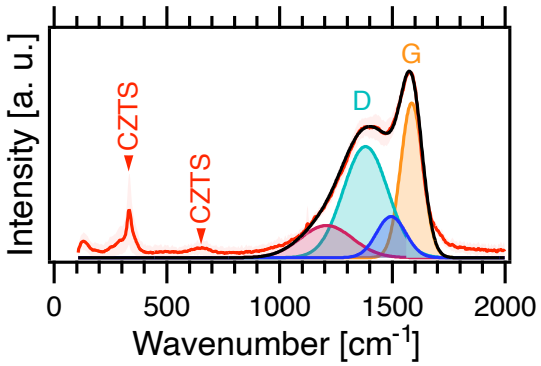

Figure 2.3. Raman spectrum of powdered CZTS NPs, with focus on the graphitic carbon region. CZTS peak, and graphene D and G peaks are labeled. A four-point linear background subtraction was used to eliminate fluorescence.

Moreover, the synthesized nanometer scaled graphitic carbon flakes are comparable in size to the scale of the NPs – with approximate crystallite size of 6.35 nm – making them indistinguishable from NPs through electron microcopy (see **Figure 2.12**). As such, this reaction byproduct can easily be overlooked within micrographs of deposited NP films. Thus, by measuring Raman spectra at high wavenumbers (1000 – 1800 cm^{-1}), this technique is comparatively effective in detecting graphic carbon within NP blends. This is critical as the decomposition of OLA can occur for comparable NP syntheses.

2.3.3. Distribution and Structure of Graphitic Carbon within Deposited Nanoparticle Films

Traditional models of the ligand behavior during NP sintering involves desorption, restructuring, and isolation into a residual carbon-rich FGL,[199,214,238] as shown in **Scheme 2(a)**.[199,214,238] From our Raman investigations, we have observed that graphitic carbon is formed even during the synthesis of the NPs, rather than forming solely during the sintering step. Unless able to isolate the graphitic carbon between synthesis and sintering, it is likely that this residual

carbon layer will remain unavoidable as nanostructured graphitic carbon is unable to evaporate below the 500 °C sintering temperature.[239] As such, in understanding the mechanisms of carbon phase segregation within the final sintered film, the evolution of the FGL can be understood or potentially mitigated.

To address this, **Scheme 2.1(b–d)** includes three alternative models that consider the presence of graphitic carbon at the time of deposition. First (**Scheme 2.1(b)**), in conjunction with the stabilizing ligand (OLA), the graphitic material may anchor to the NPs surface as an encapsulant.[240] During the sintering process, both organic materials desorb and migrate towards the substrate, ultimately forming the FGL. Alternatively (**Scheme 2.1(c)**), the graphitic carbon and NPs may exist as a mixture. The graphitic carbon can be functionalized with OLA,[202,227] allowing the phase to be dispersed homogeneously in the NPs ink, only to segregate during sintering. In either instance, the carbon-based material diffuses towards the substrate during the sintering process, forming a carbon-rich FGL underneath large grains of the active material. In contrast, if the graphitic carbon forms a heterogeneous mixture that aggregates during deposition (**Scheme 1(d)**), the FGL will form prior to sintering. In this case, instabilities between NP and graphic carbon allows for graphic carbon isolation without simultaneously removing the capping ligand required for deposition. This can result in an overall reduction of the FGL in sintered films, as much, if not all of the graphitic carbon can be removed prior to sintering.

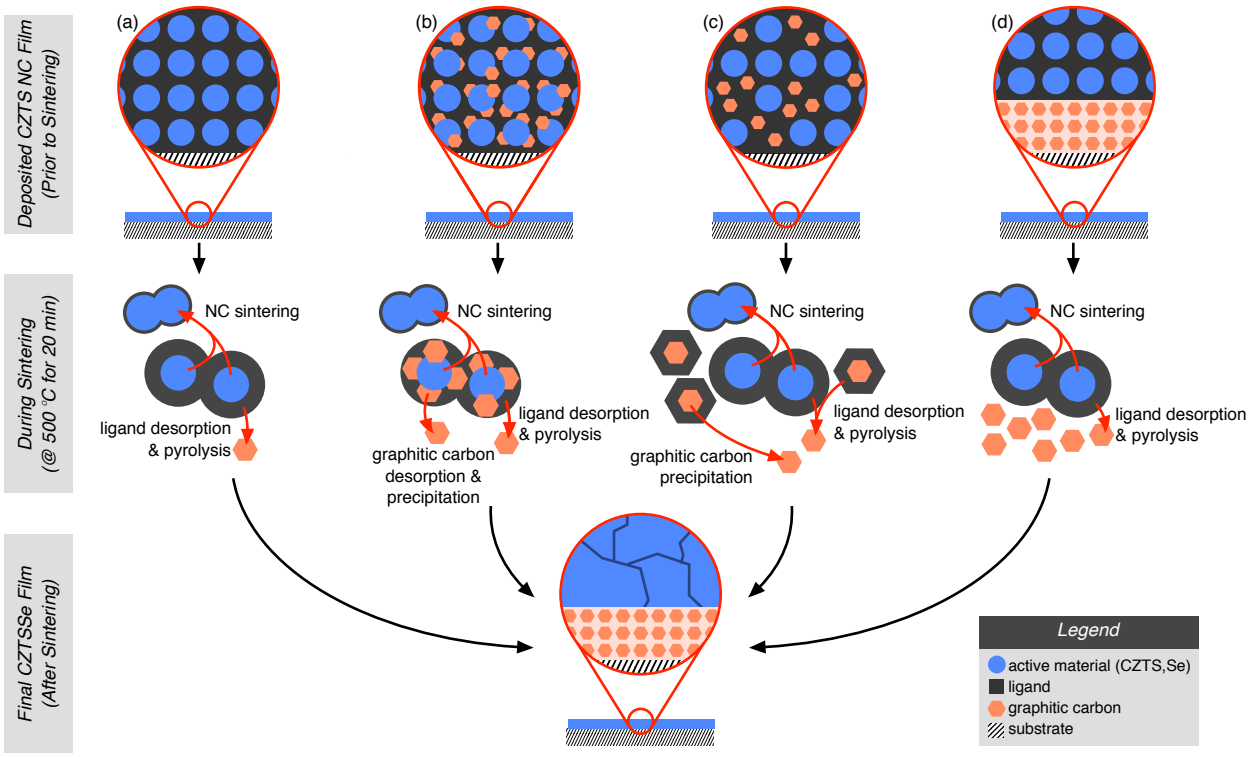

Scheme 2.1. Simplified **(a)** traditional model of NP and grain growth account for ligand desorption and pyrolysis during sintering. Alternative models include the presence of graphitic carbon at the time of deposition. This includes **(b)** CZTS NPs capped with OLA and graphitic carbon, **(c)** homogeneous mixture of OLA-capped NPs and OLA-functionalized graphitic carbon, and **(d)** heterogeneous mixture of OLA-capped NPs and graphitic carbon. All models result in a large-grain layer of the active sintered material above a fine-grained graphitic carbon layer.

To evaluate these models, GDOES was used to identify the carbon distribution throughout the as-deposited CZTS NP films (**Figure 2.4**) prior to sintering. While progressing through the depth of the film, the concentration of active material (CZTS) remains consistent across the first two-thirds of the film. Thereafter, the material's concentration rapidly drops off. Within the top half of the film, the concentration of carbon follows the same trend as the active material. However, closer to substrate, the carbon content reaches an apex immediately after CZTS is diminished. This

bimodal distribution of carbon signifies that there is a segregation between the NPs and residual carbon immediately after deposition (*i.e.*, prior to sintering), in agreement with the theory presented in **Scheme 2.1(d)**. It is plausible that carbon content within the top half of the film arises from the capping ligand while graphitic carbon settles towards the substrate during the room-temperature drying process. Remarkably, the carbon peak associated with CZTSSe's graphitic FGL (see **Figure 2.13**) is spatially consistent with the carbon peak observed in the as-deposited material, further indicating the graphitic FGL is established prior to sintering or other thermal treatments, such as annealing. However, the chemical nature of carbon throughout the film is indeterminate by GDOES, and, as such, other techniques for exploration of the carbon identity are needed.

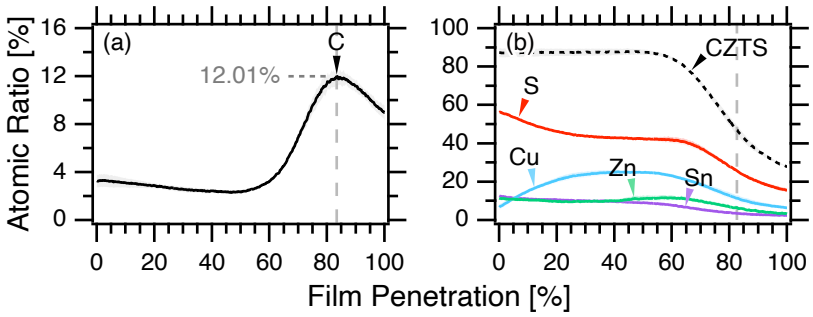

Figure 2.4. GDOES spectra signifying the spatial composition of **(a)** CZTS (summation of Cu, Zn, Sn, and S atomic percentages) and **(b)** carbon. 0% corresponds to the surface of the sample, and 100% indicates substrate penetration (active layer thickness varies from 750 nm – 1500 nm as determined *via* a profilometer).

The carbon structure present within the CZTS film was studied to ascertain whether **Scheme 2.1(d)** is an accurate model. **Figure 2.5** includes XPS data collected on four separate GDOES craters at increasing depths within a CZTS film. Deconvoluted high resolution C 1s spectra consists of up to four peaks which represent C=O (~288.5 eV), C–O/C–S (~286.5 eV), C–

C sp^3 (~285.0 eV), and C=C sp^2 (~283.7 eV) moieties.[224,241] Intermittent atomic percentage of these moieties and relevant binding modes are quantified in **Table 2.1** (see **Figure 2.14** for full XPS survey spectra and corresponding compositions).

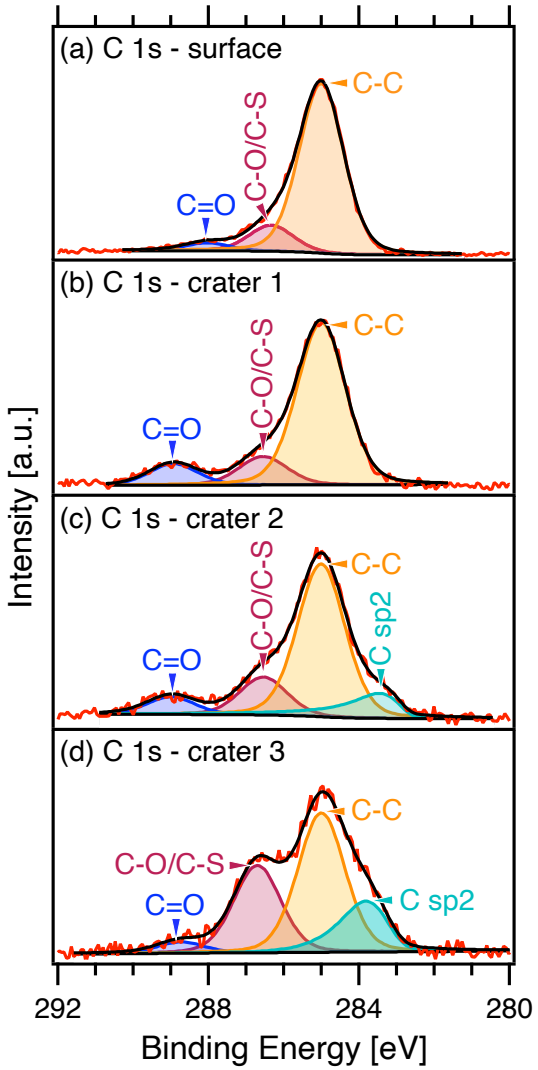

Figure 2.5. High resolution XPS spectra on the C 1s peaks of CZTS NP at the **(a)** samples surface (0% through the film), **(b)** ~25% through the film, **(c)** ~50% though the film, and **(d)** ~75% through the film (in reference to GDOES percentage through the film, **Figure 2.4**).

Sp^3, C=O, and C-O/C-S binding energies are detectable throughout the bulk of the film. The predominance of sp^3 bonding is associated with the ligand's aliphatic backbone.[242] C=O and C–O/C–S bonding are also attributed to the ligand. The conversion of an amine into a C=O containing amide or thioamide (C=S) has been previously been identified during the sulfur mixing in pure octylamines.[150,215,243] Similarly, during NP synthesis C–S bonds originate from ionic sulfur chains reducing the ligand's double bond to abridge OLA molecules, forming a polysulfide.[150,215,243,244]

Table 2.1. XPS Concentration (Atomic Percentages) of Elements of Interest within CZTS NP Samples

	(a) Surface (%)	(b) Crater 1 (%)	(c) Crater 2 (%)	(d) Crater 3 (%)
C 1s	**53.7**	**30.2**	**36.2**	**41.3**
C=O	3.9	10.0	7.2	3.9
C-O/C-S	12.8	13.5	15.8	29.9
C-C	83.3	76.5	63.6	47.8
C sp^2	0.0	0.0	13.4	18.4
O 1s	**29.4**	**39.5**	**44.0**	**51.8**
CZTS	**17.0**	**30.3**	**19.8**	**7.0**
Cu $2p_3$	14.4	10.8	11.6	17.6
Zn $2p_3$	5.2	31.9	42.2	51.0
Sn $3d_3$	19.6	23.5	13.9	9.8
S 2p	60.8	33.6	32.4	21.6

The total concentrations of carbon (C 1s), oxygen (O 1s) and CZTS (summation of Cu $2p_3$, Zn $2p_3$, Sn $3d_3$, and S 2p) are bolded. The relative concentration associated with carbon bonding (C=O, C−O/ C−S, C−C, C sp2) and CZTS (Cu $2p_3$, Zn $2p_3$, Sn $3d_3$, and S 2p) are included. Full compositional data and parent survey spectra are included in **Figure 2.14**.

Variation in composition throughout the film can be attributed to a change in carbon phase. While sp^3 bonding associated with the ligand's backbone decreases with film ablation, the overall C 1s carbon concentration mirrors the bimodal carbon distribution as observed in GDOES data. The increase of C 1s is accompanied by a rise of sp^2 carbon which is only detectable in the latter half of the film, near the film's substrate. In agreement with Raman spectroscopy results, the presence of sp^2 carbon indicates the formation of graphitic carbon from the decomposition of

OLA.[224,241] Moreover, XPS data offers further insight to the structure of the graphitic carbon. The presence of C=O and C–O/C–S binding energies and increase O 1s are indicative of graphene oxide (GO). The mutual increase of C–O moieties and sp^2 are attributed to carboxyl and epoxy groups of GO,[200,224] with additional carbonyl groups stemming from C=O.[200,224]

The persistence of sp^3 binding and lack of a satellite peak associated with π-π* delocalized electrons (between 288 eV and 293 eV)[224] signifies the formation of nonconductive GO flakes. In addition to sp^3 binding being connected to poor conjugation of GO, sp^3 within the latter half of the film is also associated with the trace amorphous carbon identified in **Figure 2.3**.[202,241]

2.3.4. Acetylacetonate v *Chloride Precursors: Source of Oxygen*

CZTS was synthesized under inert conditions (under N_2 atmosphere), however oxidized carbon was detected. To understand the origin of oxygen within the GO flakes, both the ligand and precursor materials were investigated. If the incorporation of oxygen into the pyrolyzed material stemmed from ligand impurities in technical grade OLA (70 % pure), such as nitroalkanes as reported by other authors,[212] then it is expected that the ligand will on pyrolyze into GO under inert conditions. However, as indicated by Raman spectra, as shown in **Figure 2.2**, only bonding modes corresponding with the OLA's structure (*i.e.,* aliphatic alkene) are detected. ^{1}H NMR of the ligand agrees with reference spectra for OLA, with no detection of carbonyl nor amide functional groups (see **Figure 2.17**). Further, TGA on the ligand both under air and inert conditions (N_2) was performed, (**Figure 2.6**). During pyrolysis in air, by 225 °C, 63.31% of the material remained, which dropped to 9.24% by 300 °C. This result agrees with the decomposition observed in **Figure 2.1**, where the ligand is only partially decomposed by 225 °C, and is heavily pyrolyzed by 300 °C. Under N_2, over 99% of OLA's mass had been lost by 266.1 °C, reflected by the spectra and image

on N_2 annealed OLA in **Figure 2.6(b)**. This full volatilization of the organic material under inert conditions further signifies that the oxygen source that contributes to GO is not innate to the ligand.

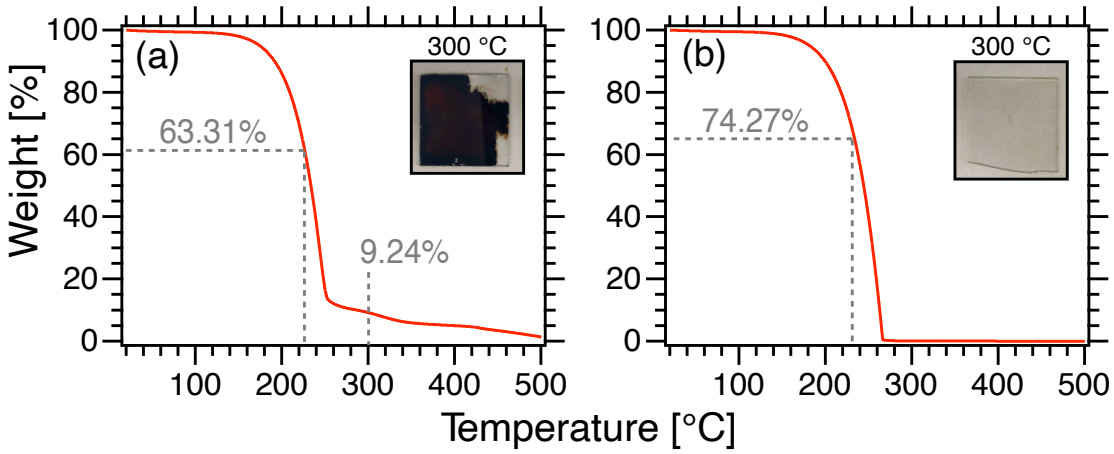

Figure 2.6. TGA weight loss profiles of OLA both dynamically heated in **(a)** air and under **(b)** N_2. Both figures include a photograph inset of OLA annealed at 300 °C under their respective atmosphere.

As oxygen containing acetylacetonate precursors were used in the synthesis of CZTS NPs, the oxygen source may be a direct result of precursor selection. To explore the influence oxygen content has on the formation of GO, a chloride-based CZTS NP synthesis was conducted under the same reaction conditions utilized in the acetylacetonate-based synthesis. As shown in **Figure 2.7(a)**, Raman spectra of powdered CZTS NPs synthesized with chloride precursors still yields the signature D and G bands of graphitic material. However, the overall intensity of these peaks is diminished in comparison to that observed for acetylacetone-based reactions. The presence of amorphous material, as indicated by the broad peak at 1200 cm^{-1} is further evidence that some structural decomposition of the organic material has occurred, but the resulting pyrolyzed material is less graphitic and more amorphous in nature. Additional signals corresponding to the original OLA ligand are detectable, as highlighted by the C-C and C-H bonding modes in **Figure 2.7(a)**.

As such, it is apparent that less structural decomposition of OLA occurred for chloride-based syntheses, albeit some graphitic material did form. Nonetheless, GDOES of deposited chloride-based CZTS NP films result in the formation of a carbon-rich layer (**Figure 2.7(b)**), comparable to that observed for acetylacetonate-based CZTS NPs (**Figure 2.4(a)**), in compliance with **Scheme 1(d)**. The formation of this carbon layer suggests that the amorphous-graphitic material still forms a heterogeneous dispersion with the CZTS NPs.

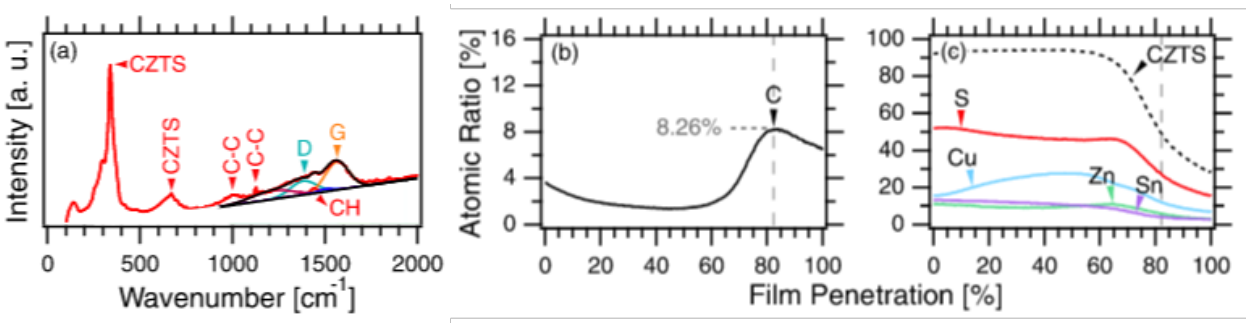

Figure 2.7. Raman spectrum of **(a)** powdered CZTS NPs produced via chloride precursors. D and G peaks are identified. GDOES spectra of chloride-based CZTS NP films, which include **(b)** the film's carbon profile and **(c)** the film's CZTS profiles (Cu, Zn, Sn, and S).

The persistence of this of carbon layer despite the lack of oxygen sources during the synthesis of CZTS NPs indicates that the formation of pyrolyzed OLA byproducts is not solely contingent on the presence of oxygen. This is observed through the ligand pyrolysis that occurs during the selenization of CZTS NP films at temperatures exceeding 500 °C under inert conditions,[199,214,238] thus, the decomposition of OLA cannot be entirely dependent on oxygen; rather, the formation of graphitic carbon is aided by oxygen. Other external factors introduced during synthesis may also contribute to the decomposition of OLA. Notably, the formed polysulfide[150,215,243,244] can decompose to forming graphitic residue upon annealing under inert conditions.[145]

2.3.5. Washing of Nanoparticles: Isolation of Graphene Oxide

In identifying methods to isolate GO, a reduction of the FGL can be achieved prior to the sintering process. Due to the polarity of GO's functional groups,[200,224] the flakes will form a heterogeneous mixture with CZTS NPs, in support for our theory illustrated in **Scheme 1(d)**.[200,224] This allows for opportunity to isolate the GO prior to deposition, as it is expected that these GO will readily aggregate and crash-out of the nonpolar solvents used to disperse the CZTS NPs.

In order to isolate the GO, the powdered CZTS NPs were first dispersed in toluene and IPA (1:1). Centrifugation was performed, promoting the dense CZTS NPs to precipitate while the GO remained dispersed in solvent. Upon supernatant collection, a rotovap was used to dry the precipitate down into a powdered material (see **Figure 2.16**). The collection of the GO from the NPs is confirmed through Raman spectroscopy of the collected powdered material (**Figure 2.8(a)**). High error between 150 cm^{-1} to 300 cm^{-1} is indicative of residual CZTS, however, compared to the Raman spectrum of CZTS NPs (**Figure 2.3**) this CZTS is only present in trace amounts, and the isolated material is primarily comprised of GO.

The collected supernatant was subjected to suspension-stability tests in both nonpolar and polar solvents. As OLA-capped CZTS NPs are stable in nonpolar solvents (toluene), and GO's hydroxyl and epoxy groups are more stable in polar solvents (IPA),[200,224] it is expected that the GO will readily crash out of solution while in the toluene. Dilute solutions (4 mg/mL) of the isolated material were suspended in toluene and IPA as shown in **Figure 2.9**. While dispersible in toluene, flocculation occurs; the material aggregates into dense clusters until sedimentation precipitation transpires. This result is apparent within the first 10 min of dispersion (visual opacity gradient), with a majority of the material settling out of solution within 3 h. To affirm that the flocculation results from immiscibility between the polar functional groups of GO and toluene, the material

was also suspended in polar IPA. Consistent with the formation of GO the material exhibited sufficient stability first 30 min, however, after 3 h a significant portion of the material had crashed out of the suspension due to GO innate instability in solvents. As such, this section details a method to isolate GO through additional NP washing (centrifugation precipitation).

To monitor the efficacy of GO removal from the final NPs material, Raman spectroscopy on the washed powered material was performed. Resulting spectra in **Figure 2.8(b)** reveals that residual graphitic material is still present within the final NP powder. This remaining graphitic material appears to be structurally consistent with the graphitic material found in the NPs which were washed twice (**Figure 2.3**) and the graphitic material found in the collected supernatant (**Figure 2.8(a)**).

Further, while the supernatant collected from the washing process is primarily graphitic carbon, GDOES profiles within **Figure 2.8(c)** of resulting washed NP films reveal that this isolation only resulted in a small reduction of carbon within the observed FGL (< 2%). This offers further evidence that only partial isolation of GO was achieved through the washing methods used in this work, and, the carbonaceous residue that arises from OLA pyrolysis is not solely GO.

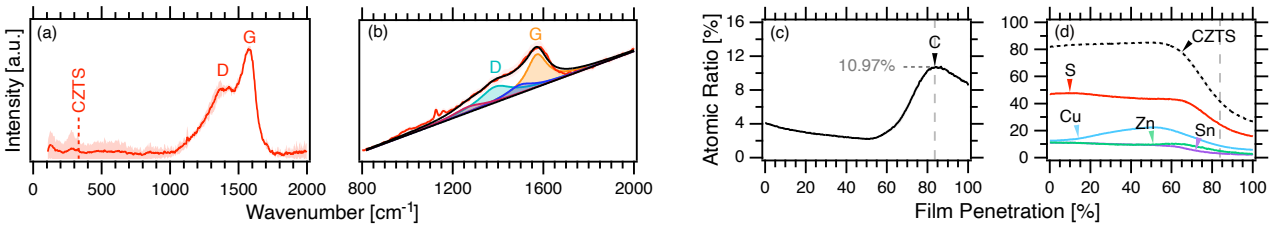

Figure 2.8. Raman spectrum of **(a)** powdered supernatant material after subsequent washes. CZTS peak labeled is absent, while D and G peaks are identified. **(b)** Raman spectra of powdered CZTS NPs (focused on D and G bands) that had been washed three times. GDOES spectra of CZTS NP films which had been

washed three times, which include **(c)** the film's carbon profile and **(d)** the film's CZTS profiles (Cu, Zn, Sn, and S).

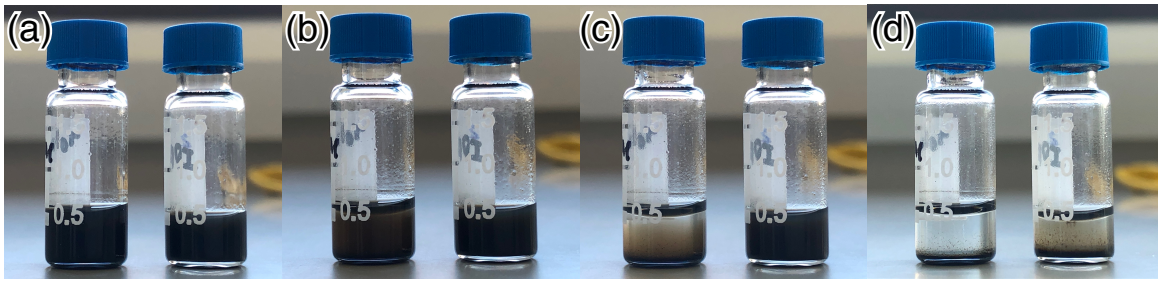

Figure 2.9. GO dispersed in (left) toluene and (right) isopropyl alcohol. Images were taken periodically starting with **(a)** immediately after dispersion. Unperturbed dispersions after were imaged after **(b)** 10 min, **(c)** 30 min, and (**d)** 3 h.

2.4. Conclusions

In this study, we demonstrated that OLA used in CZTS NP synthesis pyrolyzes into graphitic carbon at temperatures as low as 225 °C. Historically, it was expected that this process occurs during high temperature (500 °C) sintering of deposited NP films, where the pyrolyzed ligand would be expelled into a graphitic carbon-rich fine-grained-layer underneath the active material. However, our findings reveal that OLA pyrolysis occurs during CZTS NP synthesis at 225 °C and is expected to be ubiquitous for NP syntheses that exceed the 225 °C decomposition temperature. As a result, this byproduct likely is incorporated into the synthesis of many OLA-based nanomaterials, even if post thermal treatments are not employed.[194–196]

Furthermore, this graphitic carbon is identified to be nanostructured flakes of disordered graphene oxide. To account for these findings, in this work we proposed an updated mechanism for the decomposition of OLA during NP processing: (i) decomposition into nanostructured

graphene oxide flakes, (ii) inhomogeneous dispersion in NP ink, and (iii) sedimentation during deposition.

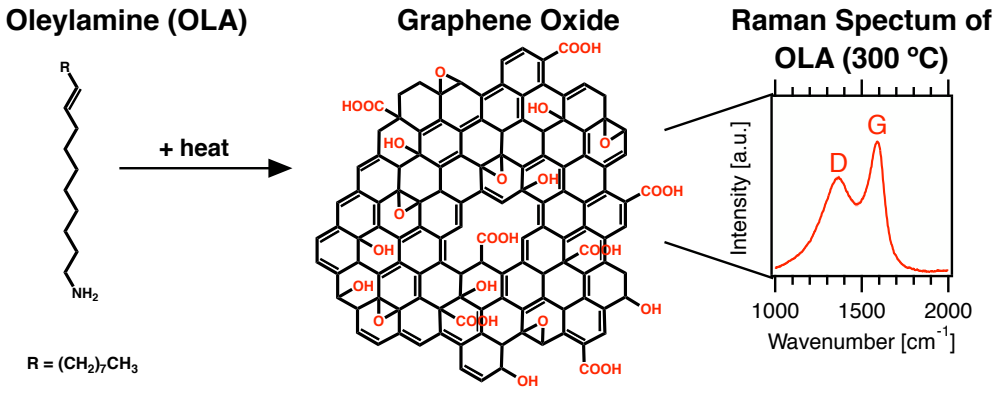

Figure 2.10. Summary of the decomposition process of OLA that occurs during CZTS nanoparticle synthesis.

As it is now evident that byproducts are produced prior to film sintering, alternative low temperature treatments are utilized to remove this material. Herein, this includes sequential washing of the NP ink in solution. In identifying methods to isolate graphene oxide post-synthesis, a strategy towards reducing the FGL within sintered films, or removing the byproduct within other OLA-based syntheses, is established.

2.5. Supporting Information

To compare the size of the graphitic flakes to CZTS NPs, the NPs were characterized via XRD and TEM. Through XRD, the mean crystallite size (τ) is calculated by the Scherrer equation:

$$\tau\ (crystallite\ size) = \frac{K\lambda}{\beta cos\theta} \qquad \textbf{(Eqn. 2.2)}$$

Here, K is the shape factor, a constant of 0.9 is used for spherical NPs. The wavelength, λ, is 1.54 Å. The peak breadth, β, and corresponding Bragg angle, θ, were collected for the three most predominant planes, (112), (200), and (312). Here, Scherrer equation provides crystallite sizes of 15.5 nm ± 1.4 nm. However, TEM micrographs of NPs (**Figure 2.11**) indicated a broader size dispersion, with particle sizes varying from 5 nm to 70 nm in diameter.

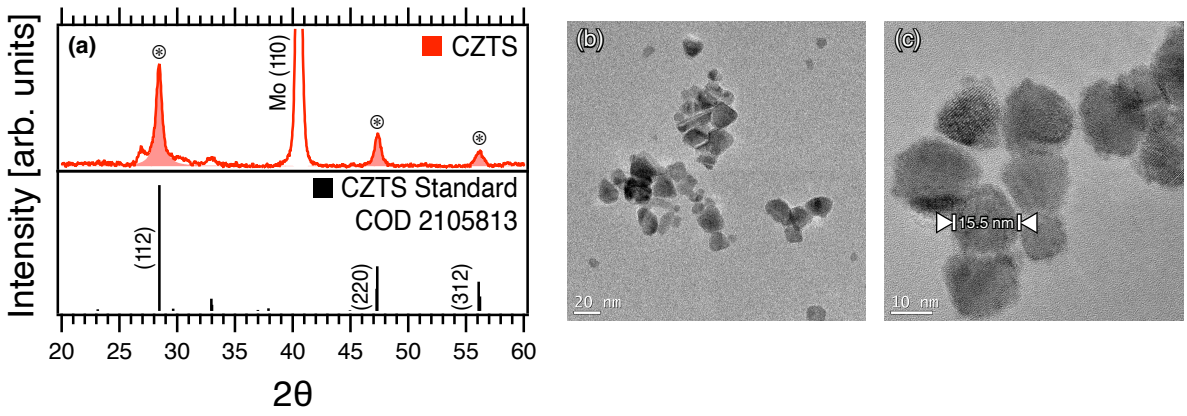

Figure 2.11. (a) XRD of CZTS NPs on Mo/SLG substrate and **(b-c)** TEM micrographs of CZTS NPs.

As discussed in the main text of this chapter, the average size of any particular graphene oxide structure is only ~ 6 nm in diameter. Therefore, these graphene oxide flakes are otherwise indistinguishable from CZTS NPs (which have NPs in sizes ranging from 5 – 70 nm). Figure 2.3.10a's cross section micrograph of the as-deposited NP film displays how the material is visually consistent from top to bottom. Visually, the graphene oxide structure is observable after NP sintering, where large grains of the active material (CZTSSe) are separated from the residual fine-grained carbon layer (**Figure 2.12**).

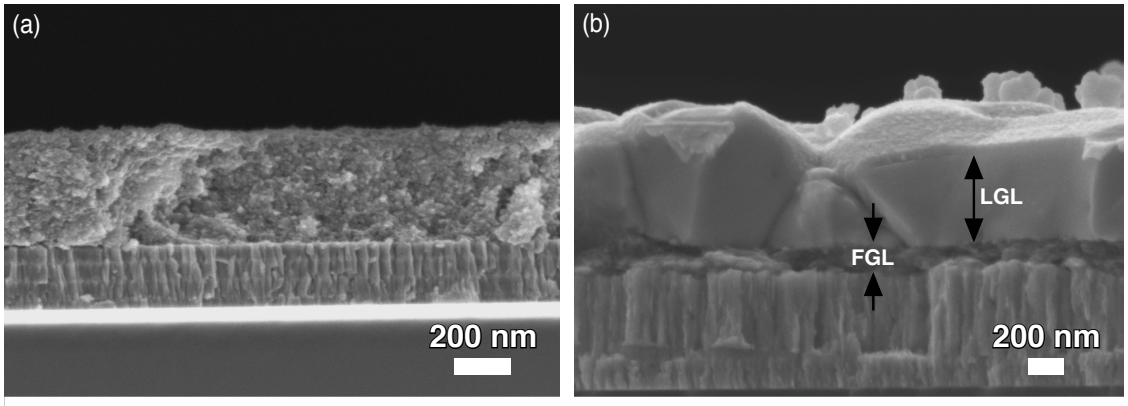

Figure 2.12. Cross sectional scanning electron microscopic (SEM) images of **(a)** deposited CZTS NP film and **(b)** sintered CZTSSe films with labeled bilayer structure. Each sample is prepared on a Mo/SLG substrate (2.5 cm × 2.5 cm substrates). Substrates were shaped by diamond scribing, then mechanically fracturing the SLG substrate.

As this chapter is aimed to focus on the pre-sintered CZTS films, **Figure 2.13** aims to further contrast the carbon distribution of pre- and post-sintered films. GDOES of deposited CZTS and CZTSSe films atomic ratios are normalized within the first half of the film to their respective stoichiometric ratios. Low signal H, N, and O are normalized with a background subtraction, while C was normalized with no background subtraction. Nonuniformities in CZTS concentration is likely due to particle size disparity between multiple ternary and binary secondary phases. Regardless, this compositional variation is eliminated during the selenization phase, as secondary phases are obliterated and a single uniform kesterite CZTSSe phase is produced. In CZTS NP films, the C concentration peaks near the substrate, nearly identical to the position where C peaks for sintered CZTSSe samples. This is found to be a predecessor to the fine-grain-layer visually observed in sintered films. However, C is present throughout the entire film, unlike the elements of CZTSSe. We attribute this to the carbon coating the nanoparticles (*ie*, the OLA ligands) in the first half of the film, which correlates well with the H, O, and N concentrations. For CZTSSe, this

hydrocarbon material has likely been either volatilized or decomposed to grow the fine-grain-layer, leaving behind graphitic carbon at the back contact. Interestingly, the concentration of Se and N in the selenized sintered films mirrors the concentration of C, indicating that the graphene oxide flakes contain selenium and nitrogen functionalization or dopants.

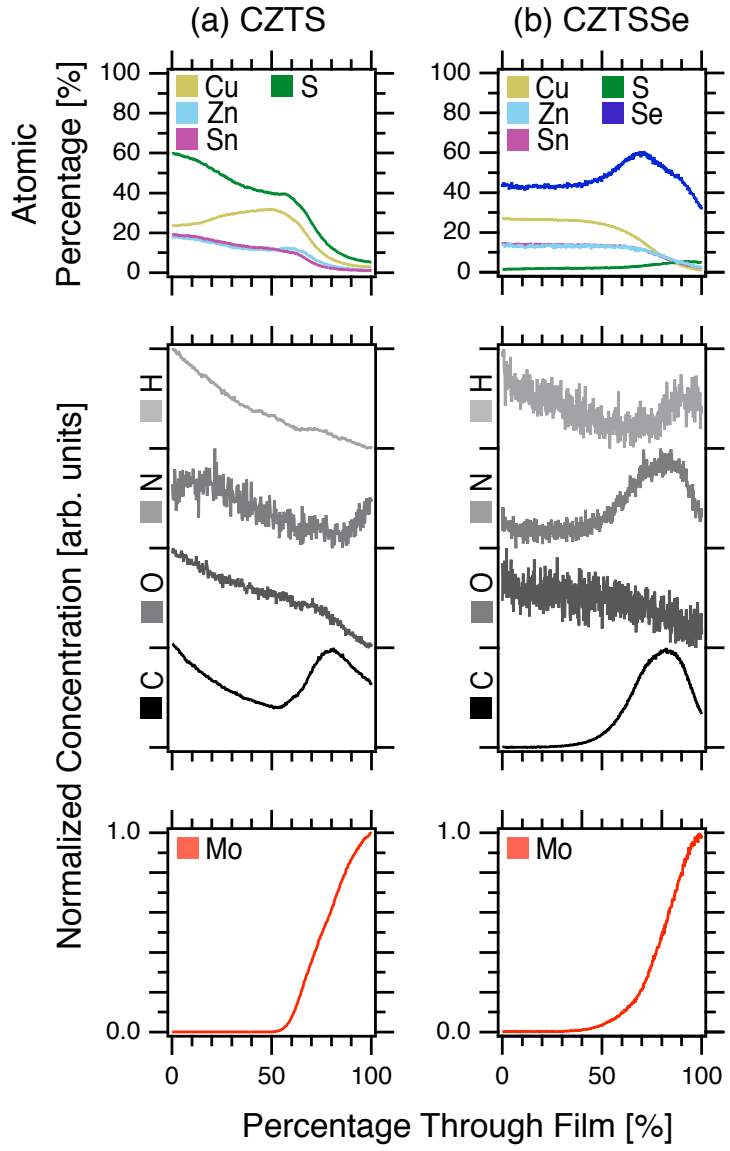

Figure 2.13. GDOES detailing spatial compositions of the active material (Cu, Zn, Sn, S/Se), organic-based materials (H, N, O, C), and substrate material (Mo) for both **(a)** CZTS and **(b)** CZTSSe.

Full survey XPS spectra reveals a diminishing of active material (Cu, Zn, Sn, and S) with film penetration, shown in **Figure 2.14**. Throughout the film, residual substrate material contamination (Mo, Si, and Na) is observed, likely detectable due to a consequence of GDOES ion bombardment. Beyond the surface of the film, the O and C concentrations appear to be relatively constant, however, the declining O content and bimodal C is only noticeable after removing residual contamination (as discussed in main text of this chapter).

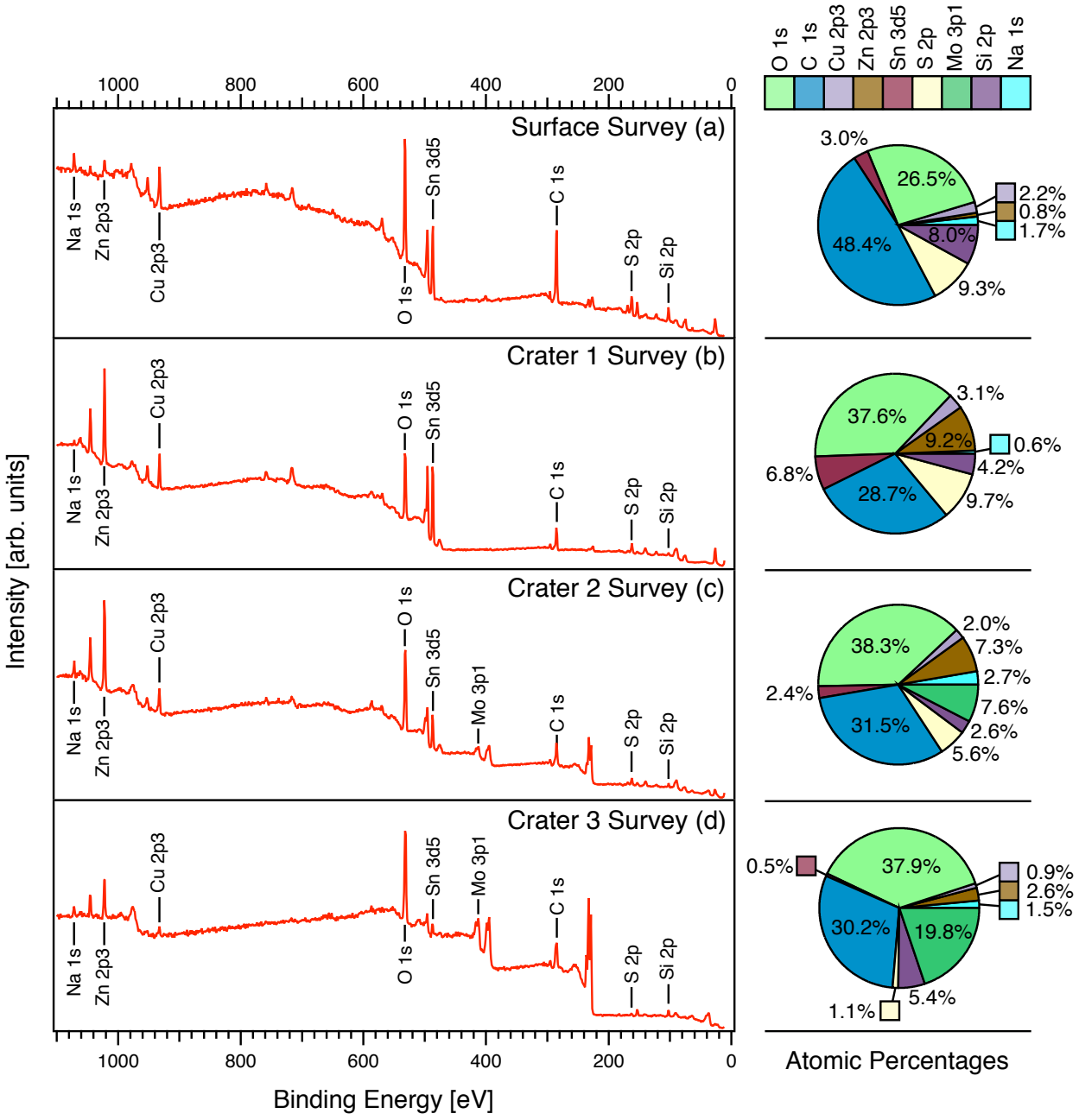

Figure 2.14. Full survey XPS spectra of CZTS NP films and their corresponding atomic percentages. Spectra are collected at **(a)** the surface the film, **(b)** 25% through the film, **(c)** 50% through the film, and **(d)** 75% through the film (in reference to GDOES ablation).

As previously mentioned, when sulfur is in solution with oleylamine, a polysulfide forms from the cross-linking of linear sulfur chains at OLA's double bond. This process is visually confirmed through the known color change of sulfur (yellow) in OLA (clear) to a deep red solution. The temporal evolution of this process is depicted in **Figure 2.15**, below.

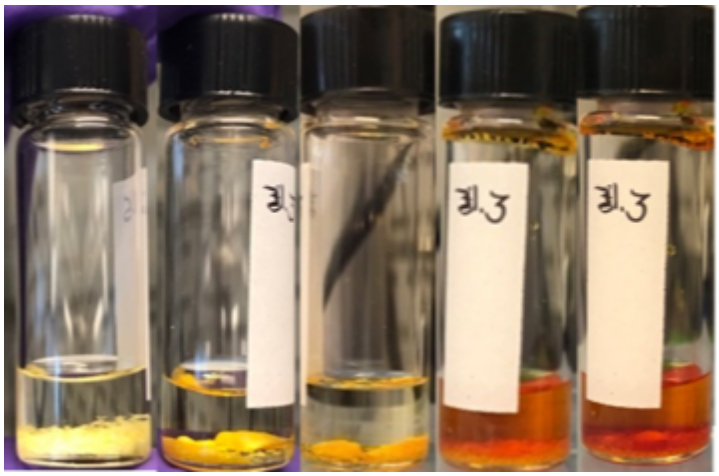

Figure 2.15. Evolution of 1 M oleylamine (clear) – sulfur (yellow) solution at room temperature into ionic sulfur (red) over the duration of 20 min.

In **Figure 2.16**, the supernatant from the third wash was collected after all material had crashed out of solution (second photo). The solvent was carefully decanted, and the remaining material was dried via a rotovap. The remaining powdered material was then used for further characterization.

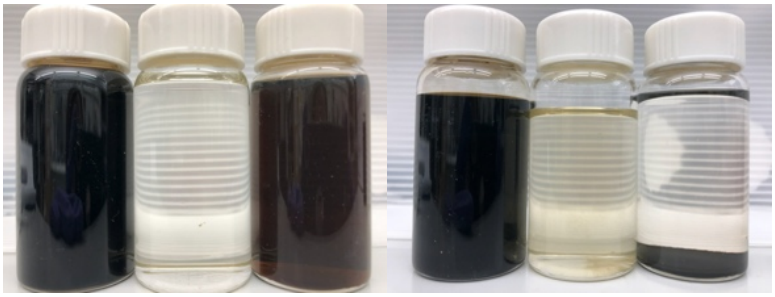

Figure 2.16. Photographs (in order) of the first, second, and third collected supernatants from NP washing. The first photograph was taken immediately after collection, while the second photograph is of the unperturbed material ~ 2 weeks after collection.

Finally, below is the ^{1}H NMR spectrum of OLA. Notably, collected spectra does not contain any chemical shifts between 3.3 – 4 ppm (alcohols) or above 9 ppm (aldehydes and carboxylic acids).

Figure 2.17. ^{1}H NMR (300 MHz, CDCl3) δ 5.45 – 5.31 (m, 1H), 2.69 (t, J = 6.9 Hz, 1H), 2.03 (q, J = 6.4 Hz, 2H), 1.45 (q, J = 6.8 Hz, 1H), 1.39 – 1.24 (m, 8H), 1.18 (s, 1H), 0.89 (t, J = 6.4 Hz, 2H).). Same spectra of OLA (20 mg/mL $CDCl_3$) is referenced against the chemical structure of OLA.

Chapter 3: Influence of Ligand Structure and Precursor Selection on Ligand Decomposition during Nanoparticle Synthesis

This chapter is reproduced from published work entitled "Ligand Decomposition during Nanoparticle Synthesis: Influence of Ligand Structure and Precursor Selection," *Chem. Mater.* 2023, 35, 2, 570-583. doi: 10.1021/acs.chemmater.2c03006.[245]

3.1. Introduction

Beyond the ligands' indispensable contribution to NP synthesis, there are emerging reports that reveal that the ligand undergoes structural changes to form new products during synthesis.[154,155,190,192,246] These byproducts may form from structural changes in the ligand's functional group,[155,190,246] polymerization of the ligand backbone,[154] or ligand decomposition into graphitic materials.[192] For instance, the 1-octodecene ligand has been reported to auto-polymerize during the synthesis of chalcogenide and metal oxide NPs, which was attributed to the heightened reactivity of the ligand's terminal double bond and potentially the metal precursor's ability to catalyze olefin polymerizations.[154] Oleylamine (OLA) and other olefins have been shown to polymerize into polysulfides in the presence of elemental sulfur,[247–249] a common precursor used in chalcogenide NP syntheses.[165–167,247–251] In our previous work, during the synthesis of

Cu_2ZnSnS_4 (CZTS) NPs with elemental sulfur and the OLA ligand, graphitic and amorphous carbon formed.[192]

While the polymerization and aromatization of olefins have been widely studied in the field of polymer science, ligand decomposition (*i.e.*, polymerization and graphitization) during NP synthesis is an emerging observation. Traditional polymerization of olefins is most commonly achieved through the use of Ziegler-Natta and metallocene catalysts and co-catalysts,[156,159,160,252–254] cationic reactions with acidic reagents,[255] anionic reactions with nucleophilic reagents,[254–256] or radical reactions.[254,255] The decomposition of olefin monomers into cyclic moieties such as polycyclic aromatic hydrocarbons and nano-graphite has been described *via* Diel-Alders reactions,[58,176,257] intermolecular cyclization,[257] and thermal cracking.[176,177,179,257] Additionally, pyrolysis (*i.e.,* thermal decomposition)[58,187,258] and solvothermal treatments[58,183] of organic monomers have been used to synthesize carbon-based NPs, or carbon dots. The unsaturated (olefin) organic monomers used in these studies overlap with the wide library of ligands used in NP synthesis, including α-olefins,[252,253] amines,[183,247–249] and carboxylic acids.[167,169–171,175–177,179,187,257,259] All of these mechanisms are reviewed in more detail in **Chapter 1** (**Section 1.2.5**.) In addition to the use of ligands in these reactions, variables such as temperature and metal catalysts overlap with the temperatures and metal precursors (*e.g.,* acetylacetonate) used to synthesize NPs. As such, it is critical to understand which conditions result in ligand decomposition during NP synthesis.

Considering the aforementioned instances of ligand polymerization and graphitization both during and outside of NP synthesis, there is interest in decoupling variables (*i.e.,* ligand functional group, ligand bond saturation, and anionic and cationic precursor selection) which results in

unintended changes in ligand structure. As such, this chapter investigates how these variables lead to the unintended ligand decomposition during NP synthesis.

We begun with the synthesis of kesterite Cu_2ZnSnS_4 (CZTS) NPs, using common amine ligands with varying bond saturation (dodecylamine (DDA), oleylamine (OLA), and linoleylamine (LOA)) and analogous carboxylic acid ligands (stearic acid (SA), oleic acid (OA), and linoleic acid (LA)), as shown in **Figure 1.12**. These ligands are of interest as they are commonly used in NP synthesis and operate as a high boiling point solvent, reducing agent, and coordination complex,[16] allowing them to be the only organic monomers required for the NP synthesis. CZTS was used as the model material system, as in the previous chapter,[192] we found that pyrolyzed carbon impurities had formed in conjunction with CZTS NPs during synthesis with the OLA ligand, elemental sulfur, and with both metal acetylacetonate and metal chloride precursors.

As synthesis contains external variables (*e.g.*, precursors) which can influence ligand decomposition, we systematically characterized the structural changes and stability of the ligand in absence of and in the presence of precursors (*i.e.*, elemental S, Cu acetylacetonate, Zn acetylacetonate, and Sn acetylacetonate). This enabled us to directly study the influence of ligand bond saturation, functional group, and precursor selection on ligand decomposition.

Through a combination of structural (Raman Spectroscopy) and thermal (thermal gravitational analysis, TGA) analyses, we identify how bond saturation, functional group, and sulfur content all influence the pyrolysis, or thermal decomposition, of the organic ligand; ligands which contain double bonds, have amino-groups, and which are heated in the presence of elemental sulfur were inclined to form graphitic species. Additionally, we find that the individual elements selected (M = Cu, Zn, Sn) for NP synthesis also contributes to *in situ* ligand decomposition to different extents.

3.2. Methods

3.2.1. Materials

Ligands used in this study include dodecylamine (98 %, Aldrich), octadecylamine (98 %, Aldrich), oleylamine (70 %, Aldrich), stearic acid (98 %, Aldrich), oleic acid (99 %, Aldrich), and linoleic acid (99 %, Aldrich). Linoleylamine is not commercially available, as such, this ligand was synthesized. **Figure 3.7** includes the synthetic procedure and proton nuclear magnetic resonance (H^1 NMR) of linoleylamine. The metal precursors used in NP synthesis include copper(II) acetylacetonate (99.99 %, Aldrich), zinc (II) acetylacetonate (99.995 %, Aldrich), tin(IV) bis(acetylacetonate) dibromide (98 %, Aldrich). Elemental sulfur (99.98 %, Aldrich) is used in the ligand-sulfur mixture and operates as the non-metal chalcogen precursor during NP synthesis. Solvents include isopropanol and toluene. Substrates include glass slides and soda lime glass sputtered with Mo (Mo/SLG)

Due to the relatively low purity of oleylamine (70 %), the ligand was purified following the procedure by Baranov et al.[67] This was to eliminate common impurities in OLA, such as oxygen containing unsaturated amides and nitroalkanes.[67] For comparison of all experiments and results repeated with the purified oleylamine (70 %), see **Figure 3.8**. Additionally, shorter chained dodecylamine ($C_{12}H_{27}N$) is used as the saturated amine in this work rather than octadecylamine (ODA; $C_{18}H_{39}N$) since the synthesis of CZTS was unsuccessful with the ODA ligand (see **Figure 3.9**) and DDA has previously has been used to synthesize CZTS NPs.[261]

3.2.2. 1 M Ligand-Sulfur Mixtures

A concentration of 1 mmol of elemental sulfur (32 mg) in 1 mL of ligand was used to form all 1 M ligand-sulfur mixtures. Oleylamine and linoleylamine were heated to 40 °C to form a homogenous solution with sulfur, whereas dodecylamine (solid at room temperature, T_{MP} = 28 °C) was heated to 80 °C. Upon heating and mixing amine-sulfur, all solutions turned red-orange in color and remained homogenous upon cooling to room temperature. Unlike amine-S mixtures, homogenous carboxylic acid-S solutions did not form at temperatures below the melting point of elemental sulfur (112 °C), and upon cooling, elemental sulfur precipitated from the carboxylic acid-sulfur mixture. As such, these solutions were mixed and held at 115 °C to form a homogenous clear solution until used for further experimentation or characterization.

3.2.3. NP Synthesis

The metal precursors, the selected ligand, and a stir bar (for continuous stirring) were sealed in a 100 mL 3-neck round bottom flask, which was transferred to a Schlenk line for air-free chemistry. To degas the mixture of trapped gases and volatiles, the flask was cycled a minimum of 3 times between vacuum and N_2 over 0.5 h at room temperature. Using a heating mantle, the flask was then heated to 130 °C and further degassed until bubbling commenced under vacuum. Under the flow of N_2, the solution was heated to 225 °C. The average heating rate was kept at ˜10 °C/min. For chalcogenide NP syntheses, upon reaching 225 °C, the flask was injected with the separately prepared 1 M ligand-sulfur solution. After stirring at 225 °C for 2 h, the flask was raised from the heating mantle and naturally cooled down to 80 °C. A solution of 5:1 antisolvent to solvent was poured into the flask. The solution was centrifuged (13.5k rpm, 10 min) followed by decanting. Sedimented NPs were

dispersed in a 3:1 solution of antisolvent to solvent, where the centrifuging (12k rpm, 5 min) and decanting process was repeated. Residual solvent was removed with a rotavapor and samples were further dried for 24 h under vacuum prior to characterization, forming a powdered NP sample. For further details on the molar ratios of precursors, ligand concentrations, and washing procedures used during the synthesis of CZTS, metal (Cu, Zn, Sn), and chalcogenide NPs (Cu-S, Zn-S, Sn-S), see the See **Chapter *3.5.7***.

3.2.4. Structural Characterization of NP Synthesis Products

Structural characterization of synthesized inorganic NPs was carried out with X-Ray Diffraction (XRD), as XRD is ideal for identifying the phases of crystalline materials. XRD was collected with the *Bruker D8 Discover Microfocus X-ray Diffractometer* under Cu K-α (λ= 1.54 Å) radiation. Powdered NP samples were pressed onto a Mo/SLG substrate. All diffractograms were calibrated using the Mo substrate's (110) peak center at 40.501° (COD 9008543) and were compared against reference patterns to identify the NPs structure. Crystallite size of formed NPs was estimated with the Debye-Scherrer equation applied to Lorentzian peaks fitted *via* MagicPlot Software. All collected XRD diffractograms, reference diffractograms, and analyses are included in **Figure 3.14**.

To further identify the NPs and to detect carbonaceous NP reaction products, the *Renishaw InVia Raman Confocal Microscope* was used on all powdered NP samples, pressed onto a Mo /SLG substrate. Raman collection and analysis was performed with a 514 nm laser (excitation wavelength), 1200 l/mm laser grating, 10 s acquisition time, 50 × microscope objective, and spectra were fitted *via* Gaussian deconvolution. Laser power, acquisition time, and accumulations were optimized for each material to circumvent laser

ablation/florescence/detector saturation while maintaining adequate spectral signal to noise.

For CZTS NPs, 50 – 70 spots were measured at 5 % laser power (0.4 mW), with 1 – 5 accumulations collected per spot. Each spectrum had a sigmodal background which was removed by a 6-point linear background subtraction. Anchor points were applied in regions where there was no Raman scattering (100, 500 ± 25, 800 ± 25, 1700 ± 25, 2500 ± 25, and 3200 cm^{-1}). Spectra were then normalized to the highest intensity CZTS peak (˜339 cm^{-1})—an internal reference standard—followed by linear averaging. For metal and binary chalcogenide NP samples, a minimum of 20 spots (1 – 5 accumulations) were measured at 0.5 – 10 % laser power (0.04 – 0.8 mW). To normalize, each spectrum was first subtracted by its mean, then divided by its standard deviation; a process known as standard normal variate (SNV) normalization.[262] Spectra were then linear averaged and sigmodal backgrounds were removed either by a polynomial (R^2 = 0.9999) or spline fit. Peak intensities and positions were determined *via* deconvoluted Gaussian fits using MagicPlot Software following the strategies for peak fitting outlined for CZTS and secondary phases (*e.g.*, Fernandes *et al* [207] and Cheng *et al* [208]) and the NIST Chemistry WebBook Raman database. Sample-specific Raman spectra, and analyses all accompany the XRD diffractograms in **Figure 3.14**.

3.2.5. Thermal Decomposition of Ligands and Ligand-Sulfur Mixtures

Information on the ligand's and ligand-sulfur mixture's thermal stabilities are obtained by thermogravitational analysis (TGA) and the first derivative of TGA (DTG), as outlined by ISO 11358-1, ASTM E2550-21, and ASTM E1131-20 standards.[263–265] Dynamic TGA was performed using the *TA Instruments Q20 ThermoGravimetric Analyzer*,

which measures a material's mass loss (displayed as weight percent [%]) as a function of temperature. TGA was collected *via* heating 38.6 ± 1.4 mg of material (in a platinum crucible) at a fixed rate (10 °C/min) in an inert environment (40 mL/min of N_2).[263–265] N_2 was used to avoid material combustion, and the exhaust was bubbled through a NaOH solution to quench produced H_2S (*g*) from ligand-S mixtures. The DTG spectra were obtained from the first derivative with respect to temperature of the TGA spectra, and offers additional information on fluctuations in the rate and temperature ranges of mass loss.[263–265]

As TGA does not offer information on a material's structure, additional structural characterizations of thermally decomposed products were needed. However, residue from TGA was too minimal to collect for further characterization. To obtain larger quantities of decomposed material at elevated temperatures, 3 mL of the ligand or 3 mL of the 1 M ligand-sulfur mixture was heated in a round bottom flask with a heating mantel following the same conditions used in NP synthesis (*e.g.*, degassing, heating rate, N_2). Aliquots were collected at 130 ºC after 1 h, 225 ºC after 2 h and 300 ºC after 2 h. To collect sample at 500 ºC—which exceeds the temperature limits of the heating mantel—3 mL of the material was deposited into a glass scintillation vial, which was placed within a graphitic crucible. The crucible was loaded into a tube furnace and degassed several times, alternating between vacuum and N_2 (5 min per cycle). Under N_2 flow (100 mL/min) and at atmospheric pressure, the sample was heated to 500 °C at a ramp rate of 10 °C/min, to remain consistent with the conditions used during synthesis and TGA collection. Exhaust was bubbled through a NaOH solution to quench produced H_2S (*g*). The samples were held at 500 °C

for 30 min, followed by rapid cooling. Samples were exposed to air once at room temperature and collected for subsequent characterization.

3.2.6. Structural Characterization of Ligands and Ligand-Sulfur Mixtures

Structural differences in the organic ligands, ligand-sulfur solutions, and their decomposed products were characterized with both Raman Spectroscopy and Fourier-transform infrared spectroscopy (FTIR), complementary vibrational spectroscopy techniques which are used to identify a materials molecular structure.[209]

Raman Spectroscopy spectra were collected with the same *Renishaw InVia Raman Confocal Microscope* used to characterize NP samples (514 nm excitation wavelength, 1200 l/mm laser grating 10 s acquisition time, 10 % laser power (0.8 mW), 50 × objective magnification). Each sample was measured 10 times at different spots ensure homogeneity. A 5th order polynomial (R^2 = 0.9999) background subtraction was performed on materials with high florescent sigmodal backgrounds, otherwise a fitted spline background subtraction was performed with MagicPlot Software. Peak centers, breadths, and intensities were determined *via* deconvoluted Gaussian fits for the organic ligand (*e.g.*, Larkin)[209] and for carbon byproducts (Sadezky *et al* [210] and Merlen *et al* [211]).

FTIR was also performed using the *Thermo Scientific Nicolet 8700.* Prior to use, compressed N_2 was used to exhaust air in the system, and the detector was cooled with liquid N_2. Samples were deposited onto an attenuated total reflection (ATR) attachment, and data was collected under continuous N_2 flow (30 psi). Each FTIR spectra is a summation of 128 acquisitions.

^{1}H NMR was additionally used to further identify changes in the ligand's structure. The *Bruker AV300 Spectrometer* was used to collect ^{1}H NMR spectra at 300 MHz. $CDCl_3$

was used as the solvent. Chemical shifts offset was calibrated using the $CDCl_3$ peak centered at 7.26 ppm.

3.3. Results and Discussion

3.3.1. Decomposition of Amine and Carboxylic Acid Ligands During the Synthesis of CZTS Nanoparticles

As covered in **Chapter 2**, ligand decomposition was first observed during the synthesis of kesterite Cu_2ZnSnS_4 (CZTS) with the commonly used monounsaturated oleylamine (OLA) ligand.[192] To screen ligands for decomposition during NP syntheses, we first synthesized Cu_2ZnSnS_4 (CZTS) NPs with an extended library of ligands (saturated and unsaturated amine and carboxylic acid ligands), pictured in **Figure 1.12**: DDA (saturated amine), OLA (monounsaturated amine), LOA (polyunsaturated amine), SA (saturated carboxylic acid), OA (monounsaturated carboxylic acid), and LA (polyunsaturated carboxylic acid).

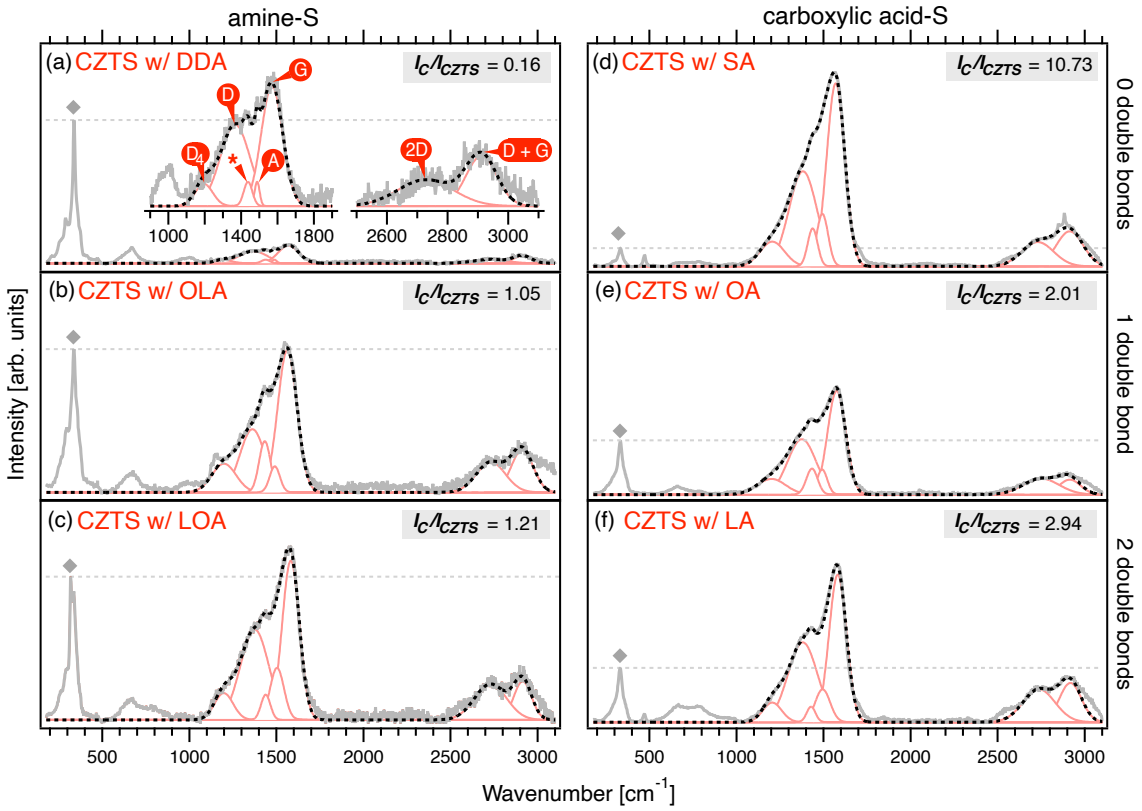

Figure 3.1. Figure 2. Raman spectra for all CZTS NPs synthesized with ligands of varying functional group and bond saturation. CZTS samples were synthesized with either (a, b, d) amines and (d, e, f) carboxylic acid ligands, and the ligand had either (a, d) no double bonds, (b, e) one double bond, or (c, f) two double bonds. The relative intensities of amine spectra are comparable, and the intensities in e & f are comparable. Deconvoluted Gaussian fits and their peak assignments are included in spectrum (a). Across each spectrum the signature CZTS peak at 339 cm^{-1} is identified (diamond symbol), the intensity of CZTS ($\boldsymbol{I_{CZTS}}$) is emphasized (dashed line), and the intensity ratio between CZTS (at 339 cm^{-1}) and carbon (maximum between 1000 to 1800 cm^{-1}, $\boldsymbol{I_C}$) is listed assignments.

Raman spectroscopy was used for both the identification of Raman active CZTS phases and of organic species, which is displayed in **Figure 3.1**. In Raman spectroscopy, the vibrational modes associated with inelastically scattered photons are used to identify

the structure of crystals and molecules.[209,266] The measured energy associated with these scattering events—and thus the Raman shift (cm^{-1})—is dependent on the bond's characteristic molecular energy levels. In addition to Raman shift, scattering intensities also offer valuable information as the intensity of scattering is dependent on the bond's characteristic polarizability.[209,266] Thus, the relative intensities between Raman bands are often used for additional assessment of a material's structure.

Raman spectroscopy of CZTS NPs points at the formation of kesterite CZTS (289, 339, and 660 cm^{-1}) in addition to a carbonaceous material across all samples (1000 – 1800 cm^{-1}). This region hosts the characteristic bands of highly structured carbon,[210,211,267–272] (*i.e.,* graphene, graphite, nano-diamond, nano-wires and nano-tubes, fullerenes) and other carbon impurities (*i.e.,* amorphous carbon, pyrolytic carbon, carbon dots,[58] and polycyclic aromatic hydrocarbons[268,272]). By deconvoluting the Raman signals between 1000 – 1800 cm^{-1}, we were able to infer the material's structure (see **Table 3.1** for the observed Raman shifts and their deconvoluted assignments).

Across all CZTS samples, we identified the presence of graphitic and amorphous carbon. Graphitic carbon was identified by a high intensity band, denoted the G- ("graphene") band.[210,211,267–272] As disorder is introduced, this peak broadens and splits, introducing a lower intensity D- ("defect") band. For high structure and low disorder (e.g., graphite), these peaks would be distinct with a narrow full-width half-max.[211] Conversely, if disorder further increases, the D_4-band[210] and the A- band emerge, which are associated with disordered graphite, polyenes, ionic impurities, or structured amorphous carbon.[210,211] In addition to observing the G- and D-bands, we also identified the lower intensity D_4- and A-bands, indicating the presence of amorphous carbon. Within this region, an additional

peak was present across all samples between 1429 and 1439 cm^{-1}, which we were unable to confidently assign to known carbon or CZTS scattering bands.

Further, the two low intensity broad bands observed between 2500 and 3100 cm^{-1} correspond with the second order out of plane vibrations of graphene and graphite; the 2D-band[210,211] and the G + D-band.[210] The position of the 2D-band and its relative intensity in relation to the G-band (I_{2D}/I_G) are used to further identify the material's structure. For monolayer graphene, I_{2D}/I_G is ˜3 and its 2D-band is centered between 2680 – 2700 cm^{-1}. As disorder increases, I_{2D}/I_G is reduced to ~ 0.3 and the 2D-band shifts to 2720 – 2740 cm^{-1}.[211] Here, we observed an I_{2D}/I_G ratio of 0.20 ± 0.05 for all samples, further indicating the formation of highly disordered graphitic carbon during the synthesis of CZTS NP.

Table 3.1. Raman assignments

Observed Raman Shift [cm^{-1}]	Assigned Vibrational Mode[210,211]
1197 – 1205	D_4-band, amorphous carbon with graphitic domains, trans-polyacetylene (TPA), ionic impurities
1362 – 1381	D-band, disordered graphitic lattice
1427 – 1439	*unassigned*
1489 – 1502	A-band, amorphous carbon
1562 – 1582	G-band, ordered graphitic lattice
2729 – 2749	2D-band, second order resonance
2913 – 2916	D + G-band, resonance

The breadth of the G- and D-band, detection of D_4- and A-bands, and low I_{2D}/I_G ratio are all consistent with the presence of alkylated graphitic flakes, such could be in the form of highly oriented pyrolytic graphite (HOPG), graphene quantum dots, carbon dots,

or soot.[58,210,211,273] As such, Raman spectroscopy reveals that all organic ligands used in this study—regardless of bond saturation or functional group—formed a highly defective graphitic carbon during CZTS NP synthesis. In **Chapter 2**, *via* XPS we identified the presence of sp^2 carbon and oxygen-based bonding consistent with graphene oxide. Herein, this material will be simply referred to as "carbon impurity." The ligands used for NP synthesis are expected to be the carbon source for these impurities, a result of *in-situ* ligand decomposition.

In addition to utilizing Raman scattering intensity for structural identification, it also offers information on material concentration, which is proportional to intensity.[209,266,274] For mixtures of unknown concentrations, normalization of the Raman spectra to an internal standard (*i.e.*, a reference material) is performed to extract the relative intensity between the standard and the material(s) of interest.[209,266,275] Thus, fluctuations in the relative intensities across spectra can be directly correlated with fluctuations in relative concentrations. Here, normalization to our internal standard—the CZTS peak at 339 cm^{-1}—was performed to allow us to compare relative concentrations of carbon across samples.

The normalized intensity between CZTS NPs and the carbon impurity are reported in **Figure 3.1** as I_C/I_{CZTS}. While there are no discernible structural differences between the carbon residue across CZTS samples, the relative concentration of carbon residue did vary depending on ligand selection.

For amine-synthesized samples, as the number of bonds increased along the ligand backbone, the relative intensity of the carbon impurity rose from I_C/I_{CZTS} = 0.16 (DDA, 0 double bonds), to 1.05 (OLA, 1 double bond), to 1.21 (LOA, 2 double bonds). Notably, the observed increase in concentration was significantly more pronounced between 0 and 1

double bond (a 6.5 × increase) than between 1 and 2 double bonds (1.2 × increase). The *in-situ* decomposition of unsaturated amines during CZTS synthesis may be attributed to the increased reactivity of alkenes and dienes. This would be in agreement with a previous study in which the use of saturated amines mitigated *in-situ* polymerization ligand during NP synthesis.[154]

Unlike amines, carboxylic acid-synthesized samples did not exhibit the same bond-saturation dependent trend. While I_C/I_{CZTS} increased similarly between 1 and 2 double bonds (a 1.5 × increase between OA and LA), the I_C/I_{CZTS} of the SA (0 double bonds, I_C/I_{CZTS} = 10.73) was considerably greater than that of the unsaturated carboxylic acids; 2.01 for OA, and 2.94 for LA. This is contrary to what we observed with the saturated amine (DDA), which has the lowest concentration of carbon impurities across all samples.

The stark difference in SA's decomposition may result from poorer NP washing after synthesis. SA's higher melting point (T_{MP} = 69 °C) resulted in the ligand solidifying during NP washing, limiting the removal of excess ligand, reflected by relatively high concentration of the ligand backbone being detected after synthesis (CH_2 and CH_3 at 2849 and 2882 cm^{-1}).[209] As washing can reduce impurities,[192] it is plausible that the efficacy of washing would also influence the final concentration of carbon within CZTS sample synthesized with SA. Therefore, it is important to directly compare the decomposition of ligands under controlled conditions, as in the absence of precursors or other variables, including NP washing.

3.3.2. Thermal Stabilities of Amine and Carboxylic Acid Ligands

Heretofore, all ligand decomposition studies were conducted in the presence of metal and non-metal precursors to synthesize CZTS NPs. This served to better understand the ligands'

tendency, or lack thereof, to decompose during NP synthesis. However, due to the number of variables present during synthesis (*e.g.,* precursors, washing procedure), it is challenging to discern the contribution of the ligand's innate structure (*i.e.,* bond saturation and functional group) to the observed decomposition. To elucidate how the ligand's structure influences decomposition, we performed thermal gravitational analysis (TGA) to investigate the ligand's intrinsic thermal stability when isolated from external variables used in NP synthesis (*i.e.*, metallic and non-metallic precursors). To conduct this investigation, we performed thermal gravitational analysis (TGA) of the ligands used in this study.

A material is considered thermally stable until a thermal event begins, which is signified by the onset of mass loss (denoted as '*On*'). These thermal events may occur due to material vaporization, pyrolysis into volatile species, or a chemical reaction which produces volatile species.[263,264,276] After the offset of mass loss (denoted as '*Off*') either no material remains, or, residual material is present. Generally, thermally stable residue can form from impurities included within the material, from the product(s) of pyrolysis, or, from the product(s) of a chemical reaction. A rise in thermal stability arises from an increase in crystallinity, molecular weight, or bond energy.[277,278] The prevalence of stable products results in further mass remaining until exceeding the temperature threshold required for a subsequent thermal event to occur.[263,264,276] As thermal events are bound by fluctuations in the rate of mass loss, the first derivative of TGA—known as the derivative thermogravimetry (DTG) spectra—is also used to further extract information on the apex of mass loss (denoted by '*I,*' for inflection point) and the rates of mass loss (ΔWt%/ΔT).[263,264,276]

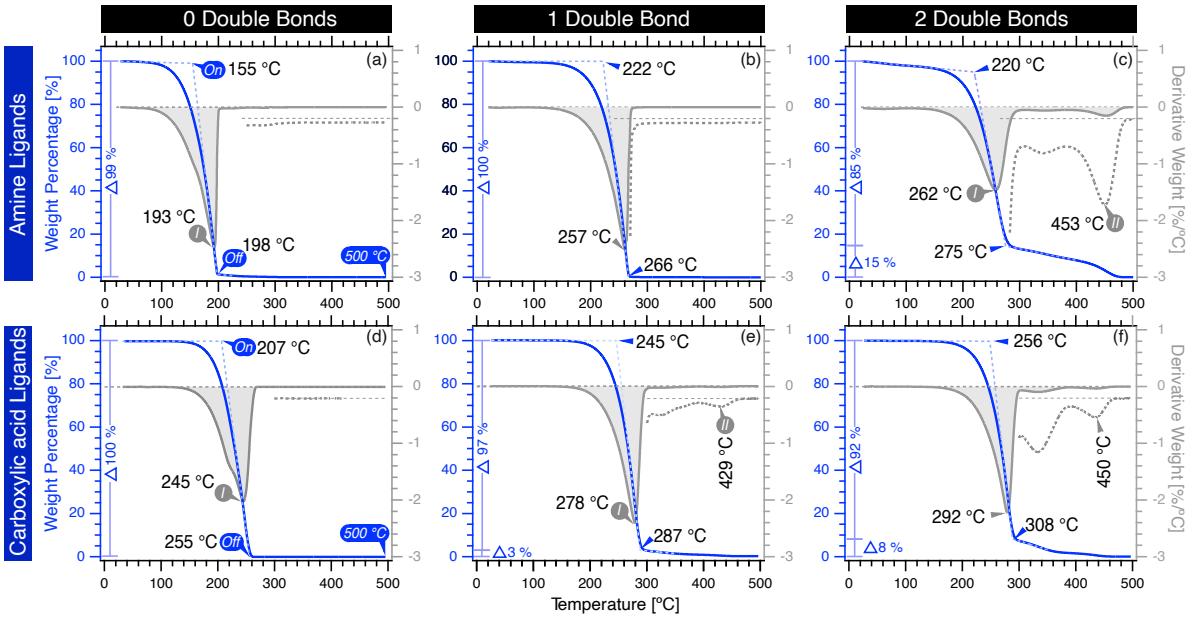

Figure 3.2. TGA (blue) mass loss profiles and overlayed derived DTG (grey) curves for (a-c) amine ligands and (d-f) carboxylic acid ligands with varying bond saturation (0 – 2 double bonds). This includes **(a)** DDA, **(b)** OLA, **(c)** LOA, **(d)** SA, **(e)** OA, and LA. For clarity, the DTG signal is amplified by 10 × between 250 ºC and 500 ºC for all samples (grey dashed inset). Points '*On*' and '*Off*' along the TGA spectra correspond with the extrapolated onset and offset temperatures of thermal events, points *I* and *II* (when present) along the DTG spectra correspond with the inflection points of separate thermal events. To the left of each curve, the changes in mass loss between *On* and *Off* ($Wt\%_{Off}$–$Wt\%_{On}$) and between the *Off* and 500 ºC ($Wt\%_{500\,°C}$–$Wt\%_{Off}$). From these extrapolated and extracted values, we identified relevant temperatures (T_{On}, T_{I}, T_{Off}, T_{II}), mass losses ($Wt\%_{On}$, $Wt\%_{Off}$, $Wt\%_{500\,°C}$), and rates of mass loss ($Wt\%_{I}/T_{I}$, $Wt\%_{II}/T_{II}$). These values are listed in **Table 3.2**.

The TGA and DTG curves in **Figure 3.2** show that under inert conditions and in the absence of all NP precursors, bond saturation and functional group influences the ligand's thermal stability. For both amines and carboxylic acids, the ligand's innate thermal stability (T_{On}, T_{I}, and T_{Off}) increased with the number of double bonds. Additionally, the amine ligands comparatively had lower thermal stabilities then the carboxylic acids.

In addition to the contrasting temperatures of first thermal event, mass loss percentages were also considered. Between room temperature (20 – 25 ºC) and 500 ºC, DDA, OLA, and SA underwent one thermal event which did not produce a stable residue ($Wt\%_{Off} = \leq 1$; $Wt\%_{500\,^{\circ}C} \leq 0.05$ %). A different result occurred for LOA, OA, and LA; residual material was present following T_{Off}. For LOA, a relatively substantial 14.5 % ($Wt\%_{Off}$) of material remained following the ligand's first thermal event at 262 °C (T_I). This residual material was eliminated following a second thermal event (T_{II} = 453 °C). Similar to LOA, residue remained ensuing the first thermal events of OA ($Wt\%_{Off}$ = 2.9 %) and LA ($Wt\%_{Off}$ = 8.3 %) and was eliminated after a final thermal event at T_{II} > 400 °C.

From these variations in mass residue, we observe additional trends based on bond saturation and functional group. For both saturated amine and carboxylic acid ligands, stable carbon products did not form. Upon introducing a double bond along the ligand backbone, results diverged depending on functional group: OLA (amine) experienced a similar TGA profile to that of the saturated ligands, while OA (carboxylic acid) had a small fraction of material remain. As the numbers of double bonds increased to two, the amount of residual material increased for both amines and carboxylic acids, with residue being more pronounced for LOA then that of LA.

As established, the origins of the observed mass loss event can result from (1) vaporization, (2) pyrolysis into volatile species, or a (3) chemical reaction. As only ligands were used and the experiment was conducted in inert atmosphere, the probability of a reaction occurring with molecular oxygen is low. However, both vaporization and pyrolysis are plausible. While the first thermal event of ligands does not appear to align with their reported boiling points (T_{BP}, included in **Table 3.2**), vaporization can occur at $T \neq T_{BP}$ when

isothermal sample heating is not achieved or when vapor pressure is not carefully regulated.[279] As these parameters were not controlled during our experiments, it is possible that the first thermal event could correspond to vaporization of the ligand.

Alternatively, pyrolysis might have occurred. In the biofuel industry, the pyrolysis of carboxylic acids ligands have been studied. The pyrolysis of SA,[177,179,257] OA,[176,179,257] and LA[175,179,257] results in the formation of both volatile (*e.g.*, CO (*g*) and CO_2 (*g*), short chain hydrocarbons) and stable decomposition products (*e.g.,* alkenes, alkanes, branched hydrocarbons, and both mono- and poly-aromatics) from decarboxylation and deoxygenation of the functional group and thermal cracking of the ligand backbone.[175–177,179,257] In this work, we observe that nearly 100 % of SA was eliminated by T_{Off}, which would be in agreement with pyrolysis studies in which ~ 95 % of SA is converted into gaseous products.[177] The presence of residue at T_{Off} for OA[176] and LA[175] is also consistent with the reported pyrolysis for the ligands, where a stable liquid product is formed during thermal decomposition.[175,176] The formation of these stable produces for OA and LA—and lack thereof for SA—is attributed to the increased reactivity of alkenes and dienes. If pyrolysis is occurring during the first thermal event, we additionally observe that saturated DDA and monounsaturated OLA does not decompose into a stable residue, while polyunsaturated LOA does. Thus, across both functional groups, the double bonds would have contributed to the conversion of the ligand into stable decomposition products.

Regardless of the mechanism that occurred during the first thermal event, from TGA it is evident that saturated SA and DDA, and monounsaturated amine OLA did not inherently produce thermally stable carbon products. Therefore, external variables used during the synthesis of CZTS NPs (*i.e.,* precursors) most likely contributed to their

observed *in-situ* decomposition into carbon impurities (**Figure 3.2)**. For ligands which produced stable products (monounsaturated OA, and polyunsaturated LA, and LOA), the amount of ligand converted into residue increased with the number of double bonds, in agreement with other pyrolysis studies.

3.3.3. Thermal Stability of Amine-Sulfur and Carboxylic Acid-Sulfur Mixtures

In **Section 1.3.2.**, ligand pyrolysis studies were conducted in the absence of precursors used in the synthesis of NPs to better understand how the ligand's bond saturation and functional groups influences its innate thermal stability. Interestingly, we observe a dichotomy between NP synthesis results from **Section 1.3.1.** and isolated ligand results from **Section 1.3.2.**, indicating that precursors complicate the ligand's ability to pyrolyze during synthesis.

As elemental sulfur is a common chalcogenide precursor used in the synthesis of chalcogenide NPs—including in the synthesis of CZTS—we additionally used TGA and DTG to compare changes between the innate ligand's thermal stability and that of 1 M ligand-sulfur mixtures (3.5 – 4 wt/Wt% of sulfur to ligand), referred to as 'ligand-S'. The TGA and DTG profiles of ligand-S are displayed in **Figure 3.3** and are directly comparable to the profiles in **Figure 3.2**. **Table 3.2** also includes relevant extracted values from TGA and DTG, for both ligand and ligand-S.

Initially, the mass loss profile of the ligand-S mixtures appears to mirror that of their innate ligand. However, there are several distinct differences upon sulfur inclusion. Between ligand and ligand-S, the maximum change in T_I was respectively -2 and +2 °C for DDA and SA (0 double bonds), -14 and +3 °C for OLA and OA (1 double bond), and -20 and +5 °C for LOA and LA (2 double bonds). Thus, by observing the temperatures

associated with the first thermal event, we see that (1) compared to amines, amine-S mixtures have a net decline in thermal stability, (2) compared to carboxylic acids, carboxylic acids-S mixtures have a net increase in thermal stability, (3) this effect is considerably more pronounced for amine-S than that of carboxylic acids-S, and (4) the difference in T_1 between ligand and ligand-S increases with the number of double bonds. Therefore, in the presence of elemental sulfur, amine ligands either experienced a decrease in ligand volatility, more readily pyrolyzed into volatile compounds, or, a chemical reaction occurred between the amine and sulfur to produce volatile compounds (the inverse would apply for carboxylic acid-S).

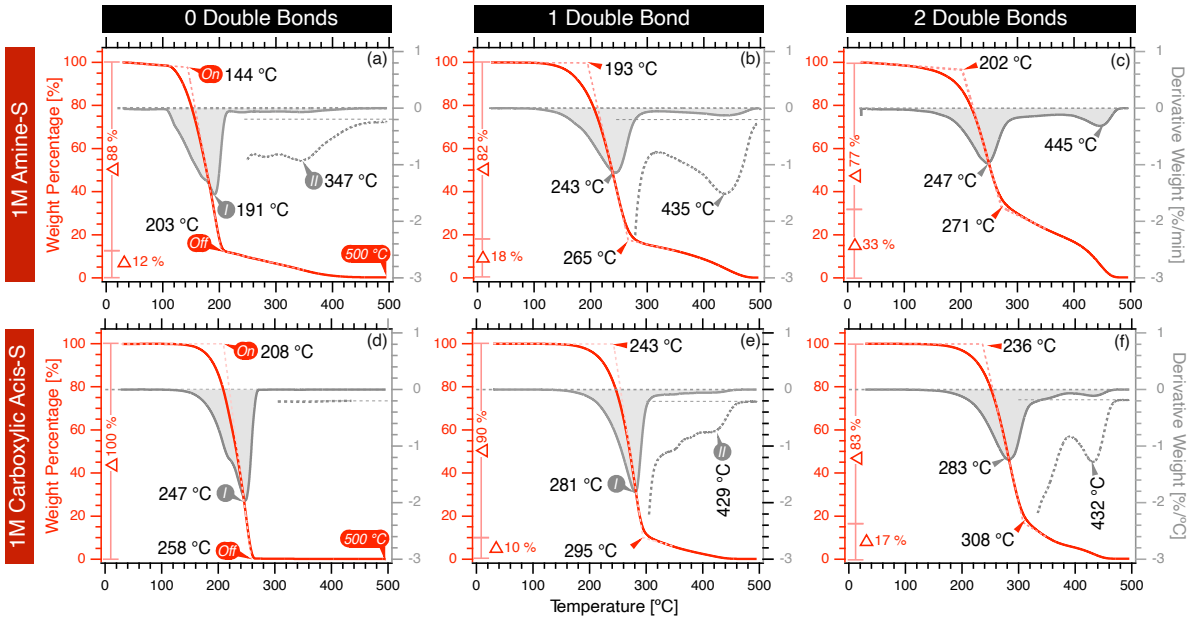

Figure 3.3. TGA (red) mass loss profiles and overlayed derived DTG (grey) curves **(d-f)** 1 M carboxylic acid-S mixtures with varying bond saturation. This includes **(a)** DDA-S, **(b)** OLA-S, **(c)** LOA-S, **(d)** SA-S, **(e)** OA-S, and LA-S. For clarity, the DTG signal is amplified by 10 × between 250 ºC and 500 ºC for all samples (grey dashed curve), excluding LOA-S. Identification of key

features is performed as described in **Figure 3.2**, which contains the TGA and DTG of corresponding ligands without the inclusion of elemental sulfur. These values are listed in **Table 3.2**.

Table 3.2. Key values extracted from TGA and DTG of ligand and ligand-S mixtures

	DDA	DDA-S	OLA	OLA-S	LOA	LOA-S	SA	SA-S	OA	OA-S	LA	LA-S
Wt/Wt% of S/ligand [%]	—	4.0	—	3.9	—	—	—	3.8	—	3.6	—	3.6
Boiling Point												
T_{BP} [°C]	247	—	364	—	—	—	361	—	360	—	230	—
Extrapolated Onset (*On*)												
T_{On} [°C]	155	144	222	193	220	202	207	208	245	243	246	236
$Wt\%_{On}$ [%]	99.1	98.2	98.8	99.7	95.1	96.5	99.9	100.0	99.6	99.9	99.7	99.9
Inflection Point *(I)*												
T_I [°C]	193	191	257	243	262	247	245	247	278	281	278	283
$\Delta Wt\%_I/\Delta T_I$ [%/°C]	-2.47	-1.52	-2.25	-1.14	-1.46	-0.97	-2.02	-1.96	-2.41	-1.81	-2.22	-1.24
Extrapolated Offset (*Off*)												
T_{Off} [°C]	198	203	266	265	275	271	255	258	287	295	287	308
$Wt\%_{Off}$ [%]	1.4	12.3	0.4	17.6	14.5	32.8	0.1	0.3	2.9	10.0	8.3	17.0
Inflection Point (*II*)												
T_{II} [°C]	—	347	—	435	453	445	—	—	429	429	434	432
$\Delta Wt\%_{II}/\Delta T_{II}$ [%/°C]	—	-0.07	—	-0.13	-0.15	-0.31	—	—	-0.01	-0.01	-0.03	-0.11
End of run (*500 °C*)												
$Wt\%_{500\,°C}$ [%]	0.06	0.24	0.01	0.14	0.05	0.25	0.10	0.15	0.07	0.23	0.11	0.26

Changes in mass residue upon sulfur inclusion were also observed. While the heating of DDA and OLA ligands did not produce thermally stable carbon products, residue was present after the heating of both DDA-S and OLA-S. Upon completion of the first thermal event, a significant percentage ($Wt\%_{Off,\ DDA\text{-}S}$ = 12.3 %; $Wt\%_{Off,\ OLA\text{-}S}$ = 17.6 %) of material remained. Assuming the ligand and sulfur did not react, they may have separately volatized or pyrolyzed—appearing as two-step mass loss—with the inflection points separately corresponding to the ligand and to elemental sulfur. While T_I of ligand-S agrees with T_I of the ligands, T_{II} ($T_{II,\ DDA\text{-}S}$ = 347 ºC; $T_{II,\ OLA\text{-}S}$ = 435 ºC) cannot be assigned to elemental sulfur (see **Figure 3.10** for elemental sulfur's TGA profile). This indicates that residual material present at T_{off} is not residual elemental sulfur, rather a ligand-S decomposition or reaction product. Unlike with DDA-S and OLA-S, the inclusion of sulfur had no effect on SA-S mass loss profile. This is notable, as the decomposition of SA was observed during the synthesis of CZTS NPs, indicating that variables other than elemental sulfur and ligand structure (*i.e.,* metal precursors) must be responsible for the *in-situ* decomposition of SA.

Unlike DDA, OLA, and SA ligands, LOA, OA, and LA ligands did produce thermally stable carbon products upon heating. Compared to LOA, LOA-S experienced a significant increase in the amount of residue; from 14.5 % ($Wt_{Off,\ LOA}$) to 32.8 % ($Wt_{Off,\ LOA\text{-}S}$). The LOA-S product continued to lose mass until being fully eliminated following a second thermal event at 445 ºC (T_{II}). OA-S and LA-S similarly preserved a respective 10.0 % and 17.0 % ($Wt\%_{Off}$), a relative increase compared to their innate ligand counterparts. This residual material was similarly reduced following a second thermal event, which occurred at similar temperatures for OA-S (T_{II} = 439 ºC) and LA-S (T_{II} = 432 ºC).

From these TGA and DTG results, it is apparent that the inclusion of elemental sulfur influences the formation of residue, and, the amount of residue which forms is dependent on the ligand's innate structure. Across both amines-S and carboxylic acids-S, we observed that the $Wt\%_{Off,\ ligand\text{-}S}$ was consistently greater than $Wt\%_{Off,\ ligand}$. Additionally, the amount of residue consistently increased with the number of double bonds. Notably, this was considerably more pronounced for amine ligands than of carboxylic acids; there was a 11 – 18 % increase in $Wt\%_{Off}$ for amine-S, and a 0 – 9 % increase in $Wt\%_{Off}$ for carboxylic acid-S. These results signify that (1) when compared to carboxylic acid ligands, the interaction between sulfur and amine favors the formation of stable carbon products, and, (2) the interaction between sulfur and double bonds contribute to the formation of stable carbon products.

Amine-S decomposition may have been more favorable than carboxylic acid-S due to the interactions between the ligand and sulfur. Sulfur is known to undergo a ring opening reaction facilitated by nucleophilic amines, transforming cyclic S_8 into anionic linear sulfur chains which can then further react with a ligand to produce volatile H_2S (g) and thioamides, amidine oligomers, or alkylammonium polysulfides of different thermal stabilities.[164,166,249,280] This may be why amine-S exhibited a decrease in the onset of decomposition (release of volatile reaction products) and an increase in stable residue (formation of stable reaction products). In contrast, carboxylic acids do not favorably undergo nucleophilic ring opening with elemental sulfur, thus additives are commonly used to enhance miscibility and to catalyze chemical reactions to form C–S bonds.[169,171,281] This is reflected in our observations of dissolving sulfur the ligands (see **Methods**). The poor miscibility and reactivity between carboxylic acids and sulfur may be why the observed

fluctuations in both critical temperatures and residual mass upon sulfur inclusion was dampened compared to amines.

The increased residue for ligands with double bonds is likely attributed to enhanced degree of polymerization and aromatization alkenes—and even more-so—dienes can undergo, due to the heightened reactivity of double bonds. As previously discussed, the pyrolysis of innate ligands with double bonds has been reported to result in the formation of stable products, including alkenes, alkanes, branched hydrocarbons, and both mono- and poly-aromatics.[175–177,179,257] With the inclusion of elemental sulfur, additional reactions may transpire. Alkenes, which specifically includes OLA, OA, and LA, have previously been reported to be polymerized by ionic sulfur *via* a reaction referred to as inverse vulcanization.[166,169,249,277] This mechanism involves the crosslinking of unsaturated ligands at their allylic sites by ionic linear sulfur chains to form polysulfides.[166,249,277] As number of double bonds increases, so does the potential molecular weight and thus thermal stability of the products. This is reflected in our TGA results; as the number of double bonds increased, the T_{II} (thus, thermal stability) of the residual material also increased, which may be attributed to an increase in the molecular weight or bond energies of reaction products. The amount of material converted into a stable product also increased with the number of double bonds, again indicating a trend between bond saturation and reactivity.

By these observations, it is feasible that the material remaining between T_{Off} and T_{II} is comprised of stable reaction products (oligomers, polysulfides) which may be precursors to the alkylated graphitic products detected after NP synthesis. Alternatively, the present products may contain alkylated graphitic products following pyrolysis. As TGA does not provide structural information, we used Raman spectroscopy, FTIR, and ^{1}H NMR to identify the material at $T_I < T < T_{II}$ (see **Figure 3.4 and 3.12-3.13**).

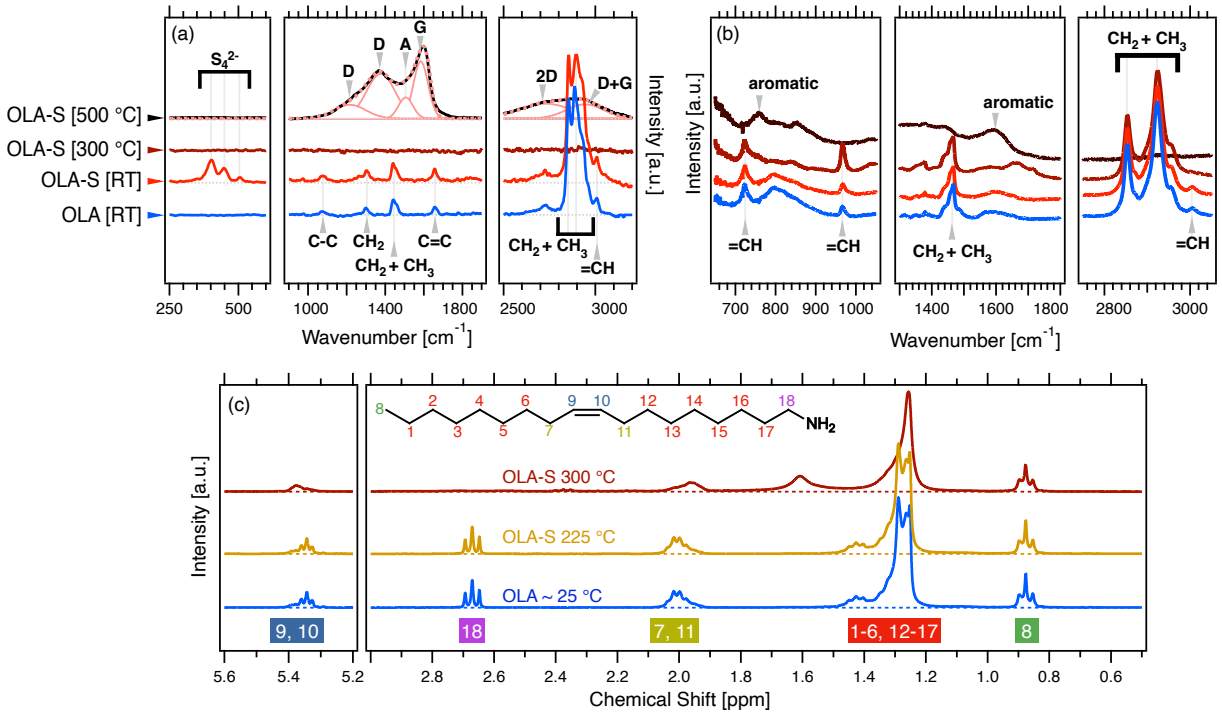

Figure 3.4. Truncated **(a)** Raman, **(b)** FTIR, and **(c)** ^{1}H NMR of OLA and OLA-S heated at varying temperatures under N_2. See supporting information for OLA-S's structure at additional temperatures (**Figure 3.12**), equivalent spectra reproduced for OA and OA-S (**Figure 3.13**), and integrated areas of ^{1}H NMR signals (**Table 3.4**).

At room temperature, signature CH_2, CH_3, C-C, C=C, and =CH bonding modes of OLA were detected *via* Raman and FTIR.[260,282] Upon mixing OLA with sulfur, we did not detect Raman bands associated with elemental sulfur (see **Figure 3.10**). Rather, the emergence of peaks at 403, 447, and 505 cm^{-1} were identified, which correspond with ionic sulfur (S_4^{2-}), in agreement with ring-opening of elemental sulfur by the amine ligand.[248,283,284]

With increased heating of the OLA-S, the Raman spectrum showed signs of fluorescence and was no longer well resolved.[248] Fluorescence can arise from the formation of polysulfides or carbon dots.[187,260,285] As we could not elucidate structural information from

Raman, FTIR and ^{1}H NMR were important supplements. From 130 – 225 °C, there was no notable changes in OLA's structure. However, at 300 °C ($T_I < T_{300\,°C} < T_{II}$), we begun to see degradation of the double bond; there was a decline in =CH (FTIR, at 3010 cm^{-1}) and a decline in allylic and vinylic hydrogen bonding (^{1}H NMR, at ~5.2 ppm and 2.0 ppm, respectively). ^{1}H NMR additionally shows an 81 % reduction of signal associated with the ligand's alpha carbon (Cα), indicating a reaction with or decomposition of the amine functional group occurred. While there is a relative decrease in the integrated signal associated with the innate ligand structure, FTIR and ^{1}H NMR reveal that much of the original hydrocarbon structure remains intact by 300 °C, consistent in structure with the formation of a polysulfide.[249] Following the decomposition of the stable product (polysulfide) at T_{II}, Raman spectra of the material is again discernable ($T_{500\,°C}$) – notably, we see the presence of the D_4-, D-, A-, and G-bands, and no bands associated with the starting ligand. At $T_{500\,°C}$, FTIR also shows an elimination of hydrocarbon peaks, with a spectrum that is representative of early stage soot formation.[272]

Similar results were found for OA-S (see **Figure 3.13**). From FTIR, the dominant change in structure of carboxylic acid-S includes attenuation of =CH and the functional group's C=O signal (1709 – 1720 cm^{-1}). The changes in ^{1}H NMR mirror that of amine-S; at $T_{300\,°C}$ the most significant spectral changes were intensity reductions in allylic and vinyl sites. There was also a 24 % reduction in intensity of the Cα signal, relatively less of a change within the ligand's functional group compared to amines.

These structural changes are consistent with decomposition at the double bond sites and of functional groups into a polysulfide,[175–177] rather than the conversion of ligand-S into alkylated graphitic impurities *via* pyrolsysis.[286] However, above T_{II}, (> 347 °C) we confirmed that these products carbonized into the same alkylated graphitic product detected

after NP synthesis at 225 °C. As graphitic carbon was detected within CZTS NPs synthesized with both amines and carboxylic acids, it appears that the introduction of metallic precursors contributes to the *in-situ* ligand pyrolysis at temperatures below T_{II}.

3.3.4. Precursor Selection Dependent Pyrolysis of Oleylamine During NP Synthesis

Thus far, alkylated graphitic carbon has been detected during the synthesis of CZTS NPs at 225 °C. In the absence of metal precursors, we observe that both amine and carboxylic acid ligands can form stable carbon products. Despite graphitic carbon being detected in all CZTS samples, the extent and tendency of pure ligands to decompose is dependent on bond saturation and functional group. Additionally, decomposition into graphitic material occurs at temperatures that exceed our synthesis conditions. This indicates that metal precursors—the final materials used in the synthesis of CZTS NPs—contribute to the *in-situ* decomposition of ligands. To understand the influence of the metal precursors used in CZTS NP synthesis, the copper, zinc, and tin based acetylacetonate ($(acac)_2$) precursors were separately heated with OLA in both the absence and presence of elemental sulfur. This enabled further decoupling of the effect that metallic precursors and the non-metallic elemental sulfur precursor have on ligand pyrolysis.

To isolate the sole effect of precursors it would be ideal to avoid forming NPs. However, NPs favorably form under our reaction conditions. Thus, heating the ligands with precursors resulted in the synthesis of both metal (sulfur-free) and binary metal-chalcogenide (sulfur-containing) NPs. **Table 3.3** includes the full list of synthesized samples and their identified NP phases. Full structural confirmation and analysis of the synthesized materials *via* Raman spectroscopy and XRD is provided in **Figure 3.14**. OLA was selected as the standard ligand since TGA results reveal that this ligand is relatively

benign in absence of all precursors but is still capable of complex decomposition when pyrolyzed in the presence of elemental sulfur.

Akin to that of the CZTS NPs and the pyrolyzed TGA residue, we identified the structure of organic products for the NPs by observing the region between 1000 – 1800 cm^{-1}, as highlighted in **Figure 3.5**. Both Zn-S and Sn NP Raman signals were oversaturated with high fluorescence, suppressing all distinct signals, and making these materials ineligible for further carbon-based analyses.

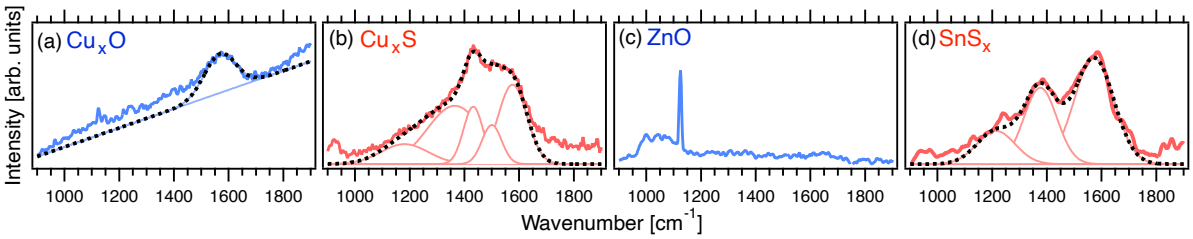

Figure 3.5. Raman spectra for NPs synthesized with **(a-b)** $Cu(acac)_2$, **(c)** $Zn(acac)_2$, and **(d)** $SnBr_2(acac)_2$ organometallic precursors, all labeled by their resulting formed NPs. The peak centers of carbon-based modes are labeled and deconvoluted with Gaussian fits, if possible. Full structural analysis of each NP (Raman and XRD) is found in supplemental **Figure 3.13**. The relative intensities are not comparable, and no background subtraction was used CuO_x spectra, rather a linear background fit between 900 and 1900 cm^{-1} is included with the spectra.

Table 3.3. Reactants and Products from Synthesized NP Samples

Sample	Reactants	Inorganic Products
Cu NPs	OLA, $Cu(acac)_2$	Cu, CuO, Cu_2O
Cu-S NPs	OLA, $Cu(acac)_2$, S	CuS, $Cu_{1.8}S$
Zn NPs	OLA, $Zn(acac)_2$	ZnO
Zn-S NPs	OLA, $Zn(acac)_2$, S	ZnS, ZnO
Sn NPs	OLA, $SnBr_2(acac)_2$	Amorphous Sn
Sn-S NPs	OLA, $SnBr_2$ $(acac)_2$, S	SnS, Sn

Cu NPs synthesized with OLA resulted in a weak broad peak centered at 1568 cm^{-1}, fitted in **Figure 3.5**. The peak position would align with a G-band assignment, indicating there was graphitic structure. However no other assignments from **Table 3.1** were distinguishable in the Cu NP's Raman spectra. As sp^3 hybridization increases and overtakes sp^2 hybridization, graphitic material becomes increasingly amorphous. In Raman, this is reflected by a broad G-band and the disappearance of a distinguishable D-band,[282] which resembles our Cu NP Raman spectra. Zn NPs even more so did not share the same carbon structure identified from CZTS synthesis, with no graphitic or amorphous bands being detectable. Rather, detected bands can be assigned to the Raman spectra of OLA (see **Figure 3.11**). This includes the C–C bonding (1058 and 1124 cm^{-1}) and OLA's highest intensity CH_2 and CH_3 scattering modes between 2830 and 2925 cm^{-1}.[209]

Unlike the sulfur-free syntheses, the carbon impurity present from CZTS synthesis appears been found in Cu-S and Sn-S NP samples. In Cu-S NPs, Raman signals associated with the structured G- and D-bands, the defective/amorphous D_4- and A-bands, an unidentified band at 1431 cm^{-1}, and second order graphitic bands were all identified. When directly compared to the products from Cu NP's synthesis, it is evident that the inclusion of elemental sulfur led to the formation of carbon impurities with more similar structure to that of CZTS, which has more sp^2 structure. Akin to Cu-S, Sn-S NPs had formed structured carbon, with the G-, D-, D_4-, and second order bands being detected. Fitting of the A- band and unassigned band from 1427 – 1439 cm^{-1} were not necessary to deconvoluted Sn-S NP carbon signal.

In summary, Raman revealed that the sulfur-based synthesis of Cu-S and Sn-S led to the formation of carbon impurities which are structurally similar to the carbon found in

CZTS samples. The Cu NP sample also formed carbon residue, but with a more amorphous structure. Zn was the only NP sample to have the original ligand's structure (OLA) detectable after synthesis and no indication of decomposed carbon products. This means that the OLA remained stable at 225 °C when heated with $Zn(acac)_2$, whereas the ligand decomposed when exposed to $Cu(acac)_2$ and $SnBr_2(acac)_2$ precursors and their synthesized NPs.

Both metal precursors and the formed NPs and have been used in catalysis. M-$(acac)_2$ precursors are versatile catalysts which participates in a wide library of low-temperature organic reactions, which commonly includes oligomerization, polymerization and poly-condensation, hydrogenation, isomerization, trans-esterification, and can also be used as catalysts in reactions between sulfur and organic monomers, including inverse vulcanization.[156,157,172,173,287,288] Additionally, all of our formed NPs (CZTS, Cu, CuO, Cu_2O, Cu_xS, ZnO, ZnS, Sn, and SnS) are either chemically, photochemically, or electrochemically catalytic, and can catalyze the reactions with or the degradation of organic materials.[65,102,108,112,289,290] As such, it is possible that the metal precursors and formed NPs are catalytically promoting ligand decomposition at 225 °C.

To our knowledge, reactions facilitated by Cu, Zn, and Sn catalysts do not extensively include the aromatization and graphitization of organic materials. However, metals foils (including Cu) are used as catalysts in low temperature production of graphene sheets from organic monomers.[291]

These results raise additional questions which are open for further study, such as the mechanisms guiding how the precursors or formed NPs may catalyze ligand decomposition. Additionally, factors such as reaction time and temperature may also modulate ligand decomposition by impacting reaction kinetics. Tailoring precursor

selection, reaction time, and reaction temperature may assist in mitigating or controlling *in situ* ligand decomposition.[5,68]

3.4. Conclusions

Recent works have revealed that organic ligands used in the synthesis of inorganic nanoparticles are capable of decomposing into polymeric and graphitic impurities during synthesis. To identify the origins of this complex *in situ* ligand decomposition, this work investigated the decomposition profiles of ligands with varying structure to identify the influence of functional group (amines and carboxylic acids) and bond saturation (fully saturated to polyunsaturated) on decomposition. Using thermal analysis (TGA) and structural analyses (Raman Spectroscopy, FTIR, and ^{1}H NMR), we find that bond saturation is the largest determining factor in decomposition, with a higher number of unsaturated bonds correlating with a greater affinity of ligand decomposition. However, regardless of bond saturation, decomposition was not substantial when in absence of precursor materials, revealing that ligand decomposition during NP synthesis primarily results from external variables.

Upon pyrolyzing the ligands in the presence of elemental sulfur—a common chalcogenide precursor used in inorganic NP synthesis—the ligand-sulfur mixture's decomposition profiles diverged from their corresponding intrinsic ligand. Pyrolyzed ligand-sulfur mixtures yielded a thermally stable byproduct, which was comparatively more prevalent for unsaturated ligands and for amines, indicating that bond saturation and ligand functional group influences decomposition.

When employing these observations into the synthesis of CZTS, Cu_xO, Cu_xS, ZnO, ZnS, SnS_x, and SnO_x NPs, it was observed that the metal precursors selection also plays a significant role in ligand decomposition. Notably, the formation of alkylated graphitic impurities were

identified in the synthesis of CZTS, independent of ligand functional group. We observed similar ligand decomposition for Cu-S and Sn-S syntheses, lesser decomposition with only Cu precursors, and no decomposition with only Zn precursors.

Decoupling the variables that lead to ligand decomposition during NP synthesis is important step toward reducing or controlling the formation of byproducts. Future studies can focus on synthesis conditions (*i.e.*, time, temperature), investigating decomposition within the wide library of ligands (*e.g.,* thiols, hydroxyls, phosphines and phosphine oxides, polymers, proteins), and the influence of sulfur precursors (*e.g.,* thiols, thiourea, thiosulfates, thiolates, thiocarbamates), other chalcogenide precursors (*e.g.,* elemental selenium, selenium oxides, selenourea, elemental tellurium, alkyl tellurides, chalcogenide based metal-organic precursors), and metal precursors (*e.g.,* acetates, nitrates, halides, carbonyls, sulfates) used in NP synthesis.[16,292–294]

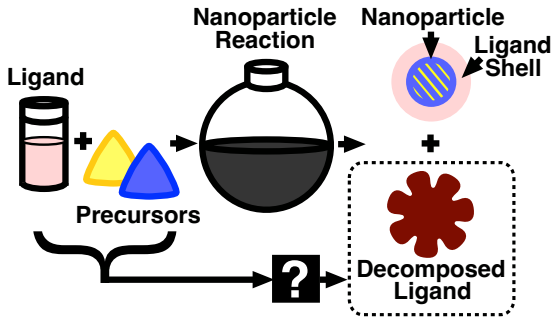

Figure 3.6. Raman spectra for NPs synthesized with **(a-b)** $Cu(acac)_2$, **(c)** $Zn(acac)_2$, and **(d)** $SnBr_2(acac)_2$ organometallic precursors, all labeled by their resulting formed NPs. The peak centers of carbon-based modes are labeled and deconvoluted with Gaussian fits, if possible. Full structural analysis of each NP (Raman and XRD) is found in supplemental **Figure 3.14**. The relative intensities are not comparable, and no background subtraction was used CuO_x spectra, rather a linear background fit between 900 and 1900 cm^{-1} is included with the spectra.

3.5. Supporting Information

3.5.1. Synthesis of Linoleylamine

Materials

Linoleic acid (Sigma Aldrich), $SOCl_2$ (TCI), ammonium hydroxide (ACS reagent), $LiAlH_4$ (Sigma Aldrich)

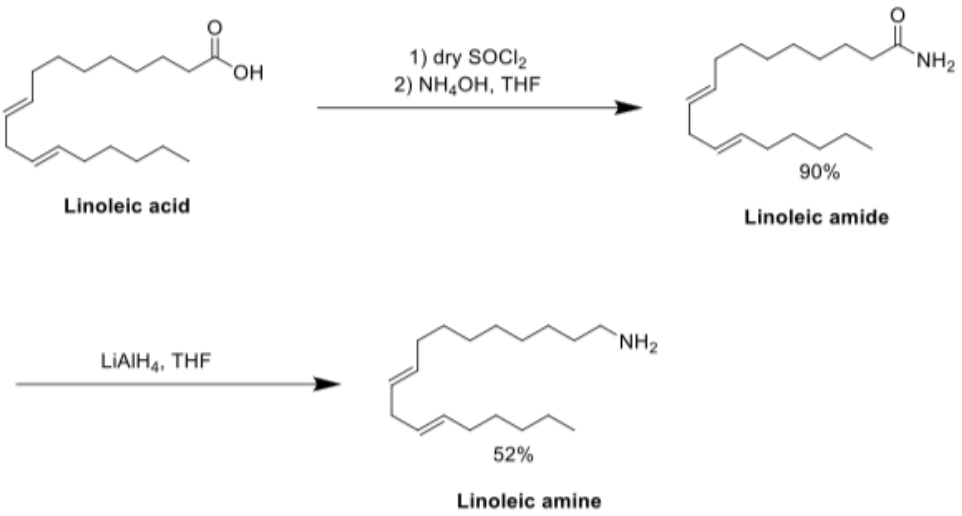

Scheme 3.1. Synthetic procedure for the production of linoleylamine (LOA).

Synthesis

1) **Linoleic amide**. Linoleic acid (9g, 32 mmol) was added into a 250 mL round bottom flask. The flask was transferred into an ice bath under nitrogen flow. After the system was cooled down, thionyl chloride (16.4g/10ml, 137mmol) was injected into the flask dropwise. With the addition completed, the system was slowly heated to 50 °C for 2 hours for complete conversion. The flask was later transferred to a rotavapor to remove the excessive thionyl chloride under lower pressure until a clear yellow liquid was obtained. 50 mL of tetrahydrofuran was added to dissolve the clear yellow liquid, and the flask was again put into an ice bath. To the same 250 ml round bottom flask, an excessive amount of 27 wt% ammonium hydroxide aqueous solution (22 g, 160 mmol) was added slowly. After completion, the system was stirred overnight. On the second day, the reaction was extracted with dichloromethane (50

mL) for 3 times, and the dichloromethane portion was then washed with brine before being dried with $MgSO_4$. A white-off solid (7.7g, 90% yield) was obtained after the solvent was removed. The solid was dried overnight under vacuum and used directly in the next reaction.

2) **Linoleic amine.** In nitrogen, linoleic amide (4.7 g, 16.8 mmol) was added to an oven-dried 100 mL flask, followed by the addition of 50 mL anhydrous tetrahydrofuran. The reaction was then put into an ice bath. 25 mL of $LiAlH_4$ (1 M solution in tetrahydrofuran) was then injected into the reaction dropwise and the ice bath was removed after the injection was complete, allowing the reaction to slowly warm up to room temperature. The reaction was then stirred overnight, before being quenched with aqueous $NaHCO_3$ solution, and extracted with dichloromethane. The dichloromethane portion was then washed with brine before being dried with $MgSO_4$. The residue was passed down silica gel columns using 0-8% methanol and 1% triethylamine in a dichloromethane gradient. A light yellow oil (2.31g, 51% yield) was obtained after the solvent was removed. ^{1}H NMR (300 MHz, Chloroform-*d*) δ 5.45 – 5.26 (m, 4H), 2.77 (t, *J* = 6.1 Hz, 2H), 2.67 (t, *J* = 6.9 Hz, 2H), 2.04 (q, *J* = 6.6 Hz, 4H), 1.59 – 1.06 (m, 18H), 0.97 – 0.74 (m, 3H).

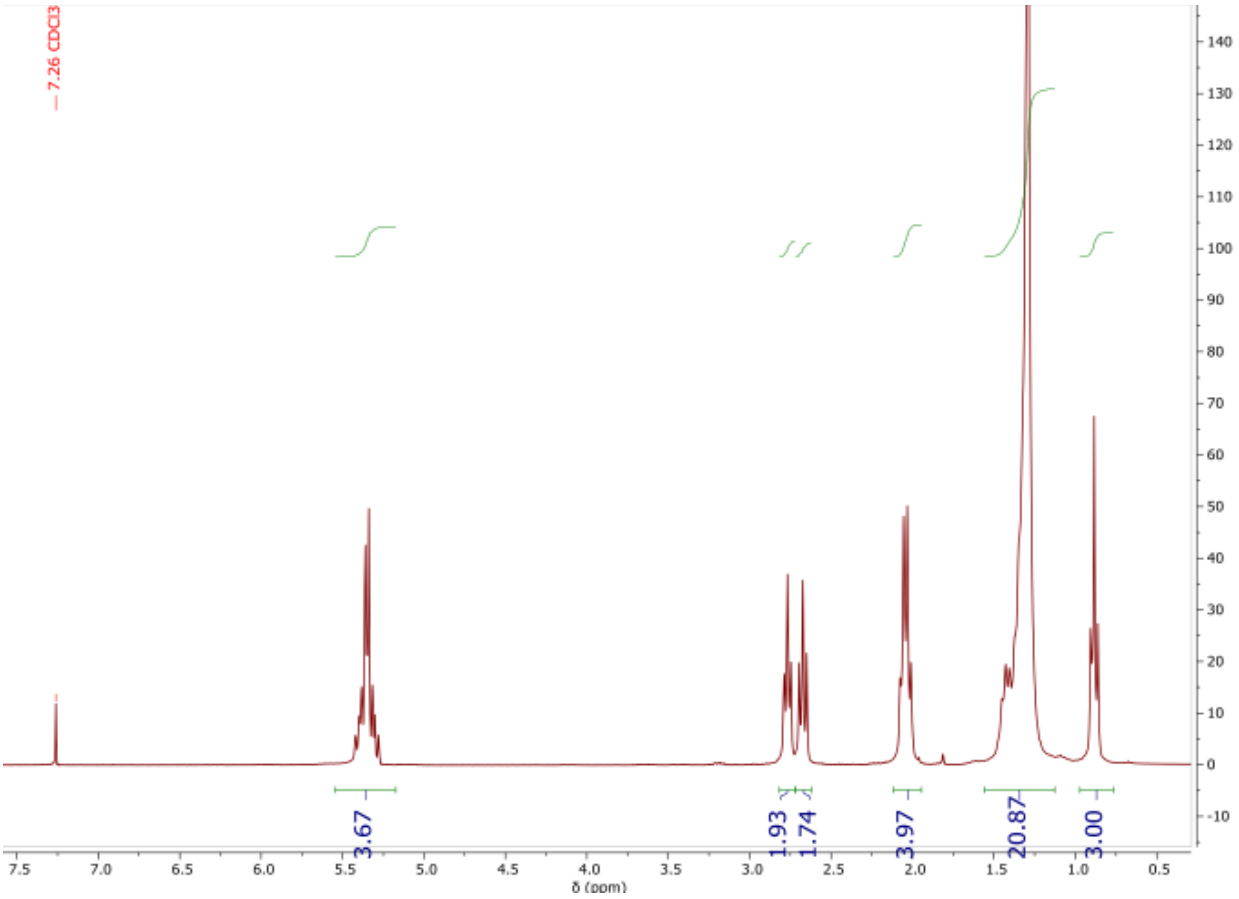

Figure 3.7. The ^{1}H NMR spectrum of linoleic amine.

3.5.2. Synthesis of Metal Oxide and Metal Sulfide NPs

Precursors

- **CZTS:** 0.5 mmol $Cu(acac)_2$, 0.25 mmol of $Zn(acac)_2$, 0.25 mmol of $SnBr_2(acac)_2$, and 1 mmol of S, 4.3 mL of select ligand (DDA, OLA, LOA, SA, OA, or LA).
- **Cu:** 0.5 mmol $Cu(acac)_2$, 10 mL of OLA.
- **Cu-S:** 1 mmol $Cu(acac)_2$ and 1 mmol of S, 11 mL of OLA.
- **Zn:** 0.5 mmol of $Zn(acac)_2$, 10 mL of OLA.
- **Zn-S:** 1 mmol $Zn(acac)_2$ and 1 mmol of S, 11 mL of OLA.
- **Sn:** 0.5 mmol of $SnBr_2(acac)_2$, 10 mL of OLA.

- **Sn-S:** 1 mmol $SnBr_2(acac)_2$ and 1 mmol of S, 11 mL of OLA.

Metal/Metal oxides synthesis

1. In a 100 mL round bottom flask, 0.5 mmol of metal precursor material is dissolved into 10 mL of OLA at room temperature in under N_2 (Schlenk line).
2. Sample is degassed by cycling between N_2 and vacuum for ~1 h at room temperature, and again for ~1 h at 130 °C.
3. Sample is heated to 225 °C for 2 h under N_2.
4. Sample is naturally cooled to 80 °C, followed by washing.

Metal chalcogenide synthesis

1. In a 100 mL round bottom flask, the metal precursor material(s) are dissolved into 3.3 –10 mL of OLA at room temperature in under N_2 (Schlenk line).
2. Sample is degassed by cycling between N_2 and vacuum for ~1 h at room temperature, and again for ~1 h at 130 °C.
3. Sample is heated to 225 °C. At 225 °C, 1 mL of a separately prepared 1 M OLA-S solution is rapidly injected into the 3-neck flask.
4. Sample is held at 225 °C for 2 h under N_2.
5. Sample is naturally cooled to 80 °C, followed by washing.

Washing of amines

1. The first wash was done with a 5:1 ratio of antisolvent (IPA) to solvent (toluene). Centrifuged at 13500 rpm for 10 minutes.

2. Supernatant was decanted, and the NP pellet was redispersed in solvent. The final washing step was done with a 3:1 ratio of antisolvent to solvent. Centrifuged at 12000 rpm for 5 minutes.
3. Supernatant was decanted, and residual solvent was removed with a rotovapor.

Washing of carboxylic acids

1. The first wash was done with a 5:1 ratio of antisolvent (toluene) to solvent (IPA). Centrifuged at 13500 rpm for 10 minutes.
2. Supernatant was decanted, and the NP pellet was redispersed in solvent. The final washing step was done with a 3:1 ratio of antisolvent to solvent. Centrifuged at 12000 rpm for 5 minutes.
3. Supernatant was decanted, and residual solvent was removed with a rotovapor.

3.5.3. Effect of Ligand Purity

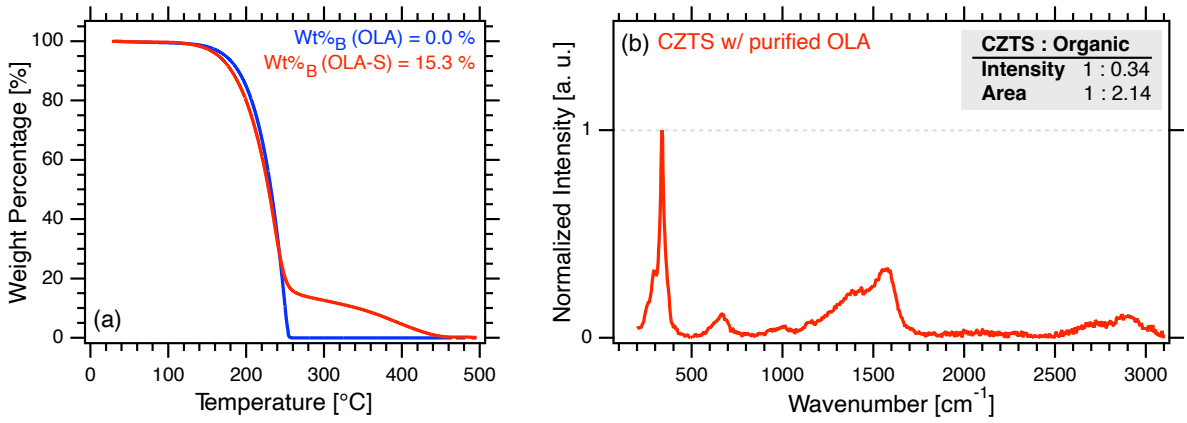

Figure 3.8. (a) TGA profile of purified OLA (blue) and OLA-S (red). **(b)** Raman spectrum of CZTS NPs synthesized with purified OLA.

Out of all ligands used in this study, OLA had the lowest purity (technical grade, 70 %). Technical grade OLA is relevant to study as it is low-cost, commercially available, and is often used in NP synthesis without purification.[260] However, to test how ligand purity influences the formation of carbon impurities, purification was performed on technical grade OLA as *via* the procedure first described by Baranov et al.[67] Despite ligand purification using methods, similarly structured carbon impurities were present after synthesis (**Figure 3.8**). However, the average concentration of carbon decreased from I_C/I_{CZTS} = 1.05 (OLA, 70 %) to 0.32 (OLA, purified). Regardless, influence of bond saturation on carbon concentration was preserved, with a 2.0 × increase between 0 and 1 double bond and a 3.8 × increase between 1 and 2 double bonds.

3.5.4. Effect of Ligand Backbone Length

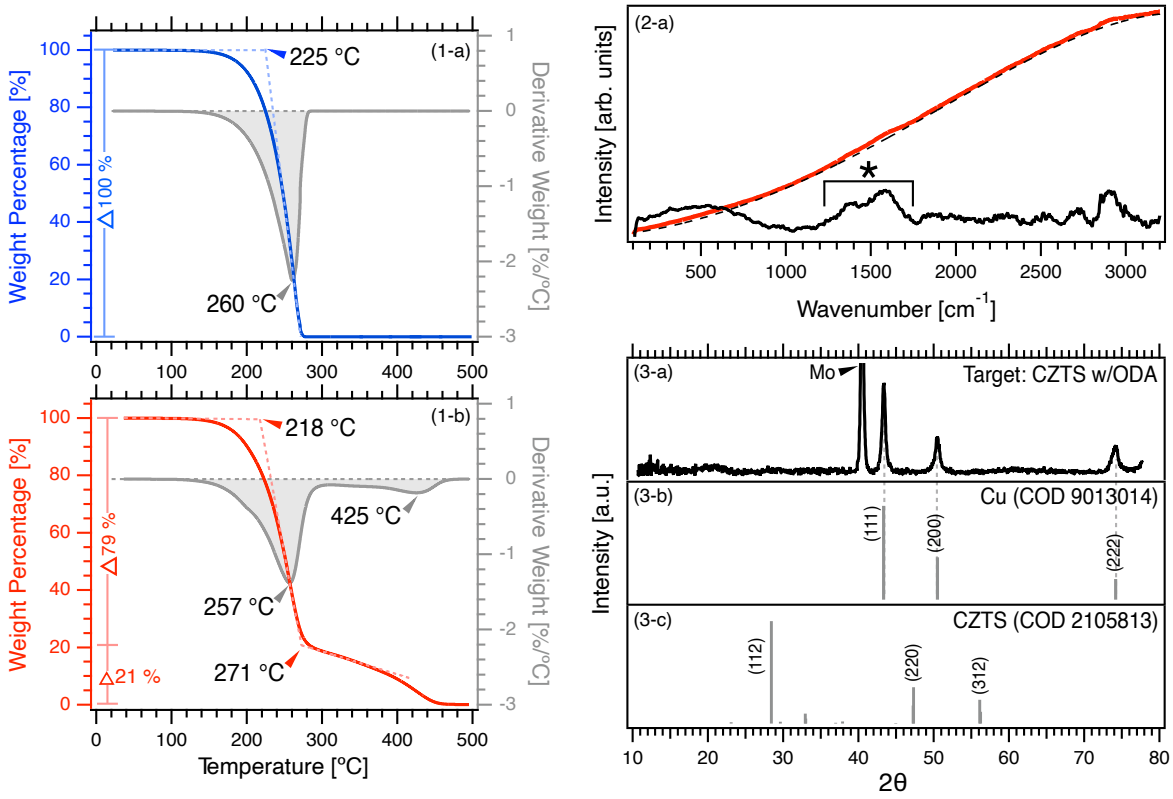

Figure 3.9. TGA profiles (colored) and DTG curves (grey) of (1a) ODA and (1b) 1 M ODA-S. Raman spectra (2a) of CZTS NP sample synthesized with ODA. The black Raman spectrum is after baseline subtraction: the raw spectra (red) and was fit with a 5th order polynomial (black, dashed). The carbon bands are emphasized (*). XRD diffractograms of the sample (3a) and relevant reference spectra (3b, Cu; 3c, CZTS).

Octadecylamine (ODA) has a more comparable chain length to the other ligands used in this study (C = 18). However, dodecylamine (DDA, C = 12) is used in the main manuscript of this study. The thermal stability of ODA (**Figure 3.9-1a**) was consistent observations from the DDA ligand (*i.e.,* did not form decomposition products). The most notable difference in stability was with the ligand-S mixtures; with an increase in carbon atoms, there was also an increase in the Wt%$_{Off}$ (Wt%$_{Off,\ DDA\text{-}S}$ = 12 %; Wt%$_{Off,\ ODA\text{-}S}$ = 21

%), such that $Wt\%_{Off,\ ODA\text{-}S}$ is comparable to that of monounsaturated OLA-S ($Wt\%_{Off,\ OLA\text{-}S}$ = 18 %).

The largest difference with the increase of carbon atoms was with the synthesis of CZTS NPs: while reaction conditions were consistent with all the other syntheses, CZTS NPs did not form. Rather, only Cu NPs were detected *via* XRD (**Figure 3.9-3a,b**). While Raman suggests that ligand decomposition occurred (**Figure 3.9-2a**), due to the lack of reference CZTS NPs, no information regarding the composition of carbon impurities can be extracted.

3.5.5. Characterizations of Elemental Sulfur and the OLA ligand

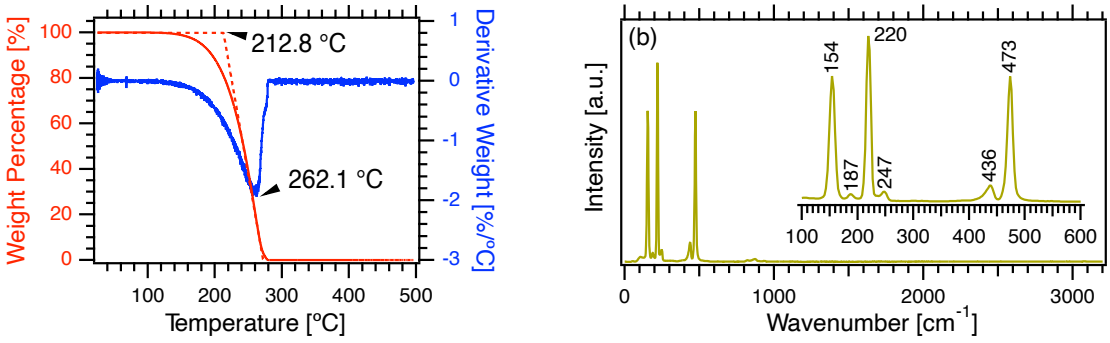

Figure 3.10. **(a)** TGA (red) and DTG (blue) profiles of elemental sulfur. **(b)** Raman spectrum of elemental sulfur

The effect that elemental sulfur has on each ligand-S mixtures TGA profile was determined by collecting TGA on elemental sulfur in absence of all ligands. For elemental sulfur, one thermal event occurred with an extracted T_I = 262 °C and $Wt\%_{Off} \leq 1$ %. When compared to ligand-S mixtures which have two thermal events (**Figure 3.3**), the residual material present at T_{Off} cannot be solely attributed to elemental sulfur. First, the Wt% of sulfur accounts for only 3 – 4 % of the 1 M mixtures total mass, less than the difference

between $Wt\%_{Off,\ ligand}$ and $Wt\%_{Off,\ ligand\text{-}S}$ for all samples (excluding SA-S). Additionally, $T_{I,\ S}$ = 262 °C, which does not align with the decomposition of temperature of residual materials ($T_{II,\ ligand\text{-}S} \geq 347$ °C.

Raman of elemental sulfur was also performed to determine if elemental sulfur was present within Raman spectra of ligand-S mixtures and CZTS. Elemental sulfur was not detected, indicating that this material was consumed.

.

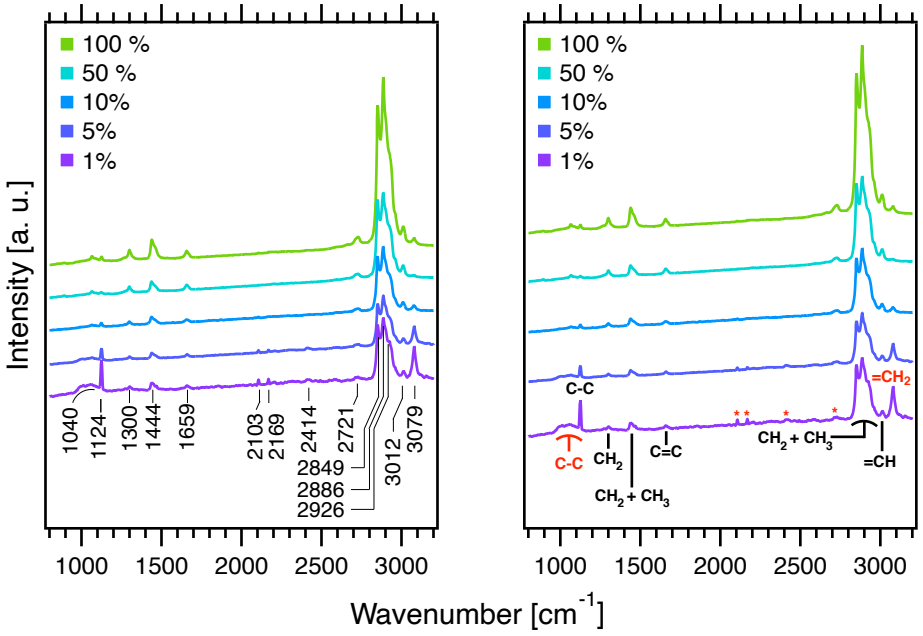

Figure 3.11. Raman spectra of technical grade OLA taken between power of 1% to 100%. Includes identified bonding modes labeled by **(a)** wavenumber and **(b)** structure. Starred peaks were unable to be identified. [209]

Similar peak positions are used to identify DDA and LOA.[1] The notable difference between DDA, OLA, and LOA is the bonding mode at 1444 cm^{-1}, associated with C=C bonding. The spectrum in **Figure 3.11** additionally shows that the innate ligand is stable between 1 % (0.08 mW) and 100 % (8 mW) laser power.

3.5.6. Characterizations of the OLA-S and OA-S Decomposition Products

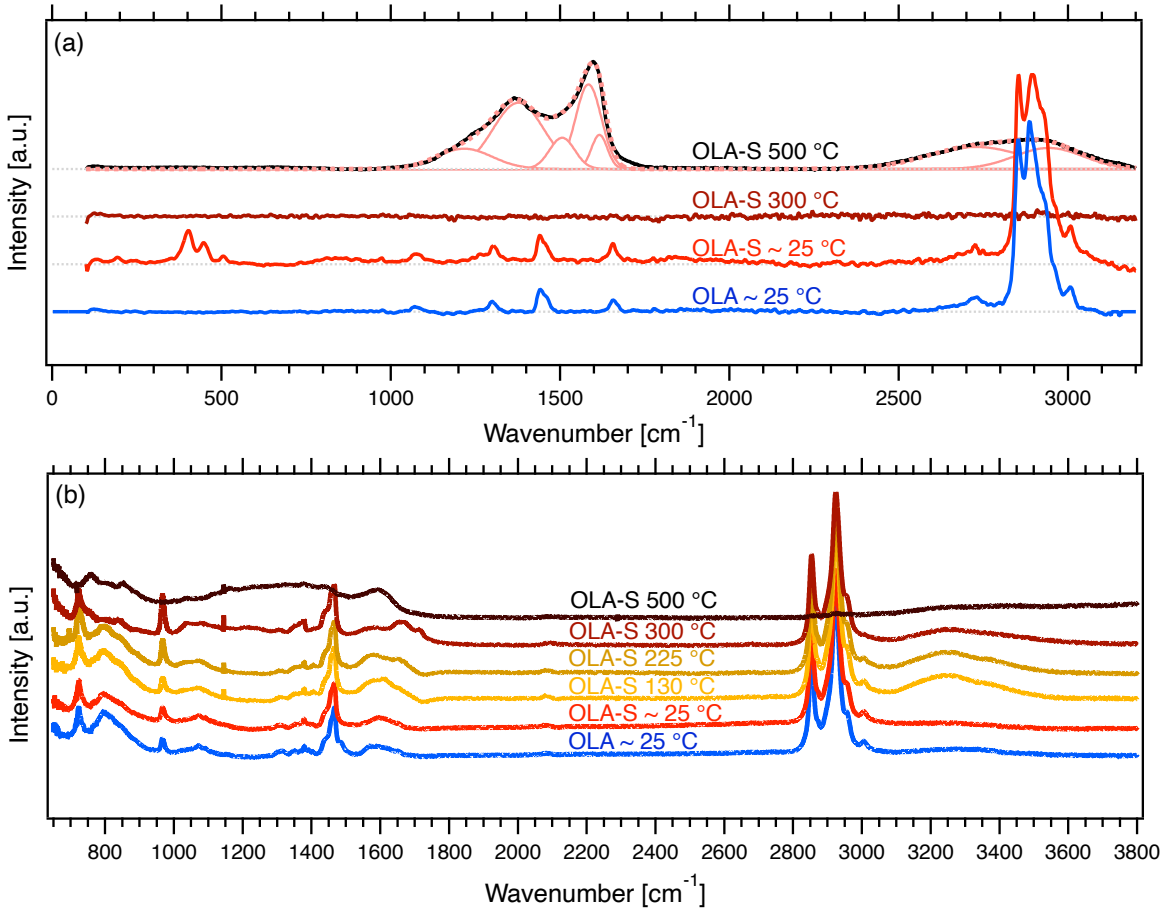

Figure 3.12. Full (a) Raman and **(b)** FTIR spectra of OLA and OLA-S heated at varying temperatures under N_2.

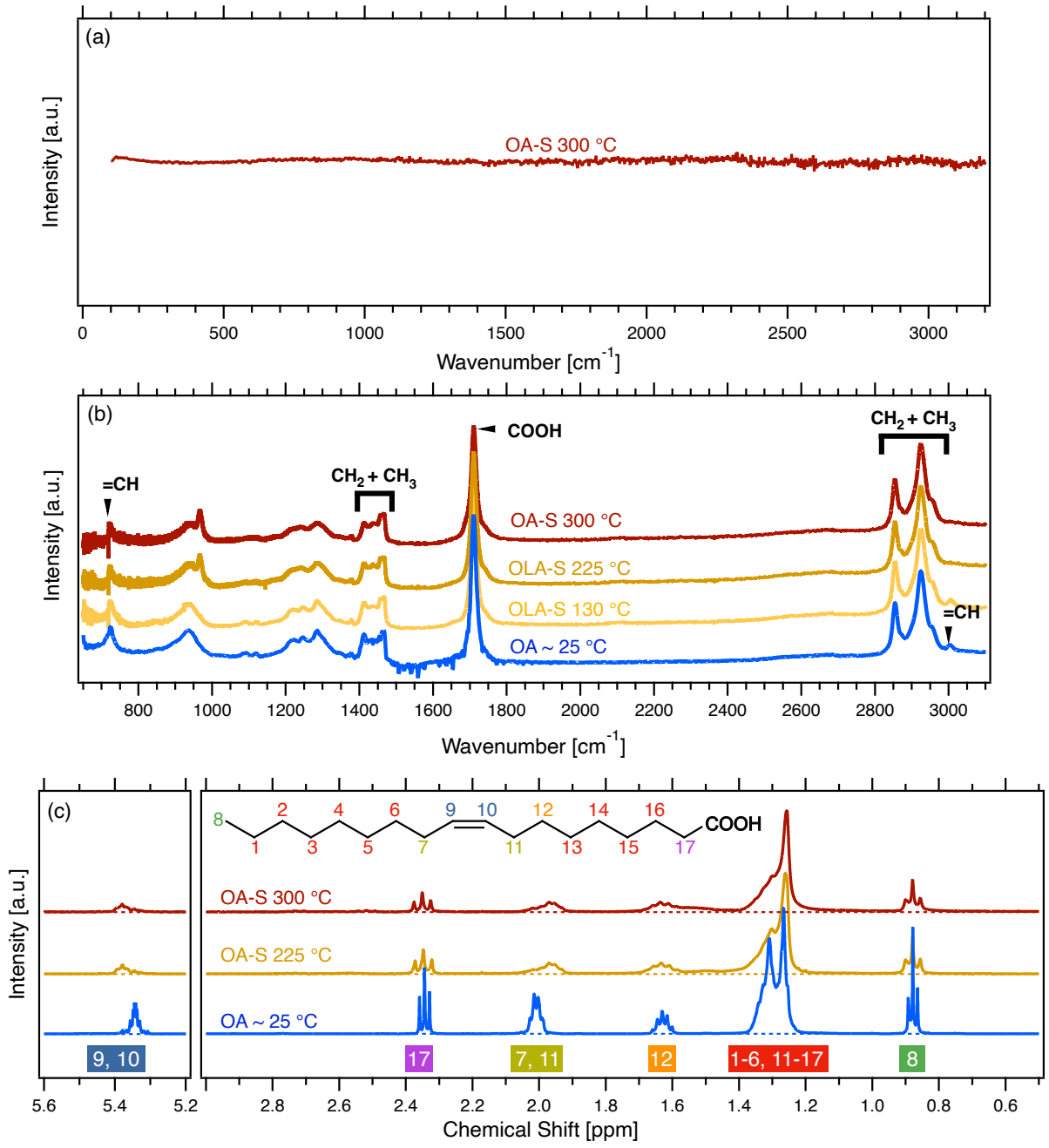

Figure 3.13. Full **(a)** Raman, **(b)** FTIR, and **(c)** ^{1}H NMR spectra of OA and OA-S heated at varying temperatures under N_2.

Table 3.4. ^{1}H NMR assignments and integrated areas

Range [ppm]	Assignment		OLA RT	OLA-S 225 °C	OLA-S 300 °C	OA RT	OA-S 225 °C	OA-S 300 °C
(5.45 – 5.25)	Vinyl	Integral:	0.57	0.56	0.43	0.62	0.33	0.33
(2.73 – 2.61)	Cα (COOH)	Integral:	0.67	0.66	0.13	--	--	--
(2.40 – 2.25)	Cα (CNH_2)	Integral:	--	--	--	0.70	0.66	0.53
(2.12 – 1.90)	Allylic	Integral:	1.21	1.20	0.94	1.25	0.86	0.54
(1.72 – 1.52)	12, alkyl	Integral	--	--	--	0.72	0.99	0.94
(1.52 – 1.17)	Alkyl	Integral:	9.19	9.11	7.51	6.91	6.75	3.68
(0.97 – 0.79)	* Methyl	Integral:	1.00	1.00	1.00	1.00	1.00	1.00
(6.0 – 0.5)		Total fraction	96 %	96 %	73 %	95 %	85 %	78 %

* Integrated areas are normalized to the area of the methyl peak (0.97 – 0.79 ppm). The total fraction is the percentage of integrated signal (area) associated the above listed assignments in relation to the total integrated signal between 6.0 – 0.5 ppm.

Similar to Raman spectroscopy, the relative intensities (here, the relative integrated areas) of peaks holds significant information, allowing us to compare changes in relative concentration. In **Table 3.4**, integration ranges, their assignments, and relative integrated areas are reported. The integrated areas are relative to the area of the methyl peak.

3.5.7. Structural Analysis of all Synthesized NPs

This section includes the Raman spectra and XRD diffractograms of binary NPs synthesized in this study, including Cu (**Figure 3.13-1**), Cu-S (**Figure 3.14-2**), Zn (**Figure 3.14-3**), Zn-S (**Figure 3.14-4**), and Sn-S (**Figure 3.14-5**).

Structural analysis of the metal NPs reveals that a mixture of metal/metal-oxides phases were present. Metal oxide formation may stem from the synthesis of a core metallic NP which forms an oxide shell upon exposure to air.[3] Materials characterizations indicates that Sn/SnO did not form; rather, an amorphous tin-based material was produced. While crystalline SnO NPs have been produced under similar mild reaction conditions with OLA and OA and $Sn(Et_2Dtc)_2$ precursors,[295] we aimed to preserve reaction conditions across

materials for accurate cross examination. Thus, the synthesized metallic Sn material is not present in most of the results and discussion. The synthesis of chalcogenide NPs followed by structural analysis reveals that Cu_xS, ZnS, and SnS_x were successfully synthesized under the same conditions. However, Raman spectra of ZnS was oversaturated and did not yield distinct signals, making it ineligible for carbon-based analyses. Additionally, for all NP samples, we estimated the NP crystallite size *via* XRD (Scherrer equation, **Eqn. 2.2).**

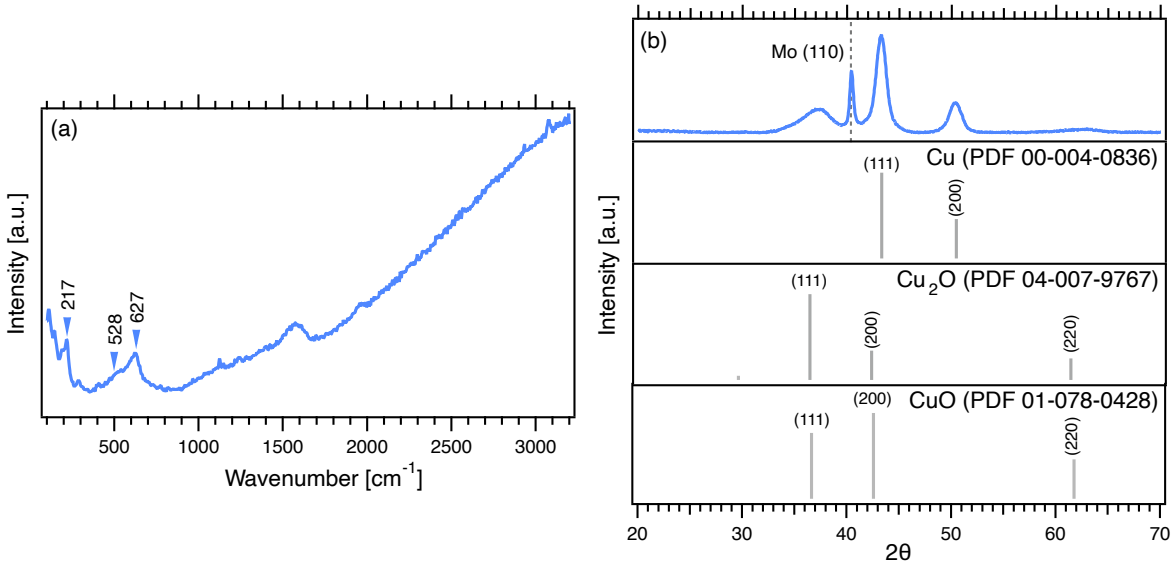

Figure 3.14-1: Cu. (a) Raman spectrum and **(b)** XRD diffractograms of Cu/Cu_xO NPs samples. No background subtraction was applied (Raman). XRD refence patterns are listed (including Mo COD 9008543).

The sulfur free synthesis resulted in a mixture of Cu and Cu_xO (x = 1, 2) phases. It is plausible that the sulfur free synthesis yielded Cu NPs, which formed an oxide shell upon exposure to air.[296]

XRD diffractograms of the targeted Cu NCs showed Cu and Cu_xO had formed. Cu's (111) and (200) planes were identified and can exclusively be assigned to Cu. In addition, CuO and/or Cu_2O were detected, where both phases were identified by peaks at the same Bragg angle. Cu is

Raman inactive, thus was not detected in the Raman spectra. Both CuO (289, 528, and 627) and Cu_2O (112, 146, and 217 cm^{-1}) were detected *via* Raman spectroscopy.

Via Scherrer analysis, crystallite sizes were estimated. From fitting the Cu (111), and (200), and planes, we estimate a crystallize size of 8.8 ± 0.9 nm. We additionally estimate a crystallite size of 3 nm from the Cu_xO (111) plane.

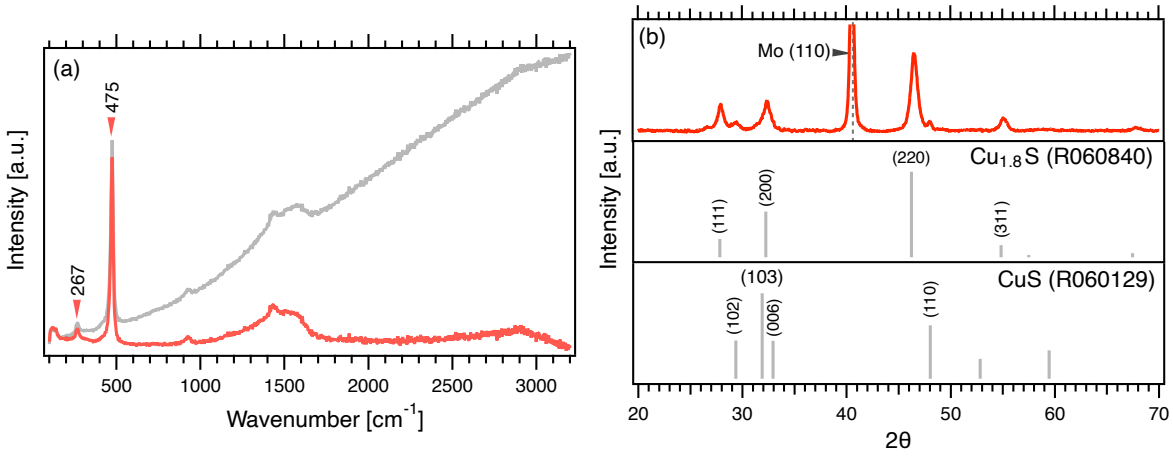

Figure 3.14-2: Cu-S. (a) Raman spectra and **(b)** XRD diffractograms of Cu_xS NPs samples. The grey Raman spectrum is prior to background subtraction, and the red spectrum is after a 4-point linear background subtraction is applied. XRD reference patterns are listed (includes Mo COD 9008543, $Cu_{1.8}S$ R060840, and CuS R060129). *CuS: R060129; $Cu_{1.8}S$: R060840; Cu_2S: R050067; Mo: COD 9008543*

The sulfur-based synthesis resulted in a mixture of Cu_xS (x = 1, 1.8) and showed no signs of oxidation.

The synthesis of Cu_xS yielded CuS and $Cu_{1.8}S$. Each of these phases are expressed *via* XRD as hexagonal covellite (CuS), and digenite-chalcocite ($Cu_{1.8}S$), with signals associated with digenite-chalcocite being more intense than that of covellite. The Raman spectra identifies CuS (267 cm^{-1} and 475 cm^{-1}). $Cu_{1.8}S$ is not Raman active and was not detected.

Via Scherrer analysis, crystallite sizes were estimated to be 14.4 ± 1.2 nm.

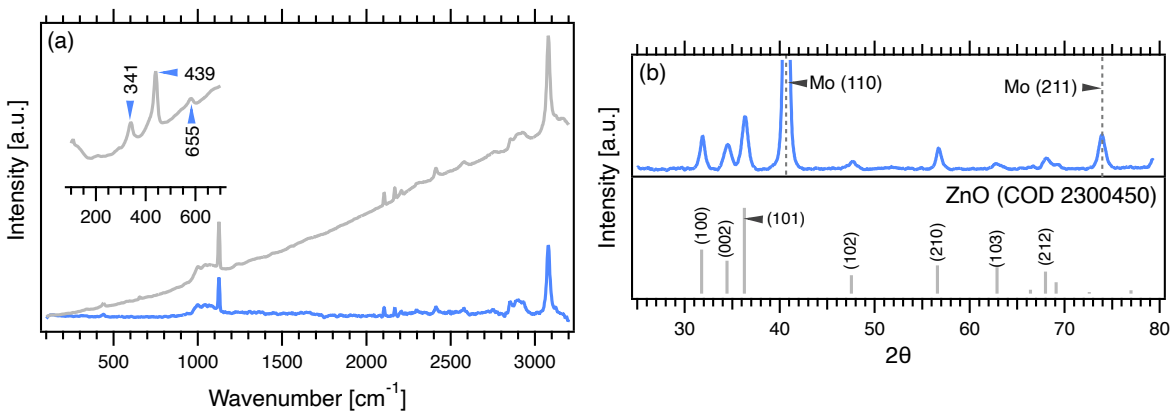

Figure 3.14-3: Zn. (a) Raman spectra and **(b)** XRD diffractograms of ZnO NPs samples. The grey Raman spectrum is prior to background subtraction, and the blue spectrum is after a 4-point linear background subtraction is applied. XRD reference patterns are listed (includes Mo COD 9008543 and ZnO COD 2300450).

The sulfur free synthesis resulted in ZnO, absent of the targeted Zn phase. This may be due to reaction conditions favoring the formation of ZnO phases over Zn.[297]

XRD of the targeted Zn NCs show hexagonal zincite (ZnO) had formed, entirely absent of the signature Zn planes. Raman spectra of the ZnO sample was also not straightforward. While low intensity ZnO scattering bands at 341, 437, and 655 cm^{-1} were detected, a signature peak at 521-565 cm^{-1} is absent.

Additionally, the ZnO nm crystallite size is estimated to be 15.1 ± 3.4 nm (Scherrer calculation) *via* the (100), (002), and (101) planes of ZnO.

Finally, the ZnO Raman signal had a notable overlap with OLA'S (**Figure 3.10**). This includes a broad C–C (1058 and 1124 cm^{-1}), several unassigned signals (2015, 2168, and 2412 cm^{-1}) and $=CH_2$ (3079 cm^{-1}).[209] The ZnO sample also has a broad peak from 2830 to 2970 cm^{-1}, which upon deconvolution appears to be comprised of three peaks at 2851, 2884, and 2924 cm^{-1}, which corresponds with OLA's CH_2 and CH_3 bonding.[209]

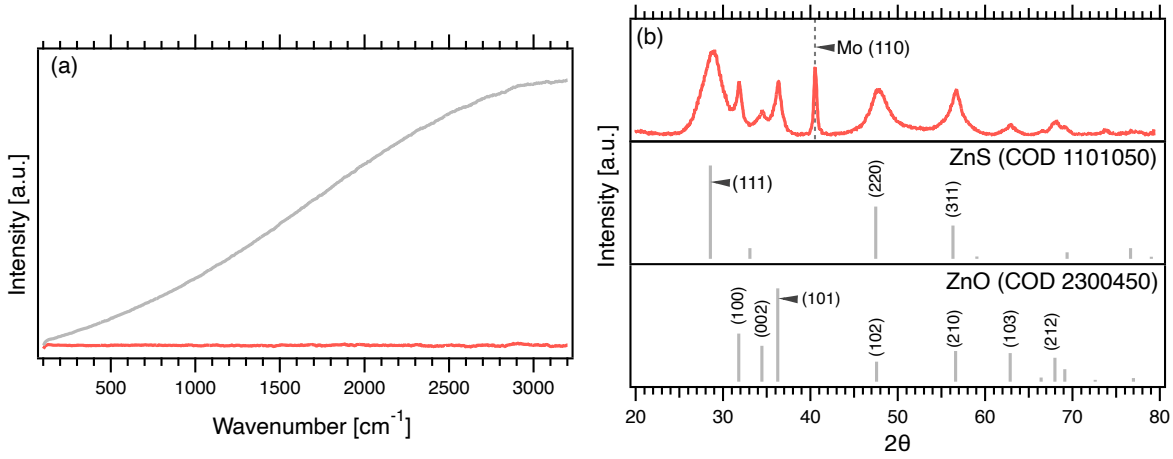

Figure 3.14-4: Zn-S. **(a)** Raman spectra and **(b)** XRD diffractogram of ZnS NPs samples. The grey Raman spectrum is prior to background subtraction, and the red spectrum is after a 5th order polynomial background subtraction is applied. XRD reference patterns are listed (includes Mo COD 9008543 and ZnS COD 1101050, and ZnO COD 2300450).

The synthesis of ZnS NPs lead to a mixture of ZnS and ZnO phases.

Cubic sphalerite ZnS was identified by the material's three most predominate planes; (111), (220), and (311) planes, which were all observed. In addition to ZnS detection, ZnO is detected by the presence of unique signature identified by the (100), (102), and (101), (103), and (212) planes. The Raman spectra was less conclusive. Rather than the expression of ZnS and ZnO Raman signatures from 100 – 1200 cm^{-1},[3] a broad florescent background is observed.

Crystallite size (7.15 ± 3.6 nm) was estimated from the 5 peaks of highest intensity (from both from ZnS and ZnO assignments).

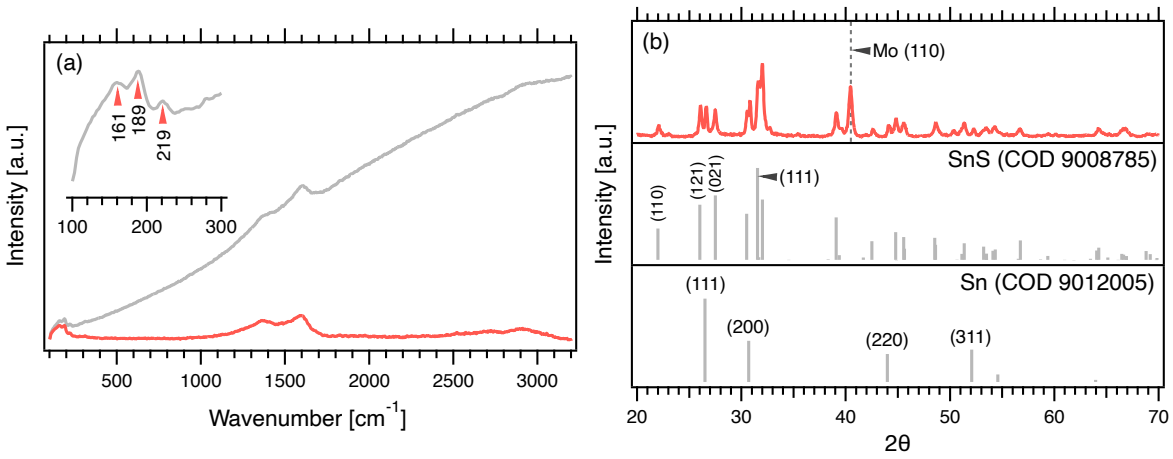

Figure 3.14-5: Sn-S. (a) Raman spectra and **(b)** XRD diffractogram of SnS NPs samples. The grey Raman spectrum is prior to background subtraction, and the red spectrum is after a 4-point linear background subtraction is applied. XRD reference patterns are included (includes Mo COD 9008543 and SnS COD 9008785 and Sn COD 9012005).

The synthesis of sulfur-based synthesis of SnS and Sn. Orthorhombic herzenbergite (SnS) was detected by the material's three most predominate planes; (021), (111), and (040) at 27.5°, 31.6°, 32.0°. Additionally, unaccounted for signals of the XRD pattern can be assigned to Sn (111), (220), and (311). Raman of the SnS sample further matched the NPs to the orthorhombic SnS, with the materials signature modes at 161 cm^{-1}, 189 cm^{-1}, and 219 cm^{-1} all being identified.[113]

SnS NPs size was estimated to be 28.8 ± 5.5 nm (Scherrer calculation) *via* the (110), (121), (021) planes of SnS.

The Sn NP synthesis is not included in this study; XRD revealed amorphous material had formed (*i.e.*, no diffraction pattern formed) and the Raman background was significantly high (similar to **Figure 3.14-4(a)**), overpowering all the signal and leaving no distinguishable peaks.

Chapter 4: Ligand Selection Dependent Grain Growth

4.1. Introduction

As discussed within **Chapter 1**, dense micron-sized grains are ideal for semiconducting materials such as CZTSSe. An increased grain size reduces the number of interface sites for parasitic carrier electron-hole recombination, thereby improving overall device conductivity. A common approach for forming dense large grains is to sinter CZTS NPs in a Se-rich fluxing atmosphere (selenization).

Recent work has indicated that the final morphology of CZTSSe is also sensitive to the ligand capping material on the CZTS NPs. Several studies have shown that increasing the weight percentage of carbon of the capping material results in larger grain growth compared to stripped NPs or ligands with a lower molecular weight.[135,140,142,145,191] These studies indicate that the capping agent plays a more central role in the sintering process of CZTS NPs than prior works (which predict ligands desorb and calcinate during high temperature sintering (> 400 °C)).[119,135]

Herein, we investigated the impact of ligand selection on sintered nanoparticle films. We compared three alkylamine ligands: dodecylamine (DDA), oleylamine (OLA), and linoleylamine (LOA). Sharing similar backbone length, structure, and anchoring functional group, these ligand's

properties diverge in the number of unsaturated bonds along the hydrocarbon backbone; DDA is fully saturated (0 double bonds), OLA is an alkene (1 double bond), and LOA is a diene (2 double bonds).

To evaluate the effect of the ligand on grain growth, we first synthesized and characterized CZTS NPs using SEM and XRD. While we observed strong similarities across synthesized NPs with different ligands, we found the final morphology and grain size of selenized CZTSSe varied. This work provides a potential strategy for engineering grain size during sintering without altering processing conditions such as temperature, time, or pressure.

4.2. Methods

4.2.1. Prior Methodology: Synthesis and Characterization of CZTS and CZTSSe

Methods from **Chapter 2** and **3** detail the synthesis, processing, and characterization of CZTS NPs and selenized CZTSSe films. In this chapter, we use previously described CZTS NPs which were synthesized with either DDA, OLA, or LOA ligands, and with metal acetylacetonate and elemental sulfur precursors. As particle size influences sintering and densification, we altered the solvent (*i.e.,* ligand) concentration to control particle size during NP synthesis. Specifically, to synthesize smaller DDA NPs, the concentration of DDA was increased to 15 mL. After synthesis and isolation (washing) of NPs, the CZTS NPs were suspended into a NP ink and deposited for selenization.

For the characterization of CZTS and CZTSSe films, previously described methods for as Raman Spectroscopy, XRD, SEM, EDS, XPS, TGA, and GDOES were all used. Specifically, material confirmation and comparison was performed *via* Raman Spectroscopy, XRD, EDS, and

XPS, and particle size analysis was conducted through a combination of SEM and XRD. The only method which had modifications was for TGA. Here, we performed TGA on the CZTS NPs with the same instrumentation (*TA Instruments Q20 ThermoGravimetric Analyzer*) and followed similar methods (10 °C/min, 40 mL/min of N_2, platinum pan), however smaller sample sizes were used (6.3 ± 4.0 mg).

4.2.2. Additional Techniques: Grain Size Analysis and NP Stability

Per ligand sample (*i.e,* DDA, OLA, LOA), the grain sizes were determined from top-down SEM micrographs. Grain area was quantified with ImageJ from a minimum of 5 separate substrates (2 images per substrate). Grain size represents the calculated diameter of each grain, determined from the measured grain area. Y-axis is the probability density [counts], normalized by dividing counts by a power-law function ($\boldsymbol{d_{of\ total\ area}/d}$ [μm/μm]).

In addition to TGA, differential scanning calorimetry (DSC) was performed with *TA Instruments DSC 2500* to characterize the NPs thermal stability. Samples (5.3 ± 0.8 mg) were loaded onto an aluminum pan and heated and cooled at a rate of 10 °C/min under continuous N_2 flow (50 mL/min).

4.3. Results and Discussion

4.3.1. Ligand Influence on the Formation of CZTS NPs

As discussed in ***Chapter 1.1.3.2***, NP size influences grain growth due to a decrease in melting point temperature, an effect known as size-dependent melting point depression.[135] Since smaller NPs are intrinsically less stable than larger NPs, small particles will melt at lower temperatures, expediting the coarsening and densification during sintering. Thus, to adequately

compare sintered CZTSSe films made from DDA-. OLA-, and LOA-capped CZTS NPs, we first estimated the size of synthesized CZTS NPs through XRD and SEM. Through XRD, the mean crystallite size ($\boldsymbol{\tau}$) is calculated by the Scherrer equation:

	Equation	Description
(**Eqn. 4.1**)	$\tau = \frac{K\lambda}{\beta\cos\theta}$	For spherical particles, $\boldsymbol{K}$ is ˜0.9, and the incident wavelength used was 1.54 Å. The three most planes of CZTS (*i.e.,* (112), (200), and (312)) were used to estimate the mean crystallite size.

$\boldsymbol{\tau}$ = crystallite size [nm] $\boldsymbol{K}$ = shape factor [a.u.]; $\boldsymbol{\lambda}$ = incident wavelength [nm]; $\boldsymbol{\beta}$ = peak breadth [°]; $\boldsymbol{\theta}$ = Bragg angle [°]

From the Scherrer equation, crystallite sizes were estimated to be 21.0 ± 3.7 nm for DDA-capped NPs, 15.5 nm ± 1.4 nm for OLA-capped NPs, and 12.0 nm ± 1.5 nm for LOA-capped NPs when synthesized under the same conditions. From **Figure 4.1(b),** we observe that the peaks broaden as the crystallite size decreases, in agreement with **Eqn. 4.1** ($\boldsymbol{\beta^{-1} \propto \tau}$) and microscopy images of the NPs (**Figure 4.1(c)**). NP size is typically dependent on the concentration of precursors and the ligand, reaction time, and temperature. Since we used identical reaction conditions (*i.e.,* concentration, time, temperature) across all samples, we observed that increasing the number of double bonds along the ligand backbone (DDA < OLA < LOA) correlates with smaller NPs ($\boldsymbol{\tau_{DDA} > \tau_{OLA} > \tau_{LOA}}$).

Our observed change in NP size may be a result of ligand sterics.[69] While all three ligands have the same amine functional group (and therefore the same binding energies, reducing ability, and coordination bonding), the rigidity of the ligands' backbones differ, increasing with the number of double bonds. Further, bulkiness of unsaturated ligands is amplified by elemental sulfur, which branches together ligands at double bond sites to form a polysulfide with higher molecular weight (*e.g.*, **Figure 1.13**).[146,150,153,166,298] When these bulky ligands or polysulfides bind to a

monomer, the monomer's mobility decreases, resulting in slower nucleation and growth rates.[69] Additionally, due to steric hinderance, bulkier ligands become more effective at screening the diffusion of ions into and out of the nuclei, further slowing the growth rate of particles. Because of the double bonds within unsaturated OLA and polyunsaturated LOA, they are expected to form polysulfides, which may be why CZTS NPs synthesized with these ligands resulted in smaller nanoparticles than with saturated DDA, which lacks double bonds. In summary, during synthesis we that observe that double bonds limit diffusion, resulting in smaller NPs.

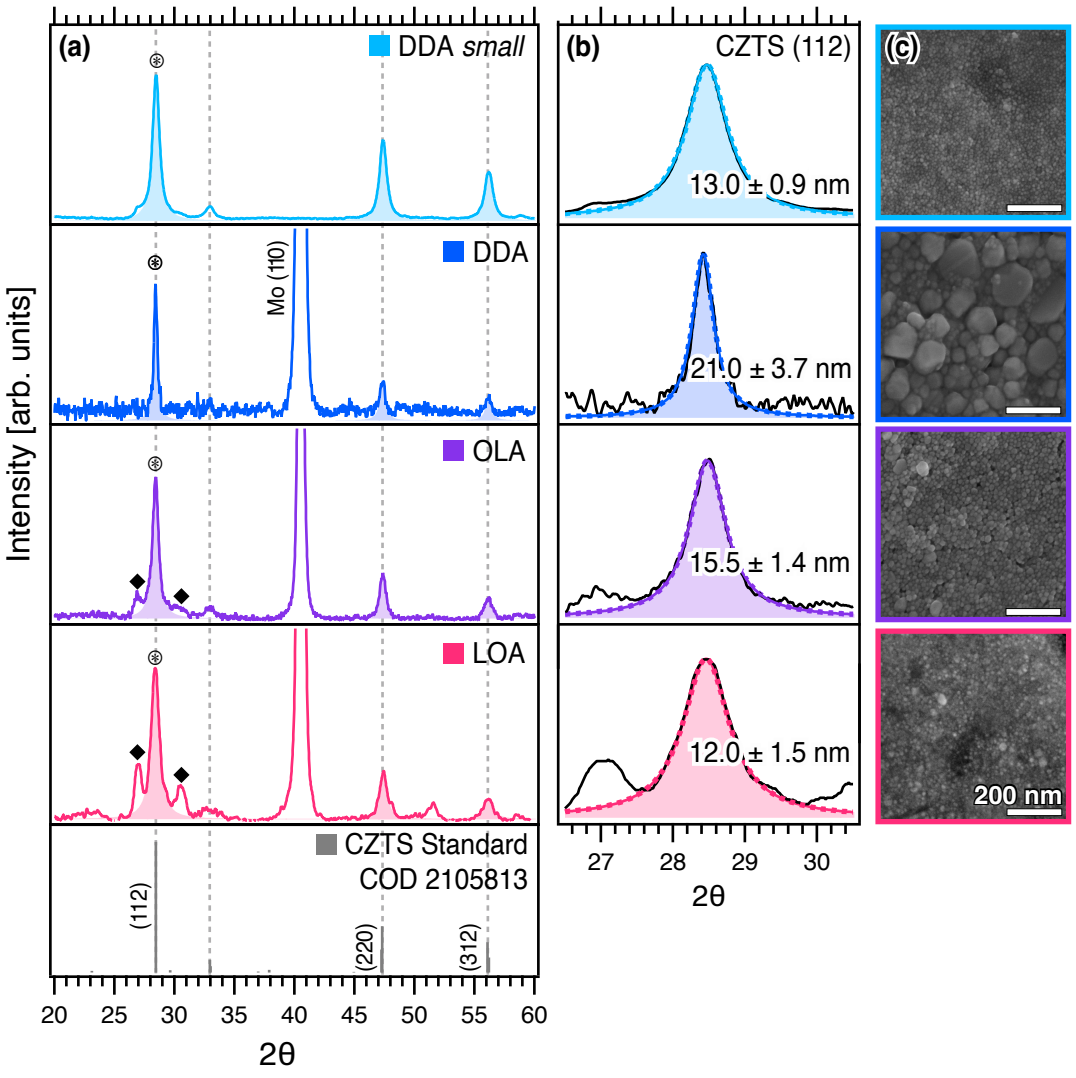

Figure 4.1: (a) XRD diffractogram of deposited thin films of CZTS NPs capped with DDA, OLA, and LOA ligands. The (112), (220), and (312) planes of the CZTS kesterite lattice are highlighted by the dashed grey lines, and have their Lorentzian fits displayed. **(b)** Truncated XRD diffractogram of CZTS NPs centered around the (112) plane (marked *via* ⊛) with the peak's Lorentzian fit and crystal size displayed. **(c)** Top-down SEM images of the deposited NP films prior to sintering. Scale bars for all insets are 200 nm. Peaks marked with black diamonds are associated with wurtzite ZnS. Intensity normalized to the (112) peak.

We realized that the size discrepancy of DDA-based NPs (2nd row of **Figure 4.1**) was likely to influence grain growth during sintering. To ensure that DDA-based NP samples were comparable to the OLA and LOA-based samples, we further decreased supersaturation concentrations during synthesis (see methods).[299] As a result, CZTS NPs (13.0 ± 0.9 nm) were successfully synthesized with DDA (top row of **Figure 4.1**, '*DDA small*') and were more comparable in size with the OLA- and LOA-based particles, thereby improving our ability to compare sintered NP films.

In addition to NP size, we also ensured similarities in the crystal structure across samples. To undergo a phase transition (*i.e.,* recrystallize into a new phase or crystal structure), additional energy is required which dampens the rate of mass diffusion and thus the rate of grain growth. Using XRD, we observed that across all samples, kesterite CZTS was the primary phase across all NP samples. Growth of the CZTS NPs is expected to stem from the interdiffusion of Sn^{4+} and Zn^{2+} into the Cu_2S lattice to form CZTS,[9,84] a mechanism that occurs readily as Cu_2S, CZTS, and intermediate phases have all cubic structures with tetragonal bonding:[84,300]

(**Scheme 4.1**)
$$Cu_2S\ (cubic) + Sn^{4+} \rightarrow Cu_2SnSe_3(cubic) + Zn^{2+} \rightarrow Cu_2ZnSnS_4\ (cubic)$$

For both DDA samples, only kesterite (cubic) CZTS phase was identified, in agreement with **Scheme 4.1**. However, synthesis with OLA and LOA resulted in a second crystalline material: wurtzite (hexagonal) ZnS (observed by the XRD signals at 27.03° and 30.60° 2θ). While binary and ternary derivatives of CZTS can readily form during synthesis due to the narrow stability of the kesterite CZTS phase, cubic ZnS (sphalerite) is the more stable polymorph of hexagonal ZnS under similar reaction conditions (*e.g.*, see **Figure 3.14-4**).[300]

It is plausible that the formation of the hexagonal ZnS phase results from slight differences in S concentration between DDA, OLA, and LOA. Lower concentrations of sulfur (< 1 mmol) result in the preferential formation of wurtzite ZnS.[301] While we consistently used 1 mmol of S, increasing the number of double bonds increases the number of sulfur atoms occupied by cross linking the ligands (confirmed *via* XPS in **Figure 4.13** for OLA and LOA), decreasing the concentration of available sulfur monomers for nucleation.[150]

Because the concentration of ZnS increases with the number of double bonds, comparing each synthesized CZTS sample may be partially limited. During the sintering of CZTS NPs, Zn ions are the last to diffuse.[84] Thus, the presence of a ZnS phase is not likely to impact the formation of CZTSSe from CZTS.[84] Otherwise, we found no significant differences in shape and phase between CZTS NPs.

4.3.2. Ligand influence on CZTSSe Grain Growth

We first contrasted differences in the structure of CZTSSe films selenized under identical conditions. XRD diffractograms in **Figure 4.2** show that upon annealing the deposited CZTS NPs in a selenium rich atmosphere, auxiliary CZTS and ZnS phases were eliminated, revealing a single phase of kesterite CZTSSe ($(Cu_2ZnSn(S_{0.1}Se_{0.9})_4$) across all samples. This result emphasizes that

all samples were fully selenized into kesterite CZTSSe under the same sintering conditions (20 min at 500 °C).[191]

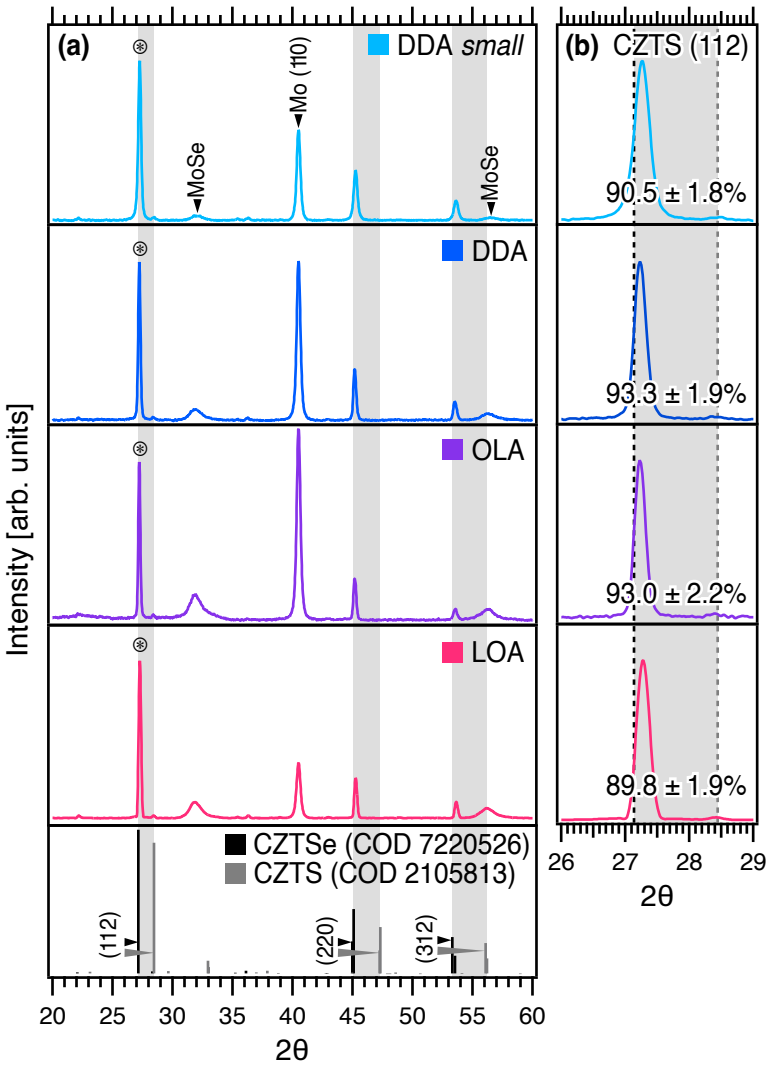

Figure 4.2: (a) XRD diffractogram of selenized thin films of CZTSSe from DDA, OLA, and LOA-based samples. **(b)** Truncated XRD diffractogram centered around the (112) plane of CZTSSe (marked *via* ⊛) The percent selenization of each $Cu_2ZnSn(S_xSe_{x-1})_4$ is reported by calculating the difference in lattice spacing from pure CZTS ($x = 1$) and CZTSe ($x = 0$). For all samples $x = \sim 0.1$. Intensity is normalized to the (112) peak.

Cross-sectional micrographs were collected to observe grain height. The area of grains from top-down micrographs was quantified to obtain the grain size distribution of selenized films. Across samples, several differences in grain size ($\boldsymbol{d}$) and grain density ($\boldsymbol{\rho_G}$) were observed.

As shown in **Figure 4.3(d)**, the grain size of LOA-based films was the largest with an average size of 1.33 μm and a wide grain size distribution ($\boldsymbol{d_{max}}$ = 3.7 μm). Despite the different sizes of DDA- and OLA-based CZTS NPs, the average grain sizes and distributions across resulting CZTSSe films were very comparable ($\boldsymbol{d_{avg,\,DDA}}$ = 0.79 μm, $\boldsymbol{d_{avg,\,OLA}}$ = 0.78 μm). When the size of DDA synthesized particles was reduced, the average grain size increased ($\boldsymbol{d_{avg,\,DDA\,small}}$ = 0.93 μm). Therefore, when considering CZTS NPs of comparable sizes (*i.e.,* DDA *small*, OLA, and LOA samples), there was no consistent trend between the average grain size and number of double bonds along the ligand backbone.

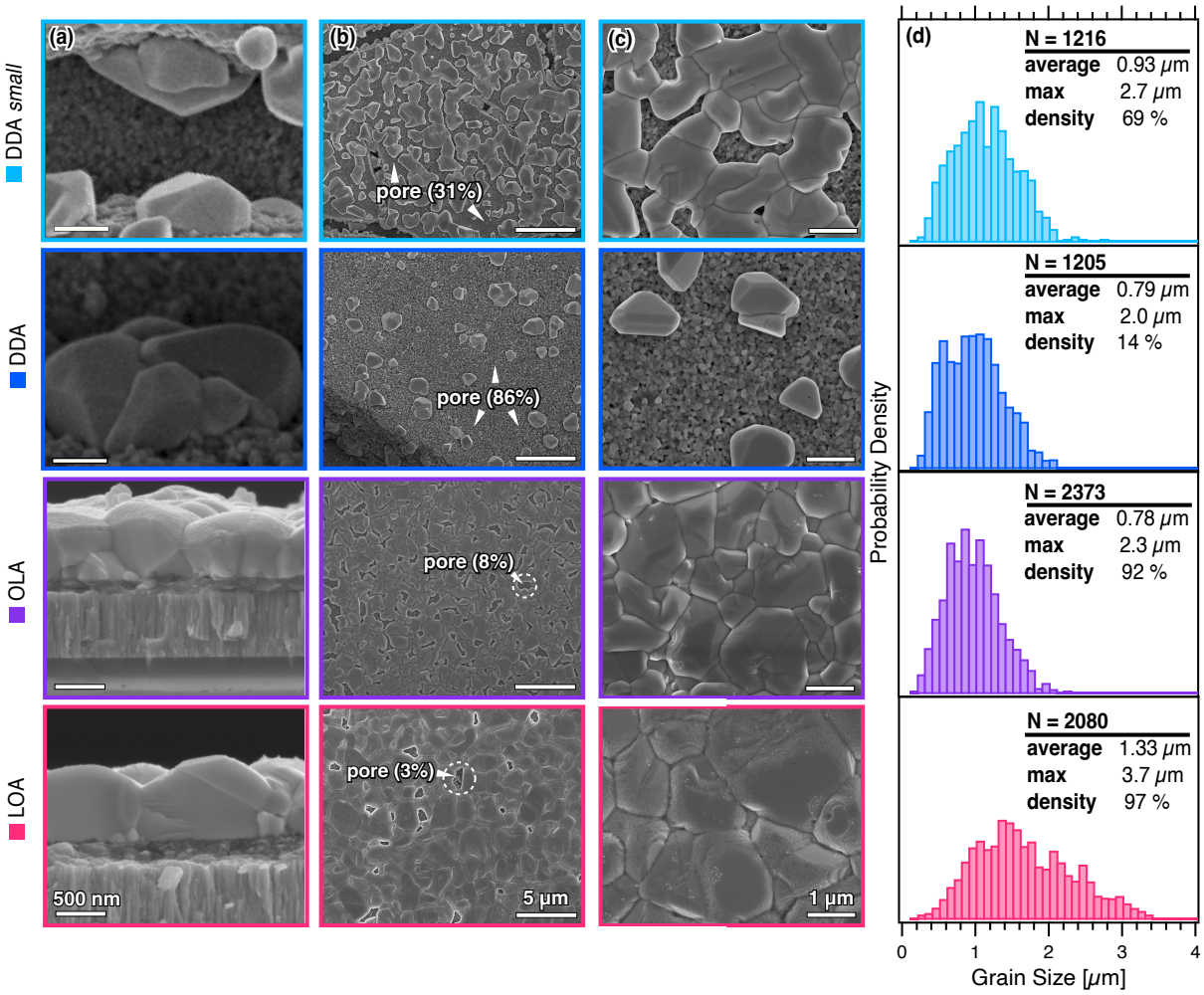

Figure 4.3. SEM micrographs include **(a)** cross-section images of selenized samples (scale bar 500 nm), **(b)** top-down images of samples (scale bar 5 µm) with a pore highlighted (dashed white circle) and the average pore density across all samples labeled, and **(c)** zoomed in top-down images (scale bar 1 µm). **(d)** The grain size distribution collected for each selenized material, determined by calculating the average diameter of each grain, with the same y-axis intensity (probability density) for each distribution.

Table 4.1. Grain size and densification

	DDA *small*	DDA	OLA	LOA
d_{avg}	0.93	0.79	0.78	1.33
d_{med}	0.88	0.71	0.74	1.26
d_{max}	2.7	2.0	2.3	3.7
ρ_G	69 %	14 %	92 %	97 %
ρ_P	31 %	86 %	8 %	3 %
v	1.2	1.7	1.7	0.56

$\boldsymbol{d}$ = grain size, or the grain diameter calculated from the area of the grain [μm]; $\boldsymbol{d_{avg}}$ = average grain size [μm]; $\boldsymbol{d_{med}}$ = median grain size [μm]; $\boldsymbol{d_{max}}$ = maximum grain size [μm]; $\boldsymbol{\rho_G}$ = grain density, or the percentage of densification calculated by subtracting the percentage of space occupied by pores [%]; $\boldsymbol{\rho_P}$ = pore density, or the percentage of the film not occupied by grains [%]; $\boldsymbol{v}$ = the number of grains that occupy 1 μm^2 (excluding pore channels) [grains/μm^2].

However, we observed a trend between the number of double bonds and the density of large grains. In **Figure 4.3(b)**, regions where large CZTSSe grains did not form are highlighted (pores). For NPs of similar size, the density of these pores ($\boldsymbol{\rho_P}$) consistently decreased as the number of double bonds increased from $\boldsymbol{\rho_{P,\ DDA\ small}}$ = 31 %, $\boldsymbol{\rho_{P,\ OLA}}$ = 8 %, to $\boldsymbol{\rho_{P,\ LOA}}$ = 3 %. Therefore, the densification (the density of large grains ($\boldsymbol{\rho_G}$)) increased as we increased the number of double bonds within the ligand. We also observed that $\boldsymbol{\rho_P}$ depended on NP size: smaller DDA NPs resulted in less pore space ($\boldsymbol{\rho_{P,\ DDA\ small}}$ = 31 %) then larger DDA NPs ($\boldsymbol{\rho_{P,\ DDA}}$ = 86 %).

The difference in $\boldsymbol{d}$ and $\boldsymbol{\rho_G}$ offer insight into the rate of densification and grain growth. Films with $\boldsymbol{\rho_G}$ < 90 % lie within the 'intermediate stage' of the sintering process, pictured in **Figure 1.6** (**Chapter 1**). Both of our DDA samples fall within this intermediate stage with a low $\boldsymbol{\rho_G}$ (14 – 69 %). While $\boldsymbol{\rho_G}$ increased to 92 % for OLA samples, the grain size remained unchanged, indicating that the rate of densification increased while the samples were still in early stages of growth. Increasing the number of doubles bonds (LOA) led to a further increase in both $\boldsymbol{\rho_G}$ (97 %) and grain size. These results provide evidence that the number of double bonds in the ligand positively correlates with the rate of densification.

Using ligands with higher bond saturation may provide an effective strategy in decreasing the activation energy of the sintering process without increasing time, pressure, or temperature.

4.4. Conclusions

Here, we synthesized CZTS NPs with ligands of varying bond saturation: dodecylamine (DDA, 0 double bonds), oleylamine (OLA, 1 double bond), and linoleylamine (LOA, 2 double bonds) ligands. We found that CZTS NP size and phase purity increases with increasing bond saturation, and that NP size can be modulated by ligand concentration during synthesis. Upon synthesizing NPs of comparable sizes, we found that bond saturation and NP size exert significant influence on the final grain size and densification. Most notably, grain density consistently increased with the number of double bonds. Additionally, the ligand containing a higher concentration of double bonds (*i.e.,* LOA) formed of comparatively larger CZTSSe grains. These results signify that the ligand used within synthesis, especially unsaturated ligands, serve an advantageous role during the NP sintering.

4.5. Preliminary and Future Works

4.5.1. Mechanism of the Ligand During Sintering

While this work has determined that LOA-based CZTS NPs exhibit superb grain growth, the underlying mechanism for this must still be explored. To understand how something as trivial as bond saturation can result in the observed differences in sintered film morphology, we tested two hypotheses: (1) the ligand desorption influences the rate of sintering and (2) the ligand operates as a fluxing agent which promotes grain growth.

4.5.1.1 Ligand desorption

During sintering, the initial step required for the necking (adjoining) of NPs is the desorption of the encapsulation layer (as discussed in **Chapter 1.1.3**). Therefore, the rate or temperature of ligand desorption influences early stages of the sintering process. As all encapsulation ligands in this work have an amine functional group, the strength of adhesion (lability) should be comparable across samples. However, the coordination or chelation of encapsulation ligands varies due to differences in the steric hindrance within the ligand backbone. (As discussed, as the number of double bonds increases, there will be more cross-linking with sulfur to form higher molecular weight polysulfides.[85,87,91,140,142,146,150,153,302,303]) Generally, chelated and bulkier ligands require more energy (*i.e.*, higher temperatures) and longer durations (*i.e.,* slow rate) to desorb from the surface.[115,116,199,304] Bulkiness and chelation also influence grafting density which may counter this effect, as large molecules with high steric bulk will have fewer anchoring groups per NP surface site.[115,116,199,304] To monitor the desorption of the different encapsulating ligands, we performed differential scanning calorimetry (DSC) on the CZTS NP samples.

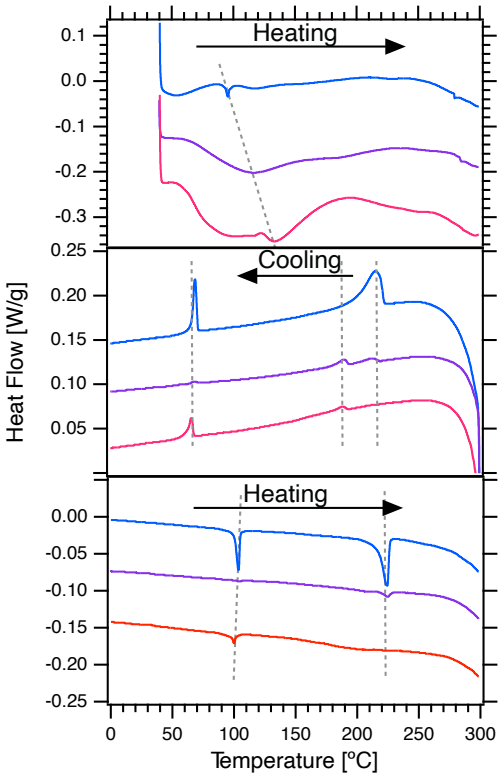

Figure 4.4. DSC of (blue) CZTS-DDA NPs, (purple) CZTS-OLA NPs, and (pink) CZTS-LOA NPs samples. The DSC cycle scan includes the **(a)** heating **(b)** cooling, and **(c)** re-heating of the NPs. Endothermic processes are negative (endo down).

From DSC of the NPs, during heating all samples experienced an endothermic process (which likely corresponds with either ligand desorption or NP melting)[305,306] that increased with the number of double bonds within the ligand backbone. The sintering mechanism of CZTS-OLA and CZTS-LOA initiating at higher temperatures is likely a result of increased ligand bulkiness and chelation due to the polymerization of alkenes (OLA) and, to a greater extent, dienes (LOA).[115,116,199,304] NPs were then cooled and reheated to determine the reversibility of this process. Upon the cooling of NPs, two exothermic processes (which likely corresponds to the crystallization of NPs)[305,306] occurred within the same temperature ranges across all samples (~60 °C, 180–220 °C). While it is unclear as to why two separate exothermic processes occurred, this

may be interpreted as the crystallization of NPs with different thermal stabilities (*i.e.,* phases, sizes). During the second heating run, the initially observed endothermic peak disappeared, indicating that an irreversible process occurred during the first heating cycle (such as ligand desorption). In place of ligand desorption during re-heating, two endothermic peaks are observed within the same temperature ranges across all samples (~100 °C, ~225 °C). These peaks correspond well with the observed crystallization peaks, suggesting that these endothermic peaks correspond with melting.

In summary, DSC shows that increasing the number of double bonds along the ligand backbone results in higher temperatures for ligand desorption, and thus, higher temperatures to initiate sintering. Despite higher temperatures being required for desorption, LOA samples had both superior grain size and densification when compared to DDA or OLA samples. This suggests that rapidly initiating the sintering process is not required to achieve enhanced morphology. Therefore, rather than influencing the initial rate of necking, the ligand is more likely to influence the rate or activation energy of densification and grain growth.

4.5.1.2 Ligands as a fluxing agent

In previous studies, poor coarsening and densification had been reported for bare NPs and NPs encapsulated by low molecular weight or volatile ligands, whereas robust grain growth had been reported for NPs capped with organic materials which have higher molecular weights and boiling points.[142,145,191] It may be possible that the encapsulation layer wets the NP surface and promotes ion diffusion, operating as a fluxing agent.[142,145] The critical attributes of these ligands as fluxing agents would be the their thermal stability (*i.e.,* what temperature ranges will these ligands be present) and their concentrations (*i.e.,* the relative mass of fluxing material present). To investigate these attributes, we look back at our TGA spectra of the polysulfides collected in

Chapter 3. Additionally, we consider the weight loss profiles of CZTS NPs capped with these ligands.

In **Chapter 3** we identified that the polysulfide's thermal stability increased with the number of double bonds along the ligand backbone, leading to a higher percentage of polysulfide remaining present at elevated temperatures. For example, 80 % of the polysulfide volatizes by ~200 °C (DDA-S), ~260 °C (OLA-S), and ~370°C (LOA-S). LOA-based CZTS NP samples experienced the greatest mass loss during heating ($\Delta Wt\%_{500\ ^\circ C}$ = 13.4 %), meaning that their encapsulation layer had both the greatest thermal stability and the greatest weight fraction (*i.e.,* higher mass of fluxing material). Other similarly sized NPs experienced less of a difference ($\Delta Wt\%_{500\ ^\circ C,\ DDA\ small}$ = 8.5 %, $\Delta Wt\%_{500\ ^\circ C,\ OLA}$ = 8.0 %,). The (larger) DDA particles had the lowest concentration of polysulfide ($\Delta Wt\%_{500\ ^\circ C}$ = 3.9 %), likely due to their comparatively lower SA/V.

The observed increase in thermal stability and weight fraction of the encapsulation agent (*i.e.,* the diene-based polysulfide) is consistent with the observed increase in densification and grain growth of corresponding films. A hypothesis for further study may be that the presence of the encapsulation agent is beneficial for ion diffusion, and once volatilized, further ion diffusion becomes limited.

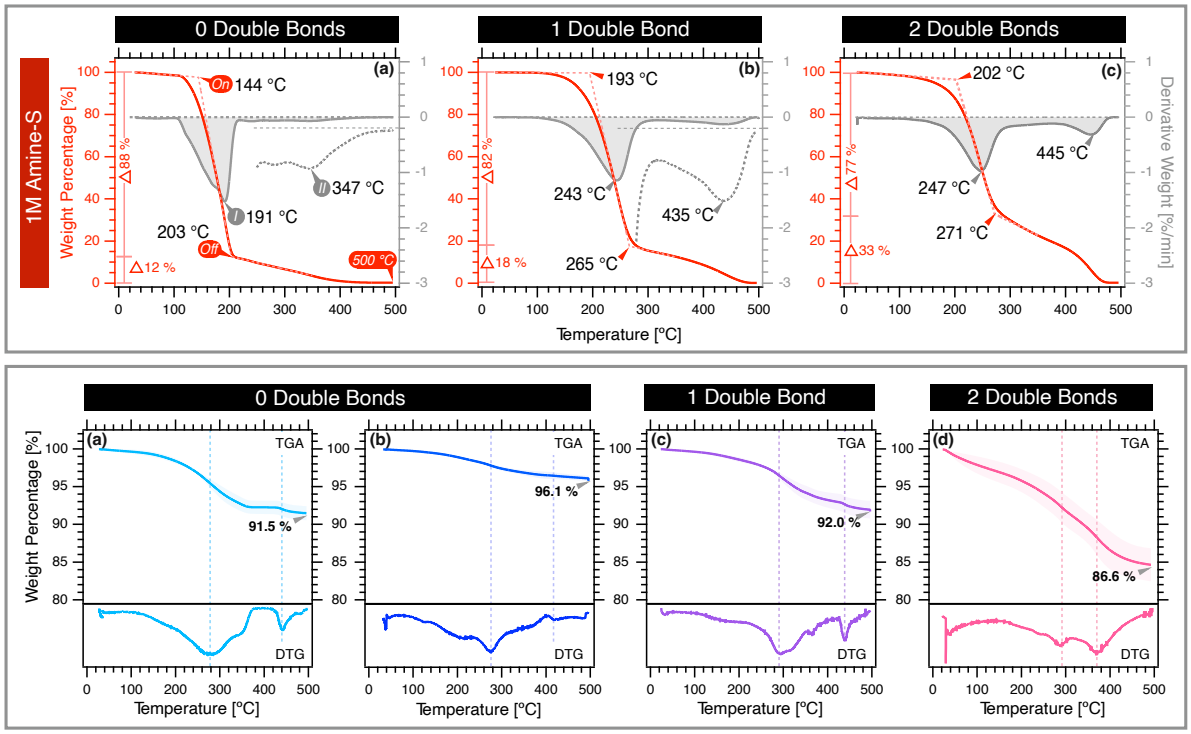

Figure 4.5. (**top panel**) TGA (red) and DTG (grey) spectra of the polysulfides made with **(a)** DDA, **(b)** OLA, and **(c)** LOA (all 1 M ligand-S solutions). (**bottom panel**) TGA and DTG spectra of CZTS NPs. Samples include **(a)** CZTS-DDA *small* NPs, **(b)** CZTS-DDA NPs, **(c)** CZTS-OLA NPs, and **(d)** CZTS-LOA NPs.

4.5.1.3 Ligands as a source of sulfur flux

Within our sintering methods, selenium is used as a fluxing agent that promotes the diffusion of ions. Sulfur and reactive sulfur gases can also be used in this fashion to sinter and react with NPs.[87,307] During sintering, it is likely that the polysulfide encapsulation agent decomposes and excess sulfur (*e.g.,* H_2S) from the polysulfide contributes to grain growth as a fluxing agent.[150,247] Due to the additional cross-linking between sulfur and alkenes, we expect the concentration of sulfur within the polysulfide to increase with the number of double bonds (confirmed in **Chapter 4.6.1** *via* XPS). To directly examine if the sulfur within the polysulfide contributes to grain growth, two methods were used (herein on only with CZTS-OLA samples).

First, we attempted to alter the carbon and sulfur concentrations of the capping ligands through both ligand stripping and exchange. This included stripping surface ligands from the CZTS NPs until they became unstable, and then finally redispersing the bare NPs with either the pure OLA ligands or a 2 M sulfur OLA mixture (high sulfur concentration). After selenization, there was no quantifiable difference in grain size across samples (reference NPs, bare NPs, and NPs capped with pure OLA or 2 M OLA-S). However, the effectiveness of the ligand exchange method is uncertain and it may be worthwhile to repeat in future works. For data from these experiments and additional discussion, see **Chapter 4.6.2**.

Our second method was to mix in excess OLA, polysulfide (OLA-S), or elemental sulfur into the NP ink prior to deposition, allowing us to systematically control the carbon and sulfur content within CZTS NP films. Here, we observed no difference in grain growth (**Figure 4.6**) for samples mixed with OLA or a 2 M OLA-S mixture, indicating that neither the ligand or nor polysulfide is operating as a fluxing material. While we incorporated the same *wt%* of material into each ink (15 *wt%*), for stronger conclusions, higher concentrations of OLA and 2 M OLA-S should be tested to confirm that there is indeed no effect of incorporating OLA or polysulfide into the NC ink. Additionally, it would be interesting to repeat this type of experiment with 2 M LOA-S, allowing for better comparison between OLA and LOA samples.

Promisingly, by simply adding in 15 *wt%* of elemental sulfur to the NP ink prior to deposition, a 20 % increase in grain size was achieved. This preliminary work shows that incorporating a small amount of fluxing material (elemental sulfur) into the NP ink may be a promising and simple approach for achieving larger grains.

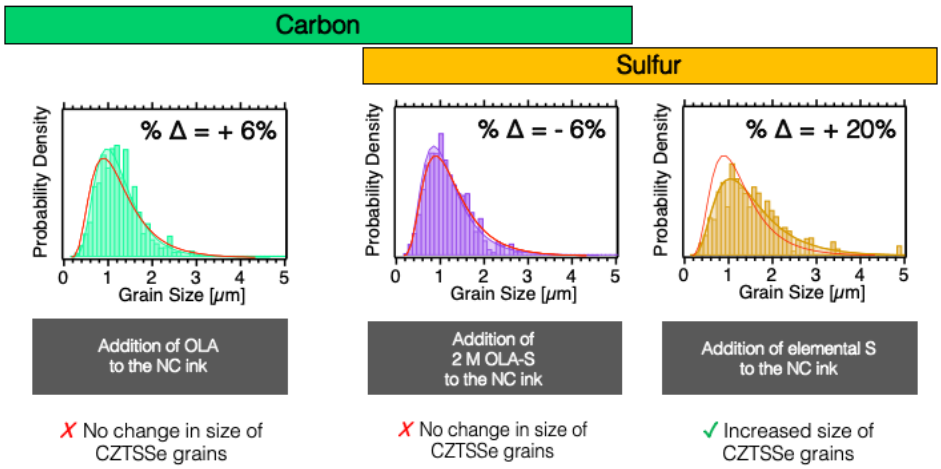

Figure 4.6. Grain size distribution of selenized films of synthesized CZTS NPs (red reference line in all spectra corresponds with standard CZTS NPs from **Figure 4.16**, which has a of d_{avg} = 0.94 μm and of d_{med} = 0.84 μm). From left to right: the same sintered CZTS NPs with 15 *Wt%* of OLA added to a 200 mg/mL NP ink (d_{avg} = 1.0 μm, d_{med} = 0.94 μm), with 15 *wt%* of 1 M OLA-S added (d_{avg} = 0.88 μm, d_{med} = 0.81 μm), and 15 *wt%* of elemental S added (d_{avg} = 1.13 μm, d_{med} = 1.03 μm).

4.5.2. Effect of Grain Size and Density on CZTSSe Electrical Properties

Theoretically, larger and denser grains should result in overall enhanced performance for CZTSSe photovoltaic devices. This is due to surfaces and interfaces, such as grain boundaries, operating as recombination sites for optically generated excited electrons.[308] As such, based off our observations from **Figure 4.3.**, we would expect the conductivity of LOA based films to be greater than that of OLA. To calculate conductivity (σ) on a subset of samples, we used a 4-point probe to measure series resistance (R) and profilometer to measure the sample's average film thickness (L). Across each sample, the area (A) is a constant (the contact surface area of the 4-point probe).

$$\sigma = \frac{L}{R * A} \qquad \textbf{(Eqn. 4.2)}$$

Table 4.2. Average resistance and thickness of different OLA and LOA samples

CZTSSe - OLA	Resistance [Ω]	Thickness [μm]	$\sigma * A * 10^{-4}$ [cm·Ω^{-1}]
S5	0.19 ± 0.01	0.59 ± 0.29	3.14
S6	0.31 ± 0.02	0.88 ± 0.32	2.86
S7	1.28 ± 0.07	1.31 ± 0.15	1.34
S8	0.56 ± 0.03	1.76 ± 0.10	3.14

CZTSSe - LOA	Resistance [Ω]	Thickness [μm]	$\sigma * A * 10^{-4}$ [cm·Ω^{-1}]
S2	0.36 ± 0.02	1.56 ± 0.03	4.31
S9	1.22 ± 0.13	1.84 ± 0.05	1.51
S10	0.27 ± 0.01	1.09 ± 0.27	4.05
S11	0.39 ± 0.05	1.27 ± 0.51	3.29
S12	1.00 ± 0.03	1.92 ± 0.05	1.92

While it appears that CZTSSe films with LOA can achieve higher conductivities (σ_{LOA} = 3.02/A * 10^{-4} cm·Ω^{-1}, σ_{OLA} = 2.62/A * 10^{-4} cm·Ω^{-1}), the error for both samples is too high to make any overarching conclusions. To further investigate, we characterized each film on a sample-by-sample basis.

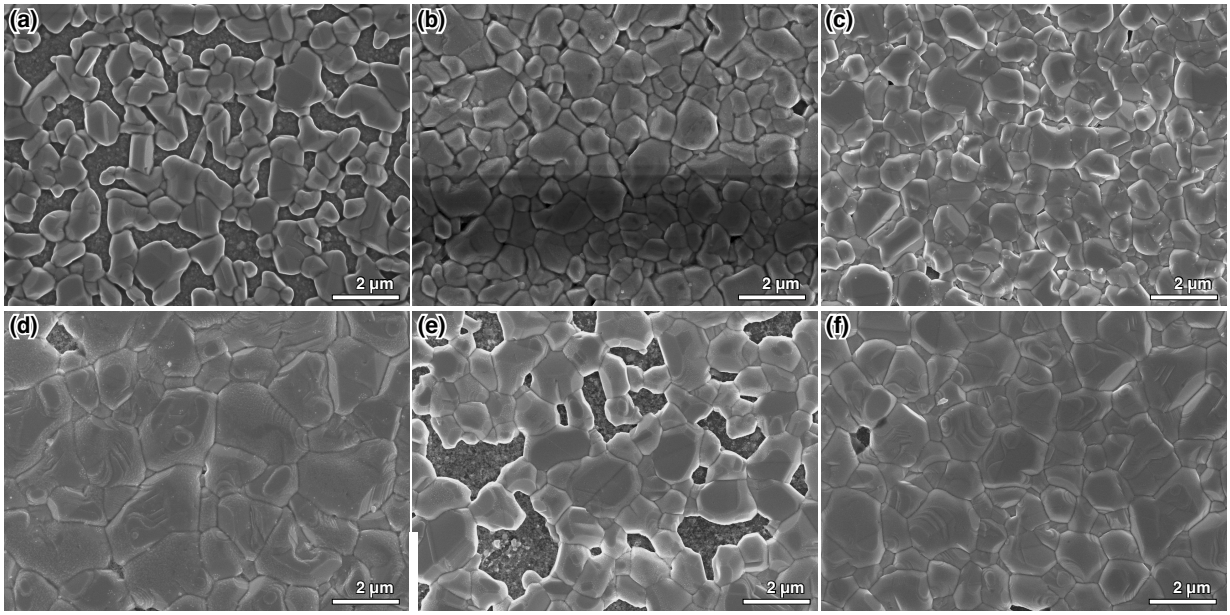

Figure 4.7. A subset of SEM CZTSSe micrographs from OLA synthesized CZTS NPs: samples **(a)** S5, **(b)** S6, and **(c)** S8. A subset of SEM CZTSSe micrographs from LOA synthesized CZTS NPs: samples **(d)** S2, **(e)** S9, and **(f)** S10 (scale bar 2 μm).

Table 4.3. Relationship between resistance and morphology

CZTSSe - OLA	$\sigma * A * 10^{-4}$ [cm·Ω^{-1}]	d_{avg} [µm]	ρ_G [%]
(a) S5	3.14	0.81	91.8 %
(b) S6	2.86	0.66	99.9 %
(c) S8	3.14	0.65	99.9 %

CZTSSe - LOA	$\sigma * A * 10^{-4}$ [cm·Ω^{-1}]	d_{avg} [µm]	ρ_G [%]
(d) S2	4.31	1.45	99.1 %
(e) S9	1.51	1.00	86.8 %
(f) S10	4.05	1.19	99.0 %

From these measurements, there is considerable variation across samples with again, no distinct trend. The only consistency is with our observations from **Figure 4.3**, where for all LOA samples, the grain size was larger than OLA samples even in regions with a lower ρ_G. However, these larger grain sizes did not directly correlate with enhanced electrical properties. While these results affirm that LOA-based films results in larger grain sizes, a considerably larger set of samples should be characterized for more accurate determination of its impact on electrical properties. Additionally, further work can be done to decouple or correlate or the influence d and ρ_G independently have on σ.

4.5.3. The Fine Grain Layer

The organic ligands are critical for the suspension of NPs in solvent, and their subsequent deposition. However, during sintering, these ligands are carbonized into a graphitic fine-grain-layer (FGL) while the nanomaterials grow into large grains. We see that from **Chapter 2**, this carbon rich FGL is already present prior to sintering due to the settling of graphitic flakes which are produced during nanomaterial synthesis.

The effect of the FGL on CZTSSe PV device properties has been explored. To assess the FGL's impact on final device performance, researchers varied the thickness of both the large-

grain-layer (LGL) and FGL.[140] When modulating the FGL thickness, as long as the LGL's thickness remained constant, no changes in performance were observed.[140,141] However, when increasing the LGL thickness, the performance of PV devices also increased, indicating that the LGL alone drives device performance.[141] Therefore, it is ideal to convert most of the NP film into a LGL. As the ligand influences the grain diameter and densification of the LGL, we also wanted to observe if the ligand influences the LGL thickness. Additionally, it is theorized that the FGL is not a detriment to device performance due to the structure of the carbonized material (*i,e.,* graphitic), so we additionally assessed the structure of the FGL for both OLA and LOA-based CZTSSe samples.

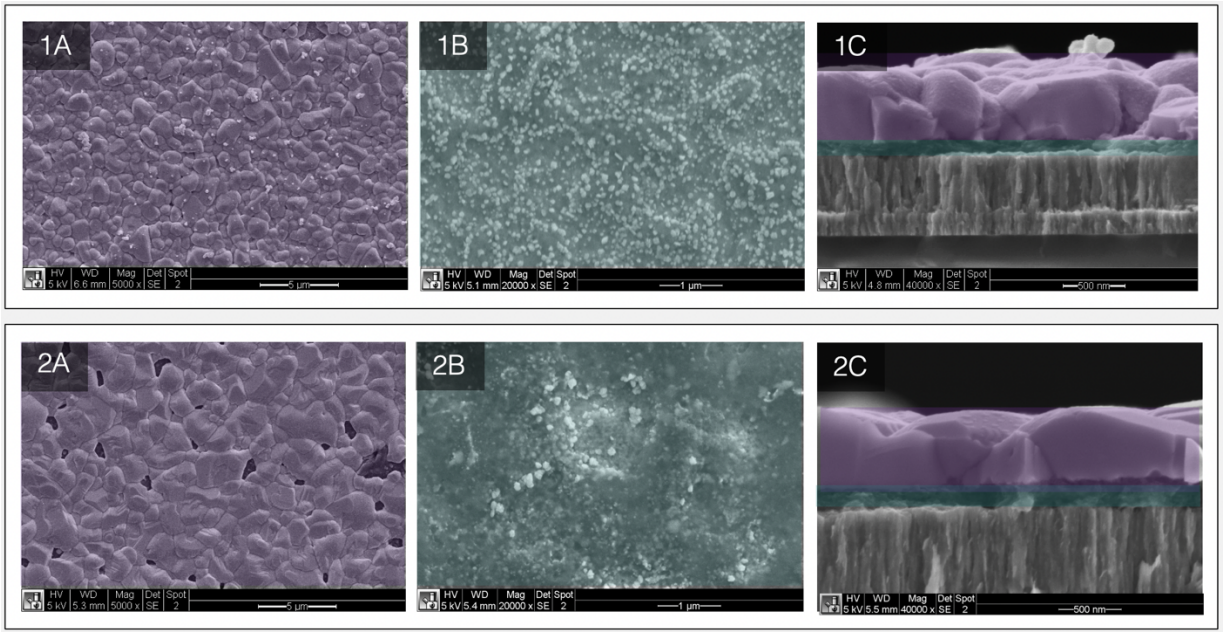

Figure 4.8. A look at the morphology of CZTSSe films including the large grains (purple) and fine grain layer (blue). (**1A-1C)** are micrographs of OLA-based films, and (**2A-2C)** are micrographs of LOA-based films.

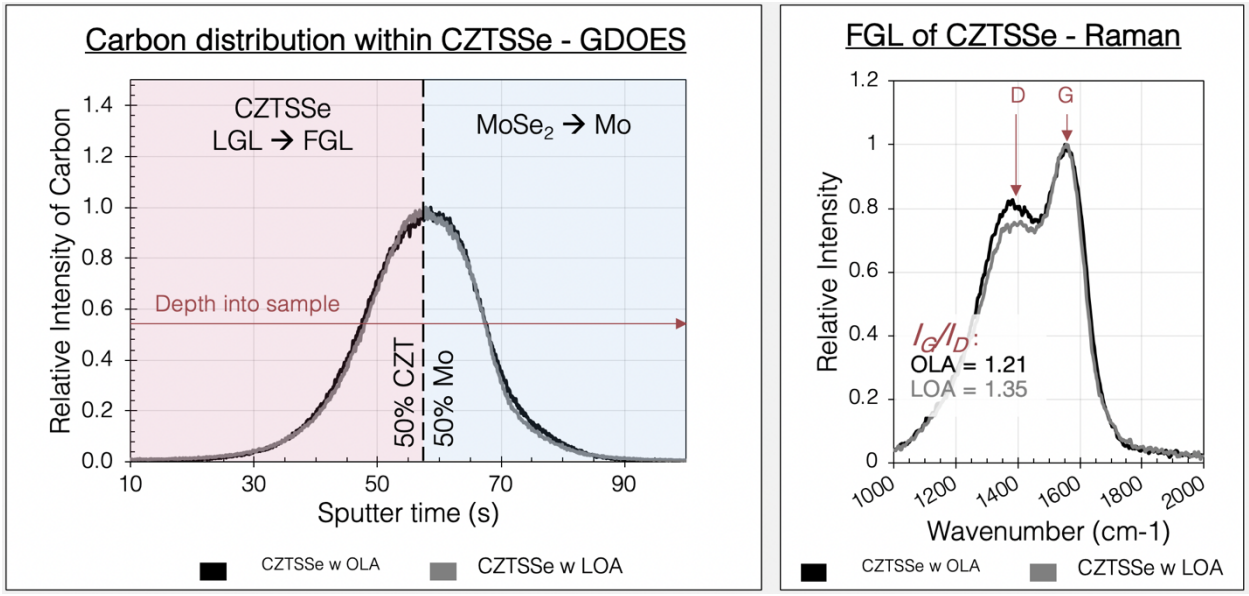

Figure 4.9. A closer look at the FGL: **(a)** GDOES spatial carbon composition profile through the CZTSSe films of for films with both OLA and LOA based ligands. **(b)** Raman spectra collected on an exfoliated CZTSSe film, where only the FGL was exposed.

While it would be ideal to observe a change in thickness ratio between the LGL and FGL, from SEM the LGL:FGL was consistent across CZTSSe-OLA and -LOA samples. From GDOES and Raman spectroscopy, we see further remarkably similar properties (carbon distribution, structure) of the FGL across both OLA- and LOA-based films. Thus, it appears that the morphological changes due to the organic ligand are confined to the grain size (diameter) and densification.

4.5.4. Suggestions for Future Works

4.5.4.1 Quantifying activation energy and the grain growth mechanism

In order to succinctly determine the mechanisms occurring during the growth, temporal studies should be conducted. By collecting datasets of images at interval times (*e.g,* 1 min, 5 min, 10 min, 15 min, *etc*.), we can better observe and contrast the stages of the sintering process (*i.e.,*

initial necking, coarsening/densification, and finally growth) for each specimen. By extracting the average grain size (***d***) and densification ($\boldsymbol{\rho_G}$) as a function of time, we can calculate and quantify significant information, such as the rate of densification and grain growth and the activation energy of grain growth.[79,80] Based off of these values, information such as the likely mechanisms and stages of grain growth can be determined.[79,80] These temporal measurements would assist in better comparing the impact each ligand has on the growth of large grains.

4.5.4.2 Grain size analysis

A major limitation of this project was the rate of processing micrographs. With current methods, rapid photo processes can be used to assist with grain boundary identification, however, to avoid gaps in boundaries and reduce noise, a final step of tracing grain boundaries by hand is necessary for high accuracy. This process is extraordinarily time consuming and limits the number of spots that can be characterized.

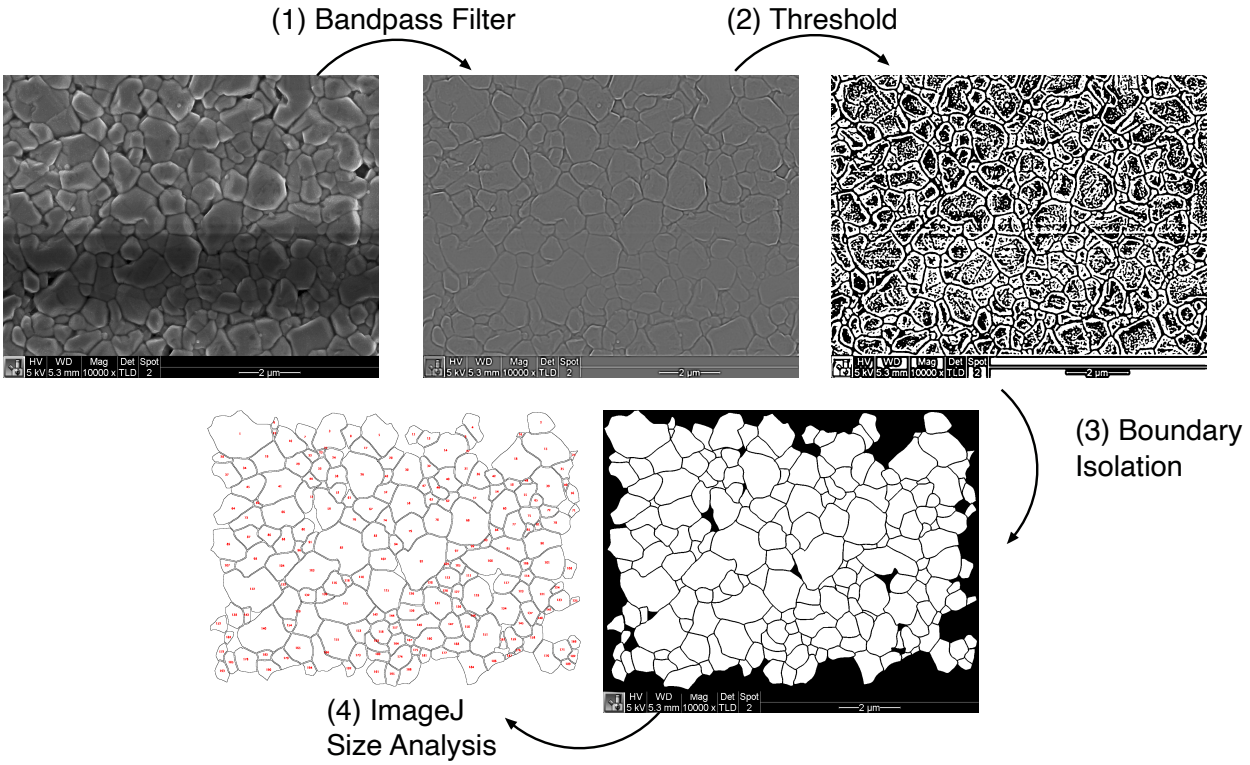

Figure 4.10. Current method of grain size quantification for SEM micrographs.

Switching to automatic methods to quantify grain size would be ideal. Electron backscatter diffraction (EBSD) is one suggested method. EBSD generates a 2D map of the crystallographic orientation of the microstructure, making EBSD a powerful tool for instantaneous grain size analysis. A current challenge of using EBSD is that atomically flat surfaces are required. Early attempts of polishing CZTSSe films were too aggressive, resulting in poor morphology. Ion milling may be a more fruitful method of eliminating surface roughness.

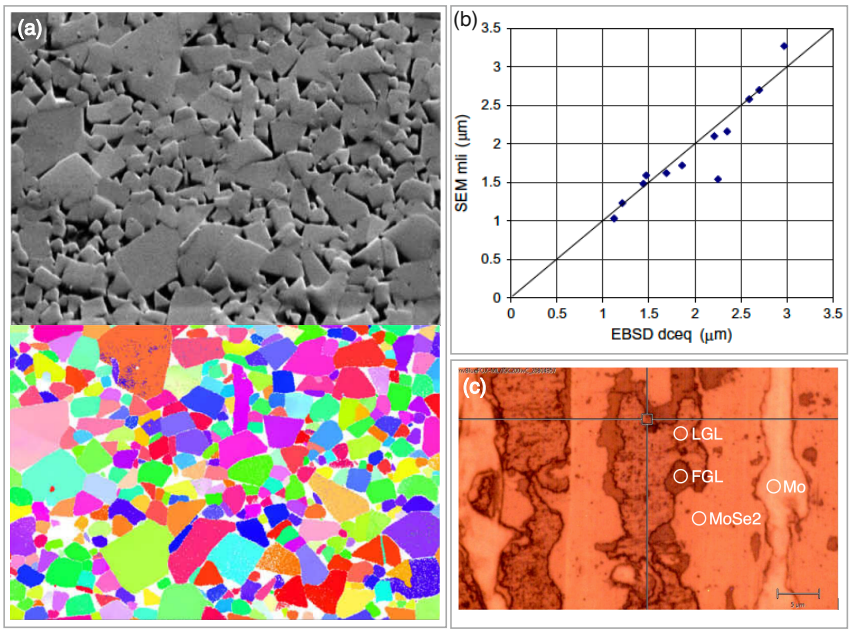

Figure 4.11. (a) Micrograph and corresponding diffraction pattern collected via EBSD from ref X,[309] **(b)** Comparison of grain size from SEM and EBSD from Ref 302,[309] and (b) initial preliminary attempts of using a bevel to polishing the surface of CZTSSe films.

4.6. Supporting Information

4.6.1. Additional Compositional and Structural Characterizations

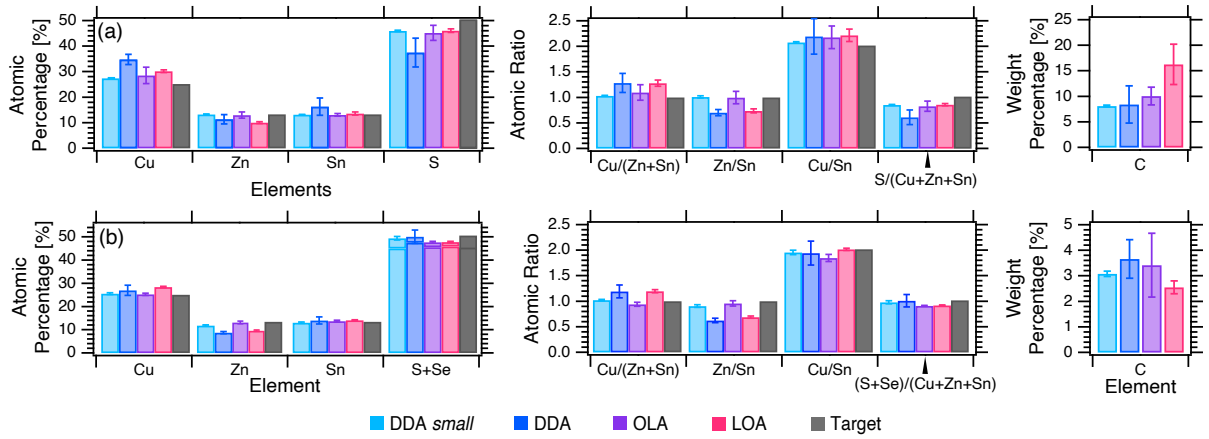

Figure 4.12. EDS of all **(a)** CZTS and **(b)** CZTSSe samples.

EDS was used to further compare the composition of each nanomaterial and was used to analyze the sample's sulfur and carbon content. If sulfur (and carbon) within the polysulfide does increase with the number of ligand double bonds, the composition should follow a trend of increasing [S/(Cu + Zn + Sn)] and [C]. While there is an increase in [C] with the number of double bonds, EDS data in **Figure 4.12** shows that the [S/(Cu + Zn + Sn)] ratios are consistent across all samples, excluding the larger DDA NPs which have a lower [S/(Cu + Zn + Sn)]. This may be a result of lower SA/V of larger particles, diminishing the concentration of surface C and S relative to the concentration of internal CZTS. Otherwise, similarities within S concentration across ligand type may be attributed to the consistent concentrations of sulfur used in the NP syntheses; within synthesis the sulfur concentration was restricted to be stoichiometric with the metal precursors. Since the EDS concentration of sulfur does not detail how the sulfur is bonded, high resolution C 1s and S 2p XPS scans were used to distinguish kesterite sulfur bonding from crosslinked sulfur.[310]

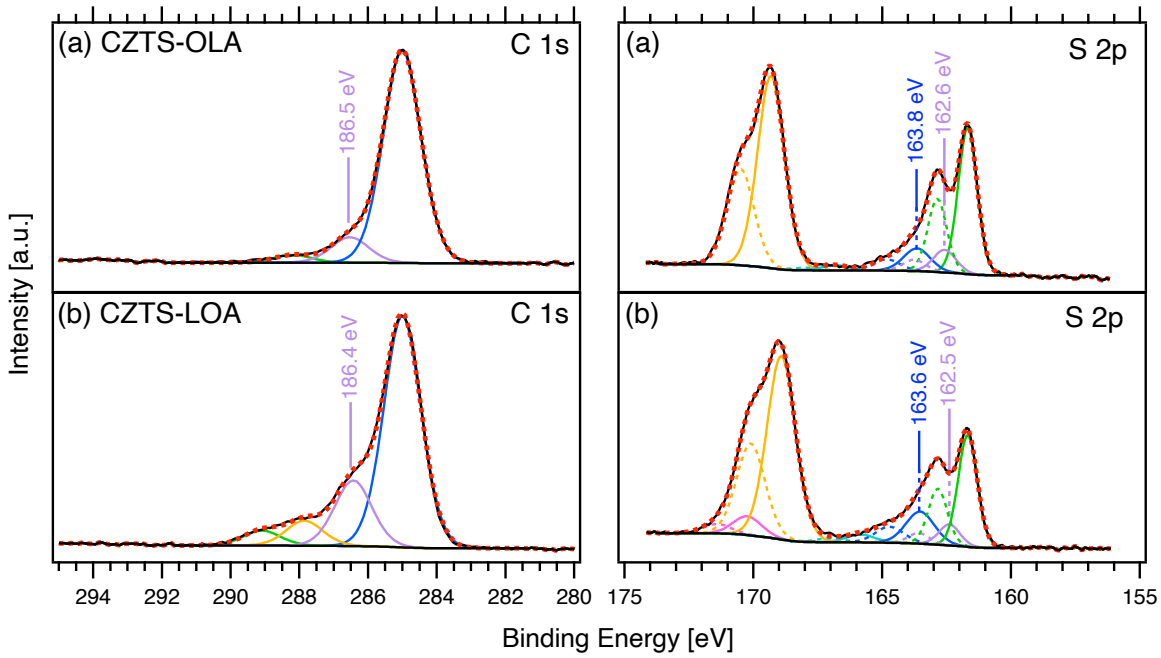

Figure 4.13. Surface XPS scans of the C 1s region and the S 2p region of CZTS NP thin films synthesized with **(a)** OLA and **(b)** LOA. To emphasize polysulfide dependent bonding, on the C 1s scan, the C-S bonding region is highlighted, and on the S 2p scan, the central and terminal S polysulfide bonding regions are highlighted. On the S 2p scans, S $2p_{3/2}$ are fit by solid lines, and corresponding S $2p_{1/2}$ are fit by dashed lines of the same color.

Table 4.4. Surface XPS scans of the C 1s region and the S 2p region of CZTS NP thin films. Each scan is the average of 2 spots/sample. Binding modes associated with the polysulfide/ligand are bolded.

Sample	Sulfur chemical state	S $2p_{3/2}$ (eV)	% Concentration	Carbon chemical state	C 1s (eV)	% Concentration
CZTS – OLA	Sulfide (S^{2-})	161.7	29.7 %	**C-C sp3**	**285.0**	**86.6 %**
	Polysulfide (terminal S)	**162.6**	**6.4 %**	**C-O/C-S**	**286.5**	**10.6 %**
	Polysulfide (central S)	**163.8**	**6.5 %**	**C=O**	**288.1**	**2.9 %**
	Sulfite (SO_3^{2-})	166.7	1.5 %			
	Sulfate (SO_4^{2-})	169.3	54.1 %			
	Sulfate (SO_4^{2-})	170.9	1.7 %			
CZTS – LOA	Sulfide (S^{2-})	161.7	25.2 %	**C-C sp3**	**285.0**	**69.8 %**
	Polysulfide (terminal S)	**162.5**	**5.3 %**	**C-O/C-S**	**286.4**	**19.2**
	Polysulfide (central S)	**163.6**	**8.8 %**	**C=O**	**287.8**	**6.7 %**

	Sulfite (SO_3^{2-})	166.0	2.1 %	**O-C=O**	**289.0**	**4.3 %**
	Sulfate (SO_4^{2-})	168.9	54.2 %			
	Sulfate (SO_4^{2-})	170.3	2.1 %			

From XPS, we observe little difference in sulfide-, sulfite-, and sulfate-based bonding, which would primarily correspond with the metal-based bonding of S in CZTS.[310] However, there is a slight increase in the total polysulfide contribution for the LOA sample (14.2 % for LOA, 13.0 % for OLA). More significantly, there were changes to the ratio between internal and terminal S of the polysulfide: the OLA sample has approximately a 1:1 ratio, whereas the relative amount of central sulfur (S-S-S) to terminal S increased to 1.64:1. This suggests there is overall more S-S-S bonding within the polysulfide of LOA samples. Additionally, the C-S bonding was a substantially increased for LOA samples (19.2 %) over OLA samples (10.6 %). These XPS results indicate that there is indeed a higher S content within the LOA polysulfide which encapsulates the CZTS NPs.

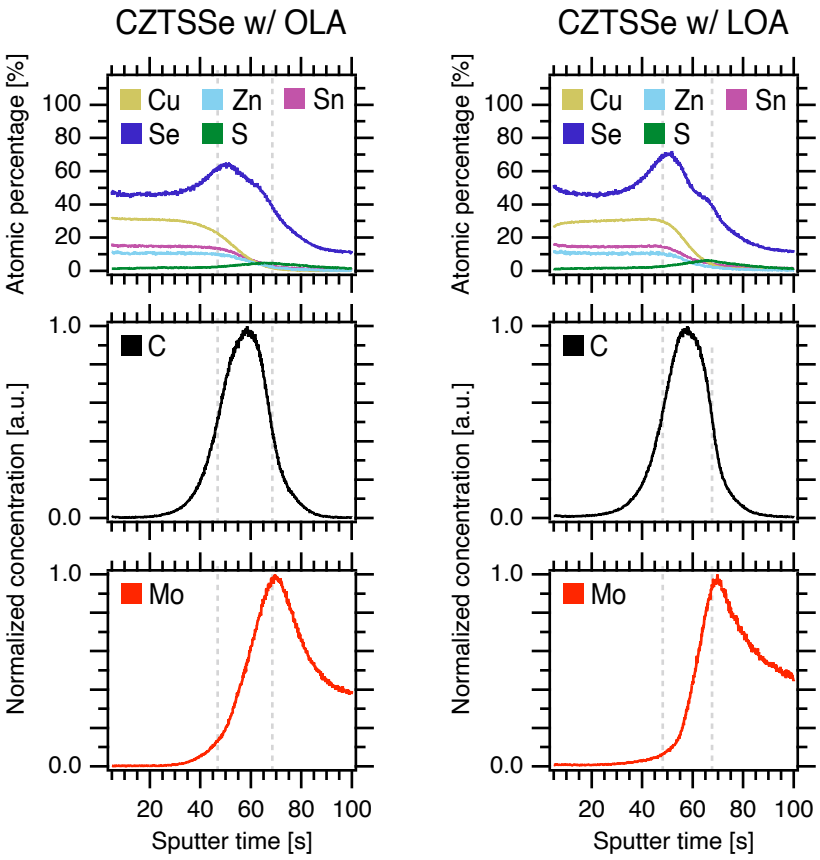

Figure 4.14. (a) Full GDOES composition profile for CZTSSe films with both **(top)** OLA and **(bottom)** LOA based ligands. The dashed lines signify different regions in the film (LGL, FGL, substrate).

4.6.2. Ligand Exchange

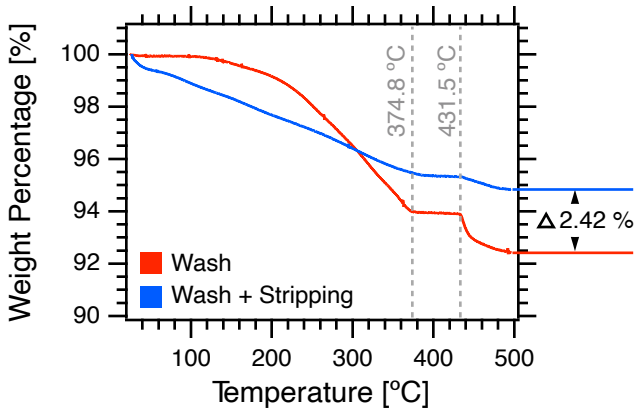

Figure 4.15. TGA of CZTS NPs washed 2 X after synthesis (standard washing procedure) compared to the same washed NPs after stripping, prior to ligand exchange.

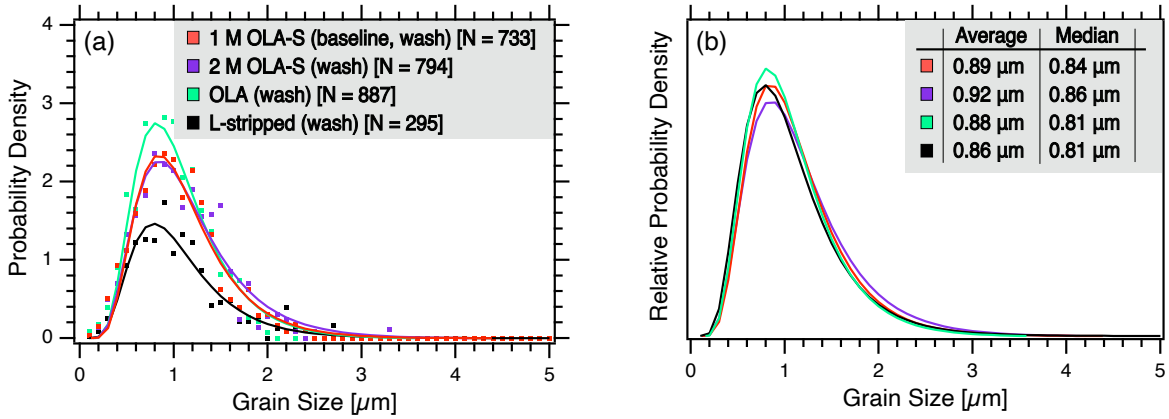

Figure 4.16. Grain size distribution of the standard NP reaction (1 M OLA-S), the same NPs after stripping (L-stripped), and rewashing with either pure OLA (OLA) or a 2 M OLA-S solution (2 M OLA-S). **(a)** The overlayed probability distribution of each sample. **(b)** Same distributions normalized to the area of the fit curve. Sample sizes, d_{avg}, and d_{med} are reported.

Chapter 5: Summary and Future Directions

5.1. Summary

In **Chapter 2**, we investigated the thermal decomposition and restructuring of OLA ligands using a combination of TGA, Raman spectroscopy, and XPS, seeking to determine the specific nature of OLA's decomposition and its ultimate incorporation into a carbon-rich fine-grain layer in CZTSSe systems. OLA is identified to decompose into nanostructured graphitic carbon, first being detectable immediately after the Cu_2ZnSnS_4 (CZTS) NP synthesis (at 225 °C), forming when CZTS was synthesized with (1) acetylacetonate and (2) chloride precursors. These graphitic flakes are identified as defective graphene oxide, which segregates from OLA-capped NPs during deposition to assemble into the carbon-rich layer which, prior to this work, was detected only after the sintering of CZTS NPs at 500 °C.

In continuation of **Chapter 2**, **Chapter 3** expands upon this investigation by studying the thermal decomposition of common ligands with varying functional groups (amines and carboxylic acids) and bond saturations (from saturated to polyunsaturated). We investigated how these ligand properties influence decomposition in absence of and in the presence of precursors used in NP synthesis. Notably, increasing the number of double bonds along the ligand backbone resulted in higher degrees of decomposition, and, graphitization is achieved from the pyrolysis of polymerized

(polysulfide) ligands. This pyrolysis occurs in the absence of metal precursors at temperatures which exceeds nanoparticle synthesis, signifying that metal precursors or the resulting nanoparticles contribute to the decomposition of ligands during synthesis at 225 °C. During the synthesis of inorganic chalcogenide NPs with oleylamine and metal acetylacetonate and sulfur precursors (Cu_2ZnSnS_4, Cu_xS, and SnS_x), the ligand pyrolyzes, producing alkylated graphitic species while there was less to no ligand decomposition during the sulfur-free synthesis with metal acetylacetonate precursors (ZnO, CuO).

Between **Chapter 2** and **Chapter 3**, we hope these results will help guide ligand selection for high temperature (≥ 225 °C) NP syntheses and improve upon reaction purity, an important consideration in many applications.

Furthermore, while the ligands used during syntheses are critical for effective deposition, post-thermal treatments (sintering) of the NP films reveal that ligand selection influences the NP grain growth and densification. In **Chapter 4**, we synthesize metal-chalcogenide CZTS NPs using ligands of varying bond saturation to tailor the morphology of sintered NP films. SEM micrographs results reveal that capping ligands with more unsaturated bonds assist in the growth and densification of CZTS upon sintering in an inert, selenium-rich environment. This is valuable as the ligands used in synthesis can be used to tailor post-processing, and thus the film's final properties.

Holistically, this work is a steppingstone in redefining the ligand's roles during both synthesis and sintering.

5.2. Future Directions

5.2.1. Mitigating Ligand Decomposition

In **Chapter 2**, we were able to partially isolate the graphitic impurities through washing. However, after 3 washes, the carbon impurities were not fully removed. With subsequent washing, capping ligands that anchored to the NC are stripped, reducing the materials ability to be suspended in solvent and redispersed for deposition. Therefore, alternative avenues for reducing these carbon impurities should be explored.

As the formation of these graphitic materials is contingent on the thermal decomposition of the ligands, it is plausible that reducing the reaction temperature can entirely circumvent ligand decomposition during nanomaterial synthesis. All nanomaterials made in this work were synthesized at 225 °C, a critical temperature for producing kesterite CZTS, as lower reaction temperatures will not yield in the desired targeted structure.[9] However, many nanomaterials can be synthesized at temperatures well below 225 °C. For example, in this work we additional synthesized Cu_xS, CuO, ZnS, and SnS NPs, which can be produced at lower temperatures (*e.g.,* room temperature – 200 °C),[107,108,295,301,311] where thermal decomposition may be mitigated. Thus, it is important to define the temperature ranges in which ligand decomposition can occur.

Additionally, in **Chapter 2** and **3**, we considered how precursor selection (*e.g.,* acetylacetonate *v* chloride, chalcogenide materials *v* sulfur free materials) influences the observed ligand decomposition. As outlined in this work, a combination of TGA and structural characterizations (*i.e.,* Raman Spectroscopy and FTIR, ^{1}H NMR, or XPS) can be effective in investigating the decomposition of ligands in either the presence or absence of precursors. While this work studies alkylamines and alkyl carboxylic acids, additional ligands (*e.g.,* phosphines, thiols) have yet to be studied and are relevant to nanomaterial syntheses. Future works may also

include investigating additional precursors of different structure and different elements. This includes alternatives to metal acetylacetonate and metal chloride precursors (*e.g.,* metal nitrates, metal acetates), sulfur precursors (*e.g.,* thiols, thiourea), and investigating new elements (*i.e.,* any element in addition to the Cu, Zn, Sn, and S). To this extent, there is a significant library of ligands and precursor materials to explore. In expanding the library of materials, researchers may establish a comprehensive and wholistic mechanism of *in situ* ligand decomposition. This would allow for the mitigation of ligands decomposition during nanomaterial synthesis.

5.2.2. Leveraging Ligand Decomposition

While carbon impurities may be undesirable, structured carbon (*e.g.,* graphene, graphite, carbon dots, carbon nanotubes, graphene nanodots, *etc.*) can hold desirable luminescent and conductive properties. More characterization (*e.g.,* UV-Vis, photoluminescence, 4-point probe) can determine additional functional properties of the carbon impurities. As it is apparent that the detected carbon impurities has a similar structure (see **Chapter 2** and **Chapter 3**), it is plausible that these impurities have useful functional properties and can be used in hybrid nanomaterials (inorganic-organic nanocomposites) systems.[186] Hybrid nanomaterial systems have been explored in several applications (*e.g,* carbon dot-silica NP nanocomposites are used in biosensing and theragnostic applications, PtCo NPs encaged in graphene as catalysts for fuel cell applications).[312,313]

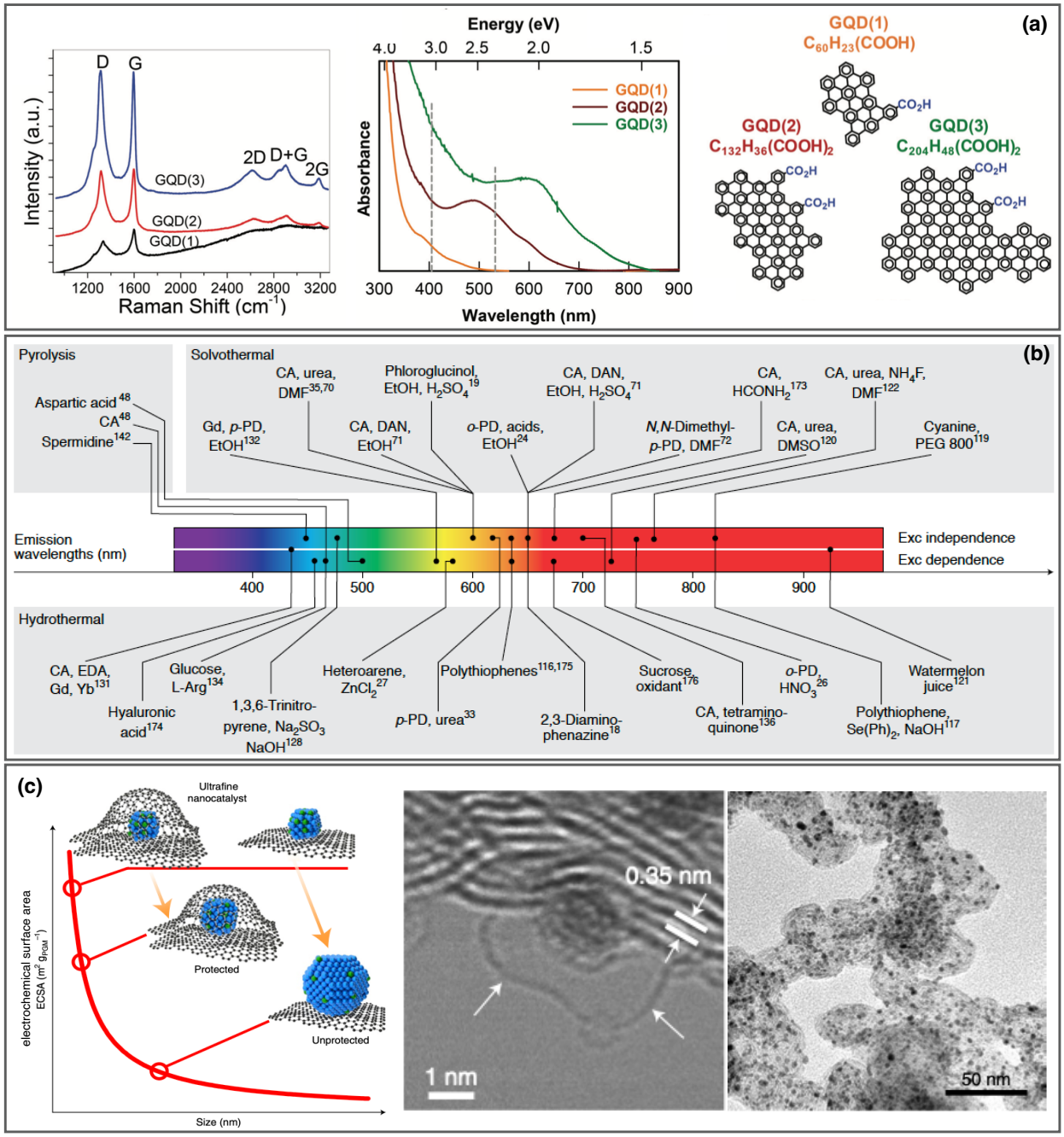

Figure 5.1. (a) Raman spectroscopy and UV-Vis of carbon dots of differing structure from Ref [314].[314] **(b)** Emission from carbon dots produced through a variety of methods from Ref [315].[315] **(c)** Example of engineered hybrid NP-structured carbon composite for fuel call applications from Ref [313].[313]

To intentionally produce hybrid nanomaterial systems, good candidates for *in-situ* organic precursor decomposition should be revisited. For example, citric acid is used as a reducing agent during synthesis of metal nanomaterials (room temperature to ˜60 °C).[316,317] Citric acid is also used as a precursor for the pyrolysis and carbonization of graphene quantum dots (200 °C).[186,315,318] It is plausible that the carbonization of citric acid will occur during the synthesis of nanomaterials at elevated temperatures (~ 200 °C), resulting in the intention production of GQD in tandem with nanomaterials.

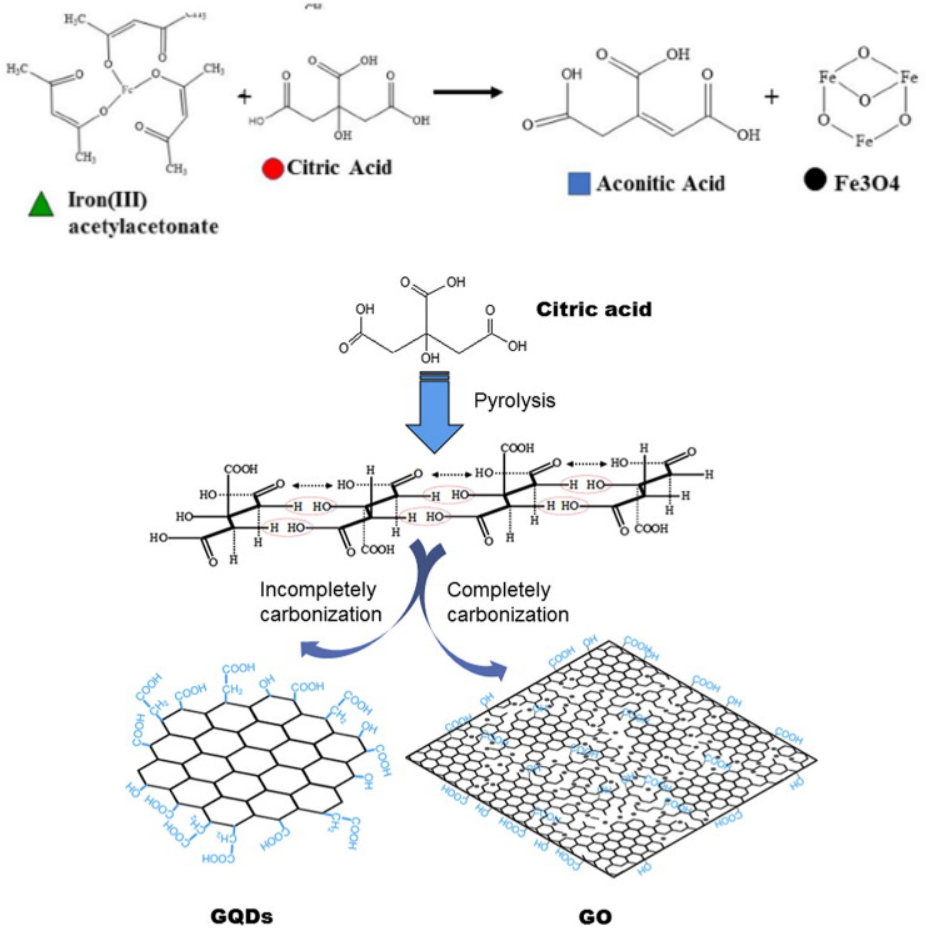

Figure 5.2. (top) Synthesis of Fe_3O_4 NPs with citric acid as a reducing agent at 200 °C from Ref [319],[319] and **(bottom)** Pyrolysis and carbonization of citric acid into graphitic material at 200 °C from Ref [318].[318]

Additionally, Ni and Cu foils have been used as catalysts for the production of graphene sheets from fatty acids (*i.e.,* unsaturated carboxylic acids) at high temperature (≥ 800 °C).[291,320] Using smaller molecules (*e.g.,* C_2H_4) can lower the temperature of graphene production of Ni and Cu foils (500 °C), and using nanoparticles can once again reduce the temperature of nucleating and growing graphitic material (300 – 500 °C). For example, metallic (*e.g.,* Fe, Co, Ni) and bi-metallic (*e.g.,* Fe–Ni, Fe–Ni, Ni–Co, Ni–Pd,) NP catalysts can be used to grow carbon nanotubes (CNTs) at 300 – 400 °C when using small molecule hydrocarbons are the carbon source (*e.g.,* C_2H_4, CH_3OH, C_2H_5OH).[291,320]

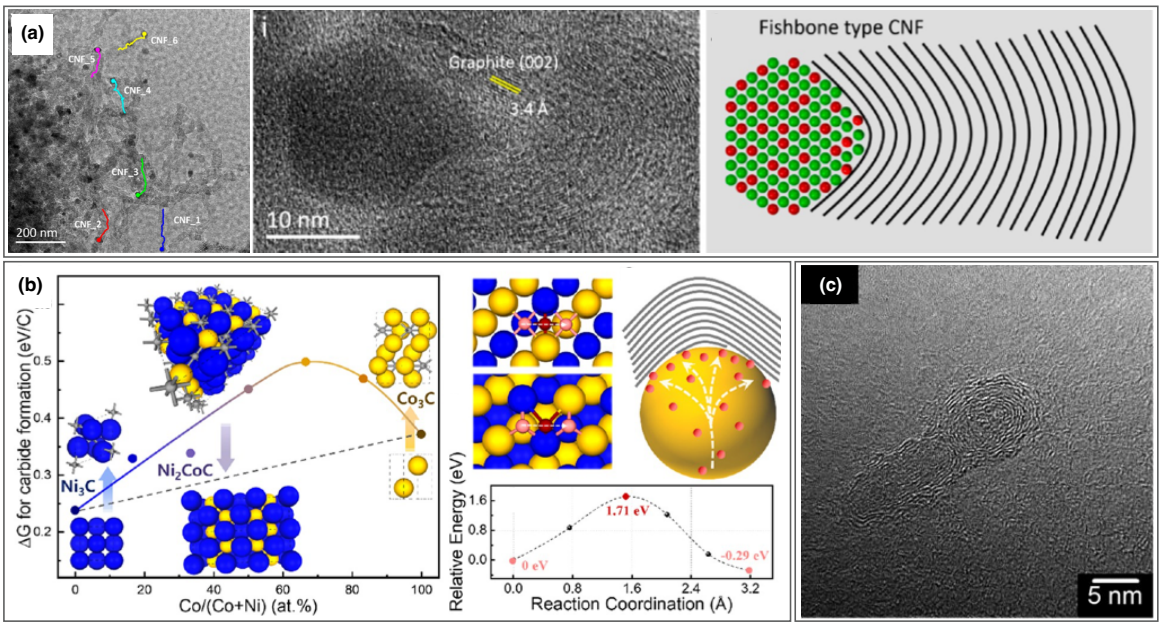

Figure 5.3. CNT's catalyzed by a Ni–Co alloyed NP at 550 °C from Ref [321]. Through **(a)** TEM observations and **(b)** DFT, here it is predicted that C_2H_4 is dissociates at the catalysts surface, C atoms diffuse through the bulk of the NP, and is nucleated into the carbon lattice.[321] Here, the NPs act as a catalyst and template for the nucleation and growth of structured carbon. **(c)** An example of fullerenes/nanosoot particles catalyzed by a Ni–Fe NPs from C_2H_4 at 300 °C from Ref [322].[322]

We see that many of the nanomaterial was used in this study (CZTS, Cu, Zn, Sn, CuS, ZnS) have catalytic properties which may contribute to decomposition. While we do not expect that our

particles are forming fishbones CNT under our reaction conditions (review **Scheme 2.1**), these NPs may be candidates for CNT nucleation and growth at higher temperatures. Additionally, as fatty acid ligands are used as the carbon precursor for graphitic materials at high temperatures,[187,291] these ligands may be a viable source of carbon for CNT production at decomposition temperatures. In these future works, in-situ TEM experiments and DFT would be useful tools for further understanding the *in-situ* decomposition of ligands.

Once efforts have been made to control the *in-situ* synthesis and the properties of carbonized ligands, ligands can be selected with intention to enhance the properties and function of hybrid materials. For example, the presence of a graphene interlayer between the CZTS NPs and the Mo substrate can reduce the formation of resistive MoS_2 during sintering (MoS_2 reduces device performance).[323] Alternatively, reduced graphene oxide (rGO) and CZTS NP nanocomposites have enhanced transport of photoexcited carriers for solar cell applications and can be used to enhance photocatalytic redox reactions.[324,325]

5.2.3. Fine-Grain-Layer

From our investigations in **Chapter 2**, we now know that the graphitic "fine-grain-layer" (FGL) identified within sintered films forms prior to sintering, and that the source of graphitic material is from the organic ligands used in synthesis. By thoroughly characterizing the thermal properties of the ligands and polysulfide (*i.e.*, capping agents), we find that this carbonization occurs between 347 and 445 °C, depending on ligand backbone and functional group (**Chapter 3**). These thermal studies provides insight into how the ligands and polysulfides will decompose and further carbonize during sintering. While there is no large structural difference between the graphitic FGL amongst our samples (**Chapter 4)**, if the structure of graphitic material can be

tailored through informed ligand selection, then it may be possible to a create a high quality FGL within sintered films which enhances charge conduction and final device properties.

5.2.4. Low Temperature Nanocrystal Densification

In the formation of large CZTSSe grains, Se or S vapor operate as fluxing agents that drives densification.[84,91,141,191] While this is a critical step for enhance the sintering kinetics, the eventual goal is to reduce the time and temperature required for sintering to further decrease the thermal budget for material processing.

In **Chapter 4**, the polyunsaturated LOA ligand used the during synthesis of CZTS NPs led to enhanced grain growth (densification and grain size) of sintered CZTSSe films. Preliminary work showed that the incorporation of sulfur atoms into the organic capping agent may be the cause of enhanced grain growth, as sulfur atoms are directly delivered to the surface of the particles during sintering. Further engineering of polysulfide or polyselenides can be performed to increase the weight percentage of fluxing atoms within the polymer and NP films.

In addition to investigating the delivery of fluxing material through the capping agent, we found that the incorporation of fluxing particles into the NP ink can also result in enhanced grain growth (**Chapter 4**). Thus, incorporating sulfur or selenium particles into the NP ink may be a promising method of initiating low temperature sintering of chalcogenide NPs.

With each of these techniques, the temporal evolution and temperature-dependent activation of sintering can be monitored.[79,80,191] Grain growth can be empirically measured at intermittent times and temperatures and compared against thermodynamic and kinetic models, allowing us to better evaluate the driving forces for the grain growth of sintered NP films.

5.3. Acknowledgements and Note from the Author

This dissertation was prepared in its entirety by Breena M. Sperry. However, this research would not be possible without the contribution of others at the University of Washington. The author thanks Tatyana Galkeo of the MSE labs (for collecting the TGA spectra in **Chapter 2**), Dr. Samantha Young from the MAF (for collecting the XPS data in **Chapter 2 and Chapter 4**), Dr. Yunping Huang (for synthesizing the LOA ligand), Dr. Nadzeya Kukhta (for collecting the ^{1}H NMR spectra in **Chapter 3**), and Lorenzo Guio (for collecting the DSC spectra in **Chapter 4**). The author also thanks the reading committee, Julian Freedland, Fatima Davila, and Reid Schur for reviewing this dissertation.

Appendix A: References

(1) An, L.; Zhang, D.; Zhang, L.; Feng, G. Effect of Nanoparticle Size on the Mechanical Properties of Nanoparticle Assemblies. Nanoscale 2019, 11 (19), 9563–9573. https://doi.org/10.1039/C9NR01082C.

(2) Albanese, A.; Tang, P. S.; Chan, W. C. W. The Effect of Nanoparticle Size, Shape, and Surface Chemistry on Biological Systems. Annu. Rev. Biomed. Eng. 2012, 14, 1–16. https://doi.org/10.1146/annurev-bioeng-071811-150124.

(3) Saion, E.; Gharibshahi, E.; Naghavi, K. Size-Controlled and Optical Properties of Monodispersed Silver Nanoparticles Synthesized by the Radiolytic Reduction Method. Int. J. Mol. Sci. 2013, 14 (4), 7880–7896. https://doi.org/10.3390/ijms14047880.

(4) Ijaz, P.; Imran, M.; Soares, M. M.; Tolentino, H. C. N.; Martín-García, B.; Giannini, C.; Moreels, I.; Manna, L.; Krahne, R. Composition-, Size-, and Surface Functionalization-Dependent Optical Properties of Lead Bromide Perovskite Nanocrystals. J. Phys. Chem. Lett. 2020, 11 (6), 2079–2085. https://doi.org/10.1021/acs.jpclett.0c00266.

(5) Li, S.; Chen, J.; Ying Tang, Y.; Yu Hu, L.; Hui Qian, W.; Zhu, D.; Chen, P. Green Synthesis of Upconversion Nanocrystals by Adjusting Local Precursor Supersaturation under Aqueous Conditions. Materials Advances 2020, 1 (8), 2707–2711. https://doi.org/10.1039/D0MA00568A.

(6) Arno, M. C.; Inam, M.; Weems, A. C.; Li, Z.; Binch, A. L. A.; Platt, C. I.; Richardson, S. M.; Hoyland, J. A.; Dove, A. P.; O'Reilly, R. K. Exploiting the Role of Nanoparticle Shape in Enhancing Hydrogel Adhesive and Mechanical Properties. Nat. Commun. 2020, 11 (1), 1420. https://doi.org/10.1038/s41467-020-15206-y.

(7) Singh, A.; Lutz, L.; Ong, G. K.; Bustillo, K.; Raoux, S.; Jordan-Sweet, J. L.; Milliron, D. J. Controlling Morphology in Polycrystalline Films by Nucleation and Growth from Metastable Nanocrystals. Nano Lett. 2018, 18 (9), 5530–5537. https://doi.org/10.1021/acs.nanolett.8b01916.

(8) Collord, A. D.; Hillhouse, H. W. Mapping the Composition Dependence of Cu2ZnSn(S,Se)4 Absorber Quality Using Composition-Spread Libraries, Photoluminescence, and Raman. Conf. Rec. IEEE Photovolt. Spec. Conf. 2013, 368–370. https://doi.org/10.1109/PVSC.2013.6744169.

(9) Irkhina, A.; Levcenko, S.; Hinrichs, V.; Plate, P.; Unold, T. Metal Acetate Based Synthesis of Small-Sized Cu2ZnSnS4 Nanocrystals: Effect of Injection Temperature and Synthesis Time. RSC Adv. 2017, 7 (19), 11752–11760. https://doi.org/10.1039/c6ra28588k.

(10) Just, J.; Sutter-Fella, C. M.; Lützenkirchen-Hecht, D.; Frahm, R.; Schorr, S.; Unold, T. Secondary Phases and Their Influence on the Composition of the Kesterite Phase in CZTS and CZTSe Thin Films. Phys. Chem. Chem. Phys. 2016, 18 (23), 15988–15994. https://doi.org/10.1039/c6cp00178e.

(11) Thanh, N. T. K.; Maclean, N.; Mahiddine, S. Mechanisms of Nucleation and Growth of Nanoparticles in Solution. Chem. Rev. 2014, 114 (15), 7610–7630. https://doi.org/10.1021/cr400544s.

(12) Boles, M. A.; Ling, D.; Hyeon, T.; Talapin, D. V. The Surface Science of Nanocrystals. Nat. Mater. 2016, 15 (2), 141–153. https://doi.org/10.1038/nmat4526.

(13) Huang, Y.; Cohen, T. A.; Sperry, B. M.; Larson, H.; Nguyen, H. A.; Homer, M. K.; Dou, F. Y.; Jacoby, L. M.; Cossairt, B. M.; Gamelin, D. R.; Luscombe, C. K. Organic Building Blocks at Inorganic Nanomaterial Interfaces. Mater. Horiz. 2022, 9 (61). https://doi.org/10.1039/d1mh01294k.

(14) Ealias, A. M.; Saravanakumar, M. P. A Review on the Classification, Characterisation, Synthesis of Nanoparticles and Their Application. IOP Conf. Ser.: Mater. Sci. Eng. 2017, 263, 032019. https://doi.org/10.1088/1757-899X/263/3/032019.

(15) Ali, A.; Shah, T.; Ullah, R.; Zhou, P.; Guo, M.; Ovais, M.; Tan, Z.; Rui, Y. Review on Recent Progress in Magnetic Nanoparticles: Synthesis, Characterization, and Diverse Applications. Front. Chem. 2021, 9. https://doi.org/10.3389/fchem.2021.629054.

(16) Heuer-Jungemann, A.; Feliu, N.; Bakaimi, I.; Hamaly, M.; Alkilany, A.; Chakraborty, I.; Masood, A.; Casula, M. F.; Kostopoulou, A.; Oh, E.; Susumu, K.; Stewart, M. H.; Medintz, I. L.; Stratakis, E.; Parak, W. J.; Kanaras, A. G. The Role of Ligands in the Chemical Synthesis and Applications of Inorganic Nanoparticles. Chem. Rev. 2019, 119 (8), 4819–4880. https://doi.org/10.1021/acs.chemrev.8b00733.

(17) Salata, O. Applications of Nanoparticles in Biology and Medicine. J. Nanobiotechnology 2004, 2 (1), 3. https://doi.org/10.1186/1477-3155-2-3.

(18) Luo, X.; Morrin, A.; Killard, A. J.; Smyth, M. R. Application of Nanoparticles in Electrochemical Sensors and Biosensors. Electroanalysis 2006, 18 (4), 319–326. https://doi.org/10.1002/elan.200503415.

(19) Matsui, I. Nanoparticles for Electronic Device Applications: A Brief Review. J. Chem. Eng. Japan 2005, 38 (8), 535–546. https://doi.org/10.1252/jcej.38.535.

(20) Choi, J.; Shin, D.-M.; Song, H.; Lee, D.; Kim, K. Current Achievements of Nanoparticle Applications in Developing Optical Sensing and Imaging Techniques. Nano Converg. 2016, 3 (1), 30. https://doi.org/10.1186/s40580-016-0090-x.

(21) Narayan, N.; Meiyazhagan, A.; Vajtai, R. Metal Nanoparticles as Green Catalysts. Materials (Basel) 2019, 12 (21), 3602. https://doi.org/10.3390/ma12213602.

(22) Cao, G. Nanostructures & Nanomaterials: Synthesis, Properties & Applications; Imperial College Press: London, 2004.

(23) Bayda, S.; Adeel, M.; Tuccinardi, T.; Cordani, M.; Rizzolio, F. The History of Nanoscience and Nanotechnology: From Chemical–Physical Applications to Nanomedicine. Molecules 2019, 25 (1), 112. https://doi.org/10.3390/molecules25010112.

(24) Reibold, M.; Paufler, P.; Levin, A. A.; Kochmann, W.; Pätzke, N.; Meyer, D. C. Carbon Nanotubes in an Ancient Damascus Sabre. Nature 2006, 444 (7117), 286–286. https://doi.org/10.1038/444286a.

(25) Pradell, T.; Climent-Font, A.; Molera, J.; Zucchiatti, A.; Ynsa, M. D.; Roura, P.; Crespo, D. Metallic and Nonmetallic Shine in Luster: An Elastic Ion Backscattering Study. Journal of Applied Physics 2007, 101 (10), 103518. https://doi.org/10.1063/1.2734944.

(26) Heiligtag, F. J.; Niederberger, M. The Fascinating World of Nanoparticle Research. Materials Today 2013, 16 (7–8), 262–271. https://doi.org/10.1016/j.mattod.2013.07.004.

(27) Nanoeffects in Ancient Technology and Art and in Space. In Fundamentals and Applications of Nano Silicon in Plasmonics and Fullerines; Elsevier, 2018; pp 497–518. https://doi.org/10.1016/B978-0-323-48057-4.00016-5.

(28) Hough, R. M.; Noble, R. R. P.; Reich, M. Natural Gold Nanoparticles. Ore Geology Reviews 2011, 42 (1), 55–61. https://doi.org/10.1016/j.oregeorev.2011.07.003.

(29) Sharma, V. K.; Filip, J.; Zboril, R.; Varma, R. S. Natural Inorganic Nanoparticles – Formation, Fate, and Toxicity in the Environment. Chem. Soc. Rev. 2015, 44 (23), 8410–8423. https://doi.org/10.1039/C5CS00236B.

(30) De Yoreo, J. J. Principles of Crystal Nucleation and Growth. Reviews in Mineralogy and Geochemistry 2003, 54 (1), 57–93. https://doi.org/10.2113/0540057.

(31) Ehrenfreund, P.; Foing, B. H. Fullerenes and Cosmic Carbon. Science 2010, 329 (5996), 1159–1160. https://doi.org/10.1126/science.1194855.

(32) The First Nanotechnologists. The New York Times. https://archive.nytimes.com/www.nytimes.com/imagepages/2005/02/21/science/20050222_NANO1_GRAPHIC.html (accessed 2022-10-05).

(33) Lyklema, J. Colloidal Models. A Bit of History. Journal of Colloid and Interface Science 2015, 446, 308–316. https://doi.org/10.1016/j.jcis.2014.10.052.

(34) Feynman, R. P. There's Plenty of Room at the Bottom. Engineering and Science 1960, 23 (5), 23–36.

(35) Novoselov, K. S.; Geim, A. K.; Morozov, S. V.; Jiang, D.; Zhang, Y.; Dubonos, S. V.; Grigorieva, I. V.; Firsov, A. A. Electric Field Effect in Atomically Thin Carbon Films. Science 2004, 306 (5696), 666–669. https://doi.org/10.1126/science.1102896.

(36) Aldakov, D.; Lefrançois, A.; Reiss, P. Ternary and Quaternary Metal Chalcogenide Nanocrystals: Synthesis, Properties and Applications. Journal of Materials Chemistry C 2013, 1 (24), 3756–3776. https://doi.org/10.1039/c3tc30273c.

(37) Cho, H.-H.; Yang, H.; Kang, D. J.; Kim, B. J. Surface Engineering of Graphene Quantum Dots and Their Applications as Efficient Surfactants. ACS Appl. Mater. Interfaces 2015, 7 (16), 8615–8621. https://doi.org/10.1021/acsami.5b00729.

(38) Jaber-Ansari, L.; Hersam, M. C. Solution-Processed Graphene Materials and Composites. MRS Bulletin 2012, 37 (12), 1167–1175. https://doi.org/10.1557/mrs.2012.182.

(39) Rastogi, A.; Tripathi, D. K.; Yadav, S.; Chauhan, D. K.; Živčák, M.; Ghorbanpour, M.; El-Sheery, N. I.; Brestic, M. Application of Silicon Nanoparticles in Agriculture. 3 Biotech 2019, 9 (3), 90. https://doi.org/10.1007/s13205-019-1626-7.

(40) Greener, J.; Pearson, G.; Cakmak, M. Roll-to-Roll Manufacturing: Process Elements and Recent Advances, 1st ed.; Greener, J., Pearson, G., Cakmak, M., Eds.; John Wiley & Sons Ltd: Hoboken, 2018.

(41) Mertens, K. Photovoltaics - Fundamentals, Technology and Practice, 1st ed.; John Wiley & Sons Ltd: West Sussex, 2014.

(42) Rao, C. N. R.; Thomas, P. J.; Kulkarini, G. U. Nanocrystals: Synthesis, Properties and Applications; Hull, R., Osgood, R.M., Jr., Parisi, J., Warlimont, H., Eds.; Springer: Berlin, 2007.

(43) Paire, M.; Delbos, S.; Vidal, J.; Naghavi, N.; Guillemoles, J. Solar Cell Materials: Developing Technologies; Conibeer, G., Willoughby, A., Capper, P., Kasap, S., Eds.; John Wiley & Sons Ltd: West Sussex, 2014. https://doi.org/10.1587/transfun.E100.A.176.

(44) Kumar, M.; Dubey, A.; Adhikari, N.; Venkatesan, S.; Qiao, Q. Strategic Review of Secondary Phases, Defects and Defect-Complexes in Kesterite CZTS-Se Solar Cells. Energy and Environmental Science 2015, 8 (11), 3134–3159. https://doi.org/10.1039/c5ee02153g.

(45) Fu, R.; Feldman, D. J.; Margolis, R. M.; Woodhouse, M. A.; Ardani, K. B. U.S. Solar Photovoltaic System Cost Benchmark: Q1 2017; 2017. https://doi.org/10.2172/1390776.

(46) Mitzi, D. B. Solution Processing of Inorganic Materials; Mitzi, D. B., Ed.; John Wiley & Sons Ltd: Hoboken, New Jersey, 2009.

(47) Hillhouse, H.; Beard, M. Solar Cells from Colloidal Nanocrystals: Fundamentals, Materials, Devices, and Economics. Current Opinion in Colloid and Interface Science 2009, 14 (4), 245–259. https://doi.org/10.1016/j.cocis.2009.05.002.

(48) Eric J. Mittemeijer. Fundamentals of Materials Science: The Microstructure–Property Relationship ... - Eric J. Mittemeijer - Google Books; Springer, 2010.

(49) Koch, C.; Ovid'ko, I.; Seal, S.; Veprek, S. Structural Nanocrystalline Materials: Fundamentals and Applications - Carl C. Koch, Ilya A. Ovid'ko, Sudipta Seal, Stan Veprek - Google Books; 2007.

(50) Purple, T.; Romans, T.; Lycurgus, T. Basics of Nanocrystals. Nanocrystals: Synthesis, Properties and Applications 1–23. https://doi.org/10.1007/978-3-540-68752-8_1.

(51) Aigner, W.; Bienek, O.; Falcão, B. P.; Ahmed, S. U.; Wiggers, H.; Stutzmann, M.; Pereira, R. N. Intra- and Inter-Nanocrystal Charge Transport in Nanocrystal Films. Nanoscale 2018, 10 (17), 8042–8057. https://doi.org/10.1039/C8NR00250A.

(52) Bi, C.; Wang, Q.; Shao, Y.; Yuan, Y.; Xiao, Z.; Huang, J. Non-Wetting Surface-Driven High-Aspect-Ratio Crystalline Grain Growth for Efficient Hybrid Perovskite Solar Cells. Nature Communications 2015, 6, 1–7. https://doi.org/10.1038/ncomms8747.

(53) Zhang, R.; Khalizov, A.; Wang, L.; Hu, M.; Xu, W. Nucleation and Growth of Nanoparticles in the Atmosphere. Chemical Reviews 2012, 112 (3), 1957–2011. https://doi.org/10.1021/cr2001756.

(54) Karthika, S.; Radhakrishnan, T. K.; Kalaichelvi, P. A Review of Classical and Nonclassical Nucleation Theories. Crystal Growth & Design 2016, 16 (11), 6663–6681. https://doi.org/10.1021/acs.cgd.6b00794.

(55) Lee, J.; Yang, J.; Kwon, S. G.; Hyeon, T. Nonclassical Nucleation and Growth of Inorganic Nanoparticles. Nature Reviews Materials 2016, 1 (8), 1–16. https://doi.org/10.1038/natrevmats.2016.34.

(56) Camargo, P. H. C.; Rodrigues, T. S.; Anderson, G. M. da S.; Wang, J. Controlled Synthesis: Nucleation and Growth in Solution. In Metallic Nanostructures: From Controlled Synthesis to Applications; Xiong, Y., Lu, X., Eds.; 2015; pp 49–58. https://doi.org/10.1007/978-3-319-11304-3.

(57) Fundamentals of Homogeneous Nucleation and Growth. 3.

(58) Xia, C.; Zhu, S.; Feng, T.; Yang, M.; Yang, B. Evolution and Synthesis of Carbon Dots: From Carbon Dots to Carbonized Polymer Dots. Adv. Sci. 2019, 6 (23), 20190. https://doi.org/10.1002/advs.201901316.

(59) Polte, J. Fundamental Growth Principles of Colloidal Metal Nanoparticles - a New Perspective. CrystEngComm 2015, 17 (36), 6809–6830. https://doi.org/10.1039/c5ce01014d.

(60) Hoyt, J. J. Phase Transformations; McMaster Innovation Press, 2010.

(61) Thanh, N. T. K.; Maclean, N.; Mahiddine, S. Mechanisms of Nucleation and Growth of Nanoparticles in Solution. Chemical Reviews 2014, 114 (15), 7610–7630. https://doi.org/10.1021/cr400544s.

(62) Lee, J.; Yang, J.; Kwon, S. G.; Hyeon, T. Nonclassical Nucleation and Growth of Inorganic Nanoparticles. Nature Reviews Materials 2016, 1 (8), 1–16. https://doi.org/10.1038/natrevmats.2016.34.

(63) Becker, R.; Döring, W. Kinetic treatment of germ formation in supersaturated vapour. Ann. Phys. 1935, 416 (8), 719–752. https://doi.org/10.1002/andp.19354160806.

(64) LaMer, V. K.; Dinegar, R. H. Theory, Production and Mechanism of Formation of Monodispersed Hydrosols. J. Am. Chem. Soc. 1950, 72 (11), 4847–4854. https://doi.org/10.1021/ja01167a001.

(65) Jayaraman, V. K.; Hernández-Gordillo, A.; Bizarro, M. Importance of Precursor Type in Fabricating ZnO Thin Films for Photocatalytic Applications. Mater. Sci. Semicond. Process 2018, 75, 36–42. https://doi.org/10.1016/j.mssp.2017.11.015.

(66) Pourrahimi, A. M.; Liu, D.; Pallon, L. K. H.; Andersson, R. L.; Martínez Abad, A.; Lagarón, J.-M.; Hedenqvist, M. S.; Ström, V.; Gedde, U. W.; Olsson, R. T. Water-Based Synthesis and Cleaning Methods for High Purity ZnO Nanoparticles – Comparing Acetate, Chloride, Sulphate and Nitrate Zinc Salt Precursors. RSC Adv. 2014, 4 (67), 35568–35577. https://doi.org/10.1039/C4RA06651K.

(67) Zhang, L. J.; Chen, F. Y.; Tong, J. Z.; Chen, G. D.; Huang, H. J.; Shen, X. C. Controlled Growth of ZnSe Nanocrystals by Tuning Reactivity and Amount of Zinc Precursor. Journal of Chemistry 2013, 2013, 1–6. https://doi.org/10.1155/2013/791437.

(68) Yu, W. W.; Wang, Y. A.; Peng, X. Formation and Stability of Size-, Shape-, and Structure-Controlled CdTe Nanocrystals: Ligand Effects on Monomers and Nanocrystals. Chem. Mater. 2003, 15 (24), 4300–4308. https://doi.org/10.1021/cm034729t.

(69) Wang, W.; Banerjee, S.; Jia, S.; Steigerwald, M. L.; Herman, I. P. Ligand Control of Growth, Morphology, and Capping Structure of Colloidal CdSe Nanorods. Chemistry of Materials 2007, 19 (10), 2573–2580. https://doi.org/10.1021/cm0705791.

(70) Liu, J.; Liang, C.; Zhu, X.; Lin, Y.; Zhang, H.; Wu, S. Understanding the Solvent Molecules Induced Spontaneous Growth of Uncapped Tellurium Nanoparticles. Scientific Reports 2016, 6, 1–10. https://doi.org/10.1038/srep32631.

(71) Bucherl, C. N.; Oleson, K. R.; Hillhouse, H. W. Thin Film Solar Cells from Sintered Nanocrystals. Current Opinion in Chemical Engineering 2013, 2 (2), 168–177. https://doi.org/10.1016/j.coche.2013.03.004.

(72) Nishikawa, T.; Ohdaira, K.; Matsumura, H. Electrical Properties of Polycrystalline Silicon Films Formed from Amorphous Silicon Films by Flash Lamp Annealing. 2010. https://doi.org/10.1016/j.cap.2010.10.008.

(73) Rahaman, M. N. Sintering Theory and Fundamentals. https://doi.org/10.31399/asm.hb.v07.a0006117.

(74) Fang, Z. Z.; Wang, H.; Kumar, V. Coarsening, Densification, and Grain Growth during Sintering of Nano-Sized Powders-A Perspective. 2016. https://doi.org/10.1016/j.ijrmhm.2016.09.004.

(75) Fang, Z. Z.; Wang, H. Densification and Grain Growth during Sintering of Nanosized Particles. 2013. https://doi.org/10.1179/174328008X353538.

(76) Coble, R. L. Sintering Crystalline Solids. I. Intermediate and Final State Diffusion Models. Journal of Applied Physics 1961, 32 (5), 787–792. https://doi.org/10.1063/1.1736107.

(77) Li, H.; Yuan, M.; Tan, D.; Susilo, R. A.; Dong, H.; Chen, Z.; Zhao, Y.; Deng, Y.; Chen, B. Revealing the Unusual Grain Growth of Nanoparticles in Calcination: Oriented Attachment in the Solid State. CrystEngComm 2021, 23 (23), 4152–4159. https://doi.org/10.1039/D1CE00187F.

(78) Nan Wang; Yanzhou Ji; Yongbiao Wang; Youhai Wen; Long-Qing Chen. Two Modes of Grain Boundary Pinning by Coherent Precipitates. Acta Materialia 2017, 134, 226–232.

(79) Wang, Y.; Li, G.; Zhang, Y.; Li, L. Zinc Ferrite Nanoparticles: Unusual Growth Mechanism for Size-Dependent Properties. ChemistrySelect 2021, 6 (8), 1862–1869. https://doi.org/10.1002/slct.202004562.

(80) Zhang, L.; Yang, J.; Yu, H.; Pan, W. High Performance of La-Doped Y2O3 Transparent Ceramics. J Adv Ceram 2020, 9 (4), 493–502. https://doi.org/10.1007/s40145-020-0392-7.

(81) Fang, Z. Z.; Wang, H. Densification and Grain Growth during Sintering of Nanosized Particles. International Materials Reviews 2008, 53 (6), 326–352. https://doi.org/10.1179/174328008X353538.

(82) Kang, S.-J. L.; Kang, S.-J. L. Sintering: Densification, Grain Growth, and Microstructure; Materials science & engineering; Elsevier Butterworth-Heinemann: Amsterdam Heidelberg, 2005.

(83) Chernomordik, B. D.; Béland, A. E.; Deng, D. D.; Francis, L. F.; Aydil, E. S. Microstructure Evolution and Crystal Growth in Cu2ZnSnS 4 Thin Films Formed by Annealing Colloidal Nanocrystal Coatings. Chemistry of Materials 2014, 26 (10), 3191–3201. https://doi.org/10.1021/cm500791a.

(84) Mainz, R.; Walker, B.; Schmidt, S.; Zander, O.; Weber, A.; Rodriguez-Alvarez, H.; Just, J.; Klaus, M.; Agrawal, R.; Unold, T. Real-Time Observation of Cu2ZnSn(S,Se)4solar Cell Absorber Layer Formation from Nanoparticle Precursors. Physical Chemistry Chemical Physics 2013, 15 (41), 18281–18289. https://doi.org/10.1039/c3cp53373e.

(85) Clark, J.; Uhl, A.; Martin, T.; Hillhouse, H. Evolution of Morphology and Composition during Annealing and Selenization in Solution-Processed Cu2ZnSn(S,Se)4. Chemistry of Materials 2017, 29 (21), 9328–9339. https://doi.org/10.1021/acs.chemmater.7b03313.

(86) Collord, A.; Hillhouse, H. The Effect of Nanocrystal Reaction Time on Cu2ZnSn(S,Se)4 Solar Cells from Nanocrystal Inks. Solar Energy Materials and Solar Cells 2015, 141, 383–390. https://doi.org/10.1016/j.solmat.2015.05.010.

(87) Engberg, S.; Canulescu, S.; Schou, J.; Baxter, R.; Hastings, N.; Law, A.; Glass, E. J. .; Engberg, S.; Canulescu, S.; Schou, J. Liquid Phase Assisted Grain Growth in Cu2ZnSnS4 Nanoparticle Thin Films by Alkali Element Incorporation; Royal Society of Chemistry, 2018; Vol. 8. https://doi.org/10.1039/c7ra13472j.

(88) German, R. M.; Suri, P.; Park, S. J. Review: Liquid Phase Sintering. Journal of Materials Science 2009, 44 (1), 1–39. https://doi.org/10.1007/s10853-008-3008-0.

(89) Todorov, T. K.; Reuter, K. B.; Mitzi, D. B. High-Efficiency Solar Cell with Earth-Abundant Liquid-Processed Absorber. Advanced Materials 2010, 22 (20), 156–159. https://doi.org/10.1002/adma.200904155.

(90) Valant, M.; Suvorov, D.; Pullar, R. C.; Sarma, K.; Alford, N. M. N. A Mechanism for Low-Temperature Sintering. Journal of the European Ceramic Society 2006, 26 (13), 2777–2783. https://doi.org/10.1016/j.jeurceramsoc.2005.06.026.

(91) Hages, C.; Koeper, M.; Miskin, C.; Brew, K.; Agrawal, R. Controlled Grain Growth for High Performance Nanoparticle-Based Kesterite Solar Cells. Chemistry of Materials 2016, 28 (21), 7703–7714. https://doi.org/10.1021/acs.chemmater.6b02733.

(92) Zhang, M.; Efremov, M. Yu.; Schiettekatte, F.; Olson, E. A.; Kwan, A. T.; Lai, S. L.; Wisleder, T.; Greene, J. E.; Allen, L. H. Size-Dependent Melting Point Depression of Nanostructures: Nanocalorimetric Measurements. Phys. Rev. B 2000, 62 (15), 10548–10557. https://doi.org/10.1103/PhysRevB.62.10548.

(93) Lu, H. M.; Li, P. Y.; Cao, Z. H.; Meng, X. K. Size-, Shape-, and Dimensionality-Dependent Melting Temperatures of Nanocrystals. 2009, 2 (3), 7598–7602.

(94) Bourdais, S.; Choné, C.; Delatouche, B.; Jacob, A.; Larramona, G.; Moisan, C.; Lafond, A.; Donatini, F.; Rey, G.; Siebentritt, S.; Walsh, A.; Dennler, G. Is the Cu/Zn Disorder the Main Culprit for the Voltage Deficit in Kesterite Solar Cells? Advanced Energy Materials 2016, 6 (12), 1502276. https://doi.org/10.1002/aenm.201502276.

(95) Periodic Table of Toxic Elements. http://corrosion-doctors.org/Elements-Toxic/Elements.htm%5Cninternal-pdf://0.0.1.236/Elements.html.

(96) Haxel, G. B.; Hedrick, J. B.; Orris, G. J. Rare Earth Elements—Critical Resources for High Technology; 2002. https://doi.org/10.3133/fs08702.

(97) Celik, I.; Phillips, A. B.; Song, Z.; Yan, Y.; Ellingson, R. J.; Heben, M. J.; Apul, D. Environmental Analysis of Perovskites and Other Relevant Solar Cell Technologies in a Tandem Configuration. 1874 | Energy Environ. Sci 2017, 10, 1874. https://doi.org/10.1039/c7ee01650f.

(98) Jean, S. J.; Bulović, V.; Jean, J.; Brown, P. R.; Jaffe, R. L.; Buonassisi, T.; Buloví, V. Pathways for Solar Photovoltaics. Energy Environ. Sci 2015, 8, 1200–1219. https://doi.org/10.1039/c4ee04073b.

(99) Delbos, S. Këwhile Thin Films for Photovoltaics : A Review. EPJ Photovoltaics 2012, 3, 35004. https://doi.org/10.1051/epjpv/2012008.

(100) NREL. Best Research-Cell Efficiencies Chart; 2018.

(101) Zhou, H.; Hsu, W. C.; Duan, H. S.; Bob, B.; Yang, W.; Song, T. Bin; Hsu, C. J.; Yang, Y. CZTS Nanocrystals: A Promising Approach for next Generation Thin Film Photovoltaics. Energy and Environmental Science 2013, 6 (10), 2822–2838. https://doi.org/10.1039/c3ee41627e.

(102) Hunge, Y. M.; Yadav, A. A.; Liu, S.; Mathe, V. L. Sonochemical Synthesis of CZTS Photocatalyst for Photocatalytic Degradation of Phthalic Acid. Ultrason. Sonochem. 2019, 56, 284–289. https://doi.org/10.1016/j.ultsonch.2019.04.003.

(103) Guo, Q.; Ford, G.; Yang, W. C.; Walker, B.; Stach, E.; Hillhouse, H.; Agrawal, R. Fabrication of 7.2% Efficient CZTSSe Solar Cells Using CZTS Nanocrystals. Journal of the American Chemical Society 2010, 132 (49), 17384–17386. https://doi.org/10.1021/ja108427b.

(104) Wu, Q.; Xue, C.; Li, Y.; Zhou, P.; Liu, W.; Zhu, J.; Dai, S.; Zhu, C.; Yang, S. Kesterite Cu2ZnSnS4 as a Low-Cost Inorganic Hole-Transporting Material for High-Efficiency Perovskite Solar Cells. ACS Applied Materials and Interfaces 2015, 7 (51), 28466–28473. https://doi.org/10.1021/acsami.5b09572.

(105) Baig, N.; Kammakakam, I.; Falath, W. Nanomaterials: A Review of Synthesis Methods, Properties, Recent Progress, and Challenges. Mater. Adv. 2021, 2 (6), 1821–1871. https://doi.org/10.1039/D0MA00807A.

(106) Jang, S.; Seo, Y.; Choi, J.; Kim, T.; Cho, J.; Kim, S.; Kim, D. Sintering of Inkjet Printed Copper Nanoparticles for Flexible Electronics. Scripta Materialia 2010, 62 (5), 258–261. https://doi.org/10.1016/j.scriptamat.2009.11.011.

(107) Bibi, H.; Iqbal, M.; Wahab, H.; Öztürk, M.; Ke, F.; Iqbal, Z.; Khan, M. I.; Alghanem, S. M. Green Synthesis of Multifunctional Carbon Coated Copper Oxide Nanosheets and Their Photocatalytic and Antibacterial Activities. Sci Rep 2021, 11 (1), 16838. https://doi.org/10.1038/s41598-021-96316-5.

(108) Ain, N. ul; Zia-ur-Rehman; Aamir, A.; Khan, Y.; Rehman, M.; Lin, D.-J. Catalytic and Photocatalytic Efficacy of Hexagonal CuS Nanoplates Derived from Copper(II) Dithiocarbamate.

Materials Chemistry and Physics 2020, 242, 122408. https://doi.org/10.1016/j.matchemphys.2019.122408.

(109) Jiang, L.; Li, J.; Huang, K.; Li, S.; Wang, Q.; Sun, Z.; Mei, T.; Wang, J.; Zhang, L.; Wang, N.; Wang, X. Low-Temperature and Solution-Processable Zinc Oxide Transistors for Transparent Electronics. ACS Omega 2017, 2 (12), 8990–8996. https://doi.org/10.1021/acsomega.7b01420.

(110) Wang, X.; Huang, H.; Liang, B.; Liu, Z.; Chen, D.; Shen, G. ZnS Nanostructures: Synthesis, Properties, and Applications. Critical Reviews in Solid State and Materials Sciences 2013, 38 (1), 57–90. https://doi.org/10.1080/10408436.2012.736887.

(111) Gebreslassie, Y. T.; Gebretnsae, H. G. Green and Cost-Effective Synthesis of Tin Oxide Nanoparticles: A Review on the Synthesis Methodologies, Mechanism of Formation, and Their Potential Applications. Nanoscale Res Lett 2021, 16 (1), 97. https://doi.org/10.1186/s11671-021-03555-6.

(112) Cheng, F.; Zhang, X.; Mu, K.; Ma, X.; Jiao, M.; Wang, Z.; Limpachanangkul, P.; Chalermsinsuwan, B.; Gao, Y.; Li, Y.; Chen, Z.; Liu, L. Recent Progress of Sn-based Derivative Catalysts for Electrochemical Reduction of CO2. Energy Technol. 2021, 9 (1), 2000799. https://doi.org/10.1002/ente.202000799.

(113) Reddy, T. S.; Kumar, M. C. S. Co-Evaporated SnS Thin Films for Visible Light Photodetector Applications. RSC Adv. 2016, 6 (98), 95680–95692. https://doi.org/10.1039/C6RA20129F.

(114) Yu, W. W.; Wang, Y. A.; Peng, X. Formation and Stability of Size-, Shape-, and Structure-Controlled CdTe Nanocrystals: Ligand Effects on Monomers and Nanocrystals. Chemistry of Materials 2003, 15 (24), 4300–4308.

(115) Heuer-Jungemann, A.; Feliu, N.; Bakaimi, I.; Hamaly, M.; Alkilany, A.; Chakraborty, I.; Masood, A.; Casula, M. F.; Kostopoulou, A.; Oh, E.; Susumu, K.; Stewart, M. H.; Medintz, I. L.; Stratakis, E.; Parak, W. J.; Kanaras, A. G. The Role of Ligands in the Chemical Synthesis and Applications of Inorganic Nanoparticles. Chemical Reviews 2019, 119 (8), 4819–4880. https://doi.org/10.1021/acs.chemrev.8b00733.

(116) Boles, M. A.; Ling, D.; Hyeon, T.; Talapin, D. V. The Surface Science of Nanocrystals. Nature Materials 2016, 15 (2), 141–153. https://doi.org/10.1038/nmat4526.

(117) Mourdikoudis, S.; Liz-Marzán, L. M. Oleylamine in Nanoparticle Synthesis. Chemistry of Materials 2013, 25 (9), 1465–1476. https://doi.org/10.1021/cm4000476.

(118) Rossi, L. M.; Fiorio, J. L.; Garcia, M. A. S.; Ferraz, C. P. The Role and Fate of Capping Ligands in Colloidally Prepared Metal Nanoparticle Catalysts. Dalton Transactions 2018, 47 (17), 5889–5915. https://doi.org/10.1039/c7dt04728b.

(119) Mohapatra, P.; Shaw, S.; Mendivelso-Perez, D.; Bobbitt, J. M.; Silva, T. F.; Naab, F.; Yuan, B.; Tian, X.; Smith, E. A.; Cademartiri, L. Calcination Does Not Remove All Carbon from Colloidal Nanocrystal Assemblies. Nature communications 2017, 8 (1), 2038. https://doi.org/10.1038/s41467-017-02267-9.

(120) Mourdikoudis, S.; Liz-Marzán, L. M. Oleylamine in Nanoparticle Synthesis. Chem. Mater. 2013, 25 (9), 1465–1476. https://doi.org/10.1021/cm4000476.

(121) Wang, W.; Banerjee, S.; Jia, S.; Steigerwald, M. L.; Herman, I. P. Ligand Control of Growth, Morphology, and Capping Structure of Colloidal CdSe Nanorods. Chem. Mater. 2007, 19 (10), 2573–2580. https://doi.org/10.1021/cm0705791.

(122) Grubbs, R. B. Roles of Polymer Ligands in Nanoparticle Stabilization. Polym. Rev. 2007, 47 (2), 197–215. https://doi.org/10.1080/15583720701271245.

(123) Peters, J. L.; Van Den Bos, K. H. W.; Aert, S. V.; Goris, B.; Bals, S.; Vanmaekelbergh, D. L. Ligand-Induced Shape Transformation of PbSe Nanocrystals. Chem. Mater. 2017, 29, 4122–4128. https://doi.org/10.1021/acs.chemmater.7b01103.

(124) Mozaffari, S.; Li, W.; Dixit, M.; Seifert, S.; Lee, B.; Kovarik, L.; Mpourmpakis, G.; Karim, A. M. The Role of Nanoparticle Size and Ligand Coverage in Size Focusing of Colloidal Metal Nanoparticles. Nanoscale Adv. 2019, 1 (10), 4052–4066. https://doi.org/10.1039/C9NA00348G.

(125) Bokov, D.; Turki Jalil, A.; Chupradit, S.; Suksatan, W.; Javed Ansari, M.; Shewael, I. H.; Valiev, G. H.; Kianfar, E. Nanomaterial by Sol-Gel Method: Synthesis and Application. Advances in Materials Science and Engineering 2021, 2021, 1–21. https://doi.org/10.1155/2021/5102014.

(126) Yang, T.-H.; Peng, H.-C.; Zhou, S.; Lee, C.-T.; Bao, S.; Lee, Y.-H.; Wu, J.-M.; Xia, Y. Toward a Quantitative Understanding of the Reduction Pathways of a Salt Precursor in the Synthesis of Metal Nanocrystals. Nano Lett. 2017, 17 (1), 334–340. https://doi.org/10.1021/acs.nanolett.6b04151.

(127) Yu, Y.; Yang, W.; Sun, X.; Zhu, W.; Li, X.-Z.; Sellmyer, D. J.; Sun, S. Monodisperse MPt (M = Fe, Co, Ni, Cu, Zn) Nanoparticles Prepared from a Facile Oleylamine Reduction of Metal Salts. Nano Lett. 2014, 14 (5), 2778–2782. https://doi.org/10.1021/nl500776e.

(128) Glavee, G. N.; Klabunde, K. J.; Sorensen, C. M.; Hadjapanayis, G. C. Borohydride Reductions of Metal Ions. A New Understanding of the Chemistry Leading to Nanoscale Particles of Metals, Borides, and Metal Borates. Langmuir 1992, 8 (3), 771–773. https://doi.org/10.1021/la00039a008.

(129) Newman, J. D. S.; Blanchard, G. J. Formation of Gold Nanoparticles Using Amine Reducing Agents. Langmuir 2006, 22 (13), 5882–5887. https://doi.org/10.1021/la060045z.

(130) Villaverde-Cantizano, G.; Laurenti, M.; Rubio-Retama, J.; Contreras-Cáceres, R. CHAPTER 1. Reducing Agents in Colloidal Nanoparticle Synthesis – an Introduction. In Nanoscience & Nanotechnology Series; Mourdikoudis, S., Ed.; Royal Society of Chemistry: Cambridge, 2021; pp 1–27. https://doi.org/10.1039/9781839163623-00001.

(131) Cesario, D.; Furia, E.; Mazzone, G.; Beneduci, A.; De Luca, G.; Sicilia, E. Complexation of Al3+ and Ni2+ by l -Ascorbic Acid: An Experimental and Theoretical Investigation. J. Phys. Chem. A 2017, 121 (51), 9773–9781. https://doi.org/10.1021/acs.jpca.7b10847.

(132) Wei, J.; Schaeffer, N.; Pileni, M. P. Ligand Exchange Governs the Crystal Structures in Binary Nanocrystal Superlattices. Journal of the American Chemical Society 2015, 137 (46), 14773–14784. https://doi.org/10.1021/jacs.5b09959.

(133) Grubbs, R. B. Roles of Polymer Ligands in Nanoparticle Stabilization. Polymer Reviews 2007, 47 (2), 197–215. https://doi.org/10.1080/15583720701271245.

(134) Vivien, A.; Guillaumont, M.; Meziane, L.; Salzemann, C.; Aubert, C.; Halbert, S.; Gérard, H.; Petit, M.; Petit, C. Role of Oleylamine Revisited: An Original Disproportionation Route to Monodispersed Cobalt and Nickel Nanocrystals. Chem. Mater. 2019, 31 (3), 960–968. https://doi.org/10.1021/acs.chemmater.8b04435.

(135) Tiong, V. T.; Zhang, Y.; Bell, J.; Wang, H. Carbon Concentration Dependent Grain Growth of Cu2ZnSnS4 Thin Films. RSC Advances 2015, 5 (26), 20178–20185. https://doi.org/10.1039/c4ra16447d.

(136) Ingham, B.; Lim, T. H.; Dotzler, C. J.; Henning, A.; Toney, M. F.; Tilley, R. D. How Nanoparticles Coalesce: An in Situ Study of Au Nanoparticle Aggregation and Grain Growth. Chemistry of Materials 2011, 23 (14), 3312–3317. https://doi.org/10.1021/cm200354d.

(137) Li, Z.; Suslick, K. S. Chemically Induced Sintering of Nanoparticles. Angew. Chem. Int. Ed. 2019, 58 (40), 14193–14196. https://doi.org/10.1002/anie.201908600.

(138) Lee, E.; Park, S. J.; Cho, J. W.; Gwak, J.; Oh, M. K.; Min, B. K. Nearly Carbon-Free Printable CIGS Thin Films for Solar Cell Applications. Solar Energy Materials and Solar Cells 2011, 95 (10), 2928–2932. https://doi.org/10.1016/j.solmat.2011.05.048.

(139) Cao, Y.; Denny, M. S.; Caspar, J. V; Farneth, W. E.; Guo, Q.; Ionkin, A. S.; Johnson, L. K.; Lu, M.; Malajovich, I.; Radu, D.; Rosenfeld, H. D.; Choudhury, K. R.; Wu, W. High-Efficiency Solution-Processed Cu2ZnSn(S,Se)4 Thin-Film Solar Cells Prepared from Binary and Ternary Nanoparticles. Journal of American Chemical Society 2012, 134, 15644–15647.

(140) Martin, T. R.; Katahara, J. K.; Bucherl, C. N.; Krueger, B. W.; Hillhouse, H. W.; Luscombe, C. K. Nanoparticle Ligands and Pyrolized Graphitic Carbon in CZTSSe Photovoltaic Devices. Chemistry of Materials 2016, 28 (1), 135–145. https://doi.org/10.1021/acs.chemmater.5b03426.

(141) Wu, W.; Cao, Y.; Caspar, J.; Guo, Q.; Johnson, L.; Malajovich, I.; Rosenfeld, H. D.; Choudhury, K. R. Studies of the Fine-Grain Sub-Layer in the Printed CZTSSe Photovoltaic Devices. Journal of Materials Chemistry C 2014, 2 (19), 3777–3781. https://doi.org/10.1039/c4tc00391h.

(142) Williams, B.; Smeaton, M.; Trejo, N.; Francis, L.; Aydil, E. Effect of Nanocrystal Size and Carbon on Grain Growth during Annealing of Copper Zinc Tin Sulfide Nanocrystal Coatings. Chemistry of Materials 2017, 29 (4), 1676–1683. https://doi.org/10.1021/acs.chemmater.6b05058.

(143) Miskin, C.; Yang, W. C.; Hages, C.; Carter, N.; Joglekar, C.; Stach, E. A.; Agrawal, R. 9.0% Efficient Cu2ZnSn(S,Se)4 Solar Cells from Selenized Nanoparticle Inks. Prog. Photovolt: Res. Appl. 2014. https://doi.org/10.1002/pip.

(144) Martin, T. R.; Katahara, J. K.; Bucherl, C. N.; Krueger, B. W.; Hillhouse, H. W.; Luscombe, C. K. Nanoparticle Ligands and Pyrolized Graphitic Carbon in CZTSSe Photovoltaic Devices. Chemistry of Materials 2016, 28 (1), 135–145. https://doi.org/10.1021/acs.chemmater.5b03426.

(145) Huang, T. J.; Yin, X.; Tang, C.; Qi, G.; Gong, H. Influence of Ligands on the Formation of Kesterite Thin Films for Solar Cells: A Comparative Study. ChemSusChem 2016, 9 (9), 1032–1041. https://doi.org/10.1002/cssc.201600063.

(146) Lynch, M. An Investigation of Solutions of Sulfur in Oleylamine by Raman Spectroscopy and Their Relation to Lead Sulfide Quantum Dot Synthesis, University of Colorado, Boulder, 2017.

(147) Baran, V. Hydroxyl Ion as a Ligand. Coordination Chemistry Reviews 1971, 6 (1), 65–93. https://doi.org/10.1016/S0010-8545(00)80034-X.

(148) Zherebetskyy, D.; Scheele, M.; Zhang, Y.; Bronstein, N.; Thompson, C.; Britt, D.; Salmeron, M.; Alivisatos, P.; Wang, L.-W. Hydroxylation of the Surface of PbS Nanocrystals Passivated with Oleic Acid. Science 2014, 344 (6190), 1380–1384. https://doi.org/10.1126/science.1252727.

(149) Panina, N. S.; Belyaev, A. N.; Simanova, S. A. Carboxylic Acids and Their Anions. Acid and Ligand Properties. Russian Journal of General Chemistry 2002, 72 (1), 91–94. https://doi.org/10.1023/A:1015353530785.

(150) Thomson, J.; Nagashima, K.; Macdonald, P.; Ozin, G. From Sulfur-Amine Solutions to Metal Sulfide Nanocrystals: Peering into the Oleylamine-Sulfur Black Box. Journal of the American Chemical Society 2011, 133, 5036–5021.

(151) Kim, E. T.; Chung, W. J.; Lim, J.; Johe, P.; Glass, R. S.; Pyun, J.; Char, K. One-Pot Synthesis of PbS NP/Sulfur-Oleylamine Copolymer Nanocomposites via the Copolymerization of Elemental Sulfur with Oleylamine. Polymer Chemistry 2014, 5 (11), 3617–3623. https://doi.org/10.1039/c4py00073k.

(152) Kim, B.; Fredrickson, G.; Kramer, E. Effect of Polymer Ligand Molecular Weight on Polymer-Coated Nanoparticle Location in Block Copolymers. Macromolecules 2008, 41 (2), 436–447. https://doi.org/10.1021/ma701931z.

(153) Kim, E. T.; Chung, W. J.; Lim, J.; Johe, P.; Glass, R. S.; Pyun, J.; Char, K. One-Pot Synthesis of PbS NP/Sulfur-Oleylamine Copolymer Nanocomposites via the Copolymerization of Elemental Sulfur with Oleylamine. Polymer Chemistry 2014, 5 (11), 3617–3623. https://doi.org/10.1039/c4py00073k.

(154) Dhaene, E.; Billet, J.; Bennett, E.; Driessche, I. V.; De Roo, J. The Trouble with ODE: Polymerization during Nanocrystal Synthesis. Nano Lett. 2019. https://doi.org/10.1021/acs.nanolett.9b03088.

(155) De Keukeleere, K.; Coucke, S.; De Canck, E.; Van Der Voort, P.; Delpech, F.; Coppel, Y.; Hens, Z.; Van Driessche, I.; Owen, J. S.; De Roo, J. Stabilization of Colloidal Ti, Zr, and Hf Oxide Nanocrystals by Protonated Tri- n -Octylphosphine Oxide (TOPO) and Its Decomposition Products. Chem. Mater. 2017, 29 (23), 10233–10242. https://doi.org/10.1021/acs.chemmater.7b04580.

(156) Kissin, Y. Chemistry and Sterochemistry of Polymerization and Copolymerization Reactions with Transition Metal Catalysts. In Alkene Polymerization Reactions with Transition Metal Catalysts; Elsevier, 2008; pp 1–28, 65–190.

(157) Goetjen, T. A.; Liu, J.; Wu, Y.; Sui, J.; Zhang, X.; Hupp, J. T.; Farha, O. K. Metal-Organic Framework (MOF) Materials as Polymerization Catalysts: A Review and Recent Advances. ChemComm. 2020. https://doi.org/10.1039/d0cc03790g.

(158) Brintzinger, H. H.; Fischer, D.; Mülhaupt, R.; Rieger, B.; Waymouth, R. M. Stereospecific Olefin Polymerization with Chiral Metallocene Catalysts. Angew. Chem. Int. Ed. Engl. 1995, 34 (11), 1143–1170. https://doi.org/10.1002/anie.199511431.

(159) Shamiri, A.; Chakrabarti, M. H.; Jahan, S.; Hussain, M. A.; Kaminsky, W.; Aravind, P. V.; Yehye, W. A. The Influence of Ziegler-Natta and Metallocene Catalysts on Polyolefin Structure, Properties, and Processing Ability. Materials (Basel) 2014, 7 (7), 5069–5108. https://doi.org/10.3390/ma7075069.

(160) Brüll, R.; Kgosane, D.; Neveling, A.; Pasch, H.; Raubenheimer, H. G.; Sanderson, R.; Wahner, U. M. Synthesis and Properties of Poly-1-Olefins. Macromol. Symp. 2001, 165 (1), 11–18. https://doi.org/10.1002/1521-3900(200103)165:1<11::AID-MASY11>3.0.CO;2-I.

(161) Lomège, J.; Lapinte, V.; Negrell, C.; Robin, J.-J.; Caillol, S. Fatty Acid-Based Radically Polymerizable Monomers: From Novel Poly(Meth)Acrylates to Cutting-Edge Properties. Biomacromolecules 2019, 20 (1), 4–26. https://doi.org/10.1021/acs.biomac.8b01156.

(162) Zalesskiy, S. S.; Ananikov, V. P. Pd2(Dba)3 as a Precursor of Soluble Metal Complexes and Nanoparticles: Determination of Palladium Active Species for Catalysis and Synthesis. Organometallics 2012, 31 (6), 2302–2309. https://doi.org/10.1021/om201217r.

(163) Zhang, Y.; Glass, R. S.; Char, K.; Pyun, J. Recent Advances in the Polymerization of Elemental Sulphur, Inverse Vulcanization and Methods to Obtain Functional Chalcogenide Hybrid Inorganic/Organic Polymers (CHIPs). Polymer Chemistry 2019, 10 (30), 4078–4105. https://doi.org/10.1039/c9py00636b.

(164) Zhang, Y.; Pavlopoulos, N. G.; Kleine, T. S.; Karayilan, M.; Glass, R. S.; Char, K.; Pyun, J. Nucleophilic Activation of Elemental Sulfur for Inverse Vulcanization and Dynamic Covalent Polymerizations. J. Polym. Sci. 2019, 57 (1), 7–12. https://doi.org/10.1002/pola.29266.

(165) Griebel, J. J.; Glass, R. S.; Char, K.; Pyun, J. Polymerizations with Elemental Sulfur: A Novel Route to High Sulfur Content Polymers for Sustainability, Energy and Defense; Elsevier Ltd, 2016; Vol. 58. https://doi.org/10.1016/j.progpolymsci.2016.04.003.

(166) Chung, W. J.; Griebel, J. J.; Kim, E. T.; Yoon, H.; Simmonds, A. G.; Ji, H. J.; Dirlam, P. T.; Glass, R. S.; Wie, J. J.; Nguyen, N. A.; Guralnick, B. W.; Park, J.; Somogyi, Á.; Theato, P.; Mackay, M. E.; Sung, Y.-E.; Char, K.; Pyun, J. The Use of Elemental Sulfur as an Alternative Feedstock for Polymeric Materials. Nat. Chem. 2013, 5 (6), 518–524. https://doi.org/10.1038/nchem.1624.

(167) Wręczycki, J.; Bieliński, D. M.; Anyszka, R. Sulfur/Organic Copolymers as Curing Agents for Rubber. Polymers (Basel) 2018, 10 (8), E870. https://doi.org/10.3390/polym10080870.

(168) Parker, D. J.; Jones, H. A.; Petcher, S.; Cervini, L.; Griffin, J. M.; Akhtar, R.; Hasell, T. Low Cost and Renewable Sulfur-Polymers by Inverse Vulcanisation, and Their Potential for Mercury Capture. J. Mater. Chem. A 2017, 5 (23), 11682–11692. https://doi.org/10.1039/C6TA09862B.

(169) Smith, A. D.; McMillen, C. D.; Smith, R. C.; Tennyson, A. G. Copolymers by Inverse Vulcanization of Sulfur with Pure or Technical-Grade Unsaturated Fatty Acids. J. Polym. Sci. 2020, 58 (3), 438–445. https://doi.org/10.1002/pol.20190138.

(170) Smith, A. D.; Tennyson, A. G.; Smith, R. C. Sulfur-Containing Polymers Prepared from Fatty Acid-Derived Monomers: Application of Atom-Economical Thiol-Ene/Thiol-Yne Click Reactions and Inverse Vulcanization Strategies. ACS Sustain. Chem. 2020, 1 (3), 209–237. https://doi.org/10.3390/suschem1030015.

(171) Smith, A. D.; Thiounn, T.; Lyles, E. W.; Kibler, E. K.; Smith, R. C.; Tennyson, A. G. Combining Agriculture and Energy Industry Waste Products to Yield Recyclable, Thermally Healable Copolymers of Elemental Sulfur and Oleic Acid. J. Polym. Sci. 2019, 57 (15), 1704–1710. https://doi.org/10.1002/pola.29436.

(172) Wu, X.; Smith, J. A.; Petcher, S.; Zhang, B.; Parker, D. J.; Griffin, J. M.; Hasell, T. Catalytic Inverse Vulcanization. Nat. Commun. 2019, 10 (1), 647. https://doi.org/10.1038/s41467-019-08430-8.

(173) Dodd, L. J.; Omar, Ö.; Wu, X.; Hasell, T. Investigating the Role and Scope of Catalysts in Inverse Vulcanization. ACS Catal. 2021, 11 (8), 4441–4455. https://doi.org/10.1021/acscatal.0c05010.

(174) Moldoveanu, S. C. Pyrolysis of Organic Molecules: Applications to Health and Environmental Issues; 2018. https://doi.org/10.1016/C2016-0-05137-9.

(175) Asomaning, J.; Mussone, P.; Bressler, D. C. Pyrolysis of Polyunsaturated Fatty Acids. Fuel Process. Technol. 2014, 120, 89–95. https://doi.org/10.1016/j.fuproc.2013.12.007.

(176) Asomaning, J.; Mussone, P.; Bressler, D. C. Thermal Deoxygenation and Pyrolysis of Oleic Acid. J. Anal. Appl. Pyrolysis 2014, 105, 1–7. https://doi.org/10.1016/j.jaap.2013.09.005.

(177) Maher, K. D.; Kirkwood, K. M.; Gray, M. R.; Bressler, D. C. Pyrolytic Decarboxylation and Cracking of Stearic Acid. Ind. Eng. Chem. Res. 2008, 47 (15), 5328–5336. https://doi.org/10.1021/ie0714551.

(178) Kubátová, A.; Kubátová, K.;ˇ T'ávová, Ávováávová, J. S.; Seames, W. S.; Luo, Y.; Sadrameli, S. M.; Linnen, M. J.; Baglayeva, G. V; Smoliakova, I. P.; Kozliak, E. I. Triacylglyceride Thermal Cracking: Pathways to Cyclic Hydrocarbons. Energy Fuels 2012, 26, 47. https://doi.org/10.1021/ef200953d.

(179) Idem, R. O.; Katikaneni, S. P. R.; Bakhshi, N. N. Thermal Cracking of Canola Oil: Reaction Products in the Presence and Absence of Steam. Energy Fuels 1996, 10 (6), 1150–1162. https://doi.org/10.1021/ef960029h.

(180) Sarkar, S.; Bekyarova, E.; Niyogi, S.; Haddon, R. C. Diels-Alder Chemistry of Graphite and Graphene: Graphene as Diene and Dienophile. Journal of the American Chemical Society 2011, 133 (10), 3324–3327. https://doi.org/10.1021/ja200118b.

(181) Xu, X.; Ray, R.; Gu, Y.; Ploehn, H. J.; Gearheart, L.; Raker, K.; Scrivens, W. A. Electrophoretic Analysis and Purification of Fluorescent Single-Walled Carbon Nanotube Fragments. J. Am. Chem. Soc. 2004, 126 (40), 12736–12737. https://doi.org/10.1021/ja040082h.

(182) Hsu, P. C.; Chen, P. C.; Ou, C. M.; Chang, H. Y.; Chang, H. T. Extremely High Inhibition Activity of Photoluminescent Carbon Nanodots toward Cancer Cells. Journal of Materials Chemistry B 2013, 1 (13), 1774–1781. https://doi.org/10.1039/c3tb00545c.

(183) Jiang, K.; Sun, S.; Zhang, L.; Lu, Y.; Wu, A.; Cai, C.; Lin, H. Red, Green, and Blue Luminescence by Carbon Dots: Full-Color Emission Tuning and Multicolor Cellular Imaging. Angew. Chem. Int. Ed. 2015, 54 (18), 5360–5363. https://doi.org/10.1002/anie.201501193.

(184) Zhou, L.; Geng, J.; Liu, B. Graphene Quantum Dots from Polycyclic Aromatic Hydrocarbon for Bioimaging and Sensing of Fe3+ and Hydrogen Peroxide. Particle and Particle Systems Characterization 2013, 30 (12), 1086–1092. https://doi.org/10.1002/ppsc.201300170.

(185) Liu, J.; Li, R.; Yang, B. Carbon Dots: A New Type of Carbon-Based Nanomaterial with Wide Applications. ACS Cent. Sci. 2020, 6 (12), 2179–2195. https://doi.org/10.1021/acscentsci.0c01306.

(186) Dong, Y.; Shao, J.; Chen, C.; Li, H.; Wang, R.; Chi, Y.; Lin, X.; Chen, G. Blue Luminescent Graphene Quantum Dots and Graphene Oxide Prepared by Tuning the Carbonization Degree of Citric Acid. Carbon 2012, 50 (12), 4738–4743. https://doi.org/10.1016/j.carbon.2012.06.002.

(187) Rimal, V.; Shishodia, S.; Srivastava, P. K. Novel Synthesis of High-Thermal Stability Carbon Dots and Nanocomposites from Oleic Acid as an Organic Substrate. Appl. Nanosci. 2020, 10 (2), 455–464. https://doi.org/10.1007/s13204-019-01178-z.

(188) Kwon, W.; Do, S.; Lee, J.; Hwang, S.; Kim, J. K.; Rhee, S.-W. Freestanding Luminescent Films of Nitrogen-Rich Carbon Nanodots toward Large-Scale Phosphor-Based White-Light-Emitting Devices. Chem. Mater. 2013, 25 (9), 1893–1899. https://doi.org/10.1021/cm400517g.

(189) S. A., N.; P. B. C., F. Development of a Turn-on Graphene Quantum Dot-Based Fluorescent Probe for Sensing of Pyrene in Water. RSC Advances 2020, 10 (21), 12119–12128. https://doi.org/10.1039/c9ra10153e.

(190) Calcabrini, M.; Van den Eynden, D.; Ribot, S. S.; Pokratath, R.; Llorca, J.; De Roo, J.; Ibáñez, M. Ligand Conversion in Nanocrystal Synthesis: The Oxidation of Alkylamines to Fatty Acids by Nitrate. JACS Au 2021, 1 (11), 1898–1903. https://doi.org/10.1021/jacsau.1c00349.

(191) Bree, G.; Coughlan, C.; Geaney, H.; Ryan, K. M. Investigation into the Selenization Mechanisms of Wurtzite CZTS Nanorods. ACS Applied Materials and Interfaces 2018, 10 (8), 7117–7125. https://doi.org/10.1021/acsami.7b18711.

(192) Sperry, B. M.; Luscombe, C. K. Ligand Pyrolysis during Air-Free Inorganic Nanocrystal Synthesis. Chem. Mater. 2021, 33, 136–145. https://doi.org/10.1021/acs.chemmater.0c03088.

(193) Phan, C. M.; Nguyen, H. M. Role of Capping Agent in Wet Synthesis of Nanoparticles. Journal of Physical Chemistry A 2017, 121 (17), 3213–3219. https://doi.org/10.1021/acs.jpca.7b02186.

(194) Salavati-Niasari, M.; Davar, F.; Mazaheri, M.; Shaterian, M. Preparation of Cobalt Nanoparticles from [Bis(Salicylidene)Cobalt(II)]–Oleylamine Complex by Thermal Decomposition. Journal of Magnetism and Magnetic Materials 2008, 320 (3–4), 575–578. https://doi.org/10.1016/J.JMMM.2007.07.020.

(195) Huang, X.; Parashar, V. K.; Gijs, M. A. M. Nucleation and Growth Behavior of CdSe Nanocrystals Synthesized in the Presence of Oleylamine Coordinating Ligand. Langmuir 2018, 34 (21), 6070–6076. https://doi.org/10.1021/acs.langmuir.7b01337.

(196) Salavati-Niasari, M.; Davar, F.; Mazaheri, M. Preparation of ZnO Nanoparticles from [Bis(Acetylacetonato)Zinc(II)]–Oleylamine Complex by Thermal Decomposition. Materials Letters 2008, 62 (12–13), 1890–1892. https://doi.org/10.1016/J.MATLET.2007.10.032.

(197) Magdassi, S.; Grouchko, M.; Berezin, O.; Kamyshny, A. Triggering the Sintering of Silver Nanoparticles at Room Temperature. 2010. https://doi.org/10.1021/nn901868t.

(198) Engberg, S.; Canulescu, S.; Schou, J. Liquid Phase Assisted Grain Growth in Cu2ZnSnS4nanoparticle Thin Films by Alkali Element Incorporation. RSC Advances 2018, 8 (13), 7152–7158. https://doi.org/10.1039/c7ra13472j.

(199) Fichthorn, K. A.; Miron, R. A. Thermal Desorption of Large Molecules from Solid Surfaces. Physical Review Letters 2002, 89 (19), 2–5. https://doi.org/10.1103/PhysRevLett.89.196103.

(200) Dreyer, D. R.; Park, S.; Bielawski, C. W.; Ruoff, R. S. The Chemistry of Graphene Oxide. 2009. https://doi.org/10.1039/b917103g.

(201) Bucherl, C. N.; Oleson, K. R.; Hillhouse, H. W. Thin Film Solar Cells from Sintered Nanocrystals. Current Opinion in Chemical Engineering 2013, 2 (2), 168–177. https://doi.org/10.1016/j.coche.2013.03.004.

(202) Liu, Z.; Niu, S.; Wang, N. Oleylamine-Functionalized Graphene Oxide as an Electron Block Layer towards High-Performance and Photostable Fullerene-Free Polymer Solar Cells. Nanoscale 2017, 9 (42), 16293–16304. https://doi.org/10.1039/C7NR05939F.

(203) Ha, E.; Liu, W.; Wang, L.; Man, H.-W.; Hu, L.; Tsang, S. C. E.; Chan, C. T.-L.; Kwok, W.-M.; Lee, L. Y. S.; Wong, K.-Y. Cu2ZnSnS4/MoS2-Reduced Graphene Oxide Heterostructure: Nanoscale Interfacial Contact and Enhanced Photocatalytic Hydrogen Generation. Scientific Reports 2017, 7 (1), 39411. https://doi.org/10.1038/srep39411.

(204) Togashi, T.; Nakayama, M.; Hashimoto, A.; Ishizaki, M.; Kanaizuka, K.; Kurihara, M. Solvent-Free Synthesis of Monodisperse Cu Nanoparticles by Thermal Decomposition of an Oleylamine-Coordinated Cu Oxalate Complex. Dalton Transactions 2018, 47 (15), 5342–5347. https://doi.org/10.1039/C8DT00345A.

(205) Monfared, A. H.; Zamanian, A.; Beygzadeh, M.; Sharifi, I.; Mozafari, M. A Rapid and Efficient Thermal Decomposition Approach for the Synthesis of Manganese-Zinc/Oleylamine Core/Shell Ferrite Nanoparticles. Journal of Alloys and Compounds 2017, 693, 1090–1095. https://doi.org/10.1016/J.JALLCOM.2016.09.253.

(206) Dierick, R.; Van Den Broeck, F.; De Nolf, K.; Zhao, Q.; Vantomme, A.; Martins, J. C.; Hens, Z. Surface Chemistry of CuInS2colloidal Nanocrystals, Tight Binding of L-Type Ligands. Chemistry of Materials 2014, 26 (20), 5950–5957. https://doi.org/10.1021/cm502687p.

(207) Fernandes, P. A.; Salomé, P. M. P.; Da Cunha, A. F. Study of Polycrystalline Cu2ZnSnS4 Films by Raman Scattering. Journal of Alloys and Compounds 2011, 509 (28), 7600–7606. https://doi.org/10.1016/j.jallcom.2011.04.097.

(208) Cheng, A.-J.; Manno, M.; Khare, A.; Leighton, C.; Campbell, S. A.; Aydil, E. S. Imaging and Phase Identification of Cu2ZnSnS4 Thin Films Using Confocal Raman Spectroscopy. Journal of Vacuum Science & Technology A: Vacuum, Surfaces, and Films 2011, 29 (5), 051203. https://doi.org/10.1116/1.3625249.

(209) Larkin, P. Infrared and Raman Spectroscopy: Principles and Spectral Interpretation, 1st ed.; Elsevier, 2011. https://doi.org/10.1016/B978-0-12-386984-5.10001-1.

(210) Sadezky, A.; Muckenhuber, H.; Grothe, H.; Niessner, R.; Pöschl, U. Raman Microspectroscopy of Soot and Related Carbonaceous Materials: Spectral Analysis and Structural Information. Carbon 2005, 43 (8), 1731–1742. https://doi.org/10.1016/j.carbon.2005.02.018.

(211) Merlen, A.; Buijnsters, J. G.; Pardanaud, C. A Guide to and Review of the Use of Multiwavelength Raman Spectroscopy for Characterizing Defective Aromatic Carbon Solids: From Graphene to Amorphous Carbons. Coatings 2017, 7 (10), 153–208. https://doi.org/10.3390/coatings7100153.

(212) Baranov, D.; Lynch, M. J.; Curtis, A. C.; Carollo, A. R.; Douglass, C. R.; Mateo-Tejada, A. M.; Jonas, D. M. Purification of Oleylamine for Materials Synthesis and Spectroscopic Diagnostics for Trans Isomers. Chemistry of Materials 2019, 31 (4), 1223–1230. https://doi.org/10.1021/acs.chemmater.8b04198.

(213) Asomaning, J.; Mussone, P.; Bressler, D. C. Thermal Deoxygenation and Pyrolysis of Oleic Acid. Journal of Analytical and Applied Pyrolysis 2014, 105, 1–7. https://doi.org/10.1016/j.jaap.2013.09.005.

(214) Martin, T. R.; Katahara, J. K.; Bucherl, C. N.; Krueger, B. W.; Hillhouse, H. W.; Luscombe, C. K. Nanoparticle Ligands and Pyrolized Graphitic Carbon in CZTSSe Photovoltaic Devices. Chemistry of Materials 2016, 28 (1), 135–145. https://doi.org/10.1021/acs.chemmater.5b03426.

(215) Lynch, M. An Investigation of Solutions of Sulfur in Oleylamine by Raman Spectroscopy and Their Relation to Lead Sulfide Quantum Dot Synthesis, University of Colorado, Boulder, 2017.

(216) Ferrari, A. C. Raman Spectroscopy of Graphene and Graphite: Disorder, Electron-Phonon Coupling, Doping and Nonadiabatic Effects. Solid State Communications 2007, 143 (1–2), 47–57. https://doi.org/10.1016/j.ssc.2007.03.052.

(217) Childres, I.; Jauregui, L. A.; Park, W.; Cao, H.; Chen, Y. P. Raman Spectroscopy of Graphene and Related Materials. In New developments in photon and materials research; Nova Science Publishers: Hauppauge, NY, 2013; pp 403–418. https://doi.org/10.1016/B978-0-444-53175-9.00016-7.

(218) Merlen, A.; Buijnsters, J. G.; Pardanaud, C. A Guide to and Review of the Use of Multiwavelength Raman Spectroscopy for Characterizing Defective Aromatic Carbon Solids: From Graphene to Amorphous Carbons. Coatings 2017, 7 (10), 153–208. https://doi.org/10.3390/coatings7100153.

(219) Wu, J. Bin; Lin, M. L.; Cong, X.; Liu, H. N.; Tan, P. H. Raman Spectroscopy of Graphene-Based Materials and Its Applications in Related Devices. Chemical Society Reviews 2018, 47 (5), 1822–1873. https://doi.org/10.1039/c6cs00915h.

(220) Chu, P. K.; Li, L. Characterization of Amorphous and Nanocrystalline Carbon Films. Materials Chemistry and Physics 2006, 96 (2–3), 253–277. https://doi.org/10.1016/j.matchemphys.2005.07.048.

(221) Zheng, P.; Wu, N. Fluorescence and Sensing Applications of Graphene Oxide and Graphene Quantum Dots: A Review. Chemistry - An Asian Journal 2017, 12 (18), 2343–2353. https://doi.org/10.1002/asia.201700814.

(222) Hong, J.; Park, M. K.; Lee, E. J.; Lee, D.; Hwang, D. S.; Ryu, S. Origin of New Broad Raman D and G Peaks in Annealed Graphene. Scientific Reports 2013, 3 (1), 2700. https://doi.org/10.1038/srep02700.

(223) Schwan, J.; Ulrich, S.; Batori, V.; Ehrhardt, H.; Silva, S. R. P. Raman Spectroscopy on Amorphous Carbon Films. Journal of Applied Physics 1996, 80 (1), 440–447. https://doi.org/10.1063/1.362745.

(224) Dave, K.; Park, K. H.; Dhayal, M. Two-Step Process for Programmable Removal of Oxygen Functionalities of Graphene Oxide: Functional, Structural and Electrical Characteristics. RSC Advances 2015, 5 (116), 95657–95665. https://doi.org/10.1039/c5ra18880f.

(225) Caṇado, L. G.; Takai, K.; Enoki, T.; Endo, M.; Kim, Y. A.; Mizusaki, H.; Jorio, A.; Coelho, L. N.; Magalhães-Paniago, R.; Pimenta, M. A. General Equation for the Determination of the Crystallite Size La of Nanographite by Raman Spectroscopy. Applied Physics Letters 2006, 88 (16), 163106. https://doi.org/10.1063/1.2196057.

(226) Tunistra, F.; Koenig, J. L. Raman Spectrum of Graphite. Journal of Chemical Physics 1970, 53 (3), 1126–1130. https://doi.org/10.1063/1.1674108.

(227) Yang, K.; Liang, S.; Zou, L.; Huang, L.; Park, C.; Zhu, L.; Fang, J.; Fu, Q.; Wang, H. Intercalating Oleylamines in Graphite Oxide. Langmuir 2012, 28 (5), 2904–2908. https://doi.org/10.1021/la203769p.

(228) Bhuyan, Md. S. A.; Uddin, Md. N.; Islam, Md. M.; Bipasha, F. A.; Hossain, S. S. Synthesis of Graphene. International Nano Letters 2016, 6 (2), 65–83. https://doi.org/10.1007/s40089-015-0176-1.

(229) Obraztsov, A. N.; Obraztsova, E. A.; Tyurnina, A. V.; Zolotukhin, A. A. Chemical Vapor Deposition of Thin Graphite Films of Nanometer Thickness. Carbon 2007, 45 (10), 2017–2021. https://doi.org/10.1016/j.carbon.2007.05.028.

(230) Wang, J. J.; Zhu, M. Y.; Outlaw, R. A.; Zhao, X.; Manos, D. M.; Holloway, B. C.; Mammana, V. P. Free-Standing Subnanometer Graphite Sheets. Applied Physics Letters 2004, 85 (7), 1265–1267. https://doi.org/10.1063/1.1782253.

(231) Xia, C.; Zhu, S.; Feng, T.; Yang, M.; Yang, B. Evolution and Synthesis of Carbon Dots: From Carbon Dots to Carbonized Polymer Dots. Advanced Science 2019, 6 (23), 20190. https://doi.org/10.1002/advs.201901316.

(232) Hsu, P. C.; Chen, P. C.; Ou, C. M.; Chang, H. Y.; Chang, H. T. Extremely High Inhibition Activity of Photoluminescent Carbon Nanodots toward Cancer Cells. Journal of Materials Chemistry B 2013, 1 (13), 1774–1781. https://doi.org/10.1039/c3tb00545c.

(233) Dai, B.; Wu, C.; Lu, Y.; Deng, D.; Xu, S. Synthesis and Formation Mechanism of S-Doped Carbon Dots from Low-Molecule-Weight Organics. Journal of Luminescence 2017, 190, 108–114. https://doi.org/10.1016/j.jlumin.2017.04.054.

(234) Zhou, L.; Geng, J.; Liu, B. Graphene Quantum Dots from Polycyclic Aromatic Hydrocarbon for Bioimaging and Sensing of Fe3+ and Hydrogen Peroxide. Particle and Particle Systems Characterization 2013, 30 (12), 1086–1092. https://doi.org/10.1002/ppsc.201300170.

(235) Cao, Y.; Denny, M. S.; Caspar, J. V.; Farneth, W. E.; Guo, Q.; Ionkin, A. S.; Johnson, L. K.; Lu, M.; Malajovich, I.; Radu, D.; Rosenfeld, H. D.; Choudhury, K. R.; Wu, W. High-Efficiency Solution-Processed Cu2ZnSn(S,Se)4 Thin-Film Solar Cells Prepared from Binary and Ternary Nanoparticles. Journal of the American Chemical Society 2012, 134 (38), 15644–15647. https://doi.org/10.1021/ja3057985.

(236) Wu, J.-B.; Lin, M.-L.; Cong, X.; Liu, H.-N.; Tan, P.-H. Raman Spectroscopy of Graphene-Based Materials and Its Applications in Related Devices. Chemical Society Reviews 2018, 47 (5), 1822–1873. https://doi.org/10.1039/C6CS00915H.

(237) Sadezky, A.; Muckenhuber, H.; Grothe, H.; Niessner, R.; Pö Schl, U. Raman Microspectroscopy of Soot and Related Carbonaceous Materials: Spectral Analysis and Structural Information. 2005. https://doi.org/10.1016/j.carbon.2005.02.018.

(238) Engberg, S.; Canulescu, S.; Schou, J. Liquid Phase Assisted Grain Growth in Cu2ZnSnS4 Nanoparticle Thin Films by Alkali Element Incorporation. RSC Advances 2018, 8 (13), 7152–7158. https://doi.org/10.1039/c7ra13472j.

(239) Achten, C.; Andersson, J. T. Overview of Polycyclic Aromatic Compounds (PAC). Polycyclic Aromatic Compounds 2015, 35 (2–4), 177–186. https://doi.org/10.1080/10406638.2014.994071.

(240) Min, Y.; He, G.; Xu, Q.; Chen, Y. Self-Assembled Encapsulation of Graphene Oxide/Ag@AgCl as a Z-Scheme Photocatalytic System for Pollutant Removal. Journal of Materials Chemistry A 2014, 2 (5), 1294–1301. https://doi.org/10.1039/c3ta13687f.

(241) Ederer, J.; Janoš, P.; Ecorchard, P.; Tolasz, J.; Štengl, V.; Beneš, H.; Perchacz, M.; Pop-Georgievski, O. Determination of Amino Groups on Functionalized Graphene Oxide for Polyurethane Nanomaterials: XPS Quantitation vs. Functional Speciation. RSC Advances 2017, 7 (21), 12464–12473. https://doi.org/10.1039/c6ra28745j.

(242) Wilson, D.; Langell, M. A. XPS Analysis of Oleylamine/Oleic Acid Capped Fe 3 O 4 Nanoparticles as a Function of Temperature. Applied Surface Science 2014, 303, 6–13. https://doi.org/10.1016/j.apsusc.2014.02.006.

(243) Kim, E. T.; Chung, W. J.; Lim, J.; Johe, P.; Glass, R. S.; Pyun, J.; Char, K. One-Pot Synthesis of PbS NP/Sulfur-Oleylamine Copolymer Nanocomposites via the Copolymerization of Elemental Sulfur with Oleylamine. Polymer Chemistry 2014, 5 (11), 3617–3623. https://doi.org/10.1039/c4py00073k.

(244) Zhang, Y.; Glass, R. S.; Char, K.; Pyun, J. Recent Advances in the Polymerization of Elemental Sulphur, Inverse Vulcanization and Methods to Obtain Functional Chalcogenide Hybrid Inorganic/Organic Polymers (CHIPs). Polymer Chemistry 2019, 10 (30), 4078–4105. https://doi.org/10.1039/c9py00636b.

(245) Sperry, B. M.; Kukhta, N. A.; Huang, Y.; Luscombe, C. K. Ligand Decomposition during Nanoparticle Synthesis: Influence of Ligand Structure and Precursor Selection. Chem. Mater. 2023, acs.chemmater.2c03006. https://doi.org/10.1021/acs.chemmater.2c03006.

(246) Wolcott, A.; Fitzmorris, R. C.; Muzaffery, O.; Zhang, J. Z. CdSe Quantum Rod Formation Aided By In Situ TOPO Oxidation. Chem. Mater. 2010, 22 (9), 2814–2821. https://doi.org/10.1021/cm903740e.

(247) Kim, E. T.; Chung, W. J.; Lim, J.; Johe, P.; Glass, R. S.; Pyun, J.; Char, K. One-Pot Synthesis of PbS NP/Sulfur-Oleylamine Copolymer Nanocomposites via the Copolymerization of Elemental Sulfur with Oleylamine. Polym. Chem. 2014, 5 (11), 3617–3623. https://doi.org/10.1039/c4py00073k.

(248) Lynch, M. An Investigation of Solutions of Sulfur in Oleylamine by Raman Spectroscopy and Their Relation to Lead Sulfide Quantum Dot Synthesis. Undergraduate Honors Theses, University of Colorado, Boulder, USA, 2017.

(249) Thomson, J. W.; Nagashima, K.; MacDonald, P. M.; Ozin, G. A. From Sulfur-Amine Solutions to Metal Sulfide Nanocrystals: Peering into the Oleylamine-Sulfur Black Box. J. Am. Chem. Soc. 2011, 133 (13), 5036–5041. https://doi.org/10.1021/ja1109997.

(250) Reiss, P.; Carrière, M.; Lincheneau, C.; Vaure, L.; Tamang, S. Synthesis of Semiconductor Nanocrystals, Focusing on Nontoxic and Earth-Abundant Materials. Chem. Rev. 2016, 116 (18), 10731–10819. https://doi.org/10.1021/acs.chemrev.6b00116.

(251) Worthington, M. J. H.; Kucera, R. L.; Chalker, J. M. Green Chemistry and Polymers Made from Sulfur. Green Chem. 2017, 19 (12), 2748–2761. https://doi.org/10.1039/C7GC00014F.

(252) Abarca, R. Q.; Guevara, J. L.; Yazdani-Pedram, M.; Galland, G. B.; Ribeiro, D. Study of the Polymerization of 1-Octadecene with Different Metallocene Catalysts. Polym. Bull. 2002, 49 (4), 273–280. https://doi.org/10.1007/s00289-002-0103-2.

(253) Walsh, D. J.; Hyatt, M. G.; Miller, S. A.; Guironnet, D. Recent Trends in Catalytic Polymerizations. ACS Catal. 2019, 9 (12), 11153–11188. https://doi.org/10.1021/acscatal.9b03226.

(254) Erman, B.; Mark, J. E.; Roland, M. C. Chapter 7 - Vulcanization. In Science and Technology of Rubber; Elsevier, 2013; pp 337–381.

(255) Sandler, S. R.; Karo, W. Chapter 3 - Sulfide Polymers. In Polymer Syntheses; Elsevier Inc, 1996; Vol. 3, pp 73–119.

(256) Sen, M. Y. Synthesis of Middle-Chain Carboxyl- and Primary Amine-Functionalized Polystyrenes Using Anionic Polymerization Techniques. Master of Science Thesis, The University of Akron, USA, 2005.

(257) Kubátová, A.; Ŝávová, J.; Seames, W. S.; Luo, Y.; Sadrameli, S. M.; Linnen, M. J.; Baglayeva, G. V.; Smoliakova, I. P.; Kozliak, E. I. Triacylglyceride Thermal Cracking: Pathways to Cyclic Hydrocarbons. Energy Fuels 2012, 26 (1), 672–685. https://doi.org/10.1021/ef200953d.

(258) Bourlinos, A. B.; Stassinopoulos, A.; Anglos, D.; Zboril, R.; Karakassides, M.; Giannelis, E. P. Surface Functionalized Carbogenic Quantum Dots. Small 2008, 4 (4), 455–458. https://doi.org/10.1002/smll.200700578.

(259) Niu, S.; Zhou, Y.; Yu, H.; Lu, C.; Han, K. Investigation on Thermal Degradation Properties of Oleic Acid and Its Methyl and Ethyl Esters through TG-FTIR. Energy Convers. Manag. 2017, 149, 495–504. https://doi.org/10.1016/j.enconman.2017.07.053.

(260) Baranov, D.; Lynch, M. J.; Curtis, A. C.; Carollo, A. R.; Douglass, C. R.; Mateo-Tejada, A. M.; Jonas, D. M. Purification of Oleylamine for Materials Synthesis and Spectroscopic Diagnostics for Trans Isomers. Chem. Mater. 2019, 31 (4), 1223–1230. https://doi.org/10.1021/acs.chemmater.8b04198.

(261) Martin, T. R.; Katahara, J. K.; Bucherl, C. N.; Krueger, B. W.; Hillhouse, H. W.; Luscombe, C. K. Nanoparticle Ligands and Pyrolized Graphitic Carbon in CZTSSe Photovoltaic Devices. Chemistry of Materials 2016, 28 (1), 135–145. https://doi.org/10.1021/acs.chemmater.5b03426.

(262) Butler, H. J.; Ashton, L.; Bird, B.; Cinque, G.; Curtis, K.; Dorney, J.; Esmonde-White, K.; Fullwood, N. J.; Gardner, B.; Martin-Hirsch, P. L.; Walsh, M. J.; McAinsh, M. R.; Stone, N.; Martin, F. L. Using Raman Spectroscopy to Characterize Biological Materials. Nat. Protoc. 2016, 11 (4), 664–687. https://doi.org/10.1038/nprot.2016.036.

(263) Standard Test Method for Thermal Stability by Thermogravimetry; Standard ASTM E2550-21; ASTM International, 2021. https://www.astm.org/e2550-21.html (accessed 2022-06-24).

(264) Standard Test Method for Compositional Analysis by Thermogravimetry; Standard ASTM E1131-20; ASTM International, 2020. https://www.astm.org/e1131-20.html (accessed 2022-06-24).

(265) Plastics — Thermogravimetry (TG) of Polymers; ISO 11358-1:2014(E); International Standard ISO 11358-1:2014(E); International Organization for Standardization, 2014. https://www.iso.org/standard/59710.html (accessed 2022-06-28).

(266) Pelletier, M. J. Quantitative Analysis Using Raman Spectrometry. Appl. Spectrosc. 2003, 57 (1), 20A-42A. https://doi.org/10.1366/000370203321165133.

(267) Ferrari, A. C. Raman Spectroscopy of Graphene and Graphite: Disorder, Electron-Phonon Coupling, Doping and Nonadiabatic Effects. Solid State Commun. 2007, 143 (1–2), 47–57. https://doi.org/10.1016/j.ssc.2007.03.052.

(268) Castiglioni, C.; Mapelli, C.; Negri, F.; Zerbi, G. Origin of the D Line in the Raman Spectrum of Graphite: A Study Based on Raman Frequencies and Intensities of Polycyclic Aromatic Hydrocarbon Molecules. J. Chem. Phys. 2001, 114 (2), 963–974. https://doi.org/10.1063/1.1329670.

(269) Childres, I.; Jauregui, L. A.; Park, W.; Cao, H.; Chen, Y. P. Raman Spectroscopy of Graphene and Related Materials. In New developments in photon and materials research; Nova Science Publishers: Hauppauge, NY, 2013; pp 403–418. https://doi.org/10.1016/B978-0-444-53175-9.00016-7.

(270) Hong, J.; Park, M. K.; Lee, E. J.; Lee, D.; Hwang, D. S.; Ryu, S. Origin of New Broad Raman D and G Peaks in Annealed Graphene. Sci. Rep. 2013, 3 (1), 2700. https://doi.org/10.1038/srep02700.

(271) Wu, J. B.; Lin, M. L.; Cong, X.; Liu, H. N.; Tan, P. H. Raman Spectroscopy of Graphene-Based Materials and Its Applications in Related Devices. Chem. Soc. Rev. 2018, 47 (5), 1822–1873. https://doi.org/10.1039/c6cs00915h.

(272) Dippel, B.; Jander, H.; Heintzenberg, J. NIR FT Raman Spectroscopic Study of Flame Soot. Phys. Chem. Chem. Phys. 1999, 1 (20), 4707–4712. https://doi.org/DOI: 10.1039/a904529e.

(273) Wu, J.; Wang, P.; Wang, F.; Fang, Y. Investigation of the Microstructures of Graphene Quantum Dots (GQDs) by Surface-Enhanced Raman Spectroscopy. Nanomaterials 2018, 8 (10), 864. https://doi.org/10.3390/nano8100864.

(274) Colomban, P.; Slodczyk, A. Raman Intensity: An Important Tool to Study the Structure and Phase Transitions of Amorphous/Crystalline Materials. Opt. Mater. 2009, 31 (12), 1759–1763. https://doi.org/10.1016/j.optmat.2008.12.030.

(275) Favors, R. N.; Jiang, Y.; Loethen, Y. L.; Ben-Amotz, D. External Raman Standard for Absolute Intensity and Concentration Measurements. Rev. Sci. Instrum. 2005, 76 (3), 033108. https://doi.org/10.1063/1.1866952.

(276) Vyazovkin, Sergey; Koga, Nobuyoshi; Schick, Christoph. Handbook of Thermal Analysis and Calorimetry - Recent Advances, Techniques and Applications, 2nd ed.; Elsevier, 2018; Vol. 6. https://doi.org/10.1016/B978-0-444-64062-8.00006-1.

(277) Tomić, N. Z. Chapter 17 - Thermal Studies of Compatibilized Polymer Blends. In Compatibilization of Polymer Blends; A.r., A., Thomas, S., Eds.; Elsevier, 2020; pp 489–510. https://doi.org/10.1016/B978-0-12-816006-0.00017-7.

(278) Moldoveanu, S. C. Pyrolysis of Amines and Imines. In Techniques and Instrumentation in Analytical Chemistry; Elsevier, 2010; Vol. 28, pp 349–364. https://doi.org/10.1016/S0167-9244(09)02813-3.

(279) Goodrum, J. W.; Siesel, E. M. Thermogravimetric Analysis for Boiling Points and Vapour Pressure. J. Therm. Anal. Calorim. 1996, 46 (5), 1251–1258. https://doi.org/10.1007/BF01979239.

(280) Tarasova, N. P.; Zanin, A. A.; Krivoborodov, E. G.; Mezhuev, Y. O. Elemental Sulphur in the Synthesis of Sulphur-Containing Polymers: Reaction Mechanisms and Green Prospects. RSC Adv. 2021, 11 (15), 9008–9020. https://doi.org/10.1039/D0RA10507D.

(281) Miyazaki, T.; Nishino, K.; Yoshimoto, S.; Ogiwara, Y.; Sakai, N. Indium-Catalyzed Reductive Sulfidation of Aromatic Carboxylic Acids and Aldehydes with Elemental Sulfur to Prepare Symmetrical Benzyl Sulfides. Eur. J. Org. Chem. 2015, 2015 (9), 1991–1994. https://doi.org/10.1002/ejoc.201403567.

(282) Standard Guide for Raman Shift Standards for Spectrometer Calibration; Standard E1840-96; ASTM International, 2014. https://www.astm.org/e1840-96r14.html (accessed 2022-07-06).

(283) Hagen, M.; Schiffels, P.; Hammer, M.; Dörfler, S.; Tübke, J.; Hoffmann, M. J.; Althues, H.; Kaskel, S. In-Situ Raman Investigation of Polysulfide Formation in Li-S Cells. J. Electrochem. Soc. 2013, 160 (8), A1205–A1214. https://doi.org/10.1149/2.045308jes.

(284) Hannauer, J.; Scheers, J.; Fullenwarth, J.; Fraisse, B.; Stievano, L.; Johansson, P. The Quest for Polysulfides in Lithium-Sulfur Battery Electrolytes: An Operando Confocal Raman Spectroscopy Study. ChemPhysChem 2015, 16 (13), 2755–2759. https://doi.org/10.1002/cphc.201500448.

(285) McPhail, M. R.; Weiss, E. A. Role of Organosulfur Compounds in the Growth and Final Surface Chemistry of PbS Quantum Dots. Chem. Mater. 2014, 26 (11), 3377–3384. https://doi.org/10.1021/cm4040819.

(286) Sudesh; Kumar, N.; Das, S.; Bernhard, C.; Varma, G. D. Effect of Graphene Oxide Doping on Superconducting Properties of Bulk MgB2. Supercond. Sci. Technol. 2013, 26 (9), 095008. https://doi.org/10.1088/0953-2048/26/9/095008.

(287) Sodhi, R. K.; Paul, S. An Overview of Metal Acetylacetonates: Developing Areas/Routes to New Materials and Applications in Organic Syntheses. Catal. Surv. Asia. 2018, 22 (1), 31–62. https://doi.org/10.1007/s10563-017-9239-9.

(288) Dziemidkiewicz, A.; Maciejewska, M. Manganese and Nickel Acetylacetonates as Curatives for Chloroprene Rubber Based on Heck's Reaction. Materials 2021, 14 (4), 807. https://doi.org/10.3390/ma14040807.

(289) Gawande, M. B.; Goswami, A.; Felpin, F.-X.; Asefa, T.; Huang, X.; Silva, R.; Zou, X.; Zboril, R.; Varma, R. S. Cu and Cu-Based Nanoparticles: Synthesis and Applications in Catalysis. Chem. Rev. 2016, 116 (6), 3722–3811. https://doi.org/10.1021/acs.chemrev.5b00482.

(290) Cova, C. M.; Zuliani, A.; Muñoz-Batista, M. J.; Luque, R. A Sustainable Approach for the Synthesis of Catalytically Active Peroxidase-Mimic ZnS Catalysts. ACS Sustain. Chem. Eng 2019, 7 (1), 1300–1307. https://doi.org/10.1021/acssuschemeng.8b04968.

(291) Maarof, S.; Ali, A. A.; Hashim, A. M. Synthesis of Large-Area Single-Layer Graphene Using Refined Cooking Palm Oil on Copper Substrate by Spray Injector-Assisted CVD. Nanoscale. Res. Lett. 2019, 14 (1), 143. https://doi.org/10.1186/s11671-019-2976-0.

(292) Bajpai, P. K.; Yadav, S.; Tiwari, A.; Virk, H. S. Recent Advances in the Synthesis and Characterization of Chalcogenide Nanoparticles. Solid State Phenom. 2014, 222, 187–233. https://doi.org/10.4028/www.scientific.net/SSP.222.187.

(293) Malik, M. A.; Afzaal, M.; O'Brien, P. Precursor Chemistry for Main Group Elements in Semiconducting Materials. Chem. Rev. 2010, 110 (7), 4417–4446. https://doi.org/10.1021/cr900406f.

(294) Khan, M. D.; Malik, M. A.; Revaprasadu, N. Progress in Selenium Based Metal-Organic Precursors for Main Group and Transition Metal Selenide Thin Films and Nanomaterials. Coord. Chem. Rev. 2019, 388, 24–47. https://doi.org/10.1016/j.ccr.2019.02.026.

(295) Koktysh, D. S.; McBride, J. R.; Rosenthal, S. J. Synthesis of SnS Nanocrystals by the Solvothermal Decomposition of a Single Source Precursor. Nanoscale Res Lett 2007, 2 (3), 144. https://doi.org/10.1007/s11671-007-9045-9.

(296) Uk Son, S.; Kyu Park, I.; Park, J.; Hyeon, T. Synthesis of Cu2O Coated Cu Nanoparticles and Their Successful Applications to Ullmann-Type Amination Coupling Reactions of Aryl Chlorides. Chem. Commun. 2004, No. 7, 778. https://doi.org/10.1039/b316147a.

(297) J.F. Liu, Y.Y. Bei, H.P. Wu, D. Shen, J.Z. Gong, X.G. Li, Y.W. Wang, N.P. Jiang, J.Z. Jiang,. Synthesis of Relatively Monodisperse ZnO Nanocrystals from a Precursor Zinc 2,4-Pentanedionate. Materials Letters 2007, 61 (13), 2837–2840. https://doi.org/10.1016/j.matlet.2007.03.028.

(298) Lim, J.; Pyun, J.; Char, K. Recent Approaches for the Direct Use of Elemental Sulfur in the Synthesis and Processing of Advanced Materials. Angewandte Chemie International Edition 2015, 54 (11), 3249–3258. https://doi.org/10.1002/anie.201409468.

(299) Sharifi Dehsari, H.; Halda Ribeiro, A.; Ersöz, B.; Tremel, W.; Jakob, G.; Asadi, K. Effect of Precursor Concentration on Size Evolution of Iron Oxide Nanoparticles. CrystEngComm 2017, 19 (44), 6694–6702. https://doi.org/10.1039/C7CE01406F.

(300) Kumar, M.; Dubey, A.; Adhikari, N.; Venkatesan, S.; Qiao, Q. Strategic Review of Secondary Phases, Defects and Defect-Complexes in Kesterite CZTS-Se Solar Cells. Energy and Environmental Science 2015, 8 (11), 3134–3159. https://doi.org/10.1039/c5ee02153g.

(301) Dai, L.; Lesyuk, R.; Karpulevich, A.; Torche, A.; Bester, G.; Klinke, C. From Wurtzite Nanoplatelets to Zinc Blende Nanorods: Simultaneous Control of Shape and Phase in Ultrathin ZnS Nanocrystals. J. Phys. Chem. Lett. 2019, 10 (14), 3828–3835. https://doi.org/10.1021/acs.jpclett.9b01466.

(302) Ingham, B.; Lim, T. H.; Dotzler, C. J.; Henning, A.; Toney, M. F.; Tilley, R. D. How Nanoparticles Coalesce: An in Situ Study of Au Nanoparticle Aggregation and Grain Growth. Chemistry of Materials 2011, 23 (14), 3312–3317. https://doi.org/10.1021/cm200354d.

(303) Ahmad, R.; Saddiqi, N. U. H.; Wu, M.; Prato, M.; Spiecker, E.; Peukert, W.; Distaso, M. Effect of the Counteranion on the Formation Pathway of Cu2ZnSnS4 (CZTS) Nanoparticles under Solvothermal Conditions. Inorganic Chemistry 2020, 59 (3), 1973–1984. https://doi.org/10.1021/acs.inorgchem.9b03338.

(304) Shon, Y.-S.; Lee, T. R. Desorption and Exchange of Self-Assembled Monolayers (SAMs) on Gold Generated from Chelating Alkanedithiols. J. Phys. Chem. B 2000, 104 (34), 8192–8200. https://doi.org/10.1021/jp000651h.

(305) Schroffenegger, M.; Reimhult, E. Thermoresponsive Core-Shell Nanoparticles: Does Core Size Matter? Materials 2018, 11 (9), 1654. https://doi.org/10.3390/ma11091654.

(306) Jheng, L.-C.; Wang, Y.-Z.; Huang, W.-Y.; Ho, K.-S.; Tsai, C.-H.; Huang, C.-T.; Tsai, H.-S. Melting and Recrystallization of Copper Nanoparticles Prepared by Microwave-Assisted Reduction in the Presence of Triethylenetetramine. Materials 2020, 13 (7), 1507. https://doi.org/10.3390/ma13071507.

(307) Baranov, D.; Manna, L.; Kanaras, A. G. Chemically Induced Self-Assembly of Spherical and Anisotropic Inorganic Nanocrystals. Journal of Materials Chemistry 2011, 21 (42), 16694–16703. https://doi.org/10.1039/c1jm11599e.

(308) Mehner, T.; Uland, M.; Lampke, T. Analytical Model to Calculate the Grain Size of Bulk Material Based on Its Electrical Resistance. Metals 2020, 11 (1), 21. https://doi.org/10.3390/met11010021.

(309) Mingard, K. P.; Roebuck, B.; Bennett, E. G.; Gee, M. G.; Nordenstrom, H.; Sweetman, G.; Chan, P. Comparison of EBSD and Conventional Methods of Grain Size Measurement of Hardmetals. International Journal of Refractory Metals and Hard Materials 2009, 27 (2), 213–223. https://doi.org/10.1016/j.ijrmhm.2008.06.009.

(310) Fantauzzi, M.; Elsener, B.; Atzei, D.; Rigoldi, A.; Rossi, A. Exploiting XPS for the Identification of Sulfides and Polysulfides. RSC Adv. 2015, 5 (93), 75953–75963. https://doi.org/10.1039/C5RA14915K.

(311) Van Oversteeg, C. H. M.; Oropeza, F. E.; Hofmann, J. P.; Hensen, E. J. M.; De Jongh, P. E.; De Mello Donega, C. Water-Dispersible Copper Sulfide Nanocrystals via Ligand Exchange of 1-Dodecanethiol. Chem. Mater 2019, 31, 51. https://doi.org/10.1021/acs.chemmater.8b04614.

(312) Ornelas-Hernández, L. F.; Garduno-Robles, A.; Zepeda-Moreno, A. A Brief Review of Carbon Dots–Silica Nanoparticles Synthesis and Their Potential Use as Biosensing and Theragnostic Applications. Nanoscale Res Lett 2022, 17 (1), 56. https://doi.org/10.1186/s11671-022-03691-7.

(313) Zhao, Z.; Liu, Z.; Zhang, A.; Yan, X.; Xue, W.; Peng, B.; Xin, H. L.; Pan, X.; Duan, X.; Huang, Y. Graphene-Nanopocket-Encaged PtCo Nanocatalysts for Highly Durable Fuel Cell Operation under Demanding Ultralow-Pt-Loading Conditions. Nat. Nanotechnol. 2022, 17 (9), 968–975. https://doi.org/10.1038/s41565-022-01170-9.

(314) Dervishi, E.; Ji, Z.; Htoon, H.; Sykora, M.; Doorn, S. K. Raman Spectroscopy of Bottom-up Synthesized Graphene Quantum Dots: Size and Structure Dependence. Nanoscale 2019, 11 (35), 16571–16581. https://doi.org/10.1039/C9NR05345J.

(315) Đorđević, L.; Arcudi, F.; Cacioppo, M.; Prato, M. A Multifunctional Chemical Toolbox to Engineer Carbon Dots for Biomedical and Energy Applications. Nat. Nanotechnol. 2022, 17 (2), 112–130. https://doi.org/10.1038/s41565-021-01051-7.

(316) Jiang, X. C.; Chen, C. Y.; Chen, W. M.; Yu, A. B. Role of Citric Acid in the Formation of Silver Nanoplates through a Synergistic Reduction Approach. Langmuir 2010, 26 (6), 4400–4408. https://doi.org/10.1021/la903470f.

(317) Jiang, X. C.; Chen, W. M.; Chen, C. Y.; Xiong, S. X.; Yu, A. B. Role of Temperature in the Growth of Silver Nanoparticles Through a Synergetic Reduction Approach. Nanoscale Res Lett 2010. https://doi.org/10.1007/s11671-010-9780-1.

(318) S. A., N.; P. B. C., F. Development of a Turn-on Graphene Quantum Dot-Based Fluorescent Probe for Sensing of Pyrene in Water. RSC Advances 2020, 10 (21), 12119–12128. https://doi.org/10.1039/C9RA10153E.

(319) Gadgeel, A. A.; Mhaske, S. T.; Duerr, C.; Liu, K. L. In-Situ Preparation and Characterization of Aconitic Acid Capped Fe4O2 Nanoparticle by Using Citric Acid as a Reducing Agent. J Inorg Organomet Polym 2019, 29 (5), 1688–1700. https://doi.org/10.1007/s10904-019-01131-1.

(320) Robaiah, M.; Mahmud, M. A.; Salifairus, M. J.; Khusaimi, Z.; Azhan, H.; Abdullah, S.; Rusop, M.; Asli, N. A. Synthesis and Characterization of Graphene from Waste Cooking Palm Oil at Different Deposition Temperatures; Selangor, Malaysia, 2019; p 020026. https://doi.org/10.1063/1.5124656.

(321) Fan, H.; Qiu, L.; Fedorov, A.; Willinger, M.-G.; Ding, F.; Huang, X. Dynamic State and Active Structure of Ni–Co Catalyst in Carbon Nanofiber Growth Revealed by in Situ Transmission Electron Microscopy. ACS Nano 2021, 15 (11), 17895–17906. https://doi.org/10.1021/acsnano.1c06189.

(322) Chiang, W.; Sankaran, R. M. Synergistic Effects in Bimetallic Nanoparticles for Low Temperature Carbon Nanotube Growth. Adv. Mater. 2008, 20 (24), 4857–4861. https://doi.org/10.1002/adma.200801006.

(323) Vishwakarma, M.; Thota, N.; Karakulina, O.; Hadermann, J.; Mehta, B. R. Role of Graphene Inter Layer on the Formation of the MoS2-CZTS Interface during Growth. AIP Conference Proceedings 2018, 1953 (May). https://doi.org/10.1063/1.5033000.

(324) Das, S.; Sa, K.; Alam, I.; Raiguru, J.; Subramanyam, B.; Mahanandia, P. Structural and Optical Study of CZTS-Reduced Graphene Oxide Composite towards Photovoltaic Device Application. Materials Today: Proceedings 2019, 17, 131–137. https://doi.org/10.1016/j.matpr.2019.06.410.

(325) Ha, E.; Liu, W.; Wang, L.; Man, H. W.; Hu, L.; Tsang, S. C. E.; Chan, C. T. L.; Kwok, W. M.; Lee, L. Y. S.; Wong, K. Y. Cu2ZnSnS4/MoS2-Reduced Graphene Oxide Heterostructure: Nanoscale Interfacial Contact and Enhanced Photocatalytic Hydrogen Generation. Scientific Reports 2017, 7 (1), 39411. https://doi.org/10.1038/srep39411.

Appendix B: List of Publications

(1) **Sperry, B.**, Luscombe, C. "Ligand pyrolysis during air-free inorganic nanocrystal synthesis," *Chem. Mater.* 2021, 33, 136 – 145. doi: 10.1021/acs.chemmater.0c03088

(2) Huang, Y., Cohen, T., **Sperry, B.**, Larson, H., Nguyen, H., Homer, M., Dou, F., Jacoby, L., Cossairt, B., Gamelin, D., Luscombe, C. "Organic building blocks at inorganic nanomaterial interfaces," *Mater. Horiz.* 2022, 9, 61. doi: 10.1021/d1mh01294k

(3) **Sperry, B.**, Kukhta, N., Huang, Y., Luscombe, C. "Ligand decomposition during nanoparticle synthesis: influence of ligand structure and precursor selection," *Chem. Mater.* 2023, 35, 2, 570 – 583. doi: 10.1021/acs.chemmater.2c03006.

(4) **Sperry, B.**, Dou, F., Dillon, T., Tatum, W., Chapko, M., Pozzo, L. "Addressing energy poverty for initial electrification and post-disaster recovery by deploying small-scale solar in Guatemala and Puerto Rico communities," 2023 (in progress, GRID).

Appendix C: Vita

Breena Sperry grew up in a small town called Mariaville, New York. At a young age, Breena could be described as creative and curious, which first manifested into a passion in art, and later, in science. During this time, sustainability had been at the forefront of Breena's interests, and upon learning of renewable technologies in her high school chemistry class, she was both fascinated by the science and disappointed that these technologies were not more universally adopted, something she aimed to change. At the University of Albany, Breena obtained her B.S. in Nanoscale Engineering with a focus in Renewable Energy. During this time, she was able to conduct academic research on fuel cell catalysis and industry research on fuel cell assemblies. After exploring fuel cells, Breena continued her education by pursing her PhD in Materials Science and Engineering, researching solar cell materials and processing at the University of Washington. She was also able to research and deploy solar technologies as a co-founder and officer for the student group GRID (Global Renewables Infrastructure Development). After consulting for Solar Washington and the Washington State Academy of Sciences, Breena's interest in science due-diligence and communication flourished. In the future, Breena aims to further pursue clean technologies and to apply her scientific knowledge to inform stakeholders, in hopes of leading to a more sustainable world.